2013-01-08

Geomechanical Coupled Modeling of Shear Fracturing in Non-Conventional Reservoirs

Nassir, Mohammad

UNIVERSITY OF CALGARY

Geomechanical Coupled Modeling of Shear Fracturing in Non-Conventional Reservoirs

by

Mohammad Nassir

A THESIS

SUBMITTED TO THE FACULTY OF GRADUATE STUDIES

IN PARTIAL FULFILMENT OF THE REQUIREMENTS FOR THE

DEGREE OF DOCTOR OF PHILOSOPHY

DEPARTMENT OF CHEMICAL AND PETROLEUM ENGINEERING

CALGARY, ALBERTA

JANUARY, 2013

Abstract

Hydraulic fracturing is an essential tool for economical development of shale gas and tight gas reservoirs. Analysis of the performance of fracturing jobs and optimization of the treatment design requires modeling which accounts for all important features of the process and ideally covers both the treatment and post-stimulation production of the well. From micro-seismic monitoring and the stimulated wells production data it is now well established that the productivity of the wells is due not only to the classical tensile single plane fracture (SPF), but to the development of an enhanced permeability region (stimulated reservoir volume or SRV) around it caused by shear fracturing and/or stimulation of existing dual porosity. The shape and size of the SRV, and the permeability enhancement in the SRV depend on both the injection process and on the geomechanics of the reservoir (i.e., development of complex fracturing). Current techniques are not able to predict the SRV dependence on fracturing job and rock mechanics parameters, which precludes any meaningful optimization.

In this work we have developed a new 3-D coupled geomechanical and flow model for analysis and optimization of tight and shale gas stimulation treatments. The formulation includes the dynamic propagation of tensile (SPF) and shear fractures when the failure criteria are met. Non-fractured blocks are assumed to be of linear elastic material; whereas in the failed blocks, fractures and rock compliance matrices are homogenized to form an equivalent compliance matrix. Simple Mohr-Coulomb and tensile failure relationships were used as the criteria for detecting fracture creation. Hyperbolic function is implemented for each fracture normal deformation analysis which will be integrated into the elasto-plastic constitutive model to describe the fracture overall normal and shear deformation. The permeability enhancement during the fracturing process is computed and is the principal coupling between the flow and geomechanics. The region of enhanced permeability with respect to its initially low value presents what is called in the literature the stimulated reservoir volume.

Flexibility of the code to select either tensile or shear fracturing mechanism or combination of both allows various scenarios to be examined. Different cases of 2-D and

3-D simulations are presented which demonstrate some important features of the process. First, it is found that a wide SRV can result in the case where only shear fracturing is the dominant mechanism, and its width depends on the horizontal stress contrast as expected. Second, the loss of elastic coupling due to shear failure and relatively low permeability enhancement of the growing failed region require increasing pumping pressure with time for further failed zone growth, even though the injected fluid is of low viscosity (water). Further, under high injection pressure, an efficient fracture elasto-plastic constitutive model developed drives both maximum and minimum effective stresses to zero or tensile and therefore creation of tensile fracture can be predicted simultaneously with shear fracturing. This will then provide means of modeling proppant transport in some fracturing cases. The examples also show that in order to obtain a relatively wide SRV development, the effective rock cohesion should be of low magnitude. This may be explained by the presence of microfractures and other planes of weaknesses, or by reactivation of pre-existing, sealed natural fractures. Wider SRV propagation is also contributed when the initial reservoir pressure is abnormally high in magnitude. In general, closeness of the reservoir initial conditions to shear failure surface is the key reason for a wide SRV growth.

The new model is a significant step towards development of an integrated predictive tool for the optimization of shale gas development and offers a valuable insight into the (still debated) mechanics of shale stimulation. The approach, based on pseudo-continuum treatment using elasto-plasticity combined with SPF modeling has a number of advantages compared to discrete fracture network modeling which is also being pursued.

Acknowledgement

This research project would not have been possible without the kind support of many people. The author wishes to express his special gratitude to his supervisor, Prof. Tony Settari who was abundantly helpful and offered invaluable assistance, support and guidance during the course of his research project. The author definitely enjoyed the years of studies and research under his supervision. Deepest gratitude is also due to other members of the supervisory committee, Prof. Richard Wan and Dr. Mohammad Ali Bagheri. Without their knowledge and assistance this study would not have been successful. The author would like to express his thank to Prof. Laurence Lines for being a member of his Ph.D. examination committee. It is also his honor to have Prof. Anthony Ingraffea from Cornell Fracture Group as the external examiner in his examination committee.

Special thanks also to Taurus Reservoir Solution Ltd. for providing the GEOSIM software, and to Taurus employees including Dale Walters and Robert (Bob) Bachman for their kind guidance and support. The author would also like to convey thanks to NSERC (Natural Sciences and Engineering Research Council of Canada) and Industry Consortium for research in geomechanical fracturing at the University of Calgary for providing the financial support.

The author would like to express his thanks to all his graduate friends, Somayeh Goodarzi, Vivek Swami and all the fellow students in EnCana Parallel Reservoir Simulation Laboratory especially for sharing the literature and invaluable assistance.

Finally, the author wishes to express his love and gratitude to his beloved wife Reyhaneh, his parents and his parents-in-law for their endless understanding, encouragement and support through the duration of his studies.

Dedication

This dissertation is dedicated to

My wife, Reyhaneh and my parents, Abdollah and Najibeh

with all my love

TABLE OF CONTENETS

List of Tables

List of Figures

List of Symbols, Abbreviations and Nomenclature

Latin letters

A	=	area
b	=	body force vector
c	=	compressibility
d^o	=	dilation angle
D	=	material stiffness matrix
F	=	material compliance matrix, Failure function
f	=	force vector
gp	=	gauss point
J	=	Jacobean matrix
JRC	=	joint roughness coefficient
JCS	=	joint compressive strength
k_n	=	fracture normal stiffness
k_s	=	fracture shear stiffness
k_t	=	fracture tangential stiffness
K	=	permeability, stiffness matrix in finite element
K_f	=	fluid bulk modulus
K_s	=	solid bulk modulus
h	=	hardening/softening coefficient
L	=	length
m	=	mass
N	=	shape function matrix

P	=	pressure
Q	=	Plastic potential function
q	=	fluid injection/production rate
R	=	residual vector
S_0	=	cohesion
S_f	=	fracture spacing
t	=	traction force, time
T	=	fracture transformation matrix
u	=	displacement, velocity
v_j	=	joint aperture
v_m	=	maximum joint closure
V	=	volume
W	=	width
x_1, x_2, x_3	=	three axes in Cartesian coordinates

Greek letters

α	=	angle
γ	=	shear strain/displacement, gravity acceleration
γ_{coef}	=	dilation initiation coefficient
δ	=	shear displacement
ε	=	strain, strain tensor
λ	=	slip multiplier
μ	=	viscosity, peak shear strength

σ	=	normal stress, stress tensor
τ	=	shear stress
ν	=	Poisson's ratio
ϕ	=	porosity, friction angle
ϕ_b	=	basic friction angle
ϕ_r	=	residual friction angle
Ω	=	control volume
$\partial\Omega$	=	boundary of control volume

Subscripts

f	=	fracture
h, v	=	horizontal, vertical
i, j, k	=	grid or element index in x, y and z directions, respectively
min, max	=	minimum, maximum
n	=	time step index
x, y, z	=	three axils in Cartesian coordinates

Superscripts

0	=	initial status
n	=	time step
ν	=	iteration level

CHAPTER 1 - INTRODUCTION

The fabric of most geological formations is often complex and contains different features such as fractures, vugs and inclusions. Micro-fractures, macro-fractures and faults are different types of fractures distinguished by their scales from the smallest to the largest, which span several orders of magnitude. Naturally fractured reservoirs (NFR) usually are known for their abundant number of interconnected conductive fractures which substantially affect the formation fluid flow properties. In other types of reservoirs which are not even recognized as NFR, micro fractures and small non connected fissures usually exist. Although in reservoir modeling these small discontinuous micro-fractures are lumped with matrix flow properties and are often a source of anisotropy (Settari, 2007), under some specific stress conditions they may coalesce to form very conductive, larger scale channels and completely change the formation rock flow properties. Efficient management and production of these types of reservoirs requires access to an accurate, powerful tool to simulate their unusual mechanical and flow behavior. Available simulators for modeling naturally fractured and stimulated (hydraulically fractured) reservoirs are unable to capture some important phenomena which happen in these types of reservoirs. Among them, fracture shear deformation and formation of new fractures caused by shear failure appears to be of primary significance. Its importance stems from the relation of fracture permeability to the aperture of fractures, which is changing due to deformations in the reservoir.

In underground petroleum reservoirs, obtaining mine-back experiment data to study the complexity of fracture network propagation in hydraulic fracturing operation is not practicable. Until recently, the complex physics of fracture propagation was estimated and interpreted by the pressure data analysis. During the past decade microseismic monitoring and tilt fracture mapping technologies have been implemented to characterize many hydraulic fracturing treatments. The results of such mapping reveal that the stimulated zones are quite diverse, ranging from planar tensile fracture to quite complex fracture growth extended across a large region (Weijers et al., 2005; Cipolla et al., 2008).

The majority of treatments have shown off-planar and network type of fracture propagation especially in the stimulation of tight and shale gas reservoirs. The reactivation of the pre-existing planes of weakness (i.e., natural fractures, micro-fractures, fissures) during hydraulic fracturing (in particular shear displacement) trigger the micro seismic events and the observed complexities (Gale et al., 2007; Nassir et al., 2012).

Complex fracturing invalidates some of the basic assumptions made in conventional tensile fracture modeling including elastic coupling or the complete surface integral solutions (Barree and Winterfeld, 1988), constant permeability in the leak-off equation from fracture face and the 1-D assumption of the leak-off. "Elastic coupling" simply means that the entire rock mass is elastically coupled such that all stresses and deformations interact. These assumptions control the tensile fracture net pressure and the growth rate of the fracture wings as well as the containment. Barree & Winterfeld furthered illustrated that the slippage along the planes of pre-existing natural fractures leads to the loss of elastic coupling in the rock mass and each sheared block deforms separately. They concluded that understanding the implications of the slippage and shear failure on the fracturing treatment design requires further work.

In many oilfield operations in naturally fractured, conventional or non-conventional reservoirs including stimulation of coal beds and shale gas formations, SAGD (Steam Associated Gravity Drainage), water flooding, gas injection, CO_2 sequestration and waste water disposal, some type of fluid has to be injected into underground formations. In most of the time, maintaining injection pressure below formation fracturing pressure restricts economical rate of injection, especially when severe formation damage is involved. In stimulation operations, the goal is to fracture the formation intentionally. Therefore, it is of particular interest to investigate the geomechanical phenomena associated with near or above fracturing fluid injection and to determine the respective variation in well injectivity performance. These phenomena include normal/shear deformation of existing fractures and creation of new fractures by shear failure. Such mechanical behavior during high pressure fluid injection usually causes enhancement in formation permeability and is advantageous in field operations.

In a study conducted on conventional hydraulic fracturing, (Ji and Settari, 2008) modeled dynamic propagation of fracture by implementation of a fully coupled reservoir flow, fracture propagation and geomechanics. This approach comprehensively accounts for the changing stress, pressure, permeability and porosity of reservoir as well as their mutual influences. However it is assumed that only a single plane of fracture propagates in the stimulation operation which sometimes is not supported by the field observation and production analysis. In most fluid injection operations, especially in the fields subjected to high deviatoric stresses, the contribution of shear fracturing to the rock permeability enhancement is as crucial as fracture normal opening. Microseisms occurring as a result of shear slippage in the disturbed rock mass in hydraulic fracturing confirm the explained phenomenon (Warpinski and Teufel, 1987; Cipolla et al., 2008).

The influence of fracture normal deformation on permeability has recently been investigated by coupled geomechanical modeling of naturally fractured reservoirs (Bagheri and Settari, 2006); however, the effect of fracture shearing on the mechanical behavior of fractured formations is not well understood. Furthermore, Bagheri's model does not account for dynamic propagation of fractures (normal and shear) in the formation rock. Numerically, dynamic fracture propagation is defined as switching of an initially non-fractured Gauss point to a fractured Gauss point when the stress state reaches a certain failure criterion. Thereby, the main thesis objective is to investigate the effect of fracture shearing phenomena on mechanical and flow properties of the reservoir formation rock. This concept will be later used for modeling dynamic fracturing of initially non-fractured or slightly fractured formations. The critical pore pressure at which shear failure occurs, the orientation of induced fractures within the rock formation and the effect of transition from non-fracture mode to fracture mode on the geomechanics and the flow problems will also be investigated.

1.1 Research objectives

The main goal of the proposed research is to simply model fracture shearing and development of shear fracturing phenomena in the stimulation process of mainly non-conventional reservoirs, by the means of solving numerically the fluid/solid interactions

and the respective constitutive equations. To elaborate more, the objectives of the research study may be listed as follows:

1) developing a rather simple 3-D coupled flow and geomechanical code to test different constitutive models for shear behavior of fractured media and to set up and analyze example problems in large reservoir scale,
2) analysis of stress and deformation variation in fractured media with changes in traction load and pore pressure using the pseudo-continuum approach,
3) modeling of tensile and shear fracturing by pseudo-continuum method in porous media and investigating the initial reservoir conditions under which either tensile or shear fracturing is the dominant fracturing mechanism.

Bagheri and Settari (2006) have extensively investigated the application of a single fracture normal deformation in coupled geomechanical/flow simulation of naturally fractured reservoirs. Ji and Settari (2008) have improved conventional tensile fracture modeling by coupling fracture propagation with geomechanical and flow simulation. This inter-disciplinary research project will continue and extend Bagheri and Settari (2006) approach towards modeling the shear and dilation behavior of jointed rock and Ji and Settari (2008) work towards modeling combined dynamic tensile/shear fracturing. The aim is to better understand the complex physics of the fracturing problem and to implement the model for meaningful optimization of the complex fracturing.

In this work, the candidate has developed a new 3-D coupled geomechanics/ fluid flow model code similar to, but not as complex as the commercial code GEOSIM (used in Bagheri and Settari and in Ji and Settari work). The main advantage of this code is its simplicity which allows one to investigate the effect of different rock joint constitutive models on formation mechanical behavior under various loading conditions. The dynamic tensile/ shear fracturing and the resulting permeability variations in space and time in a coupled fashion can be investigated more in details.

1.2 Methodology and thesis organization

Achieving the goals of this research requires an integrated modeling in complex multidisciplinary areas of coupled fluid flow simulations, rock mechanics and fracture

mechanics. The methodology implemented to achieve the goals of this research study can be summarized as follows:

1. Literature review: the review starts with studying the literature directly pertinent to mechanical behavior of both natural and artificial fractures either separately as a medium or with matrix as pseudo-continuum. Published literature related to hydraulic fracturing during low viscosity fluid injection, coupled flow/ geomechanical simulation, and other relevant subjects is also reviewed. This review is presented in Chapter 2.

2. 3-D model development: Finite Element Method (FEM) is used to develop a 3-D coupled geomechanical - single phase fluid flow code. This code provides a framework for investigating different rock matrix or fracture constitutive models and testing methods of representing fracture networks by pseudo-continuum. In the simulator, fractures are treated in association with the matrix in the form of pseudo continuum for each element. For simplicity, single phase fluid flow FEM model has been developed to more focus on the geomechanical part of fracturing problem. In contrary to finite difference numerical method, FEM can easily handle permeability in the full tensor form with no special treatment such as Multi Point Flow Approximation, MPFA (Bagheri and Settari, 2006). The mathematical statement of the coupled flow and geomechanical system is presented in the first part of Chapter 3, followed by the development of the FEM discretization and the essential details of the numerical solution in Sections 3.1 and 3.2. Tensile and shear fracturing criteria will also be described in Sections 3.3 and 3.4.

3. Single fracture constitutive model with normal and shear mechanical behavior will be explained in detail in Chapter 4. The averaging technique for combining the intact rock and the containing fracture sets known as a “pseudo-continuum” will be also described in this chapter.

4. Model verification: different parts of the developed code will be verified using the existing analytical models in Chapter 5. Single phase fluid flow problems in radial and linear geometries are verified by their respective analytical solutions. A single

fracture deformation will be compared with both analytical and experimental data. The model will be also compared with an existing analytical solution for fractured blocks. 2-D conventional tensile fracturing analytical solution from the literature will be also used for the verification of the respective part in the code.

5. The results of the various combined tensile/shear fracturing models in form of different example problems will be presented in Chapter 6, the Field Application. The conditions under which each of the mechanism prevails will also be investigated in more detail. The input data was selected to be representative of some real shale gas reservoirs to indicate the applicability of our study for modeling hydraulic fracturing in non-conventional reservoirs.

CHAPTER 2 - LITERATURE REVIEW

Hydraulic fracturing was first introduced in the oil and gas industry in 1947 in Hudson gas field in the U.S. to increase the well productivity (Howard and Fast, 1970). The fracturing stimulation operations play a significant role in economical extraction of underground resources including oil, natural gas, geothermal energy or even water. In tight or shale gas and oil reservoirs hydraulic fracturing is a crucial step in each well completion to make the production economical.

In conventional hydraulic fracturing after isolating the interval of interest for stimulation, clear fracturing fluid (pad) is injected at relatively high rate into the interested interval until two wings of tensile fracture open up. Slurry containing proppant is next injected into the opened fracture wings to both continue with fracture propagation and to provide sufficient space for fracture conductivity by the proppant after fracture closure. If the main fracturing fluid is quite viscous such as crosslinked polymer gel, it must contain some chemicals (called breakers) which decompose the crosslinked viscous structure into low viscosity fluid after some time. The treatment fluid can then more easily flow back into the well. The cleaning process is called the “clean-up” or “flow-back” in which the fracture conductivity is recovered to a great extent.

In addition to conventional hydraulic fracturing operations, unconventional fracturing is widely practiced in many field applications including waterfracs, water injection/disposal associated fracturing, induced fracturing in heavy oil and oil sand thermal operations. High fluid leak-off from fracture plane into the formation is a known characteristic of unconventional fracturing in high permeability formations which substantially alters the stress field around the main fracture plane (Settari and Mourits, 1998).

The literature review chapter comprises of four sections. In the first section conventional fracturing is briefly touched upon. Since the main purpose of this work project revolves around off-planar or shear fracturing, mechanical behavior of rock joints is reviewed next. The third part focuses on the methods by which jointed rock

constitutive models are averaged or pseudoized. In the last section some of the studies carried out on dynamic propagation of shear fractures in petroleum reservoirs will briefly be pointed out.

2.1 Conventional tensile fracturing

In conventional fracture modeling the evolving tensile fracture dimensions are related to the injection rate and pumping time. Fracture propagation is governed by material balance between the injected fluid, fluid loss (leak-off) and the rate of increase in fracture volume (Howard and Fast, 1970). The material balance in differential form is written as follows,

$$\frac{dV_f}{dt} = q_i - q_L \tag{2.1}$$

where V_f is the fracture volume, q_i is the fluid injection rate and q_L is called the fluid leak-off rate. The fracture volume can be calculated at any time according to Eq. (2.1) but to calculate the fracture dimensions, one needs to assume specific fracture geometry and pressure distribution in the fracture. Some of the tensile fracture models are illustrated in the following sections.

2.1.1 Carter 2D fracture model

In the Carter 2D fracture model, it is assumed that the fracture grows with constant height and width, and only the fracture length increases along the fracture propagation (Carter, 1957). The pressure drop along the fracture length is negligible and the 1-D fluid leak-off at any point of fracture is a function of the exposure time of the point to the fracturing fluid. The leak-off velocity function is considered to be the same for all points and the function is expressed as below,

$$u_L(x,t) = \frac{C}{\sqrt{t - t_0(x)}}$$
$$C = \left(\frac{kc_t\emptyset}{\pi\mu}\right)^{0.5}\left(P_f - P_R\right) \tag{2.2}$$

where t is time, t_0 is simply the time when the point x is fractured, C is the leak-off coefficient, k and ϕ are the reservoir permeability and porosity, c_t is the total compressibility, μ is the fluid viscosity, P_f and P_R are the fracture and reservoir pressure respectively.

Eq. (2.1) can be rewritten in terms of fracture dimensions and combined with Eq. (2.2) as follows,

$$q_i = 2\int_0^{A_f(t)} u_L dA_f + w\frac{\partial A_f}{\partial t}, \qquad or$$
$$q_i = 2\int_0^{t} u_L(t-\alpha)\frac{dA_f}{d\alpha}d\alpha + w\frac{\partial A_f}{\partial t} \tag{2.3}$$

The solution for the fracture area during fracture propagation was obtained using Laplace transformation and is expressed as below (Howard and Fast, 1970),

$$A_f = 2h_f L_f = \frac{q_i w}{4\pi C^2}\left(e^{Z^2}\mathrm{erfc}(Z) + \frac{2}{\sqrt{\pi}}Z - 1\right) \tag{2.4}$$

where L_f is the fracture length, h_f is the fracture height and Z is a dimensionless time given by $Z = \frac{2C\sqrt{\pi t}}{w}$.

The Carter model gives appropriate solution for two cases. When the leak-off is very small in comparison with the fracture volume, it gives a linear growth of fracture length with time. On the other hand, when leak-off dominates, Eq. (2.4) gives a growth proportional to square root of time. While Carter's solution is not generally used in the design of the stimulation process, the equations for the leak-off are still used in all models which are decoupled from full reservoir flow solution.

2.1.2 KGD fracture model

Khristianovich-type model developed by Geertsma and de Klerk (KGD) is another 2D crack solution in which the fracture height remains constant during fracture propagation. The plane strain mode and smooth closure of the fracture tip (Geertsma and Klerk, 1969) are the two more assumptions in KGD analytical model.

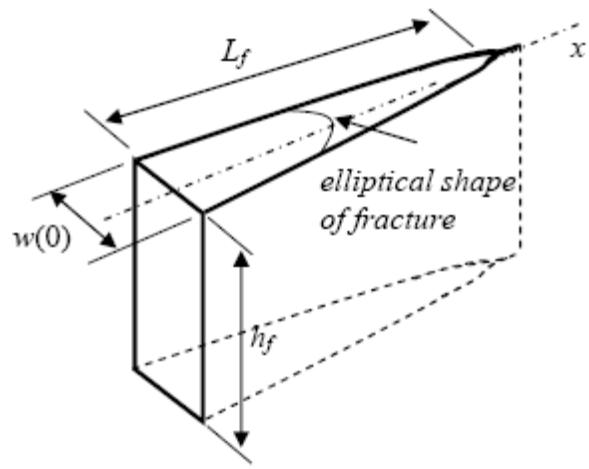

Figure 2.1 – KGD type fracture (from Ji and Settari, 2008)

The pressure gradient along the fracture is inversely proportional to cubic of the fracture width and it is expressed by the following equation (Gidley et al., 1989),

$$\frac{\partial p}{\partial x} = -\frac{12q\mu}{h_f w_f^3} \tag{2.5}$$

The pressure drop is commonly low along the fracture length except close to the fracture tip along which the major portion of the total pressure drop occurs. Since the pressure is almost constant along the fracture, the relationship between the maximum fracture width, length, net pressure and the elastic properties of the surrounding rock is given by the analytical stress solution of a single crack embedded in an infinite plane as follows (England and Green, 1963),

$$w_{max} = \frac{L_f\left(P_{wf} - \sigma_{min}\right)}{\overline{E}} = \frac{L_f P_{net}}{\overline{E}} \tag{2.6}$$

where E is Young' modulus, v is Poisson's ratio, P_{wf} is the wellbore flowing pressure and $\overline{E} = \frac{E}{4}/(1 - v^2)$. The fracture shape vs. x is found to be elliptical except close to the tip.

Eq. (2.4) can also be used for KGD model if the term w is substituted by an average width $\overline{w}$ which is related to the maximum width by $\overline{w} = \frac{\pi}{4} w_{max}$.

2.1.3 Other tensile fracturing models

Other tensile fracture models have extensively been well developed in the literature. Since the main focus of this work is not on single-plane tensile fracturing, the models are briefly pointed here but more details can be found in many references such as Economides (Economides and Nolte, 2000), Settari or Li's works (Settari, 2012; Li and Settari, 2008).

Perkins and Kern model (Perkins and Kern, 1961), further enhanced by Nordgern (Nordgern, 1972) is another 2D model in which the fracture height remains constant as the fracture grows. Pressure in any vertical cross-section is constant vertically, fracture deformation in vertical direction follows plane strain assumption and the maximum opening vertically is in the center of each cross-section. The fracture shape in each cross-section can be obtained by the same equations used for the KGD model, applied in a vertical plane.

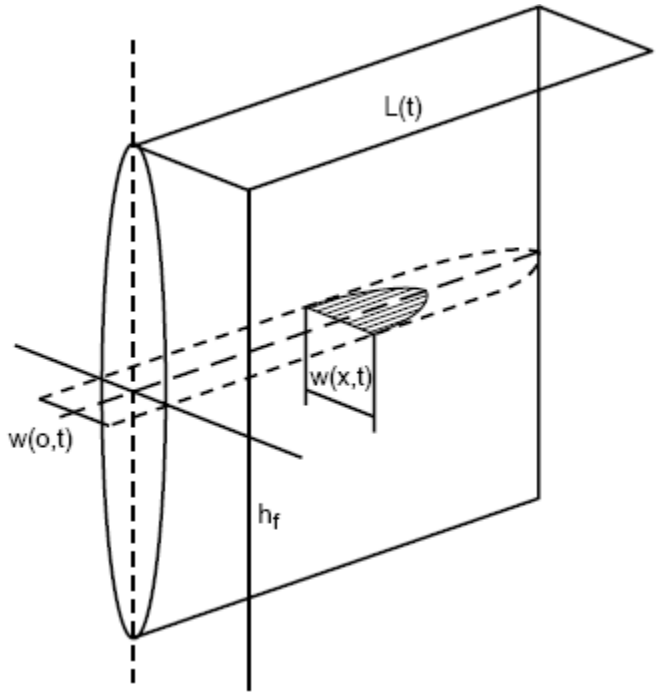

Figure 2.2 – PKN type fracture, figure from (Economides and Nolte, 2000)

For PKN geometry, similarly to KGD model, the fluid flow equations are derived and the relationships between the fracture length, width and injection time based on the fluid and rock properties and the injection rate are obtained.

3D planar fracture models (Clifton and Abou-Sayed, 1981; Cleary et al., 1983; Cleary and Lam, 1983) and pseudo-3D fracture (Settari and Cleary, 1984) models are two other kinds in which the tensile fracture is allowed to propagate along and across the fracture plane perpendicular to the minimum effective stress. In full 3D models the solution of the three dimensional elasticity deformation problem is reduced to a 2D surface integral problem along and across the fracture plane. The fluid flow is solved in the 2D in fracture plane and the fluid flow in the third direction is simply expressed by Carter leak-off term in the 2D solution. Fracture width is controlled by the net pressure acting on the fracture integral surfaces. Fracture stress intensity factor which is a measure of the stress singularity in proximity to the fracture tip controls the growth of the fracture when it reaches a critical value.

In pseudo-3D models however it is assumed that the fracture length is substantially greater than the fracture height such that deformation in each cross-section is independent of the fracture length or the distance from the fracture tip. The fracture width at any point is calculated from the fracture height at the corresponding cross-section y-z (if length is assumed to be extending in x direction) by implementing a 2D plane strain elasticity solution. An important feature of the pseudo 3D model is the key fact that through the use of the concept of “equilibrium height”, the number of independent variables is reduced to two (one space direction and time) compared with three in the full 3D model (two space directions and time). The fracture fluid flow is also reduced to a one dimensional problem along the fracture length with variable cross-sections.

The pseudo 3D model has variously been modified and implemented for practical use by different authors. For example Settari and Cleary (1984, 1986) implemented the 2D PKN model to estimate the fracture length and the 2D plane strain vertical growth solution technique to predict the fracture “dynamic” height which is linked to the lateral model. The “dynamic” height as opposed to “equilibrium” height is the novelty of their proposed model. The lumped pseudo 3D model is another simplified approach in which

the same PKN and KGD models are used to obtain fracture length and height respectively if the fracture length is much larger than the fracture height or well contained (Cleary et al., 1983; Keck et al., 1984). The above is called lumped lateral model. In the lumped vertical model it is assumed that the fracture height grows larger than the length, in which case the PKN model is used for the height calculation whereas the KGD model is applied to obtain the fracture length.

2.2 Mechanical behavior of single fracture

Many rock masses are characterized by joints, fractures and other planes of weakness which reduce the strength and deformation properties of the rock structure (Hoek, 1983; Barton, 1986). Under different loading conditions, joints with weaker strength undergo a relatively higher strain than intact rock. Mechanical deformation of a single fracture usually occurs in a normal and two shear directions, each of which possesses its own stress-strain relationship. The interaction term, dilation, has commonly been investigated along with the shear fracture shear studies. The normal deformation models will be first reviewed briefly and this will be followed by more elaborate literature review of the joint shear models in the next section. It should be brought into consideration that the two terms “fracture” and “joint” are often taken to have the same meaning in the literature and we adopt this terminology throughout this work project.

2.2.1 Fracture normal deformation

Normal deformation of a single joint has been the subject of much active research in the early investigations on mechanical behavior of the jointed rock. It was first formulated by Goodman (1976) and later by Swan (1980) in an empirical approach in which Power law mathematical function was used to approximate the relationship between the joint’s normal stress and normal deformation. Afterward, based on numerous experimental results, Bandis et al. (1983) proposed an empirical hyperbolic model for normal deformation of rock joints. This model is similar, in both formulation approach and functional form, to Goodman’s model; however, each fits best their own experimental results. It is obvious that empirical model cannot provide a reasonable

simulation of joint behavior under all laboratory test conditions. A general exponential function was later suggested by Kulatilake and Maama (2004) which proved to be the best fit for his experimental data in comparison with other empirical models. However, other models only require two experimental data points to be formulated whereas the formulation of general exponential function requires at least three experimental data points. Some theoretical models have also been developed using theories borrowed from different branches of solid mechanics; for example, the theory of plasticity, damage mechanics, and Hertz's contact theory of elasticity (Plesha, 1987; Amadei and Saeb, 1990; Jing, 1990). These approaches may suffer from the limitation that no existing mathematical theory of classical solid mechanics can conveniently represent all aspects of rock joint mechanical behavior. Hence, all approaches have one thing in common: their validity is dependent on the range of the certain experimental conditions under which they can fit the experimental data.

2.2.2 Fracture shear deformation

Under a certain normal load, the shear strength of rock joint is defined as the magnitude of the shear stress required to increase the shear displacement in a joint plane by a unit value. It is usually controlled by the confining normal stress as well as joint properties such as joint surface roughness, joint basic friction angle, joint compressive strength, rock compressive strength, and presence of infilled material. The higher the joint roughness along and the basic friction angle the higher the joint shear strength. The effective roughness of a single joint depends on the ratio of joint compressive strength over confining normal stress (Barton, 1973). The effect of infilled materials hinges on their material mechanical strength; however, it usually raises the value of the joint shear strength. The higher the intact rock compressive strength, the larger the joint compressive strength.

Numerous constitutive relationships have been proposed to model shear stress – shear strain of a single joint which also have extensively been reviewed in the literature (i.e., Karami and Stread, 2007). They usually fall into two categories. The first category is the incremental relationship, consisting of piecewise linear relationship between increment of shear stress and increment of shear strain (Archambault et al., 1990; Boulon and Nova,

1990). These relationships are usually developed by direct shear test under constant normal stress in the laboratory. The second category of constitutive relationships is the elasto-plastic relationship, derived from plasticity theory. In these constitutive models, a joint pre-peak shear behavior is usually assumed to be elastic and recoverable; whereas the post-peak shear behavior is considered to be plastic. Some other authors have modeled the pre-peak shear behavior by shear hardening concept as opposed to the purely elastic shear deformation (i.e., Saada and Bianchini, 1987; Mahin Roosta et al., 2006). In these models, the hardening parameter is assumed to be dependent on the joint roughness or on the plastic portion of the pre-peak shear deformation of the joint.

The knowledge of the peak shear strength and the respective shear displacement are two important issues in modeling the shear behavior of a single fracture. Obtaining peak shear strength criterion for rock joints has been the subject of numerous studies for the past three decades. Patton (1966), Ladanyi and Archambault (1969) and Barton (1973) were among the first to develop a rock joint shear strength criterion. Patton conducted a series of tests on the regular tooth-shape artificial joints under constant normal load. In his study he showed that the shear strength of a saw-tooth joint is controlled by the effective friction angle, summation of basic joint friction angle and the angle asperities build with fracture plane so called dilation angle. Peak shear stresses were expressed by the following equations. For low normal stress values:

$$\tau_p = \sigma_n \tan(\phi_b + \alpha) \tag{2.7}$$

and for relatively higher normal stresses

$$\tau_p = c_0 + \sigma_n \tan(\phi_b) \tag{2.8}$$

where τ_p is the peak shear stress, σ_n is normal stress, ϕ_b is basic friction angle, α is initial asperity or dilation angle and c_0 is cohesion intercept. Figure 2.3 shows a typical sketch of a joint with idealized asperity geometry, the applied normal and shear stresses and the dilation angle. It should be noted that Patton's finding is only valid at low normal stresses where no asperities are worn off.

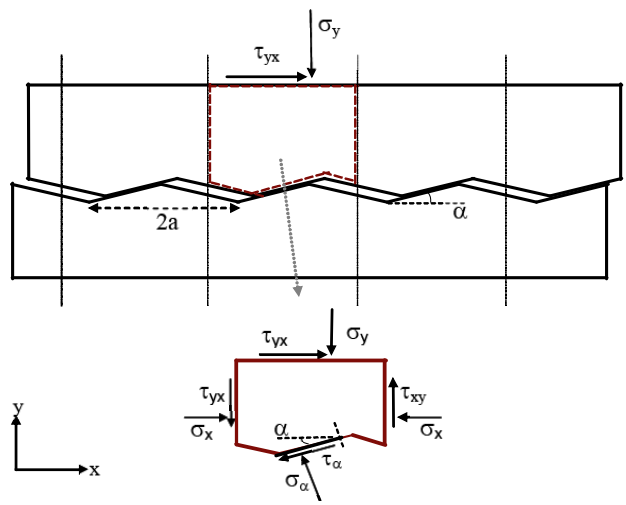

Figure 2.3- A sketch of a joint with idealized asperity geometry (Nassir et. al. 2009)

Jaeger (1971) proposed a non-linear failure criterion instead of the bilinear form of Patton's. At relatively higher normal stresses his criterion approaches Patton's model as shown in Figure 2.4. Another empirical shear strength criterion was suggested by Barton (1973) which represents a continuous failure envelope from low to high normal stresses:

$$\tau_p = \sigma_n \tan\left[JRC \log\left(\frac{JCS}{\sigma_n} \right) + \phi_b \right] \tag{2.9}$$

where *JRC* and *JCS* are the joint roughness coefficient and joint compressive strength, respectively. The first term inside the bracket in Barton's criterion (which is commonly called dilation angle) is an adverse function of normal stress. It implies that when the normal compressive stress increases, the mean effective asperity angle decreases and as a result the slope of the shear stress – normal stress curve becomes less in magnitude.

For unweathered joint surfaces *JCS* is equal to the uniaxial compressive strength of the intact rock. Compressive strength of the weathered rock is estimated to be about 0.25 of uniaxial compressive strength (Barton and Choubey, 1977). In addition, basic friction angle is replaced by residual friction angle, ϕ_r, in the equation above. Barton (1973) and Barton and Choubey (1977) suggested 10 standard profiles for different *JRC* from which by comparison *JRC* of the joint under study can be estimated. To obtain these 10 standard profiles, Barton and Choubey performed the tilt push/pull experiments on over 130 rock specimens. This criterion has the advantage of providing a gradual degradation of friction

angle with respect to increasing normal stress as opposed to Patton's bilinear shear strength criterion.

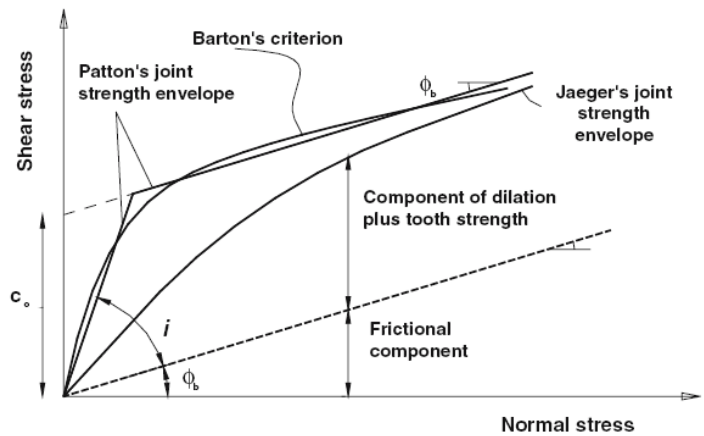

Figure 2.4- Comparison between shear strength criteria of rock joints, (Mahin Roosta et al., 2006)

The applicability of the Barton criterion is limited by the subjectivity in determining the *JRC* from the standard profiles. In addition, it only assumes an average roughness for joint surface asperities, neglecting the localized roughness and the manner in which the first and second order asperities affect the shear behavior of the rock joint. Beer et al. (2002) showed that often inherent errors are involved in estimating the *JRC* values when visual comparison technique is applied. They concluded that only for favorable joint profiles visual inspection provides an accurate estimate of *JRC*. Yang and Chiang (2000) considered the effect of localized roughness on joint surfaces in their study and have shown that the behavior of a composite tooth-shaped joint with two different angled teeth is first dominated by the steeper teeth while the lower ones participate only in the second part of shearing.

Ladanyi and Archambault (1969) provided an extension of Patton's joint model to account for the sliding and shearing mechanisms found in natural rock joints. They characterized joint shear strength in terms of dilation rate and the proportion of contact area that has been sheared off, assuming joint asperities were rigid and the effective asperity angle equals the joint dilation angle. Seidel and Haberfield (1995) have shown that the latter assumption is not always valid and possibly leads to an underestimation of

the joint shear strength if the joint real declining dilation angle is accounted for. Joint dilation angle decreases due to elastic deformation of asperities while by applying the energy principle Seidel and Haberfield proved that the peak frictional resistance remains unchanged. They also demonstrate that both the elastic and plastic behavior of the joint asperity should be considered in order to predict the joint shear strength more accurately.

To better quantify rock joint surface description parameters, some authors have used laser profilometry and fractal methods (Kulatilake et al., 1995; Kulatilake et al., 1998; Gerasseli and Egger, 2003). Kulatilake et al. proposed a peak shear strength criterion for anisotropic rock joints which not only considers the anisotropy but also accounts for the effect of backward and forward shearing directions on the peak shear strength. Afterward, they extended their method to include dilation as well as the effect of shearing through asperities on the peak shear strength. They also used the fractal dimension to characterize joint surface roughness. The effects of internal damage and surface degradation on joint shear strength behavior were not considered in their method. In addition, an average value for joint surface roughness was assigned in the criterion. In another study, Gerasselli and Egger (2003) first introduced three-dimensional surface parameters into a peak shear strength criterion. Then by using triangulation technique to present roughness on joint surface, they proposed a peak shear strength criterion as a function of the roughness and joint contact area in the shearing direction. The contacting area also changes during shearing in their method.

The aforementioned criteria are only used to estimate the peak shear strength. However, a constitutive model is needed to provide the relationship for the pre-peak shear stress and shear displacement in a single joint. Some authors suggested a simple linear model for the pre-peak shear behavior of a joint which can easily be determined when the peak shear stress and the peak shear displacement values are provided (Nguyen and Selvadurai, 1998). The experimental results reveal that this relationship cannot be estimated by a linear approximation. In the analysis of the pre-peak shear behavior Clough and Duncan (1971) non-linear hyperbolic relationship between shear stiffness k_s and normal and shear stresses σ_n and τ has been widely used in the literature and is expressed by

$$k_s = \alpha p_{atm}\left(\frac{\sigma_n}{p_{atm}}\right)^{\beta}\left(1 - R_f\,\frac{\tau}{\tau^p}\right)^2 \tag{2.10}$$

where the parameters α, β and R_f are obtained by the direct shear test in the laboratory and the peak shear stress τ^p is obtained from an appropriate shear failure criterion.

Post-peak shear behavior of a single joint is totally different from the pre-peak and it is completely plastic. Among different existing joint deformation models, the Coulomb friction linear model is perhaps the simplest and the most frequently used one in which the post-peak shear behavior is assumed to be perfectly plastic. In this approach dilation is modeled by a pre-specified angle. This model provides reasonable results for smooth joints in which dilation is not associated with joint shearing (Brady and Brown, 2004). Numerous elastoplastic models exist in the literature (i.e., Ghaboussi et al., 1973; Roberts and Einstein, 1978; Desai and Fishman, 1987; Plesha, 1987; Cundall and Lemos, 1988). In these models the state that separates elastic from plastic behavior is defined by appeal to a yield criterion in the form of peak shear stress, as discussed earlier in this review. Some of the models are capable to model the strain-softening (decrease in shear stress in the plastic stage) often observed in experimental behavior of rough joints through defining a path dependent declining friction angle. For example, Cundall and Lemos (1988) proposed a continuously yielding model to describe shear behavior of rock joints. In their model shear deformation and dilation were considered to be non-linear. Furthermore, the internal mechanism of progressive asperity damage was captured and assumed to be a function of plastic portion of the joint shear displacement.

To define the elastoplastic model, a known set of yield and potential functions are required. The yield function represents the surface at which shear yielding of joint occurs and the gradient of the potential function specifies the plastic flow direction. Idealized two-dimensional saw-tooth pattern for joint asperities, as proposed by Patton, was used by several researchers to define the joint's yield and potential functions (Roberts and Einstein, 1978; Plesha, 1987; Selvadurai and Boulon, 1995). For instance Plesha (1997)

proposed the following yield criterion and plastic potential function for joints with saw-tooth asperities:

$$F = \left|\tau \cos\alpha - \sigma \sin\alpha\right| - \left(\tau \sin\alpha + \sigma \cos\alpha\right)\tan\phi_b \tag{2.11}$$

$$Q = \left|\tau \cos\alpha - \sigma \sin\alpha\right| \tag{2.12}$$

The value of α in the above two equations does not remain constant due to asperity degradation caused by shearing. Plesha assumes that the asperity angle decreases as an exponential function of plastic work produced by shear,

$$\alpha = \alpha_0 \exp\left(-\int_0^{W^p} c dW^p\right) \tag{2.13}$$

where α_0 is the original asperity angle, c is the degradation coefficient and W^p is the plastic work produced by shear stress.

Nguyen and Selvadurai (1998) extended Plesha model to reproduce the mechanical behavior of real joints, such as dilation under shearing as well as strain softening due to surface asperity degradation. They also showed that the effective asperity angle in Plesha's model can be estimated from Barton-Bandis empirical coefficients; joint roughness coefficient (*JRC*) and joint compressive strength (*JCS*) as follows,

$$\alpha = JRC \log\left(\frac{JCS}{\sigma_n}\right) \tag{2.14}$$

Prior to peak shear stress, they assumed a linear relationship between shear stress and shear displacement. To determine the post-peak behavior, they appealed to the classical theory of interface plasticity. The applied yield and potential functions were the same as proposed by Plesha. It should be noted that the two parameters *JRC* and *JCS* are scale dependent and should be corrected when they are used for problems with different joint lengths. For example Barton et. al. (1985) proposed the following empirical equations to correct *JRC* and *JCS* for the length effect,

$$JRC_n = JRC_0 \left[\frac{L_n}{L_0} \right]^{-0.02JRC_0}$$
$$JCS_n = JCS_0 \left[\frac{L_n}{L_0} \right]^{-0.03JRC_0} \tag{2.15}$$

Jing et al. (1994) proposed a three dimensional model for rock joints with anisotropic friction and stress dependency in shear stiffness. They also validated the proposed model by the experimental results conducted on concrete replicas from two natural joint samples. Although 3-D modeling of rock joint mechanical behavior involves more complexity than 2-D model, the proposed 3-D yield and potential functions were comprehensive and at the same time simple enough to describe the joint mechanical behavior in a relatively accurate way. In this study, Jing's approach is first slightly modified and then will be applied in the developed code.

Son et al. (2004) also proposed a new elasto-plastic model for simulating softening phenomenon, dilation and surface degradation of rough rock joint. To calculate the plastic displacements after yielding, the non-associated flow rule was applied. Maksimovic's equation and Lee's empirical formula for joint shear strength were used for yield and plastic potential functions.

Now one may debate which model should be used for numerical simulation of jointed rock in fractured formations. Majority of the aforementioned shear models were formulated to match the shear experimental results obtained in the laboratory. To obtain a better match with the experimental data, some authors have tried to develop relatively more complicated models. In real field practices, there are so many uncertainties in the estimation of the parameters used in these constitutive models. Hence, the most appropriate constitutive model is the one which is rather simple meanwhile is capable of capturing the important aspects of the joint shear behavior such as changes in stress tensor and dilation. Coulomb friction model, Barton and Bandis joint model Barton et al. (1985) and the continuously yielding joint model of Cundall and Lemos (1988) are the three simple joint shear deformability criteria widely used in different codes. Simplicity of these models made them the most frequently used ones in practical applications.

Barton's shear failure criterion has been found to best represent the shear strength of rock joints over a wide range of normal stresses and various joint surfaces. This model will be discussed in more detail in this study in Chapter 4. The elasto-plastic formulation which is used in our work is a revised version of Jing et. al. (1994) model.

2.3 Jointed rock moduli

Numerical simulation of jointed rock masses can be carried out using the explicit (distinct) method or the implicit (continuum) method. The former describes the individual behavior of intact blocks and joints whereas the later employs an equivalent continuum approach which is well adapted for complex engineering problems. One of the most well known explicit methods applied in rock mechanics is the distinct element method (DEM) where the joints and intact rock blocks are modeled discretely (Cundall and Hart, 1992; Morris et al., 2004; Karami and Stread, 2007). From computational point of view, the DEM approach is quite expensive but can be used to calibrate phenomenological continuum models both for porous rock samples and in situ blocky rock masses (Kulatilake et al., 2001; Cho et al., 2007). The advantage of DEM is that it can deal with large deformations of rock masses (block separation, splitting, etc.) in a natural way. The disadvantages are in running time inefficiency and difficulties in modeling non-persistent (discontinuous) joints and cracks.

Effects of discontinuities in different rocks have been also studied in numerous analytical models in the continuum form. Singh (1973) established a continuum characterization for the mechanical properties of the jointed rock by summing the compliances of orthogonal joint sets. Gerrard (1982) and Fossum (1985) derived equivalent elastic properties for jointed rock assuming that both joints and the rock are elastic materials. Cai and Horii (1992) derived equivalent stress–strain response for jointed rock masses by assuming that the rock is elastic while the joints are elasto-plastic. They also accounted for the interactions between the joints. Gerrard and Pande (1985) have considered all the components of jointed reinforced rock to be elasto-visco plastic and derived the respective equivalent material properties.

Alternative methods to model discontinuous media include the discrete-continuum approach, (Lin and Cheng-Yu, 2006), extended finite element method, (Belytschko and Gracie, 2007) where the finite elements containing the joints are treated in a special way, and the 'thin' elements used to model joints (Desai and Fishman, 1987; Wang et al., 2003). Among the aforementioned methods, the continuum or pseudo-continuum technique is widely employed in most commercial codes such as GEOSIM owing to its simplicity and numerical efficiency.

2.4 Some previous studies on shear phenomenon in the reservoir stimulation literature

Geomechanical evidences for shear failure and shear deformation have been observed in many petroleum fields including the Ekofisk field in the Norwegian sector of the North Sea. In this field, the deviatoric stress between the vertical and horizontal stresses has built up during the production period to the shear failure level and shear fractures were created in the chalk formation. Fracture shear deformation is usually associated with dilation and permeability enhancement. This phenomenon justifies the productivity improvement during the field production period despite the pore pressure reduction and reservoir compaction (Teufel and Rhett, 1991). Chin et al. (1993) have tried to simulate the shear induced compaction of the field during the production and water injection by DYNAFLOW code. They obtained some interesting results for the field compaction but the enhancement in the formation rock permeability has not been investigated. Even for the compaction calculations, their model suffers from the simplifying assumption that the strain-stress model for the fractured weakened chalk formation was simply a multiple of the non-weakened chalk formation's strain-stress model.

Some authors have presented alternative techniques for stimulation of fractured tight gas, coal beds or hot dry rock (HDR) reservoirs in which conventional hydraulic fracturing (single planar model) was inadequate. Barree and Winterfeld (1988) have shown that in hydraulic fracture modeling, some assumptions such as elastic coupling implemented in plain-strain or the complete surface integral solutions are invalid for many reservoirs which are susceptible to complex fracturing. These assumptions control

the rate of the growth of fracture wings and containment as well as the predicted net pressure. In their study, it was explained that the shear or slippage along the natural fracture planes or cleats in coals leads to the loss of elastic coupling in the rock mass and each shear block deforms separately. They concluded that additional work is required to fully understand the implications of the slippage and shear failure on the treatment design.

Complex fracture propagation has attempted to be captured based on the interaction between the main induced fracture plane and the pre-existing natural fractures (Hossain et al., 2002; Dahi-Taleghani and Olson, 2009; Rahman and Rahman, 2009; Tao et al., 2009; Chuprakov et al., 2010; Jeffrey et al., 2010; McLennan et al., 2010; Keshavarzi and Mohammadi, 2012). The fracturing complexity is believed to be primarily to natural fractures which have been cemented and sealed during the diagenesis process (Laubach, 2003; Gale et al., 2007) however can act as weak path for non-planar fracture propagation. In some of the studies fracture/ rock geomechanics solution is coupled with the fracture flow solution through iterative or explicit coupling techniques (Settari and Mourits, 1998). In these studies the natural fractures join the main plane when they are touched by the tip of the main fracture. Required refined meshing and high running time have forced majority of the example problems to be limited to 2-D plane-strain assumptions. Lack of a good descriptive constitutive model for the elements containing fractures might be considered as another limitation of such models.

Hossain et al. (2002) in a comprehensive study on the Cooper Basin reservoirs in Central Australian (characterized by high deviatoric stresses and pre-existing natural fractures) investigated the effect of shearing of existing fractures and fissures on the formation rock permeability enhancement in hydraulic fracturing practices. Their model stochastically simulates field-representative natural fractures by processing field data from cores, logs, and other sources. When a fluid is injected into the reservoir, additional poroelastic stress which opposes the fracture pressure ("back stress") develops, and increases the normal stress acting on the fracture plane. The reactive back stress in their study was simply calculated simply from a formula derived for opening of a single fracture in a porous elastic medium. In other words, rather than solving the geomechanical part separately and coupling it with the flow model, the whole

geomechanical effect was incorporated using some empirical correlations and simple equations.

Palmer et al., (2007) have attempted to model the complex phenomena happening in hydraulic fracturing of Barnett shale in the Fort Worth basin. The micro-seismic cloud around the wellbore has convinced them to think of a failed/stimulated reservoir volume (FRV/SRV) containing both shear and tensile fractures rather than assuming only a single plane of tensile fracture. In their study, at first they assumed that a stationary vertical fracture (with fixed height and length) existed and the pore pressure changes were described by confocal elliptical zones when the formation has being stimulated. Next, these zones were examined for shear failure. The stress change due to the compression of the inflated central fracture was approximated by Sneddon equation (Sneddon and Lowengrub, 1969).

The injection permeability was then approximated from the FRV value by trial and error. No orientation was estimated for the stimulated fractures within the failure zone around the wellbore. To apply this approach one needs to know the production histories of different stimulated wells in a specific field as well as each well's net fracturing pressure and the microseismic data which map out the extend of the failed zone. Then it will be possible to model the fracture stimulation for the new wells drilled in the same field. This is a reasonable, practical modeling technique; however, more physics still needs to be integrated in it. Similar to Hossain et. al. approach, their model cannot accurately solve the problem for the displacements and stresses.

In the above studies, a comprehensive model has not yet been developed to distinctly solve the geomechanical part of the proposed problem in parallel, coupled fashion with the flow solution. Dynamic combined tensile and shear fracturing as well as the mechanical behavior of the induced jointed rock by changes in pore pressure require further studies. Moreover, these methods do not allow realistic prediction of the SRV as a function of different parameters and therefore are not capable of optimization of the treatments.

Bagheri and Settari (2006) have extensively investigated the application of a single fracture normal deformation in coupled geomechanical/flow simulation of naturally fractured reservoirs. Ji and Settari (2008) have improved conventional tensile fracture modeling by coupling fracture propagation with geomechanical and flow simulation. In this thesis, we continue the inter-disciplinary research and extend Bagheri and Settari (2006) approach towards modeling the shear and dilation behavior of jointed rock and Ji and Settari (2008) work towards modeling combined dynamic tensile/ shear fracturing using a new coupled geomechanical-flow code which will be described in later Chapters of this thesis.

CHAPTER 3 - MATHEMATICAL MODEL

Modeling dynamic tensile/shear rock fracturing by the means of hydraulic fracturing fluid requires combination of two disciplines; fluid flow and the rock mechanics. In this chapter the 3-D single phase fluid flow formulation by FEM is first described. Mathematical equations for modeling stress-strain behavior of a rock continuum are then formulated again by the means of FEM numerical solution. The technique implemented to employ block by block tensile/shear fracturing will be described at the end. The aim is to develop the formulations to general matrix formats for the ease of coding. The programming language used for coding is FORTRAN which is a rather simple while powerful language.

3.1 Mathematical single phase flow model

3.1.1 Differential Equation and Boundary Conditions

Fluid flow in porous media is usually described by three equations; material balance equation, Darcy transport equation and equation of state. Material balance equation for isothermal single phase flow is written as below (Lewis and Schrefler, 1998),

$$-\nabla^T.\left(\underset{\sim}{u}\right)=-\left(m^T-\frac{m^T D_T}{3K_s}\right).\frac{\partial \underset{\sim}{\varepsilon}}{\partial t}+\left[\frac{1-\phi}{K_s}+\frac{\phi}{K_f}-\frac{1}{(3K_s)^2}m^T D_T m\right]\frac{\partial p}{\partial t}+q \qquad (3.1)$$

where q is the source or sink term, K_s is grain bulk modulus and K_f is the fluid bulk modulus, u is the fluid velocity, D_T is the rock stiffness matrix, ε is the strain term, p is fluid pressure and ϕ is the rock porosity.

Velocity in the above equation is given by Darcy equation as follows,

$$\nabla^T.\left(\frac{\underset{\approx}{K}}{\mu}\nabla\left(p+\gamma_f\, z\right)\right)=-\left(m^T-\frac{m^T D_T}{3K_s}\right).\frac{\partial \underset{\sim}{\varepsilon}}{\partial t}+\left[\frac{1-\phi}{K_s}+\frac{\phi}{K_f}-\frac{1}{(3K_s)^2}m^T D_T m\right]\frac{\partial p}{\partial t}+q \qquad (3.2)$$

in which permeability is a second order tensor.

Note that when pore pressure increases, grain volume decreases; whereas, bulk volume increases.

From Eq. (3.2) we will have

$$\nabla.\left(\frac{\underset{\approx}{K}}{\mu}\nabla\left(p+\gamma_f z\right)\right)=c_{tp}\frac{\partial p}{\partial t}-c_{t\varepsilon}.\frac{\partial \underset{\sim}{\varepsilon}}{\partial t}+q \tag{3.3}$$

where

$$c_{tp}=\frac{1-\phi}{K_s}+\frac{\phi}{K_f}-\frac{1}{\left(3K_s\right)^2}m^T D_T m \tag{3.4}$$

and

$$\underset{\sim t\varepsilon}{c}=m^T-\frac{m^T D_T}{3K_s} \tag{3.5}$$

In the above equation p is a real-valued continuous bounded function. The rate of change in strain is given when the flow module is coupled with geomechanical module.

Eq. (3.2) is usually solved by means of numerical methods as most of the time there is no analytical solution, especially in problems with complex geometries. In the next section the finite element numerical method for solving the differential equation will be explained in detail.

3.1.2 FEM solution for single phase flow problem

In the numerical solution method the differential equation is first discretized over space and time. Applying appropriate boundary conditions will be required next to make the numerical problem well defined. Finally, the system of linear equations is solved by the aid of a proper solver for system of linear equations.

Compared with finite difference method (FDM), finite element method (FEM) has some advantages. General boundary conditions, complex geometry, and variable material properties can easily be handled by FEM. In most non-homogenous grid blocks, permeability is considered to be a 3 by 3 second order tensor with stress dependent elements. Since in finite element approach governing flow differential equation is

integrated over each discretized domain, permeability can be considered in its full tensor form.

In FEM we rewrite Eq. (3.2) in an equivalent weak variational form. A linear space is defined as,

V = { Functions v: v is continuous function on the domain Ω and has a piecewise continuous and bounded first partial derivatives in Ω, and v (Γ) = 0 }

In terms of computation Eq. (3.2) can be written in a more useful, direct formulation. Multiplying it by any $v \in V$, and integrating over Ω, then we have,

$$\int_{\Omega} \nabla . \left(\frac{\underset{\approx}{K}}{\mu} \nabla p \right) v d\Omega = \int_{\Omega} c_{tp} \frac{\partial p}{\partial t} v d\Omega - \int_{\Omega} \underset{\sim t\varepsilon}{c} \frac{\partial \underset{\sim}{\varepsilon}}{\partial t} v d\Omega + \int_{\Omega} q v d\Omega \tag{3.6}$$

If we apply Green's formula on the diffusive term in the above equation, then we will have,

$$\int_{\Gamma} \left(\frac{\underset{\approx}{K}}{\mu} \nabla p \right) v d\Gamma - \int_{\Omega} \left(\frac{\underset{\approx}{K}}{\mu} \nabla p \right) \nabla v d\Omega = \int_{\Omega} c_{tp} \frac{\partial p}{\partial t} v d\Omega - \int_{\Omega} \underset{\sim t\varepsilon}{c} \frac{\partial \underset{\sim}{\varepsilon}}{\partial t} v d\Omega + \int_{\Omega} q v d\Omega \tag{3.7}$$

Since v at boundaries is equal to zero, the left term in the LHS of the above equation will become zero and hence,

$$-\int_{\Omega} \left(\frac{\underset{\approx}{K}}{\mu} \nabla p \right) \nabla v d\Omega = \int_{\Omega} c_{tp} \frac{\partial p}{\partial t} v d\Omega - \int_{\Omega} \underset{\sim t\varepsilon}{c} \frac{\partial \underset{\sim}{\varepsilon}}{\partial t} v d\Omega + \int_{\Omega} q v d\Omega \tag{3.8}$$

Eq. (3.8) is called Galerkin variational or weak form of Eq. (3.6) due to the fact that the test or trial function v is assumed to be zero at all boundaries.

We now construct the FEM for solving Eq. (3.8). First, let's partition the domain into a set of subintervals I_i, and then define the finite element space as below,

V_h = { Functions v: v is continuous function on the domain Ω, v is linear on each subinterval I_i, and v (Γ) = 0 }

Now here the problem is to find $p_h \in V_h$ such that,

$$-\int_{\Omega}\left(\frac{\overset{\approx}{K}}{\mu}\nabla p_h\right)\nabla v d\Omega=\int_{\Omega}c_{tp}\frac{\partial p_h}{\partial t}v d\Omega-\int_{\Omega}\underset{\sim t\varepsilon}{c}\frac{\partial \underset{\sim}{\varepsilon}}{\partial t}v d\Omega+\int_{\Omega}qv d\Omega \tag{3.9}$$

This method is usually called the Galerkin finite element method.

We introduce the basis or shape function $\varphi_i(x_j)\in V_h,\quad i=1,2,\ldots,M,$

$$\varphi_i(x_j)=\begin{cases}1 & if\ i=j\\ 0 & if\ i\neq j\end{cases} \tag{3.10}$$

That is φ_i is a continuous piecewise linear function on Ω such that its value is one at node x_i, ($i=j$) and zero at other nodes. Higher order shape functions would definitely give more accurate results; however for simplicity the linear approximation is implemented in this study. M is the number of nodes in the discretized domain Ω.

We now seek the solution of (1.9) in form of a function $p_h(x)$ which has a unique representation through the basis functions as,

$$p_h(x)=\sum_{i=1}^{M}p_i\varphi_i(x),\quad x\in\Omega \tag{3.11}$$

where p_i is the value of pressure at any node i. If we substitute Eq. (3.11) in Eq. (3.9) and for each j, take v in Eq. (3.9) to be equal to φ_j then we will have,

$$-K_{dij}p_i=K_{tij}\frac{\partial p_i}{\partial t}-\int_{\Omega}\underset{\sim t\varepsilon}{c}\frac{\partial \underset{\sim}{\varepsilon}}{\partial t}\varphi_j d\Omega+Q,\quad i=1,2,\ldots,M \tag{3.12}$$

$j=1,2,\ldots,M$

where

$K_{d,ij}=\int_{\Omega}\left(\frac{\overset{\approx}{K}}{\mu}\nabla\varphi_i\right)\nabla\varphi_j\,d\Omega$, $K_{t,ij}=\int_{\Omega}c_{tp}\varphi_i\varphi_j d\Omega$, $S=\int_{\Omega}\underset{\sim t\varepsilon}{c}\frac{\partial \underset{\sim}{\varepsilon}}{\partial t}\varphi_j d\Omega$ and, $Q=\int_{\Omega}q\varphi_j d\Omega$

This is a system of M algebraic equations involving M unknowns $p_1, p_2, p_3,\ldots, p_M$.

The temporal term in Eq. (3.12) is also discretized over time by Implicit Euler method,

$$\frac{\partial p}{\partial t} = \frac{p^n - p^{n-1}}{\Delta t^n} \tag{3.13}$$

If we substitute Eq. (3.13) in (3.12) then the problem will be discretized both over space and time as follows,

$$-K_{dij} p_i^n = \frac{1}{\Delta t^n} K_{tij} p_i^n - \frac{1}{\Delta t^n} K_{tij} p_i^{n-1} - \int_\Omega c_{\sim t\varepsilon} \frac{\partial \varepsilon}{\partial t} \varphi_j d\Omega + Q, \qquad j = 1,2,\ldots,M \tag{3.14}$$

$$\left(\Delta t^n K_d + K_t\right) p_i^n = \left(K_t\right) p_i^{n-1} + \Delta t^n S - \Delta t^n Q \tag{3.15}$$

where

$$K_{d,ij} = \int_\Omega \left(\frac{\overset{\approx}{K}}{\mu} \nabla \varphi_i \right) \nabla \varphi_j \, d\Omega \quad , \quad K_{t,ij} = \int_\Omega c_{tp} \varphi_i \varphi_j d\Omega \quad , \quad S = \int_\Omega c_{\sim t\varepsilon} \frac{\partial \varepsilon}{\partial t} \varphi_j d\Omega \qquad \text{and,}$$

$$Q = \int_\Omega q \varphi_j d\Omega$$

Eq. **(**3.15) can also be written in form of $\Delta p = (p_i^n - p_i^{n-1})$ as follows,

$$\left(\Delta t^n K_d + K_t\right)\left(p_i^n - p_i^{n-1}\right) = -\Delta t^n K_d p_i^{n-1} + \Delta t^n S - \Delta t^n Q \tag{3.16}$$

In Eq. (3.16) if the pressure coefficient matrices, for transmissibility and storage, are assumed to be at the n-1 time step, the fluid pressure solution is called explicit (with respect to nonlinearities). On the contrary if the coefficients are forced to be at the n time step, implicit formulation of the pressure solution in the matrix form will result.

Since only single phase flow solution has been integrated into the coupled geomechanical-flow code, the explicit treatment of the coefficient matrices has found to be adequate. However, a better approach is to treat the coefficient matrices implicitly and solve the resulting non-linear equations by Newton method. Fracture creation and propagation may substantially alter the transmissibility terms and the Newton method would certainly prevent unnecessary oscillation in the pressure solution.

3.2 Mathematical geomechanical model

Galerkin weighted residual method was employed once more in this work to approximate the solution for mechanical differential equations of geomaterials. Accounting for the body forces and assuming quasi-static condition, force and momentum balance for the bulk material reads,

$$\sigma_{ij,j} + b_j = 0, \quad \sigma_{ij} = \sigma_{ji}\,; \quad i, j = 1,2,3 \tag{3.17}$$

where b_j is the body force per unit volume of the material. The strain and displacement relationship gives,

$$\varepsilon_{ij} = \frac{1}{2}\left(u_{i,\,j} + u_{j,\,i}\right), \quad \varepsilon_{ij} = \varepsilon_{ji}\,; \quad i, j = 1,2,3 \tag{3.18}$$

The variational form of linear momentum balance for the quasistatic loadings will be as follows,

$$W = \int_{\Omega}\left(grad\,\underset{\approx}{N} : \underset{\sim}{\sigma} - \underset{\approx}{N}\,\underset{\sim}{b}\right)dV - \int_{\partial\Omega}\underset{\approx}{N}\,.\underset{\sim}{t}\,dA = 0 \tag{3.19}$$

where N is the shape function and t is the traction vector. In matrix form Eq. (3.19) can be written as follows,

$$\underset{\approx}{K}\,\underset{\sim}{u} = \underset{\sim}{f} \tag{3.20}$$

where,

$$\begin{aligned} \underset{\approx}{K} &= \int_{\Omega}\left(\underset{\approx}{B}^T\,\underset{\approx}{D}^{mat}\,\underset{\approx}{B}\right)d\Omega \quad and \\ \underset{\sim}{f} &= \int_{\partial\Omega}\underset{\approx}{N}^T\,\underset{\sim}{t}\,dA + \int_{\Omega}\underset{\approx}{N}^T\,\underset{\sim}{b}\,dV - \int_{\Omega}\underset{\approx}{B}^T\,\underset{\sim}{m}\,\alpha p\,dV \end{aligned} \tag{3.21}$$

Here K is the stiffness matrix and f is the external force. In the above equations, Ω is the element volume, p is the element pore pressure and α is the Biot`s constant for porous geo-materials. The Biot's constant in terms of the grain and skeleton compressibility is defined as below,

$$\alpha = 1 - \frac{c_{gr}}{c_b} \tag{3.22}$$

3.2.1 Solving 3D Quasi-static problem using FEM

3.2.1.1 General formulation

A detailed FEM formulation of the 3-D quasi-static differential equilibrium problem subjected to different loading conditions will be addressed in this section. It should be noted here that in all of the following formulations the sign convention is positive for tensile stress. Eq. (3.17) after expanding in terms of indices can be rewritten as follows,

$$\begin{aligned}
&\frac{\partial \sigma_{11}}{\partial x_1}+\frac{\partial \sigma_{12}}{\partial x_2}+\frac{\partial \sigma_{13}}{\partial x_3}+b_1=0, && (I)\\
&\frac{\partial \sigma_{12}}{\partial x_1}+\frac{\partial \sigma_{22}}{\partial x_2}+\frac{\partial \sigma_{23}}{\partial x_3}+b_2=0 && (II)\\
&\frac{\partial \sigma_{13}}{\partial x_1}+\frac{\partial \sigma_{23}}{\partial x_2}+\frac{\partial \sigma_{33}}{\partial x_3}+b_3=0 && (III)
\end{aligned} \tag{3.23}$$

where for an infinitesimal control volume, $\sigma_{ij} = \sigma_{ji}$ (momentum balance requirement).

Here to solve the problem, we implement Galerkin variational finite element method in which the trial function and weighting function are chosen to be the same (Kaliakin, 2001). A linear space can be defined as follows:

$U = \{ u$: u is a continuous function on Ω, $\frac{\partial u}{\partial x_1}$ and $\frac{\partial u}{\partial x_2}$ are piecewise continuous and bounded on Ω $\}$

Now let's multiply Eq. (3.23-I) by u_1, Eq. (3.23-II) by u_2 and Eq. (3.23-III) by u_3 with $u_1, u_2, u_3 \in U$ and integrate them over Ω,

$$\begin{aligned}
&\int_\Omega u_1\left(\frac{\partial\left(\sigma'_{11}+\alpha p\right)}{\partial x_1}+\frac{\partial \sigma'_{12}}{\partial x_2}+\frac{\partial \sigma'_{13}}{\partial x_3}+b_1\right)d\Omega=0, && (I)\\
&\int_\Omega u_2\left(\frac{\partial \sigma'_{12}}{\partial x_1}+\frac{\partial\left(\sigma'_{22}+\alpha p\right)}{\partial x_2}+\frac{\partial \sigma'_{23}}{\partial x_3}+b_2\right)d\Omega=0 && (II)\\
&\int_\Omega u_3\left(\frac{\partial \sigma'_{13}}{\partial x_1}+\frac{\partial \sigma'_{23}}{\partial x_2}+\frac{\partial\left(\sigma'_{33}+\alpha p\right)}{\partial x_3}+b_3\right)d\Omega=0 && (III)
\end{aligned} \tag{3.24}$$

If we apply Green's formula on the above equations it results in,

$$\int_{\Gamma} u_1\left(\sigma_{11}\hat{n}_1+\sigma_{12}\hat{n}_2+\sigma_{13}\hat{n}_3\right)d\Gamma-\int_{\Omega}\left(\left(\sigma_{11}^{'}+\alpha p\right)\frac{\partial u_1}{\partial x_1}+\sigma_{12}^{'}\frac{\partial u_1}{\partial x_2}+\sigma_{13}^{'}\frac{\partial u_1}{\partial x_3}\right)d\Omega+\int_{\Omega}u_1\left(b_1\right)d\Omega=0,$$

$$\int_{\Gamma} u_2\left(\sigma_{12}\hat{n}_1+\sigma_{22}\hat{n}_2+\sigma_{23}\hat{n}_3\right)d\Gamma-\int_{\Omega}\left(\sigma_{12}^{'}\frac{\partial u_2}{\partial x_1}+\left(\sigma_{22}^{'}+\alpha p\right)\frac{\partial u_2}{\partial x_2}+\sigma_{23}^{'}\frac{\partial u_2}{\partial x_2}\right)d\Omega+\int_{\Omega}u_2\left(b_2\right)d\Omega=0, \qquad (3.25)$$

$$\int_{\Gamma} u_3\left(\sigma_{13}\hat{n}_1+\sigma_{23}\hat{n}_2+\sigma_{33}\hat{n}_3\right)d\Gamma-\int_{\Omega}\left(\sigma_{13}^{'}\frac{\partial u_3}{\partial x_1}+\sigma_{23}^{'}\frac{\partial u_3}{\partial x_2}+\left(\sigma_{33}^{'}+\alpha p\right)\frac{\partial u_3}{\partial x_2}\right)d\Omega+\int_{\Omega}u_3\left(b_3\right)d\Omega=0$$

Since the above three equations are homogeneous, they can be combined into the form of a single equation as below,

$$\begin{aligned}&\int_{\Gamma}\Big[u_1\left(\sigma_{11}\hat{n}_1+\sigma_{12}\hat{n}_2+\sigma_{13}\hat{n}_3\right)+u_2\left(\sigma_{12}\hat{n}_1+\sigma_{22}\hat{n}_2+\sigma_{23}\hat{n}_3\right)\\&+u_3\left(\sigma_{13}\hat{n}_1+\sigma_{23}\hat{n}_2+\sigma_{33}\hat{n}_3\right)\Big]d\Gamma-\int_{\Omega}\Bigg[\left(\sigma_{11}^{'}+\alpha p\right)\frac{\partial u_1}{\partial x_1}+\left(\sigma_{22}^{'}+\alpha p\right)\frac{\partial u_2}{\partial x_2}+\left(\sigma_{33}^{'}+\alpha p\right)\frac{\partial u_3}{\partial x_3}\\&+\sigma_{12}^{'}\left(\frac{\partial u_1}{\partial x_2}+\frac{\partial u_2}{\partial x_1}\right)+\sigma_{23}^{'}\left(\frac{\partial u_2}{\partial x_3}+\frac{\partial u_3}{\partial x_2}\right)+\sigma_{13}^{'}\left(\frac{\partial u_1}{\partial x_3}+\frac{\partial u_3}{\partial x_1}\right)\Bigg]d\Omega+\int_{\Omega}\left(u_1b_1+u_2b_2+u_3b_3\right)d\Omega=0\end{aligned} \qquad (3.26)$$

The total stress, effective stress and, strain components can also be written in vector form as, $\underset{\sim}{\sigma}^T=\begin{bmatrix}\sigma_{11} & \sigma_{22} & \sigma_{33} & \sigma_{12} & \sigma_{23} & \sigma_{13}\end{bmatrix}$, $\underset{\sim}{\sigma}'^T=\begin{bmatrix}\sigma_{11}^{'} & \sigma_{22}^{'} & \sigma_{33}^{'} & \sigma_{12}^{'} & \sigma_{23}^{'} & \sigma_{13}^{'}\end{bmatrix}$

$$\underset{\sim}{\varepsilon}^T=\begin{bmatrix}\varepsilon_{11} & \varepsilon_{22} & \varepsilon_{33} & \varepsilon_{12} & \varepsilon_{23} & \varepsilon_{13}\end{bmatrix} \qquad (3.27)$$

The second term on the RHS can also be written in vector form as,

$$\begin{aligned}&\int_{\Omega}\Bigg[\left(\sigma_{11}^{'}+\alpha p\right)\frac{\partial u_1}{\partial x_1}+\left(\sigma_{22}^{'}+\alpha p\right)\frac{\partial u_2}{\partial x_2}+\left(\sigma_{33}^{'}+\alpha p\right)\frac{\partial u_3}{\partial x_3}+\sigma_{12}^{'}\left(\frac{\partial u_1}{\partial x_2}+\frac{\partial u_2}{\partial x_1}\right)\\&\qquad+\sigma_{23}^{'}\left(\frac{\partial u_2}{\partial x_3}+\frac{\partial u_3}{\partial x_2}\right)+\sigma_{13}^{'}\left(\frac{\partial u_1}{\partial x_3}+\frac{\partial u_3}{\partial x_1}\right)d\Omega=\int_{\Omega}\underset{\sim}{\varepsilon}^T\left(\underset{\sim}{\sigma}'+\underset{\sim}{m}\,\alpha p\right)d\Omega\end{aligned} \qquad (3.28)$$

where $\underset{\sim}{m}^T=\begin{bmatrix}1 & 1 & 1 & 0 & 0 & 0\end{bmatrix}$

Brick type elements are assumed in the current FEM formulation. The displacement at any point is the sum of the products of displacements at the point and their respective shape functions,

$$\underset{\sim}{u} = \sum_{k=1}^{8} N_k \underset{\sim k}{u} \tag{3.29}$$

or

$$\begin{bmatrix} u_1 \\ u_2 \\ u_3 \end{bmatrix} = N_i \begin{bmatrix} u_{i1} \\ u_{i2} \\ u_{i3} \end{bmatrix} + N_j \begin{bmatrix} u_{j1} \\ u_{j2} \\ u_{j3} \end{bmatrix} + N_m \begin{bmatrix} u_{m1} \\ u_{m2} \\ u_{m3} \end{bmatrix} + N_n \begin{bmatrix} u_{n1} \\ u_{n2} \\ u_{n3} \end{bmatrix} +$$

$$N_p \begin{bmatrix} u_{p1} \\ u_{p2} \\ u_{p3} \end{bmatrix} + N_q \begin{bmatrix} u_{q1} \\ u_{q2} \\ u_{q3} \end{bmatrix} + N_r \begin{bmatrix} u_{r1} \\ u_{r2} \\ u_{r3} \end{bmatrix} + N_s \begin{bmatrix} u_{s1} \\ u_{s2} \\ u_{s3} \end{bmatrix} \tag{3.30}$$

Shape function matrix can be written in the form of

$$\underset{\approx}{N} = \begin{bmatrix} N_i & 0 & 0 & N_j & 0 & 0 & N_m & 0 & 0 & N_n & 0 & 0 \\ 0 & N_i & 0 & 0 & N_j & 0 & 0 & N_m & 0 & 0 & N_n & 0 \\ 0 & 0 & N_i & 0 & 0 & N_j & 0 & 0 & N_m & 0 & 0 & N_n \end{bmatrix}$$

$$\begin{matrix} N_p & 0 & 0 & N_q & 0 & 0 & N_r & 0 & 0 & N_s & 0 & 0 \\ 0 & N_p & 0 & 0 & N_q & 0 & 0 & N_r & 0 & 0 & N_s & 0 \\ 0 & 0 & N_p & 0 & 0 & N_q & 0 & 0 & N_r & 0 & 0 & N_s \end{matrix}\Bigg] \tag{3.31}$$

and,

$$\underset{\sim k}{u}^T = \Big[u_{i1} \quad u_{i2} \quad u_{i3} \quad u_{j1} \quad u_{j2} \quad u_{j3} \quad u_{m1} \quad u_{m2} \quad u_{m3} \quad u_{n1} \quad u_{n2} \quad u_{n3}$$
$$u_{p1} \quad u_{p2} \quad u_{p3} \quad u_{q1} \quad u_{q2} \quad u_{q3} \quad u_{r1} \quad u_{r2} \quad u_{r3} \quad u_{s1} \quad u_{s2} \quad u_{s3} \Big] \tag{3.32}$$

Hence we have,

$$\underset{\sim}{u} = \underset{\approx}{N} \underset{\sim k}{u} \tag{3.33}$$

For linear elastic materials, strain and displacement are related through the following equation,

$$\begin{bmatrix} \varepsilon_{11} \\ \varepsilon_{22} \\ \varepsilon_{33} \\ \Gamma_{12} \\ \Gamma_{13} \\ \Gamma_{23} \end{bmatrix} = \begin{bmatrix} \frac{\partial}{\partial x_1} & 0 & 0 \\ 0 & \frac{\partial}{\partial x_2} & 0 \\ 0 & 0 & \frac{\partial}{\partial x_3} \\ \frac{\partial}{\partial x_2} & \frac{\partial}{\partial x_1} & 0 \\ \frac{\partial}{\partial x_3} & 0 & \frac{\partial}{\partial x_1} \\ 0 & \frac{\partial}{\partial x_3} & \frac{\partial}{\partial x_2} \end{bmatrix} \begin{bmatrix} u_1 \\ u_2 \\ u_3 \end{bmatrix}$$

or

$$\underset{\sim}{\varepsilon} = \underset{\approx}{D}\,\underset{\sim}{u} \tag{3.34}$$

Substituting for the displacement vector

$$\underset{\sim}{\varepsilon} = \underset{\approx}{D}\,\underset{\approx}{N}\,\underset{\sim k}{u} = \underset{\approx}{B}\,\underset{\sim k}{u} \tag{3.35}$$

where the B matrix is derived as below,

$$\underset{\approx}{B} = \underset{\approx}{D}\,\underset{\approx}{N} = \begin{bmatrix} \frac{\partial N_i}{\partial x_1} & 0 & 0 & \cdots & \frac{\partial N_s}{\partial x_1} & 0 & 0 \\ 0 & \frac{\partial N_i}{\partial x_2} & 0 & \cdots & 0 & \frac{\partial N_s}{\partial x_2} & 0 \\ 0 & 0 & \frac{\partial N_i}{\partial x_3} & \cdots & 0 & 0 & \frac{\partial N_s}{\partial x_3} \\ \frac{\partial N_i}{\partial x_2} & \frac{\partial N_i}{\partial x_1} & 0 & \cdots & \frac{\partial N_s}{\partial x_2} & \frac{\partial N_s}{\partial x_1} & 0 \\ \frac{\partial N_i}{\partial x_3} & 0 & \frac{\partial N_i}{\partial x_1} & \cdots & \frac{\partial N_s}{\partial x_3} & 0 & \frac{\partial N_s}{\partial x_1} \\ 0 & \frac{\partial N_i}{\partial x_3} & \frac{\partial N_i}{\partial x_2} & \cdots & 0 & \frac{\partial N_s}{\partial x_3} & \frac{\partial N_s}{\partial x_2} \end{bmatrix} \tag{3.36}$$

In order to continue developing the equations, it is crucial to have an appropriate constitutive model' which in tensor form can be expressed as follows,

$$\underset{\sim}{\sigma}' = D_{\underset{\sim}{mat}}\,\underset{\sim}{\varepsilon} \tag{3.37}$$

With the use of **(**3.37), Eq. (3.28) will become

$$II = \int_{\Omega} \underset{\sim}{\varepsilon}^T \left(\underset{\sim}{\sigma}' + \underset{\sim}{m}\,\alpha p\right) d\Omega = \int_{\Omega} \underset{\sim}{\varepsilon}^T \underset{\approx}{D_{mat}}\,\underset{\sim}{\varepsilon}\, d\Omega + \int_{\Omega} \underset{\sim}{\varepsilon}^T \underset{\sim}{m}\,\alpha p\, d\Omega$$

After substituting displacements for strain we will have

$$\begin{aligned} II &= \int_{\Omega} \underset{\sim k}{u}^T \underset{\approx}{B}^T \underset{\approx}{D_{mat}}\,\underset{\approx}{B}\,\underset{\sim k}{u}\, d\Omega + \int_{\Omega} \underset{\sim k}{u}^T \underset{\approx}{B}^T \underset{\sim}{m}\,\alpha p\, d\Omega \\ &= \underset{\sim k}{u}^T \left(\int_{\Omega} \underset{\approx}{B}^T \underset{\approx}{D_{mat}}\,\underset{\approx}{B} d\Omega \right) \underset{\sim k}{u} + \underset{\sim k}{u}^T \int_{\Omega} \underset{\approx}{B}^T \underset{\sim}{m}\,\alpha p\, d\Omega \end{aligned} \tag{3.38}$$

The first LHS term in Eq. (3.26) contains the traction forces,

$$\bar{t}_{ext}^T = \left[\sigma_{11}\hat{n}_1 + \sigma_{12}\hat{n}_2 + \sigma_{13}\hat{n}_3 \quad \sigma_{12}\hat{n}_1 + \sigma_{22}\hat{n}_2 + \sigma_{23}\hat{n}_3 \quad \sigma_{13}\hat{n}_1 + \sigma_{23}\hat{n}_2 + \sigma_{33}\hat{n}_3\right] = \underset{\sim}{\sigma}.\underset{\sim}{n}$$

$$\underset{\sim}{n}^T = \left[\hat{n}_1 \quad \hat{n}_2 \quad \hat{n}_3\right]$$

and by writing the displacement in vector form $u^T = (u_1, u_2, u_3)$ we will have for traction term,

$$\begin{aligned} I = \int_{\Gamma} \Big[& u_1\left(\sigma_{11}\hat{n}_1 + \sigma_{12}\hat{n}_2 + \sigma_{13}\hat{n}_3\right) + u_2\left(\sigma_{12}\hat{n}_1 + \sigma_{22}\hat{n}_2 + \sigma_{32}\hat{n}_3\right) + \\ & u_3\left(\sigma_{13}\hat{n}_1 + \sigma_{23}\hat{n}_2 + \sigma_{33}\hat{n}_3\right)\Big] d\Gamma = \underset{\sim}{u}^T \int_{\Gamma} N^T \underset{\sim}{\sigma}.\underset{\sim}{n}\, d\Gamma \end{aligned} \tag{3.39}$$

If we consider the body forces then we will have,

$$\underset{\sim k}{u}^T \left(\int_{\Omega} \underset{\approx}{B}^T \underset{\approx}{D_{mat}}\,\underset{\approx}{B} d\Omega \right) \underset{\sim k}{u} + \underset{\sim k}{u}^T \int_{\Omega} \underset{\approx}{B}^T d\Omega\, \underset{\sim}{m}\,\alpha p = \underset{\sim k}{u}^T \int_{\Gamma} N^T \underset{\sim}{\sigma}.\underset{\sim}{n}\, d\Gamma + \underset{\sim k}{u}^T \int_{\Omega} N^T \underset{\sim}{b}\, d\Omega$$

$$\left(\int_{\Omega} \underset{\approx}{B}^T \underset{\approx}{D_{mat}}\,\underset{\approx}{B} d\Omega \right) \underset{\sim k}{u} = \int_{\Gamma} N^T \underset{\sim}{\sigma}.\underset{\sim}{n}\, d\Gamma - \int_{\Omega} \underset{\approx}{B}^T \alpha p\, \underset{\sim}{m}\, d\Omega + \int_{\Omega} N^T \underset{\sim}{b}\, d\Omega \tag{3.40}$$

or

$$\underset{\approx}{K}\,\underset{\sim}{u}_k = \underset{\sim}{f} \tag{3.41}$$

where

$$\underset{\approx}{K} = \int_{\Omega} \underset{\approx}{B}^T D_{mat} \underset{\approx}{B} d\Omega \quad \text{and}$$
$$\underset{\sim}{f} = \int_{\Gamma} N^T \underset{\sim}{\sigma}.\underset{\sim}{n}\, d\Gamma - \int_{\Omega} \alpha \underset{\approx}{B}^T \underset{\sim}{m}\, p d\Omega + \int_{\Omega} N^T \underset{\sim}{b}\, d\Omega \tag{3.42}$$

$\underset{\approx}{K}$ is the total stiffness matrix and $\underset{\sim}{f}$ is called the load vector which here is a summation of traction, pressure and body forces. Obtaining the components of the stiffness matrix is quite straightforward and they can be obtained using the following equation,

$$\underset{\approx}{K} = \int_{\Omega} \underset{\approx}{B}^T D_{mat} \underset{\approx}{B} d\Omega = \int_{-1}^{1}\int_{-1}^{1}\int_{-1}^{1} \underset{\approx}{B}^T D_{mat} \underset{\approx}{B} \det(J) d\xi_1 d\xi_2 d\xi_3 \tag{3.43}$$

From chain rule we know that,

$$\begin{bmatrix} \frac{\partial}{\partial \xi_1} \\ \frac{\partial}{\partial \xi_2} \\ \frac{\partial}{\partial \xi_3} \end{bmatrix} = \begin{bmatrix} \frac{\partial x_1}{\partial \xi_1} & \frac{\partial x_2}{\partial \xi_1} & \frac{\partial x_3}{\partial \xi_1} \\ \frac{\partial x_1}{\partial \xi_2} & \frac{\partial x_2}{\partial \xi_2} & \frac{\partial x_3}{\partial \xi_2} \\ \frac{\partial x_1}{\partial \xi_3} & \frac{\partial x_2}{\partial \xi_3} & \frac{\partial x_3}{\partial \xi_3} \end{bmatrix} \begin{bmatrix} \frac{\partial}{\partial x_1} \\ \frac{\partial}{\partial x_2} \\ \frac{\partial}{\partial x_3} \end{bmatrix} = J \begin{bmatrix} \frac{\partial}{\partial x_1} \\ \frac{\partial}{\partial x_2} \\ \frac{\partial}{\partial x_3} \end{bmatrix} \tag{3.44}$$

where J is the Jacobian matrix.

The above equation can be expressed in another form as,

$$\begin{bmatrix} \frac{\partial}{\partial x_1} \\ \frac{\partial}{\partial x_2} \\ \frac{\partial}{\partial x_3} \end{bmatrix} = \begin{bmatrix} \frac{\partial \xi_1}{\partial x_1} & \frac{\partial \xi_2}{\partial x_1} & \frac{\partial \xi_3}{\partial x_1} \\ \frac{\partial \xi_1}{\partial x_2} & \frac{\partial \xi_2}{\partial x_2} & \frac{\partial \xi_3}{\partial x_2} \\ \frac{\partial \xi_1}{\partial x_3} & \frac{\partial \xi_2}{\partial x_3} & \frac{\partial \xi_3}{\partial x_3} \end{bmatrix} \begin{bmatrix} \frac{\partial}{\partial \xi_1} \\ \frac{\partial}{\partial \xi_2} \\ \frac{\partial}{\partial \xi_3} \end{bmatrix} = J^{-1} \begin{bmatrix} \frac{\partial}{\partial \xi_1} \\ \frac{\partial}{\partial \xi_2} \\ \frac{\partial}{\partial \xi_3} \end{bmatrix} \tag{3.45}$$

Since the shape functions are all given in local coordinates (ξ_1, ξ_2, ξ_3), elements of the B matrix in Eq. (3.36) should be transformed from global coordinates into local coordinates as follows,

$$\frac{\partial N_k}{\partial x_1} = \frac{\partial N_k}{\partial \xi_1}\frac{\partial \xi_1}{\partial x_1} + \frac{\partial N_k}{\partial \xi_2}\frac{\partial \xi_2}{\partial x_1} + \frac{\partial N_k}{\partial \xi_3}\frac{\partial \xi_3}{\partial x_1}, \quad k = i, j, m, n, p, q, r, s$$

$$\frac{\partial N_k}{\partial x_2} = \frac{\partial N_k}{\partial \xi_1}\frac{\partial \xi_1}{\partial x_2} + \frac{\partial N_k}{\partial \xi_2}\frac{\partial \xi_2}{\partial x_2} + \frac{\partial N_k}{\partial \xi_3}\frac{\partial \xi_3}{\partial x_2}, \quad k = i, j, m, n, p, q, r, s$$

$$\frac{\partial N_k}{\partial x_3} = \frac{\partial N_k}{\partial \xi_1}\frac{\partial \xi_1}{\partial x_3} + \frac{\partial N_k}{\partial \xi_2}\frac{\partial \xi_2}{\partial x_3} + \frac{\partial N_k}{\partial \xi_3}\frac{\partial \xi_3}{\partial x_3}, \quad k = i, j, m, n, p, q, \quad (3.46)$$

or

$$\frac{\partial N_k}{\partial x_1} = \frac{\partial N_k}{\partial \xi_1} J_{11}^{-1} + \frac{\partial N_k}{\partial \xi_2} J_{12}^{-1} + \frac{\partial N_k}{\partial \xi_3} J_{13}^{-1}, \quad k = i, j, m, n, p, q, r, s$$

$$\frac{\partial N_k}{\partial x_2} = \frac{\partial N_k}{\partial \xi_1} J_{21}^{-1} + \frac{\partial N_k}{\partial \xi_2} J_{22}^{-1} + \frac{\partial N_k}{\partial \xi_3} J_{23}^{-1}, \quad k = i, j, m, n, p, q, r, s$$

$$\frac{\partial N_k}{\partial x_3} = \frac{\partial N_k}{\partial \xi_1} J_{31}^{-1} + \frac{\partial N_k}{\partial \xi_2} J_{32}^{-1} + \frac{\partial N_k}{\partial \xi_3} J_{33}^{-1}, \quad k = i, j, m, n, p, q, \quad (3.47)$$

Therefore, matrix B will become

$$\underset{\approx}{B} = \underset{\approx}{D}\,\underset{\approx}{N} = \begin{bmatrix} \frac{\partial N_i}{\partial \xi_1}\frac{\partial \xi_1}{\partial x_1} + \frac{\partial N_i}{\partial \xi_2}\frac{\partial \xi_2}{\partial x_1} + \frac{\partial N_i}{\partial \xi_3}\frac{\partial \xi_3}{\partial x_1} & 0 & \cdots \\ 0 & \frac{\partial N_i}{\partial \xi_1}\frac{\partial \xi_1}{\partial x_2} + \frac{\partial N_i}{\partial \xi_2}\frac{\partial \xi_2}{\partial x_2} + \frac{\partial N_i}{\partial \xi_3}\frac{\partial \xi_3}{\partial x_2} & \cdots \\ \vdots & \vdots & \ddots \end{bmatrix} \quad (3.48)$$

Since a linear shape function has been implemented here in the FEM formulation, the integration in Eq. (3.43) can be carried out by simply summing the respective

integrant values at eight Gauss points with the following coordinates in the local coordinates system,

$$
\begin{aligned}
gp(1) &= \left\{-1/\sqrt{3} \quad -1/\sqrt{3} \quad -1/\sqrt{3}\right\} \\
gp(2) &= \left\{1/\sqrt{3} \quad -1/\sqrt{3} \quad -1/\sqrt{3}\right\} \\
gp(3) &= \left\{1/\sqrt{3} \quad 1/\sqrt{3} \quad -1/\sqrt{3}\right\} \\
gp(4) &= \left\{-1/\sqrt{3} \quad 1/\sqrt{3} \quad -1/\sqrt{3}\right\} \\
gp(5) &= \left\{-1/\sqrt{3} \quad -1/\sqrt{3} \quad 1/\sqrt{3}\right\} \\
gp(6) &= \left\{1/\sqrt{3} \quad -1/\sqrt{3} \quad 1/\sqrt{3}\right\} \\
gp(7) &= \left\{1/\sqrt{3} \quad 1/\sqrt{3} \quad 1/\sqrt{3}\right\} \\
gp(8) &= \left\{-1/\sqrt{3} \quad 1/\sqrt{3} \quad 1/\sqrt{3}\right\}
\end{aligned}
\tag{3.49}
$$

3.2.1.2 Load vector

Different types of loads can be applied depending on the kind of the problem which is being dealt with. In order to calculate the traction term in Eq. (3.42), the matrix of the shape functions needs to be expanded in terms of local coordinates (ξ_1, ξ_2, ξ_3) as below,

$$
\underset{\approx}{N}^T = \begin{bmatrix} N_i & 0 & 0 \\ 0 & N_i & 0 \\ 0 & 0 & N_i \\ \vdots & \vdots & \vdots \\ N_s & 0 & 0 \\ 0 & N_s & 0 \\ 0 & 0 & N_s \end{bmatrix} = \frac{1}{8}\begin{bmatrix}
(1+\xi_1)(1+\xi_2)(1+\xi_3) & 0 & 0 \\
0 & (1+\xi_1)(1+\xi_2)(1+\xi_3) & 0 \\
0 & 0 & (1+\xi_1)(1+\xi_2)(1+\xi_3) \\
(1-\xi_1)(1+\xi_2)(1+\xi_3) & 0 & 0 \\
0 & (1-\xi_1)(1+\xi_2)(1+\xi_3) & 0 \\
0 & 0 & (1-\xi_1)(1+\xi_2)(1+\xi_3) \\
\vdots & \vdots & \vdots \\
(1+\xi_1)(1-\xi_2)(1-\xi_3) & 0 & 0 \\
0 & (1+\xi_1)(1-\xi_2)(1-\xi_3) & 0 \\
0 & 0 & (1+\xi_1)(1-\xi_2)(1-\xi_3)
\end{bmatrix}
\tag{3.50}
$$

The product of the transpose of the shape function matrix and the traction vector is expressed as,

$$\underset{\approx}{N}^T \underset{\sim}{\sigma}.\underset{\sim}{n} = \underset{\approx}{N}^T \begin{bmatrix} \sigma_{11}\hat{n}_1 + \sigma_{12}\hat{n}_2 + \sigma_{13}\hat{n}_3 \\ \sigma_{12}\hat{n}_1 + \sigma_{22}\hat{n}_2 + \sigma_{23}\hat{n}_3 \\ \sigma_{13}\hat{n}_1 + \sigma_{23}\hat{n}_2 + \sigma_{33}\hat{n}_3 \end{bmatrix} = \frac{1}{8}\begin{bmatrix} (1+\xi_1)(1+\xi_2)(1+\xi_3)(\sigma_{11}\hat{n}_1 + \sigma_{12}\hat{n}_2 + \sigma_{13}\hat{n}_3) \\ (1+\xi_1)(1+\xi_2)(1+\xi_3)(\sigma_{12}\hat{n}_1 + \sigma_{22}\hat{n}_2 + \sigma_{23}\hat{n}_3) \\ (1+\xi_1)(1+\xi_2)(1+\xi_3)(\sigma_{13}\hat{n}_1 + \sigma_{23}\hat{n}_2 + \sigma_{33}\hat{n}_3) \\ (1-\xi_1)(1+\xi_2)(1+\xi_3)(\sigma_{11}\hat{n}_1 + \sigma_{12}\hat{n}_2 + \sigma_{13}\hat{n}_3) \\ (1-\xi_1)(1+\xi_2)(1+\xi_3)(\sigma_{12}\hat{n}_1 + \sigma_{22}\hat{n}_2 + \sigma_{23}\hat{n}_3) \\ (1-\xi_1)(1+\xi_2)(1+\xi_3)(\sigma_{13}\hat{n}_1 + \sigma_{23}\hat{n}_2 + \sigma_{33}\hat{n}_3) \\ \vdots \\ (1+\xi_1)(1-\xi_2)(1-\xi_3)(\sigma_{11}\hat{n}_1 + \sigma_{12}\hat{n}_2 + \sigma_{13}\hat{n}_3) \\ (1+\xi_1)(1-\xi_2)(1-\xi_3)(\sigma_{12}\hat{n}_1 + \sigma_{22}\hat{n}_2 + \sigma_{23}\hat{n}_3) \\ (1+\xi_1)(1-\xi_2)(1-\xi_3)(\sigma_{13}\hat{n}_1 + \sigma_{23}\hat{n}_2 + \sigma_{33}\hat{n}_3) \end{bmatrix} \tag{3.51}$$

Now we must integrate each term of the above vector over the boundary faces of Γ. For example, if the implemented brick type element is a cubic rectangle with the length of L, width of W and height of H, the integration for the first term becomes,

$$\begin{aligned} &\frac{1}{8}\int_{\Gamma=\Gamma_1+\Gamma_2+\Gamma_3+\Gamma_4+\Gamma_5+\Gamma_6} (1+\xi_1)(1+\xi_2)(1+\xi_3)(\sigma_{11}\hat{n}_1 + \sigma_{12}\hat{n}_2 + \sigma_{13}\hat{n}_3)|J|d\Gamma \\ &= \frac{1}{4}\int_{\Gamma_2} (1+\xi_2)(1+\xi_3)(\sigma_{11}\hat{n}_1 + \sigma_{12}\hat{n}_2 + \sigma_{13}\hat{n}_3)(\hat{n}_1)\left(\frac{LH}{4}\right)d\xi_2 d\xi_3 \\ &+ \frac{1}{4}\int_{\Gamma_4} (1+\xi_1)(1+\xi_3)(\sigma_{11}\hat{n}_1 + \sigma_{12}\hat{n}_2 + \sigma_{13}\hat{n}_3)(\hat{n}_2)\left(\frac{WH}{4}\right)d\xi_1 d\xi_3 \\ &+ \frac{1}{4}\int_{\Gamma_6} (1+\xi_1)(1+\xi_2)(\sigma_{11}\hat{n}_1 + \sigma_{12}\hat{n}_2 + \sigma_{13}\hat{n}_3)(\hat{n}_3)\left(\frac{WL}{4}\right)d\xi_1 d\xi_2 \\ &= \frac{WLH}{4}\left(\frac{\sigma_{11}}{W} + \frac{\sigma_{12}}{L} + \frac{\sigma_{13}}{H}\right) \end{aligned} \tag{3.52}$$

Where the six faces are defined as

$$\Gamma_1 = \{\xi_1 = -1,\ \xi_2 \in \{-1,1\},\ \xi_3 \in \{-1,1\}\},\quad \Gamma_2 = \{\xi_1 = +1,\ \xi_2 \in \{-1,1\},\ \xi_3 \in \{-1,1\}\},$$

$$\Gamma_3 = \{\xi_2 = -1,\ \xi_1 \in \{-1,1\},\ \xi_3 \in \{-1,1\}\},\quad \Gamma_4 = \{\xi_2 = +1,\ \xi_1 \in \{-1,1\},\ \xi_3 \in \{-1,1\}\},$$

$$\Gamma_5 = \{\xi_3 = -1,\ \xi_1 \in \{-1,1\},\ \xi_2 \in \{-1,1\}\},\quad \Gamma_6 = \{\xi_3 = +1,\ \xi_1 \in \{-1,1\},\ \xi_2 \in \{-1,1\}\}$$

Finally the traction vector is reduced to the following format,

$$\underset{\sim}{f} = \int_{\Gamma} \underset{\approx}{N}^{T} \underset{\sim}{\bar{t}} d\Gamma = \frac{W^{th} L^{th} H^{th}}{4} \begin{bmatrix} \frac{\sigma_{11}}{W^{th}} + \frac{\sigma_{12}}{L^{th}} + \frac{\sigma_{13}}{H^{th}} \\ \frac{\sigma_{12}}{W^{th}} + \frac{\sigma_{22}}{L^{th}} + \frac{\sigma_{23}}{H^{th}} \\ \frac{\sigma_{13}}{W^{th}} + \frac{\sigma_{23}}{L^{th}} + \frac{\sigma_{33}}{H^{th}} \\ -\frac{\sigma_{11}}{W^{th}} + \frac{\sigma_{12}}{L^{th}} + \frac{\sigma_{13}}{H^{th}} \\ \vdots \\ -\frac{\sigma_{11}}{W^{th}} - \frac{\sigma_{12}}{L^{th}} + \frac{\sigma_{13}}{H^{th}} \\ \vdots \\ \frac{\sigma_{11}}{W^{th}} - \frac{\sigma_{12}}{L^{th}} + \frac{\sigma_{13}}{H^{th}} \\ \vdots \\ \frac{\sigma_{11}}{W^{th}} + \frac{\sigma_{12}}{L^{th}} - \frac{\sigma_{13}}{H^{th}} \\ \vdots \\ -\frac{\sigma_{11}}{W^{th}} + \frac{\sigma_{12}}{L^{th}} - \frac{\sigma_{13}}{H^{th}} \\ \vdots \\ -\frac{\sigma_{11}}{W^{th}} - \frac{\sigma_{12}}{L^{th}} - \frac{\sigma_{13}}{H^{th}} \\ \vdots \\ \frac{\sigma_{11}}{W^{th}} - \frac{\sigma_{12}}{L^{th}} - \frac{\sigma_{13}}{H^{th}} \\ \vdots \end{bmatrix} \tag{3.53}$$

Since quasi-static solution is followed above, the traction terms in nodes inside the volume surrounded by other nodes in total traction load compilation will become zero.

To calculate the load induced by changes in the element pressure, simple integration over the volume of each element is required. In Eq. (3.16) the pressure terms are the continuum pressure at the nodes of the meshed system. In order to obtain the load vector resulting from the pressure change in (3.42), the pressure terms at the Gauss integration points are required. Here we implement linear interpolation function to obtain the Gauss point pressure from the respective nodal pressure. B transpose is given in Eq. (3.48) and α (the Biot's constant) is given by the following equation,

$$\alpha = 1 - \frac{K_b}{K_{gr}} \tag{3.54}$$

where K_b is the bulk modulus and K_{gr} is the grain modulus.

3.2.1.3 FEM solution flowchart

The FEM solution flowchart is depicted in Figure 3.1. The model is first initialized based on the problem initial effective stress and displacement. The stiffness matrix for each element is then calculated and compiled together with matrices for other elements to obtain the global or total stiffness matrix. At the current time level the internal force vector is calculated from the current effective stress by

$$\underset{\sim}{F}_{Int}\Big|_n = \int_{\Omega} \underset{\approx}{B}^T \underset{\sim}{\sigma}'_n \, d\Omega \tag{3.55}$$

All incremental loads (i.e., pore pressure, temperature and traction) are calculated and the external force is calculated using the following equation,

$$\underset{\sim}{F}_{ext} = \underset{\sim}{F}_{Int}\Big|_n + \Delta \underset{\sim}{F}_{ext} \tag{3.56}$$

The residual force vector is defined as the difference between the external force and the internal force vectors as follows,

$$\underset{\sim}{R} = \underset{\sim}{F}_{ext} - \underset{\sim}{F}_{Int} \tag{3.57}$$

Now it is the time to solve the system of linear equations for the displacement vector. Incremental displacement and strain vectors for each element can then be obtained from the global displacement vector and Eq. (3.35). Next, the effective stress for each element must be updated for the strain increment. By knowing the updated effective stress, the internal force vector for each element after any Newton iteration can then be calculated by Eq. (3.55). If the material constitutive model is linear elastic, the calculated total internal vector will be the same as the total external force vector which means that the use of more iterations is not needed. However, if the constitutive model is non-linear, the obtained total internal force is not usually the same as total external force vector (i.e., forces are out of balance). In this case the difference between the total external and internal forces is applied to the solution in subsequent iterations until the norm of the

residual vector falls below a specified small convergence norm. The iteration technique (called Newton Iteration) is widely used in FEM codes to eliminate out of balance forces.

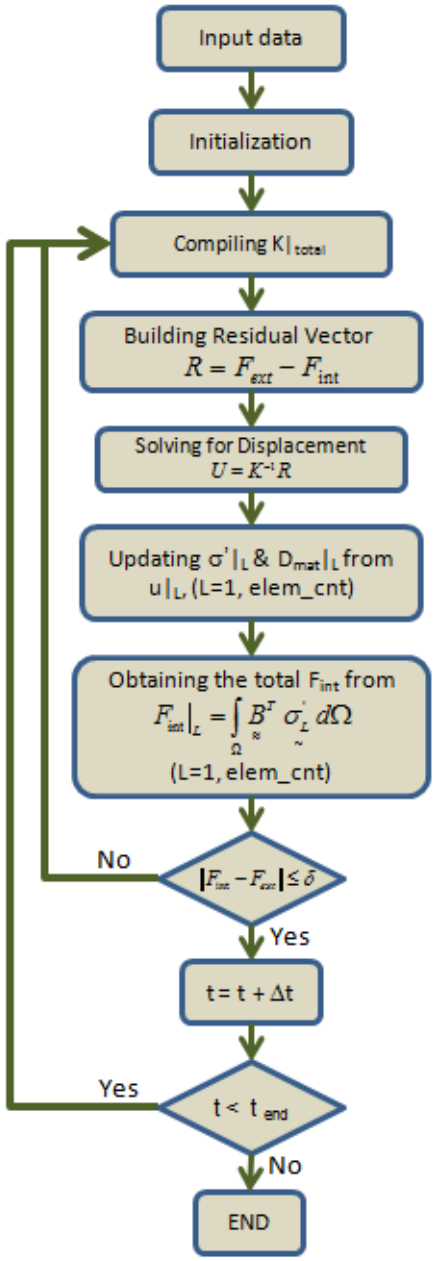

Figure 3.1 – Geomechanical loop flowchart

3.2.1.4 More on updating the stress vectors

In any Newton iteration, the effective stresses should be updated. The procedure is rather straightforward. After Eq. (3.41) has been solved for the displacement, the respective nodal displacements for any element are extracted from the total displacement vector. Eq. (3.35) is next used to find each element's strain tensor from its respective nodal displacements. In order to update the effective stress, Eq. (3.37) can simply be used, if the D matrix remains constant with changes in effective stress. Otherwise integration of the D matrix over sub increment of strain will be required,

$$\underset{\sim}{\sigma}'_{plus} - \underset{\sim}{\sigma}'_{curr} = \int_{\underset{\sim}{\varepsilon}_{curr}}^{\underset{\sim}{\varepsilon}_{plus}} \underset{\approx}{D}_T \, d\underset{\sim}{\varepsilon} \tag{3.58}$$

where the above integration for the fractured block is carried out by a numerical technique. Changes in total stress can be obtained from changes in the effective stresses and changes in the pressure according to the following equation,

$$\Delta\sigma = \Delta\sigma' - \alpha\Delta p \tag{3.59}$$

where the variation in the fluid pressure in the above equation comes from the fluid flow solution.

3.2.1.5 Internal force

In Eq. (3.40), if the nodal displacement term is moved into the left integral expression, the product of the *B* matrix and *u* vector will give the strain of the element, ε. Finally the integration of the product of B transpose and strain over the element volume will result in a kind of force which is called the element internal force,

$$\left(\int_{\Omega} \underset{\approx}{B}^T \underset{\approx}{D}_{mat} \underset{\approx}{B} d\Omega\right) \underset{\sim}{u}_k = \left(\int_{\Omega} \underset{\approx}{B}^T \underset{\approx}{D}_{mat} \left(\underset{\approx}{B} \underset{\sim}{u}_k\right) d\Omega\right) = \int_{\Omega} \underset{\approx}{B}^T \underset{\sim}{\sigma}' d\Omega = F_{Int} \tag{3.60}$$

In majority of real rock mechanical problems, the rock stiffness or the D matrix is a function of stress and varies within each time step solution. Therefore the resultant

internal force is not usually equal to the external force vector which necessitates the use of Newton iteration to eliminate these out of balance forces.

3.2.1.6 Divergence control in Newton solution

The solution technique implemented in the code developed in this thesis is the full Newton iteration in which the tangent matrix is updated at any iteration. A faster but less stable technique is 'quasi-Newton' method where the tangent matrix is calculated only at the beginning of a time step. The latter technique works well for problems with small degrees of non-linearity; however, the injection/fracturing problem in this study is highly non-linear which requires the full Newton method implication. The main source of the non-linearity comes from the normal deformation of a fracture and the substantial changes in the normal stiffness ranging from zero to infinity within quite subtle change of aperture.

In order to make the Newton method globally convergent, one needs to implement a line search algorithm in which at any iteration and after the full Newton update, the residual vector norm is checked to be less than the residual norm calculated from the previous iteration. In case of divergence (i.e., increasing norm), the Newton update is scaled back until the updated state is a better solution compared with the current state. Cutting the Newton update into half is an easy way to obtain the scaling parameter; but the optimum technique is to find the minimum of a quadratic or cubic functions for the first and subsequent steps respectively (Dennis and Schnabel, 1983; Wawrzynek, 1997).

At any Newton iteration we will have two states: the current and updated. Current state refers to the properties which have successfully been calculated from the previous iteration. The residual vector norm with the negative sign at the current state is called the initial slope for the search line which is defined as $n_{ini} = -norm(R_c)$. A measure of the quality of the solution, m, for the current state can also be defined as $m_c = m_{ini} = norm(R_c)/2$.

When the current residual vector is applied to the system of linear equations with updated tangent, a displacement vector is obtained which is called the Newton displacement. Now the question is: For obtaining the trial displacement, should the whole

Newton displacement be added to the current displacement vector or should only a fraction of it (λ) be used? This is expressed by

$$\Delta u_t = \Delta u_C + \lambda\, \Delta u_N \tag{3.61}$$

For the first step λ is assumed to be 1; accordingly the internal force and the quality of solution at the plus step can be calculated ($m_p = norm(R_p)/2$). If m_p is less than m_c, then we proceed with λ = 1; otherwise a quadratic model is used to obtain an approximate for λ only for the first step as follows:

$$\lambda = \frac{-n_{ini}}{2\left(m_p - m_c - n_{ini}\right)} \tag{3.62}$$

When λ is known, the trial displacement can be obtained from Eq. (3.61). Accordingly the new internal force and the new "plus" quality of solution can be calculated ($m_p = norm(R_p)/2$). m_p will again be checked to be less than m_c, if it is not, then one needs to minimize a cubic function to find a better approximation for λ as below,

$$\lambda = \frac{-b + \sqrt{b^2 - 3an_{ini}}}{3a} \tag{3.63}$$

Where a and b can be obtained by the following equations,

$$\begin{Bmatrix} a \\ b \end{Bmatrix} = \frac{1}{\lambda - \lambda_{prev}} \begin{bmatrix} 1/\lambda & -1/\lambda_{prev}^2 \\ -\lambda_{prev}/\lambda & \lambda/\lambda_{prev}^2 \end{bmatrix} \begin{Bmatrix} m_p - m_c - \lambda n_{ini} \\ m_{p,prev} - m_c - \lambda_{prev} n_{ini} \end{Bmatrix} \tag{3.64}$$

In the internal iteration loop used for finding λ, the "*prev*" subscript in the above means the "*curr*" state from the previous iteration.. For example if we are at iteration 2, λ is from iteration 1 and λ_{prev} is one, m_p calculated at the iteration 2; whereas $m_{p,prev}$ at iteration 1 and so on.

If for any reason the above procedure was unsuccessful and the Newton loop diverged, the solution will definitely require to be repeated using a smaller time increment (i.e., time step delta time must be cut). The technique explained in this section has been implemented in the developed code.

3.3 Tensile fracturing

A tensile fracture located in an infinite continuum generally will propagate if the stress intensity factor at the tip of the fracture reaches the critical fracture intensity factor according to the linear elastic fracture mechanics (Sneddon and Lowengrub, 1969; Gidley et al., 1989). In this study, since the effective stress for each grid block at any time step is available from the FEM solution, a different, simple criterion is implemented. To define the stress condition at which tensile failure occurs we require

$$\sigma'_3 = -T \tag{3.65}$$

Therefore the fracture will propagate if the minimum principal effective stress in the Gauss point next to the last fractured gauss point falls below the tensile strength of the rock material. Here we are not using a fracture mechanics criterion, but rather a strength criterion. After failure the minimum effective stress of the Gauss point will be set to zero and the forces between the failed Gauss point and the Gauss points around it will be rebalanced afterwards. Pseudo-continuum technique is then used to define the constitutive model of the failed block.

3.4 Shear fracturing

Shear fracturing in brittle materials has been the subject of numerous studies in the literature both on micro and macro scales. Micro-scale analysis of shear fracturing is not the subject of the current work; however, the concepts are useful for analysis on a macro sale. Based on the classical fracture theory in brittle rock materials, under certain deviatoric stress (i.e., triaxial test), strain localizations will lead to coalescence of local micro planes of weaknesses into a rupture pattern which may or may not result in sharp discontinuity such as shear band or fracture. Under some other loading condition such as constant shear loading by fluid pressurization, the failure can also occur by diffuse instability mechanism in homogeneous kinematic field with no strain localization pattern (Wan et al., 2011). From mathematical point of view failure is described by a burst in the kinematic energy or a negative in second order work of a given material system which is

caused by a sudden change in the material micro-structure or sharp decrease in the grain contacts (Nicot et al., 2007). The second order work in derivative form is simply defined as,

$$dW^{(2)} = d\sigma_{ij} d\epsilon_{ij} \quad \forall \|d\varepsilon\| \neq 0 \tag{3.66}$$

The above equation is more of a generalized failure of which fracture is a special case. In case of fracturing, for example in brittle materials, the orientation of macro-fracture planes vary in different experiments depending on the rock mineralogy, heterogeneity, anisotropy etc., and usually build an acute angle between 20° to 35° with respect to the axial loading direction.

The technique implemented here to model shear fracturing is based on the Mohr-Coulomb shear failure criterion. The failure criterion requires the difference between the maximum and minimum effective stress to be large enough for the Mohr circle to touch the shear failure surface as shown in Figure 3.2 by the dashed line.

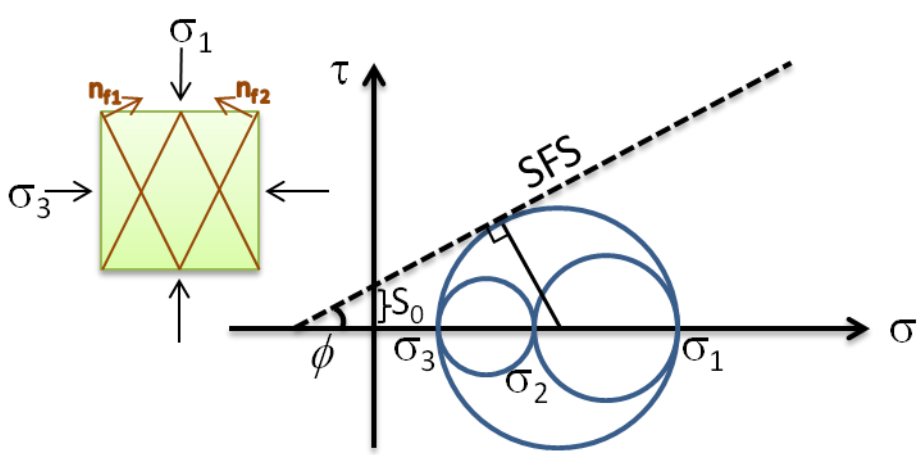

Figure 3.2 – Mohr-Coulomb circle and shear failure criterion

In the principal stress coordinates system, the Mohr-Coulomb shear failure is simply expressed as follows,

$$\sigma_1 = 2S_0 \frac{\cos \emptyset}{1 - \sin \emptyset} + \sigma_3 \frac{1 + \sin \emptyset}{1 - \sin \emptyset} \tag{3.67}$$

where σ_1 and σ_3 are the maximum and minimum principal stresses, S_0 is the rock cohesion and ϕ is the rock internal friction angle.

After shear failure occurrence in a rock material, based on our simple assumption two conjugate sets of fractures are added to the rock constitutive model and hereafter the fractured rock material is treated as a "pseudo-continuum". The orientations of the two fracture sets are calculated as follows (Nassir et al., 2010; Nassir et al., 2012),

$$\vec{n}_{f1} = \vec{n}_1 \cos\beta + \vec{n}_3 \sin\beta\,, \quad \vec{n}_{f2} = \vec{n}_1 \cos\beta - \vec{n}_3 \sin\beta\,, \quad \beta = \frac{\Phi}{2} + \frac{\pi}{4} \tag{3.68}$$

where $n_1 = n_1(n_{1x}, n_{1y}, n_{1z})$ and $n_3 = n_3(n_{3x}, n_{3y}, n_{3z})$ are the maximum and minimum principal stresses directions.

Shear failure is associated with a sudden release of kinetic energy. A special technique is implemented to soften the high deviatoric stress to a residual level or decrease the mobilized friction angle from a hypothetical peak value to a residual friction angle. At the moment of fracturing, the peak mobilized friction angle, the hypothetical, in the plane of created fracture is obtained from the respective normal and shear stresses acting on the plane of fracture as follows,

$$\emptyset_p = \arctan\left(\frac{\tau}{\sigma_n}\right) \tag{3.69}$$

According to Mohr-Coulomb criterion for the intact rock at the time of fracturing the shear stress is

$$\tau = \sigma_n \tan\emptyset + S_0 \tag{3.70}$$

where σ_n is given by

$$\sigma_n = \frac{(\sigma_1 + \sigma_3)}{2} - \frac{(\sigma_1 - \sigma_3)}{2}\sin\emptyset \tag{3.71}$$

If ϕ in the above equation is written as the summation of basic friction angle, ϕ_b, and a declining angle, α, an exponential function for the declining angle has been introduced in the numerical method according to the following equation,

$$\alpha = \alpha_p \exp(-mu^p) \tag{3.72}$$

where u^p is the plastic shear displacement and m is the exponential coefficient. The function will then drive the peak friction angle to a residual friction angle, which is the same as the friction angle of the induced fractures. The main question in implementing the above technique is how to find a correct value for the m parameter. Figure 3.3 illustrates how this mobilized friction angle softening technique reduces the deviatoric stress to a residual value after shear fracturing. A decline coefficient of 100 m^{-1} was used in this example problem. In real cases the m coefficient may be a relatively difficult parameter to estimate. Furthermore, very high value of m parameter usually leads to divergence problems in the Newtonian solution.

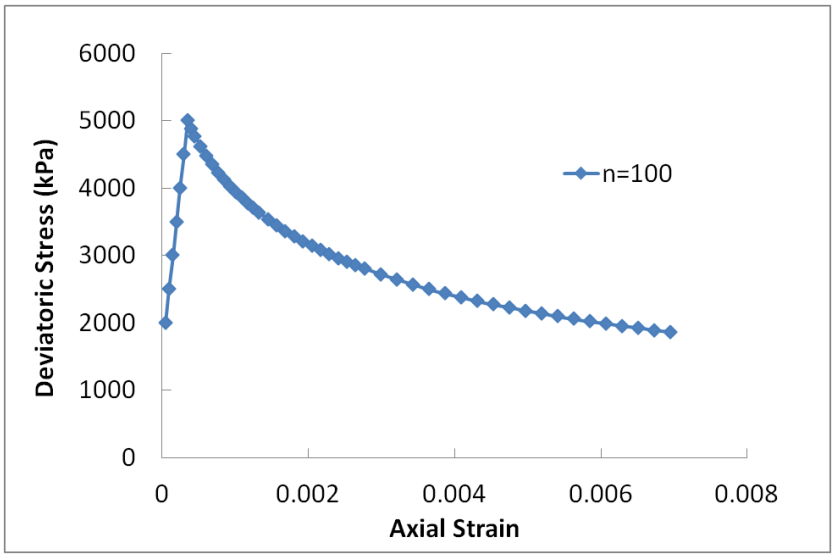

Figure 3.3 – Shear fracturing and deviatoric stress softening by declining mobilized friction angle technique in a triaxial test

In the next chapter it will be shown that when the above mentioned friction angle softening technique is used, usually only the maximum stress declines and as a result reduces the deviatroic stress to a residual level. Sometimes using the mobilized friction angle technique leads to some numerical convergence problem especially when approaching the tensile stress region. An alternative technique to release the kinetic energy or reducing the deviatoric stress from the peak to a residual in the FEM solution is

the penalty method. After failure the residual deviatoric stress is controlled by the induced fracture shear resistance. The failure function for a fracture with zero cohesion is simply written as follows,

$$\tau = \sigma_n \tan \varphi_f \tag{3.73}$$

where φ_f is the induced fracture friction angle. As mentioned before, a certain amount σ_n must be subtracted from the maximum principal stress to allow transition of failure function from the intact rock to the fracture plane. So if σ_1 and σ_3 are the maximum and minimum principal stresses when shear fracturing occurs in an intact rock, the required value of normal stress drop, $\Delta\sigma_n$, can be obtained by the following equations. Requiring that the stress state after the correction is at the failure surface with the residual angle φ_f gives,

$$\frac{1}{2}\,(\sigma_1 - \Delta\sigma_n - \sigma_3)\cos\emptyset = \left(\frac{1}{2}\,(\sigma_1 - \Delta\sigma_n + \sigma_3) - \frac{1}{2}\,(\sigma_1 - \Delta\sigma_n - \sigma_3)\sin\emptyset\right)\tan\varphi_f \tag{3.74}$$

and, solving this for $\Delta\sigma_n$ we get

$$\Delta\sigma_n = \frac{(\sigma_1 + \sigma_3)\tan\varphi_f - (\sigma_1 - \sigma_3)\cos\emptyset - (\sigma_1 - \sigma_3)\sin\emptyset\tan\varphi_f}{\left(\tan\varphi_f - \cos\emptyset - \sin\emptyset\tan\varphi_f\right)} \tag{3.75}$$

After principal stresses have been modified in the principal coordinates and then transformed back from the principal coordinates to the global coordinates system, the forces will be rebalanced to account for the deliberate change in the fractured block stress tensor due to failure. The internal forces prior and after stress modification are calculated and the difference between the two will be applied in form of an incremental load in the FEM solution to rebalance the stress field in the blocks around the failed block. It should be noted that the external force vector remains the same as the internal force vector before the stress modification. The above mentioned technique can be graphed by axial stress vs. axial displacement in a triaxial test on a brittle rock as shown in Figure 3.4. The applied stress is increased up to a peak value at which the rock fails and a sudden decrease in the axial stress will result.

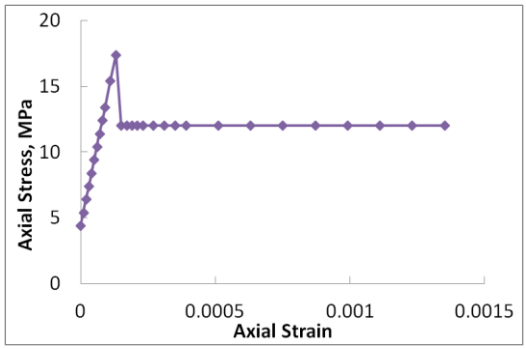

Figure 3.4 – Shear fracturing and sudden axial stress drop after the failure to a residual value in a triaxial test

In the next chapter we will present some examples showing that under some reservoir initial conditions, secondary fracturing might also occur. In that case the same procedure explained above for the primary fracturing will be repeated for the second set of shear fractures. This repeated failure mode (when the secondary fracturing takes place) is referred to here as the "crushing" of the block.

3.5 Coupling algorithm

As explained earlier in this work the flow, geomechanical and fracture creation modules are coupled explicitly during each time step. Pressure variations in all the Gauss points are calculated in the flow module which indeed acts as the source of external forces for the geomechanical part. Effective stresses updated in the geomechanical section, are then checked in the failure module for either tensile or shear fracture creation. The permeability changes due to creation and deformation of the fracture system are carried into the flow solution for the next time step. Figure 3.5 depicts the coupling algorithm between the different modules.

A more accurate flow/geomechanical solution can be obtained by extending the explicit coupling shown in Figure 3.5 into iterative coupling by defining some convergence criteria (Settari and Mourits, 1994). The results after the convergence will be so close to the case where the solid and fluid interaction equations are solved simultaneously or the solution is fully coupled.

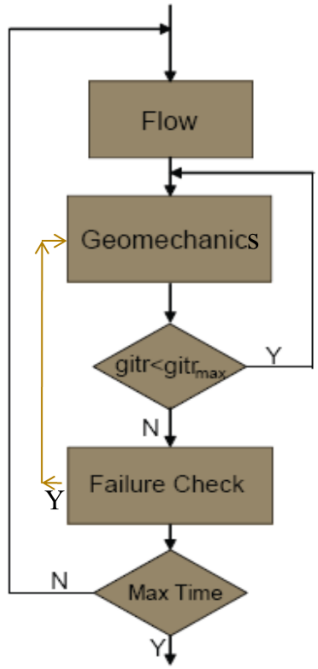

Figure 3.5 – flow, geomechanical and failure modules explicit coupling flowchart

CHAPTER 4 - CONSTITUTIVE MODELS

Within the realm of continuum mechanics, an appropriate constitutive model will be required to describe the mechanical behavior of different rocks or to model them by Finite Element Methods. Constitutive laws basically relate the confining effective stress acting on a continuum and the resultant strain.

A discontinuity may be considered as being a continuum if the discontinuous points can be related by some constitutive formulas. If the mechanical behavior of the embedded fractures (joints) in a damaged rock is known, the whole fractured rock can also be pseudoized as a continuum or in more appropriate words as a "pseudo-continuum". In this chapter the constitutive models for individual fractures (joints) and next for the fractured rock mass will be derived and described.

4.1 Intact rock constitutive model

Since the main focus of this research is to investigate the influence of fracture mechanical behavior on the overall fractured blocks stress strain performance, the intact rock is simply assumed to be of linear elastic type (LE). The intact rock constitutive model for an LE material is expressed as follows,

$$\begin{bmatrix} \sigma'_{11} \\ \sigma'_{22} \\ \sigma'_{33} \\ \sigma'_{12} \\ \sigma'_{13} \\ \sigma'_{23} \end{bmatrix} = \frac{E}{(1+\upsilon)(1-2\upsilon)} \begin{bmatrix} 1-\upsilon & \upsilon & \upsilon & 0 & 0 & 0 \\ \upsilon & 1-\upsilon & \upsilon & 0 & 0 & 0 \\ \upsilon & \upsilon & 1-\upsilon & 0 & 0 & 0 \\ 0 & 0 & 0 & \frac{(1-2\upsilon)}{2} & 0 & 0 \\ 0 & 0 & 0 & 0 & \frac{(1-2\upsilon)}{2} & 0 \\ 0 & 0 & 0 & 0 & 0 & \frac{(1-2\upsilon)}{2} \end{bmatrix} \begin{bmatrix} \varepsilon_{11} \\ \varepsilon_{22} \\ \varepsilon_{33} \\ \gamma_{12} \\ \gamma_{13} \\ \gamma_{23} \end{bmatrix} \tag{4.1}$$

and in tensor form,

$$\underset{\sim}{\sigma}' = \underset{\approx}{D}\,\underset{\sim}{\varepsilon} \tag{4.2}$$

where E is the Young's modulus and v is the Poisson's ratio. This formulation is also valid for nonlinear elastic behavior if the equations are written in an incremental form. In this case the stiffness matrix D is nonlinear and must be evaluated at the current stress.

4.2 Single fracture constitutive model

4.2.1 Fracture normal deformation

Bandis et al. (1983) suggested a hyperbolic model to describe normal deformation of a single fracture under compressive stress as below (Bandis et al., 1983),

$$\sigma'_n = \frac{k_{ni}\Delta v}{1-\dfrac{\Delta v}{\Delta v_{\max}}} \tag{4.3}$$

where Δv_j, k_{ni}, $\Delta v_{\max}$ respectively are the joint normal deformation, initial normal stiffness and the maximum joint closure. Normal stiffness of the joint can be obtained by taking the derivative of the normal effective stress with respect to the normal deformation.

$$k_n = \frac{\partial \sigma'_n}{\partial \Delta v} = \frac{k_{ni}}{\left(1-\dfrac{\Delta v}{\Delta v_{\max}}\right)^2} = k_{ni}\left[1-\frac{\sigma'_n}{\Delta v_{\max} k_{ni} + \sigma'_n}\right]^{-2} \tag{4.4}$$

Initial normal stiffness, k_{ni}, is a measure of the joint normal toughness at initial load. The effect of initial normal stiffness on mechanical deformation of a sample joint is shown in Figure 4.1 . It is observed that the normal toughness of a joint is a strong function of the initial normal stiffness.

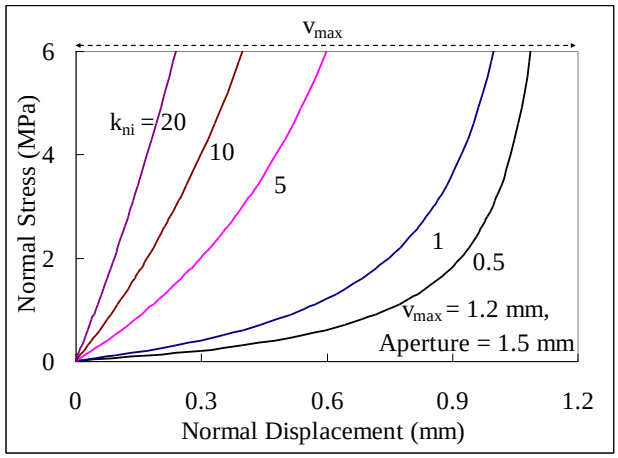

Figure 4.1 – Normal stress vs. normal deformation of a single fracture with different fracture initial stiffness

4.2.2 Fracture peak shear strength and shear deformation

The general form of the empirical shear strength criterion based on joint surface parameters proposed by Barton is as shown below (Barton et al., 1985),

$$\tau = \sigma'_n \tan\left[JRC_n \log\left(\frac{JCS_n}{\sigma'_n} \right) + \phi_r \right] \tag{4.5}$$

where JRC_n, JCS_n, ϕ_r and σ_n are mobilized joint roughness coefficient, joint wall compressive strength, residual friction angle of the rock mass, and applied normal effective stress, respectively. The term enclosed by brackets in Eq. (4.5) is called the peak friction angle and its first term is usually referred to as the dilatancy angle.

JRC_n can be obtained by the following equation (Barton et al., 1985),

$$JRC_n = \frac{\alpha - \phi_r}{\log\left(\frac{JCS_n}{\sigma'_{no}} \right)} \tag{4.6}$$

where α is the tilt angle in the tilt test when sliding occurs. In the above equation *JRC* is specifically related to peak shear strength and ranges between 1 and 15. For non-dilatant joint surfaces (smooth joint), the value of α is equal to residual friction angle, ϕ_r.

Note that in the above equations, *JRC* and *JCS* were corrected for changes in length from laboratory scale to in situ scale values by the following equations (Barton et al., 1985),

$$JRC_n = JRC_0 \left[\frac{L_n}{L_0} \right]^{-0.02JRC_0} \tag{4.7}$$

$$JCS_n = JCS_0 \left[\frac{L_n}{L_0} \right]^{-0.03JRC_0} \tag{4.8}$$

If rock joint surfaces remain unweathered during shearing, residual friction angle will be the same in magnitude as basic friction angle, ϕ_b. Wearing or degradation of asperities causes residual friction angle to be usually smaller than basic friction angle.

In general, at any given shear displacement (δ) before the respective peak value, the shear strength can be obtained in Eq. (4.5) by defining a mobilized friction angle, ϕ' (*mob*) as,

$$\phi'(mob) = JRC_n(mob)\log\left(\frac{JCS_n}{\sigma_n^{'}} \right) + \phi_r \tag{4.9}$$

where $JRC_n(mob)$ is the mobilized joint roughness coefficient and ϕ_r is the residual angle. $JRC_n(mob)$ can be obtained by the following equation as suggested by Barton et. al.,

$$JRC(mob) = JRC(peak)\frac{\phi'(mob) - \phi_r}{\phi'(peak) - \phi_r} \tag{4.10}$$

The magnitude of the mobilized friction angle varies from zero up to the peak shear angle. $JRC_n(mob)$ in the above equations changes within the following range.

$$\frac{-\phi_r}{\log\left(\frac{JCS_n}{\sigma'_{no}} \right)} \le JRC_n(mob) \le JRC_n \tag{4.11}$$

At peak shear stress, the following empirical equation was developed from analysis of 650 shear tests which can provide an estimate of the peak shear displacement, δ^p (Barton and Bandis, 1982).

$$\delta^p = \frac{L_n}{500}\left[\frac{JRC_n}{L_n}\right]^{0.33} \tag{4.12}$$

Here L_n is the sample length and JRC_n is its respective roughness coefficient. The simplest relation between shear stress and strain before failure will be written in a linear form as,

$$\tau = k_t\delta, \qquad 0 \le u_t \le u_t^{peak} \tag{4.13}$$

where k_t , the shear or tangent stiffness, can be obtained by the following equation:

$$k_t = \frac{\sigma_n \tan\left[JRC_n \log\left(\frac{JCS_n}{\sigma_n}\right) + \phi_r\right]}{\frac{L_n}{500}\left[\frac{JRC_n}{L_n}\right]^{0.33}} \tag{4.14}$$

As discussed in the previous section, most experimental data indicate that this relationship is not linear. A non-linear function should be implemented to describe the pre-peak shear stress –shear displacement behavior of a single joint.

4.2.3 New hyperbolic empirical equation for shear deformation

To describe a single joint shear behavior, an empirical hyperbolic function is proposed here by the authors to fit the experimental data obtained by Barton as (Nassir et al., 2009):

$$\tau = \frac{au_s}{1 + bu_s} \tag{4.15}$$

where τ and u_s are shear stress and shear displacement respectively. a and b are two constants which will be defined later in this section. The above equation is similar to

what Barton et. al. suggested for normal deformation of a single joint. To obtain *a* and *b* in the above correlation, at least two non-zero sets of data points are required. One is the available data at peak shear stress and peak shear displacement. The other is the point at which dilation begins in the fracture shearing process.

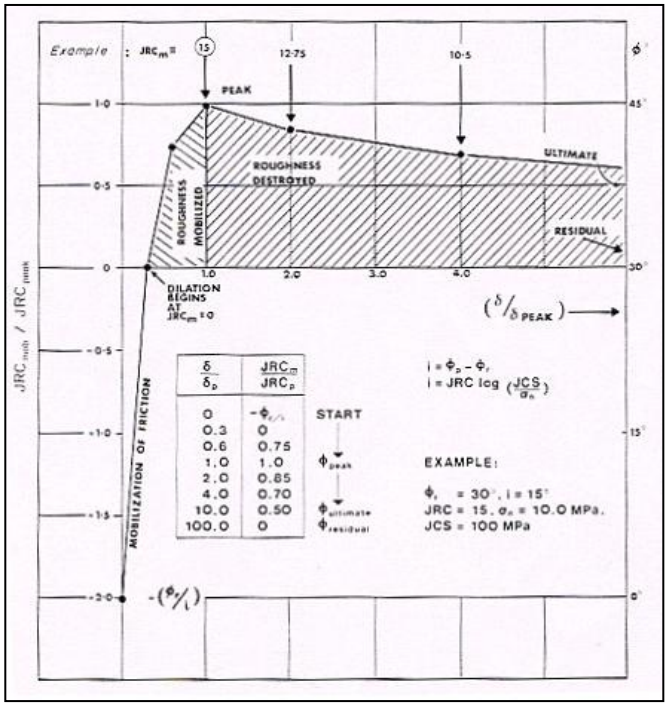

Figure 4.2 – Axial stress vs. axial strain of fractured blocks with different fracture orientations (Barton et al., 1985)

Results of experiments performed by Barton et al. showed that dilation initiates when u_s/u_s^p is around 0.3, at which point the mobilized friction angle is equal to the basic friction angle as shown in Figure 4.2. Let's define γ_{coef} as the fraction of peak shear displacement at which dilation initiates. Then, in other words, at $u_s = \gamma_{coef}.u_s^p$, the amount of shear stress will be $\sigma'_n \tan(\phi_b)$. This point can be used as the second data point to calculate *a* and *b* parameters in Eq. (4.15) which are then obtained by the following equations:

$$b = \frac{1 - \dfrac{\sigma_n^{'} \tan(\phi_b)}{\tau^p \gamma_{coef}}}{u_s^{\ p}\left(\dfrac{\sigma_n^{'} \tan(\phi_b)}{\tau^p} - 1\right)}, \quad a = \frac{\tau^p\left(1 + b u_s^{\ p}\right)}{u_s^{\ p}} \tag{4.16}$$

Shear stiffness in differential form can be obtained by differentiating shear stress in Eq. (4.15) with respect to shear displacement as follows:

$$k_t = \frac{d\tau}{du_s} = \frac{a}{(1 + b u_s)^2} = \frac{(a - \tau b)^2}{a} \tag{4.17}$$

The effects of *JCS*, *JRC* and γ_{coef} on shear behavior of a joint are shown in Figure 4.3. *JRC* and *JCS* have the same effect on shear stiffness of the joint. Lower values of *JRC* and *JCS* result in stiffer shear resistance at lower shear stress levels and softer shear resistance at higher shear stress values (Figure 4.3a). *JCS* does not influence the peak shear displacement while higher *JRC* is associated with greater peak shear displacement. This is due to the fact that the peak shear displacement in Eq. (4.12) is only a function of *JRC* and the length of the joint, not *JCS*. The curvature of the functions is highly affected by γ_{coef} as shown in Figure 4.3b. The concave loading path turns to a convex one when γ_{coef} takes values greater than 0.824. This critical value depends on the surface (frictional) properties of the joint and can be obtained by zeroing *b* in Eq. (4.16).

$$\gamma_{coef}\Big|_{critical} = \frac{\tan(\phi_b)}{\tan\left(JRC_n \log\left(\dfrac{JCS_n}{\sigma_n^{'}}\right) + \phi_b\right)} \tag{4.18}$$

Dilation (defined as a change of joint aperture u_n due to shear) is another important phenomenon commonly associated with shearing of rough walled fractures. Dilation can be defined as a function of shear displacement and the tangent of dilation angle as:

$$d\,u_n = \tan(d_n)\,d\,u_t = \tan(d_n)\frac{1}{k_t}d\tau \tag{4.19}$$

where du_n, du_t and d_n are the normal displacement, tangential displacement and the dilation angle, respectively.

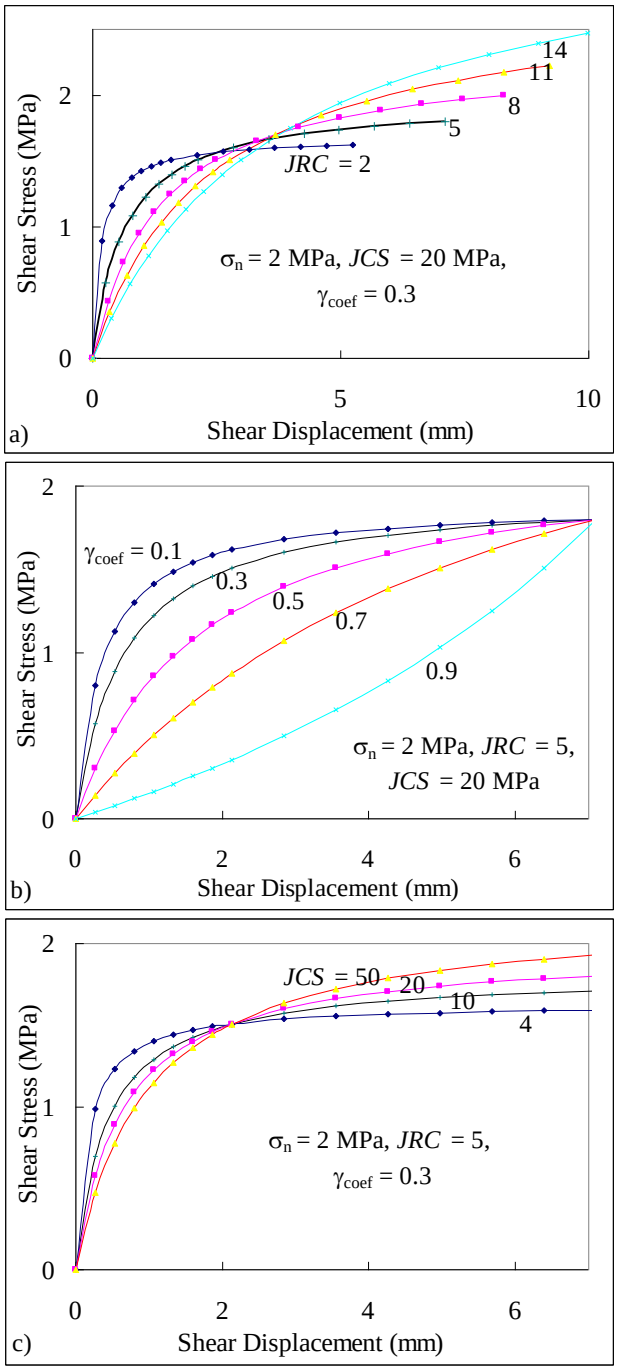

Figure 4.3 – The effect of different joint properties on the shear stress vs. shear displacement hyperbolic function (Nassir et al., 2009)

To estimate the value of the mobilized dilation angle the following empirical model was used (Barton and Choubey, 1977),

$$d_n^0(mob) = 1/2\,JRC_n(mob)\log\left(\frac{JCS_n}{\sigma_n^{'}}\right) \tag{4.20}$$

It should be noted that the above value is half of the dip angle (α) of the joint mean asperities. (Seidel and Haberfield, 1995) showed that elastic deformation of asperities in shear displacement of a joint with two initially matched faces explains the reduction in the mean asperities' dip angle. They also proved that the peak shear stress remains unchanged even though asperities elastically deform.

4.2.4 Fracture constitutive model of type I

To model the mechanical behavior of rock joints, they are considered in this work to be continuum possessing their own constitutive models, rather than treating them as discontinuities. Fracture constitutive matrix is obtained in two different ways in the current research project. The fracture constitutive model type (I) is merely a compilation of empirical models which describe the normal, shear and dilation behavior of a single fracture.

Consider a local coordinate system for a planar joint where *n* denotes the direction normal to the joint plane, and *s* and *t* are two orthogonal directions in the joint plane. The constitutive model relating displacement and stress is then expressed as follows,

$$\begin{Bmatrix} u_n \\ u_s \\ u_t \end{Bmatrix} = \begin{bmatrix} F_{11} & F_{12} & F_{13} \\ F_{12} & F_{22} & 0 \\ F_{13} & 0 & F_{33} \end{bmatrix} \begin{Bmatrix} \sigma_n^{'} \\ \tau_s^{'} \\ \tau_t^{'} \end{Bmatrix} \tag{4.21}$$

Eq. (4.21) can be rewritten in tensor form as follows,

$$\underset{\sim}{u}^J = \underset{\approx}{F}^J \underset{\sim}{\sigma}'^J \qquad \text{or} \qquad \underset{\sim}{\sigma}'^J = \underset{\approx}{K}^J \underset{\sim}{u}^J \tag{4.22}$$

where K^J is the fracture stiffness matrix and it is the inverse of the fracture compliance matrix (F^J). The diagonal terms in Eq. (4.21) can be substituted by the normal and shear stiffness Eqs. (4.4), (4.14) and (4.17) from the previous sections as follows,

$$F_{11} = \frac{1}{k_{\mathrm{n}}}\ ; \quad F_{22} = \frac{1}{k_{\mathrm{t}}}; \quad F_{33} = \frac{1}{k_{\mathrm{t}}} \tag{4.23}$$

The prime notation in Eq. **(**4.21) denotes the effective form of stress. The effective stress is important when the porous rock or fracture is saturated with fluid.

Here we have assumed that the fracture compliance matrix Eq. (4.21) is symmetric. The off-diagonal or dilation terms are obtained from Eq. **(**4.19) as shown below.

$$F_{12} = F_{13} = \tan(d_n)\frac{1}{k_t} \tag{4.24}$$

These terms represent the effect of shear stress on normal deformation (dilation). In Eq. (4.24) it is assumed that the asperity dip angles in both shear directions, strike and tangent, are the same but in general they can be different.

4.2.5 Fracture constitutive model of type II

The major difference between the first and the second types of fracture constitutive models is the way in which the shear and off-diagonal terms are treated. Elasto-plastic model is implemented in the type II formulation, in which the fracture elastic shear stiffness is assumed to be either a fraction of the intact rock shear modulus or a fraction of the fracture normal stiffness. The normal stiffness will be described by the same non-linear hyperbolic equation like in the type I fracture constitutive model. Hence the elastic part of the fracture constitutive model when the fracture elastic shear stiffness is a fraction of the intact rock shear modulus is written as follows,

$$\begin{Bmatrix} u_n \\ u_s \\ u_t \end{Bmatrix} = \begin{bmatrix} \frac{1}{k_n} & 0 & 0 \\ 0 & \frac{S_f}{\xi G} & 0 \\ 0 & 0 & \frac{S_f}{\xi G} \end{bmatrix} \begin{Bmatrix} \sigma_n^{'} \\ \tau_s^{'} \\ \tau_t^{'} \end{Bmatrix} \tag{4.25}$$

where G is the intact rock shear modulus, S_f is the fracture spacing and ξ is the shear modulus fraction as discussed above. Alternatively, the fracture elastic shear stiffness might be expressed as a fraction of the fracture normal stiffness. Then Eq. (4.25) will be rewritten as follows,

$$\begin{Bmatrix} u_n \\ u_s \\ u_t \end{Bmatrix} = \begin{bmatrix} \frac{1}{k_n} & 0 & 0 \\ 0 & \frac{1}{\eta k_n} & 0 \\ 0 & 0 & \frac{1}{\eta k_n} \end{bmatrix} \begin{Bmatrix} \sigma_n' \\ \tau_s' \\ \tau_t' \end{Bmatrix} \tag{4.26}$$

The derivation of the elasto-plastic model will be addressed in the next section.

4.2.6 Elasto-plastic formulation for fracture constitutive model type II

The contact area of a discontinuity can be idealized of a small differential zone of material in which the normal and tangential relative deformations can be decomposed into the reversible (elastic) and irreversible (plastic) parts, denoted by superscripts *e* and *p*.

$$d\underset{\sim}{u} = d\underset{\sim}{u}^e + d\underset{\sim}{u}^p \tag{4.27}$$

From the classical theory of interface plasticity, the permanent discontinuity deformations are given by the following plastic potential flow rule,

$$d\underset{\sim}{u}^p = \begin{cases} 0 & If \quad F < 0 \\ \lambda \dfrac{\partial Q}{\partial \underset{\sim}{\sigma}'} & If \quad F = 0 \end{cases} \tag{4.28}$$

where $d\underset{\sim}{u}^p$ is the plastic displacement vector and $F = F(\underset{\sim}{\sigma}, W^P)$ is the yield function which depends on stress and plastic work associated with plastic shear displacement. The value of F is negative for elastic behavior and attains zero value when slip is imminent. $Q = Q(\underset{\sim}{\sigma}', W^P)$ is the potential function whose gradient gives the direction along which plastic displacement occurs. λ is a positive scalar that specifies the amount of plastic deformation.

Elastic deformation is accompanied by stress alteration while plastic deformation corresponds to permanent sliding and other features such as dilation and bulking. Changes in effective stress are related solely to changes in elastic portion of total deformations,

$$d\underset{\sim}{\sigma}' = \underset{\approx}{K}^{e}\, d\underset{\sim}{u}^{e} \tag{4.29}$$

At a given instant in time when slip is imminent; yield function attains the zero value (F = 0). At the next instant in time the yield interface remains still zero, or in mathematical form dF = 0. By using the consistency condition for the yield function, infinitesimal change in failure function is written as follows.

$$dF = \left[\frac{\partial F}{\partial \underset{\sim}{\sigma}'}\right]^{T} d\underset{\sim}{\sigma}' + \left[\frac{\partial F}{\partial \underset{\sim}{u}^{P}}\right]^{T} d\underset{\sim}{u}^{P} = 0 \tag{4.30}$$

Since changes in effective stress only depend on elastic deformation we will have,

$$dF = \left[\frac{\partial F}{\partial \underset{\sim}{\sigma}'}\right]^{T} \underset{\approx}{K}^{e}\left(d\underset{\sim}{u} - d\underset{\sim}{u}^{p}\right) + \left[\frac{\partial F}{\partial \underset{\sim}{u}^{P}}\right]^{T} d\underset{\sim}{u}^{p} = 0 \tag{4.31}$$

$d\underset{\sim}{u}^{p}$ in the equation above can be substituted by the gradient of plastic potential from Eq. (4.28), and next it can be solved for the slip multiplier λ as shown below:

$$\lambda = \frac{\left[\frac{\partial F}{\partial \underset{\sim}{\sigma}'}\right]^{T} \underset{\approx}{K}^{e}\, d\underset{\sim}{u}}{\left[\frac{\partial F}{\partial \underset{\sim}{\sigma}'}\right]^{T} \underset{\approx}{K}^{e} \frac{\partial Q}{\partial \underset{\sim}{\sigma}'} - \left[\frac{\partial F}{\partial \underset{\sim}{u}^{P}}\right]^{T} \frac{\partial Q}{\partial \underset{\sim}{\sigma}'}} \tag{4.32}$$

From elastic constitutive law we have,

$$d\underset{\sim}{\sigma}' = \underset{\approx}{K}^{e}\left(d\underset{\sim}{u} - d\underset{\sim}{u}^{p}\right) = \underset{\approx}{K}^{e}\left(d\underset{\sim}{u} - \lambda \frac{\partial Q}{\partial \underset{\sim}{\sigma}'}\right) \tag{4.33}$$

Now let's substitute λ in the above equation,

$$d\underset{\sim}{\sigma}' = \underset{\approx}{K}^e \left(d\underset{\sim}{u} - \frac{\frac{\partial Q}{\partial \underset{\sim}{\sigma}'} \left[\frac{\partial F}{\partial \underset{\sim}{\sigma}'} \right]^T \underset{\approx}{K}^e d\underset{\sim}{u}}{\left[\frac{\partial F}{\partial \underset{\sim}{\sigma}'} \right]^T \underset{\approx}{K}^e \frac{\partial Q}{\partial \underset{\sim}{\sigma}'} - \left[\frac{\partial F}{\partial \underset{\sim}{u}^P} \right]^T \frac{\partial Q}{\partial \underset{\sim}{\sigma}'}} \right) \tag{4.34}$$

This leads to an equation most commonly used for calculating the elasto-plastic stiffness matrix of a single fracture expressed in terms of the yield and potential functions F and Q as,

$$\underset{\approx}{K}^{ep} = \underset{\approx}{K}^e - \frac{\underset{\approx}{K}^e \frac{\partial Q}{\partial \underset{\sim}{\sigma}'} \left[\frac{\partial F}{\partial \underset{\sim}{\sigma}'} \right]^T \underset{\approx}{K}^e}{\left[\frac{\partial F}{\partial \underset{\sim}{\sigma}'} \right]^T \underset{\approx}{K}^e \frac{\partial Q}{\partial \underset{\sim}{\sigma}'} - \left[\frac{\partial F}{\partial \underset{\sim}{u}^P} \right]^T \frac{\partial Q}{\partial \underset{\sim}{\sigma}'}} \tag{4.35}$$

Jing et al. proposed the following set of yield and potential functions to model mechanical behavior of a single fracture (joint) as shown below (Jing et al., 1994),

$$F = \left[\left(\frac{\tau_x}{\mu_x} \right)^2 + \left(\frac{\tau_z}{\mu_z} \right)^2 \right]^{1/2} + \sigma'_n + C \tag{4.36}$$

$$Q = \left[\left(\frac{\tau_x}{\mu_x} \right)^2 + \left(\frac{\tau_z}{\mu_z} \right)^2 \right]^{1/2} + \sigma'_n \sin\alpha \tag{4.37}$$

where C is the cohesion and μ_x and μ_z, the peak shear strength in x and y directions, are defined as:

$$\mu_x = \tan(\phi_r + \alpha_x),\ \mu_z = \tan(\phi_r + \alpha_z) \tag{4.38}$$

where α_x and α_z are the asperity angles of the rock joints in the x and z directions. The α term in Eq. (4.37) is called the dilation angle which can be taken as an average between α_x and α_z.

The gradient of F with respect to the stress vector is also expressed as,

$$\frac{\partial F}{\partial \sigma'_n} = 1,$$

$$\frac{\partial F}{\partial \tau_x} = C_x = \frac{\tau_x}{\mu_x^2\left[\left(\frac{\tau_x}{\mu_x}\right)^2 + \left(\frac{\tau_z}{\mu_z}\right)^2\right]^{1/2}}, \tag{4.39}$$

$$\frac{\partial F}{\partial \tau_z} = C_z = \frac{\tau_z}{\mu_z^2\left[\left(\frac{\tau_x}{\mu_x}\right)^2 + \left(\frac{\tau_z}{\mu_z}\right)^2\right]^{1/2}}$$

or

$$\nabla F^T = \left\{\frac{\partial F}{\partial \underset{\sim}{\sigma'}}\right\}^T = \{1 \quad C_x \quad C_z\} \tag{4.40}$$

The gradient of plastic potential function with respect to the stress vector can take the following form:

$$\nabla Q^T = \left\{\frac{\partial Q}{\partial \underset{\sim}{\sigma'}}\right\}^T = \{\sin\alpha \quad C_x \quad C_z\} \tag{4.41}$$

Fracture asperity degradation upon shearing can be expressed in terms of specific cumulative plastic shear displacement as,

$$\alpha_x = \alpha_{x0} Exp(-m|u_x^p|), \quad \alpha_z = \alpha_{z0} Exp(-m|u_z^p|) \tag{4.42}$$

The derivative of the failure function with respect to the plastic part of the displacement can also be expanded as a function of the degrading asperity angle as follows,

$$\left\{\frac{\partial F}{\partial \underset{\sim}{u}^P}\right\}^T = \left\{0 \quad \frac{\partial F}{\partial \alpha_x}\frac{\partial \alpha_x}{\partial u_x^p} \quad \frac{\partial F}{\partial \alpha_z}\frac{\partial \alpha_z}{\partial u_z^p}\right\}$$

$$= \left\{0 \quad \frac{m\alpha_x\tau_x\left(1+\mu_x^2\right)C_x}{\mu_x} \quad \frac{m\alpha_z\tau_z\left(1+\mu_z^2\right)C_z}{\mu_z}\right\} \tag{4.43}$$

$$\frac{\partial F}{\partial \alpha_x} = \frac{1}{2} \times \frac{-2\tau_x^2}{\mu_x \mu_x^2} \times \frac{1}{\left[\left(\frac{\tau_x}{\mu_x}\right)^2 + \left(\frac{\tau_z}{\mu_z}\right)^2\right]^{1/2}} \times \left(1+\mu_x^2\right) = \frac{-\tau_x\left(1+\mu_x^2\right)C_x}{\mu_x} \tag{4.44}$$

$$\frac{\partial \alpha_x}{\partial u_x^p} = -m\frac{\left|u_x^p\right|}{u_x^p}\alpha_x \tag{4.45}$$

The specific cumulative plastic work, the second term in the denominator of Eq. (4.35), then will be defined as,

$$h = \left\{\frac{\partial F}{\partial \underset{\sim}{u}^p}\right\}^T \frac{\partial Q}{\partial \underset{\sim}{\sigma}'} = \left\{0 \quad \frac{m\alpha_x\tau_x\left(1+\mu_x^2\right)C_x}{\mu_x}\frac{\left|u_x^p\right|}{u_x^p} \quad \frac{m\alpha_z\tau_z\left(1+\mu_z^2\right)C_z}{\mu_z}\frac{\left|u_z^p\right|}{u_z^p}\right\}\left\{\sin\alpha \quad C_x \quad C_z\right\}^T$$

$$h = m\left(\frac{\alpha_x\tau_x\left(1+\mu_x^2\right)C_x^2}{\mu_x}\frac{\left|u_x^p\right|}{u_x^p} + \frac{\alpha_z\tau_z\left(1+\mu_z^2\right)C_z^2}{\mu_z}\frac{\left|u_z^p\right|}{u_z^p}\right) \tag{4.46}$$

Since λ is always positive and Eq. (4.41) says the plastic shear displacement term has the same sign as the respective shear stress term, Eq. (4.46) takes the following simple form,

$$h = m\left(\left|\frac{\alpha_x\tau_x\left(1+\mu_x^2\right)C_x^2}{\mu_x}\right| + \left|\frac{\alpha_z\tau_z\left(1+\mu_z^2\right)C_z^2}{\mu_z}\right|\right) \tag{4.47}$$

The denominator of Eq. (4.35) is obtained by substituting the equivalent terms for the gradient of the failure function, the joint elastic constitutive matrix and the plastic potential gradient vector as follows:

$$A = \left[\frac{\partial F}{\partial \underset{\sim}{\sigma}'}\right]^T \underset{\approx}{K}^e \frac{\partial Q}{\partial \underset{\sim}{\sigma}'} - h = C_x^2 k_x + C_z^2 k_z + k_n \sin\alpha - h \tag{4.48}$$

From Eq. (4.35) we will have,

$$\underset{\approx}{K}^{ep} = \begin{bmatrix} k_n & 0 & 0 \\ 0 & k_x & 0 \\ 0 & 0 & k_z \end{bmatrix} - \frac{1}{A}\begin{bmatrix} k_n & 0 & 0 \\ 0 & k_x & 0 \\ 0 & 0 & k_z \end{bmatrix}\begin{bmatrix} \sin\alpha \\ C_x \\ C_z \end{bmatrix}\begin{bmatrix} 1 & C_x & C_z \end{bmatrix}\begin{bmatrix} k_n & 0 & 0 \\ 0 & k_x & 0 \\ 0 & 0 & k_z \end{bmatrix}$$

$$\underset{\approx}{K}^{ep} = \begin{bmatrix} k_n & 0 & 0 \\ 0 & k_x & 0 \\ 0 & 0 & k_z \end{bmatrix} - \frac{1}{A} \begin{bmatrix} k_n^2 \sin\alpha & k_n k_x C_x \sin\alpha & k_n k_z C_z \sin\alpha \\ k_x k_n C_x & k_x^2 C_x^2 & k_x k_z C_x C_z \\ k_n k_z C_z & k_z k_x C_z C_x & k_z^2 C_z^2 \end{bmatrix} \tag{4.49}$$

Finally, the elasto-plastic constitutive model finds the following form:

$$\begin{bmatrix} d\sigma'_n \\ d\tau_x \\ d\tau_z \end{bmatrix} = \frac{1}{A} \begin{bmatrix} k_n\left(A - k_n \sin\alpha\right) & -k_n k_x C_{Fx} \sin\alpha & -k_n k_z C_z \sin\alpha \\ -k_x k_n C_x & k_x\left(A - C_x^2 k_x\right) & -k_x k_z C_x C_z \\ -k_n k_z C_z & -k_z k_x C_z C_x & k_z\left(A - C_z^2 k_z\right) \end{bmatrix} \begin{bmatrix} du_n \\ du_x \\ du_z \end{bmatrix} \tag{4.50}$$

Eq. (4.50) shows a direct relationship between the effective stress and total displacement vectors. Dilation is non-zero if α in the equation above is greater than zero. Reader should be reminded that our convention is that tensile stress is positive in the above equations.

4.2.7 Implementation in the FEM code

Implementing elasto-plastic model in the FEM code requires special considerations. Constitutive models are usually employed in two main parts of the FEM model: in the element stiffness calculation and in the element effective stress update calculation from each element displacement.

In the effective stresses and stiffness update calculation routine, first stress change is calculated by using only the elastic part of the constitutive model and the given element total strain. If the updated stress was below the shear failure surface, the fracture constitutive model is merely elastic and the solution will be continued for the next iteration or time step. Otherwise, the elasto-plastic constitutive model as described above will be implemented to update the effective stress. The elasto-plastic solution is carried out only in time steps in which loading towards the shear failure surface occurs and in cases of unloading only the elastic portion of the fracture constitutive model is implemented.

The fracture constitutive model of type II has been used extensively in major parts of this research, especially in the modeling of dynamic shear fracture propagation as will be described in detail in the model validation chapter.

4.3 Fractured block constitutive model

In order to use the constitutive models for a joint in the conventional FEM model, it is necessary to use a pseudoization (upscaling) technique that will convert a rock mass containing fractures into a pseudo-continuum which will exhibit the same stress-strain behavior. This section describes the analytical upscaling technique which results in a constitutive model of a fractured computational block. This technique requires that the population of the fractures can be represented by several sets of parallel fractures (joints). Each set can have different orientation of fracture planes and different properties, but fractures in a given set have the same properties and constant spacing.

The average strain energy in a region of composite material can be calculated from the average of the stress and strain components within that region when the boundary traction is macroscopically uniform (Hill, 1963). Singh (1973) established a continuum characterization for the mechanical properties of the jointed rock by summing the compliances of orthogonal joint sets. Using the above concept and the fact that the compliance matrix for any existing joints can be transformed easily into the global coordinate system, Gerrard and Pande (1985) developed a pseudoization technique to obtain the equivalent modulus of a jointed rock. The transformation of the stress vector from the global coordinates for the joint *x,y,z* to local coordinates *x',y',z'* (normal, shear and tangential directions in the fracture plane) is (Cook et al., 1989),

$$\begin{aligned}&\left\{\sigma'_{x'x'} \quad \sigma'_{x'y'} \quad \sigma'_{x'z'}\right\}^T \\ &= [T]\left\{\sigma'_{xx} \quad \sigma'_{yy} \quad \sigma'_{zz} \quad \sigma'_{xy} \quad \sigma'_{yz} \quad \sigma'_{zx}\right\}^T\end{aligned} \tag{4.51}$$

where *T*, the transformation matrix, is a 6 x 3 matrix defined as shown below.

$$[T] = \begin{bmatrix} l_{x'}^2 & m_{x'}^2 & n_{x'}^2 & 2l_{x'}m_{x'} & 2m_{x'}n_{x'} & 2l_{x'}n_{x'} \\ l_{x'}l_{y'} & m_{x'}m_{y'} & n_{x'}n_{y'} & m_{x'}l_{y'} + l_{x'}m_{y'} & n_{x'}m_{y'} + m_{x'}n_{y'} & n_{x'}l_{y'} + l_{x'}n_{y'} \\ l_{x'}l_{z'} & m_{x'}m_{z'} & n_{x'}n_{z'} & m_{x'}l_{z'} + l_{x'}m_{z'} & n_{x'}m_{z'} + m_{x'}n_{z'} & n_{x'}l_{z'} + l_{x'}n_{z'} \end{bmatrix}$$

$$
\begin{aligned}
&l_{x'} = \cos(x'x),\ m_{x'} = \cos(x'y),\ n_{x'} = \cos(x'z) \\
&l_{y'} = \cos(y'x),\ m_{y'} = \cos(y'y),\ n_{y'} = \cos(y'z) \\
&l_{z'} = \cos(z'x),\ m_{z'} = \cos(z'y),\ n_{z'} = \cos(z'z)
\end{aligned}
\tag{4.52}
$$

The compliance matrix of a jointed rock containing different joint sets is obtained by summing the contributions of the individual joint sets and adding them to the intact rock compliance matrix, resulting in the following equation,

$$
\left[F^t\right] = \left[F_I\right] + \sum_{J=1}^{n_J} \frac{1}{S_J} \left[T_J\right]^T \left[F_J^l\right] \left[T_J\right] \tag{4.53}
$$

where n_J is the total number of fracture sets, T_J is the transformation matrix for the joint set J given by Eq. (4.52), and S_J is the joint spacing in the joint set J. F_I is the compliance matrix of the intact rock material which in our calculation is assumed to be linear-elastic; but can be more general if required. Eq. (4.53) implies that under a given stress variation in a jointed block the total deformation is simply the sum of the deformation in the intact rock and all the embedded joints.

The constitutive equations derived in this chapter are used in development of the FEM code explained in the theory chapter. A good and efficient constitutive law is the key to a success of an FEM solution. During our development of the code, we have observed that any singular point in the constitutive model (determinant of stiffness matrix equals to zero) could cause problems in the Newton iteration loop, and in some cases the resultant uncontrollable divergence would lead to the crash of the entire numerical solution. But as discussed in Chapter 3, the special technique implemented to handle the divergence problem in the Newton loop somehow allows the solution to pass over the singular points.

CHAPTER 5 - MODEL VERIFICATION

5.1 Single phase flow code verification

In order to prove the accuracy of the developed finite element code for modeling of fluid flow through porous media, couple of example problems are solved here for which an analytical solution exists, which is taken to be the exact solution of the fluid flow differential equations. In the next step the numerical results will be compared against the analytical solution and errors resulted from the numerical solution then will be investigated.

5.1.1 Analytical solutions

5.1.1.1 Radial transient flow

For an infinite acting reservoir, the pressure distribution solution of the diffusivity equation as a function of space and time in an axisymmetric coordinate system can be obtained by the following equation (Chen, 2008),

$$p(r,t) = p_0 + \frac{Q_{inj}\mu}{4\pi kH} Ei\left(-\frac{\emptyset\mu c_t r^2}{4kt}\right), \quad t > 0 \tag{5.1}$$

where μ is the fluid viscosity, k is the rock permeability, H is the height of the flow cross section, ϕ is the rock porosity, c_t is the total compressibility and r is radius. In the above solution, spatially it is assumed that pressure is only a function of distance from the well radius as shown in Figure 2.3. Injection rate Q_{inj} is constant and the gravity effect is ignored to simplify the analytical solution.

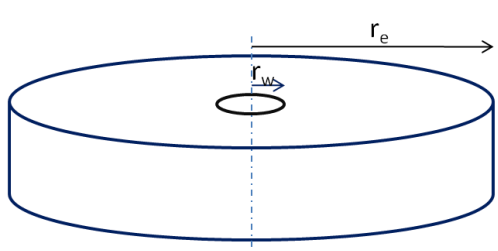

Figure 5.1- A sketch from geometry of the analytical solution

Exponential integral function, the E1 function and their relationship for a real, nonzero x are defined as follows.

$$Ei(x) = \int_{-\infty}^{x} \frac{e^t}{t} dt, \;\; E1(x) = \int_{x}^{\infty} \frac{e^{-t}}{t} dt\,; \qquad Ei(-x) = -E1(x) \tag{5.2}$$

E1(x) can be estimated by the following series given large enough upper limit to n.

$$E_1(x) = -\gamma - \ln x - \sum_{n=1}^{\infty} \frac{(-1)^n x^n}{n!\, n} \tag{5.3}$$

where γ is the Euler-Mascheroni constant which is equal to 0.5772156649… .

Table 5.1 - The example reservoir and fluid properties

ϕ =	0.2	p_i =	4500 kPa
k_h =	10 md	Q_{inj} =	1,000 m^3/Day
ρ_w =	1000 kg/m^3	r_w =	0.1414 m
μ_w =	1 cp	h =	30 m
c_f = c_r =	1.00E+06 kPa^{-1}		

To test the accuracy of the developed single phase flow code, it has been compared against the analytical solution at three arbitrary points; 0.1414m (well radius), 1.414m and 14.14m from the well center. For the well block, permeability and porosity are set to be high in magnitude to resemble the empty wellbore. Figure 5.2 illustrates the way that wellbore radius for analytical solution is chosen from the wellbore element based on the size of the well block in a Cartesian grid (r_w=0.1414m). If the wellbore radius, r_w, was selected based on the equivalent area of the well grid block, then the well block nodes would fall out of the wellbore circle; however the assumed configuration of the well block as shown in Figure 5.2 is such that the element nodes fall on the wellbore perimeter. It should be reminded that the FEM solves the pressure only at the existing nodes in the problem which then each element eight node pressures are averaged to obtain the grid block pressure.

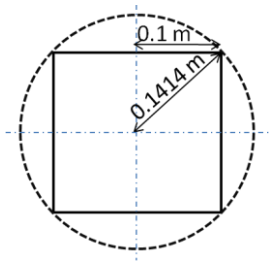

Figure 5.2- A sketch from the wellbore block 0.2 x 0.2m and the selected wellbore radius

In the selected example, the water is injected at 1000m^3/day into the center of a reservoir with the dimensions of 4000m x 4000m x 30m. The reservoir properties are given in Table 5.1. The model has been gridded in Cartesian coordinates based on a logarithmic scale from the wellbore (Aziz & Settari, 1979), in which the well block size is assumed to be 0.2 by 0.2 m (Figure 5.2). The comparisons of the results for the three arbitrary picked radii are shown in Figure 5.3, Figure 5.4 and Figure 5.5. Although the pressures are solved for nodes in FEM solution, in the developed code nodes pressures are averaged to obtain the element pressure. As one may expect and as seen in these figures, when the elements are refined, the numerical solution approaches the analytical solution. The results prove the reliability of the developed fluid flow code which will be coupled to geomechanics in the dynamic fracture modeling.

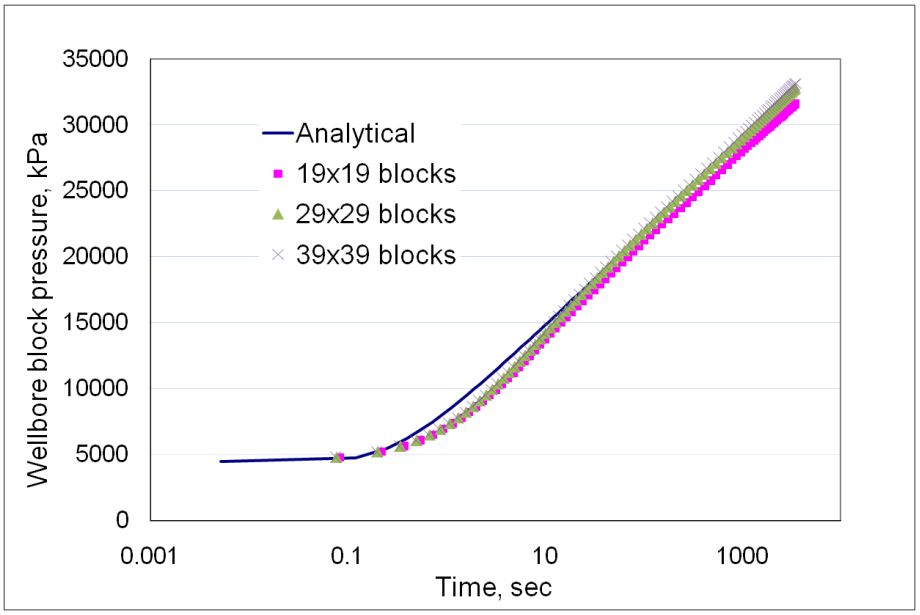

Figure 5.3- Analytical and numerical solution comparison for r = 0.1414m

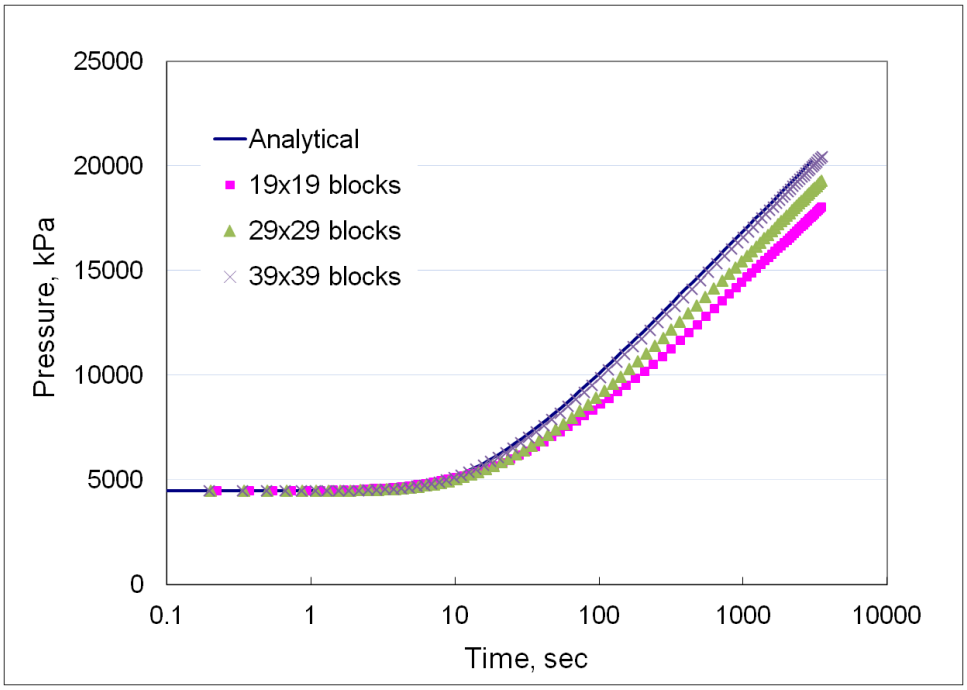

Figure 5.4- Analytical and numerical solution comparison for r = 1.414 m

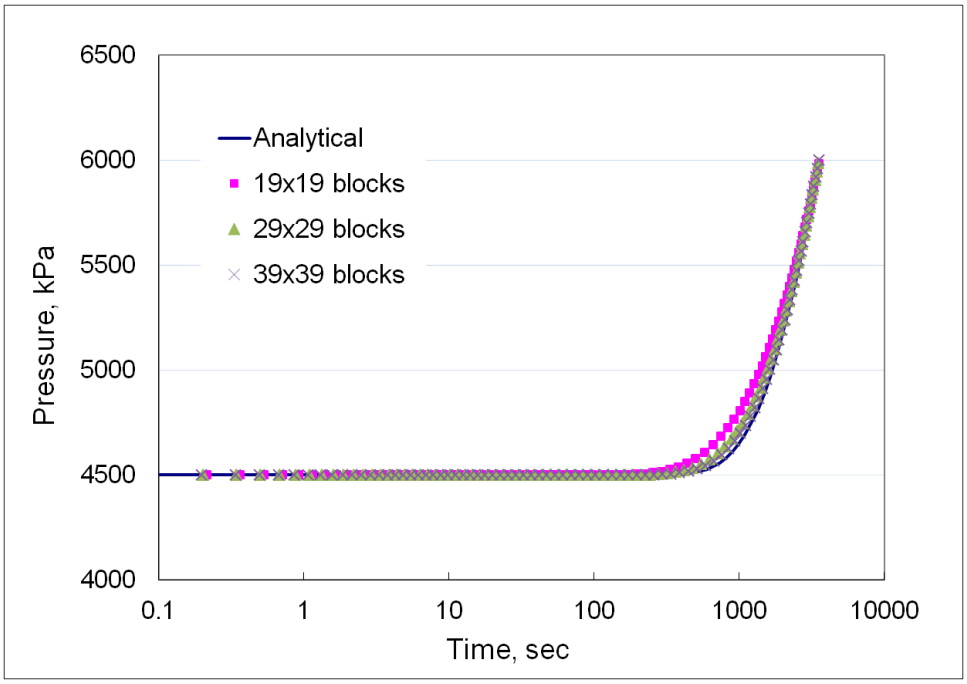

Figure 5.5- Analytical and numerical solution comparison for r = 14.14 m, element center pressure

When pressures at the 8 nodes of an element are arithmetically averaged to find the element pressure, there will be an inherent averaging error. To illustrate this fact, meshing of the model is adapted such that a certain node in the numerical solution is located exactly at the radius of 14.14 m from the center of the well grid block. The pressure vs. time for the specified node is plotted in Figure 5.6. The results can be compared with Figure 5.5 in which the depicted pressure is for the center of an element 14.14 m away from the center of the well grid block, and uses the averaging. The convergence is more rapid; an accurate match is obtained already for the 19x19 blocks case, for the node based pressure (Figure 5.6) as opposed to finer grid with element centered pressure (Figure 5.5). The discrepancy arises from the arithmetic averaging technique mentioned above.

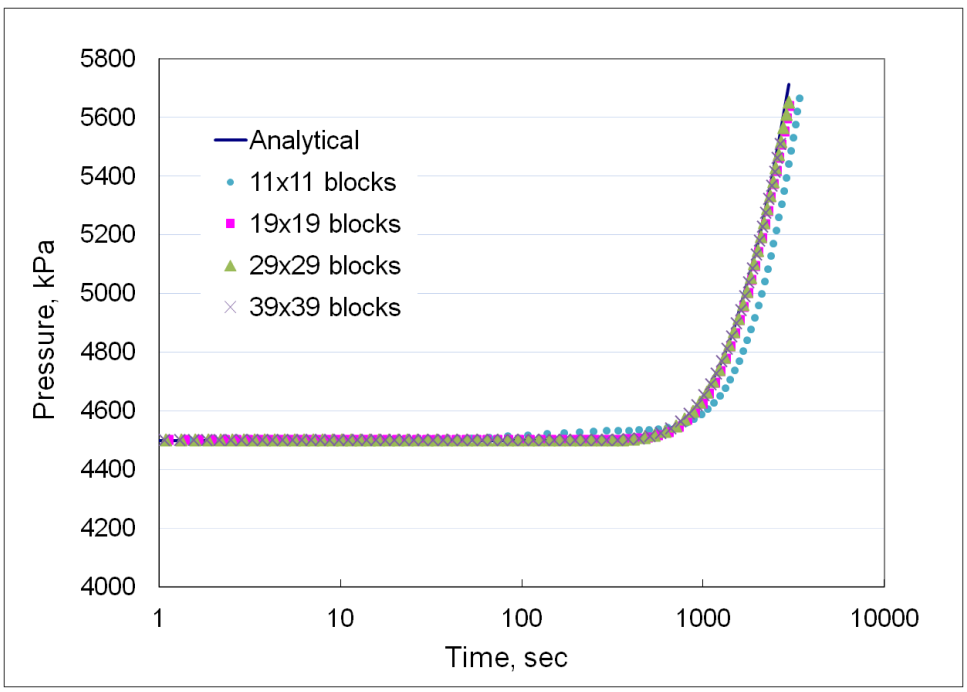

Figure 5.6- Analytical and numerical solution comparison for r = 14.14 m, node pressure

5.1.1.2 Linear flow

Transient linear flow regime with a constant flow rate q across the boundary is diagnosed by a linear profile when bottomhole pressure is plotted against the square root

of time. In this example a linear flow problem is solved both by the analytical solution and the code developed here for further flow model validation. For slightly compressible linear flow, the relationship between pressure and time is expressed as follows.

$$P_{wf} = P_i - \frac{2q}{wh}\left(\frac{\mu}{\pi k \emptyset c_t}\right)^{1/2}\sqrt{t} \tag{5.4}$$

In the example problem the width is w = 10 m, the height h = 1 m, viscosity μ = 1cp, permeability k = 1 md, porosity ϕ = 0.09, total compressibility c_t = 2x10^{-6} kPa^{-1}, total flow rate q = 100 m^3/day and the initial pressure is P_i = 64000 kPa. The comparison between the numerical and the analytical solutions is presented in Figure 5.7. The x direction grid block sizes were chosen to be irregular based on the second power of i index (x direction), which resulted in almost perfect data match.

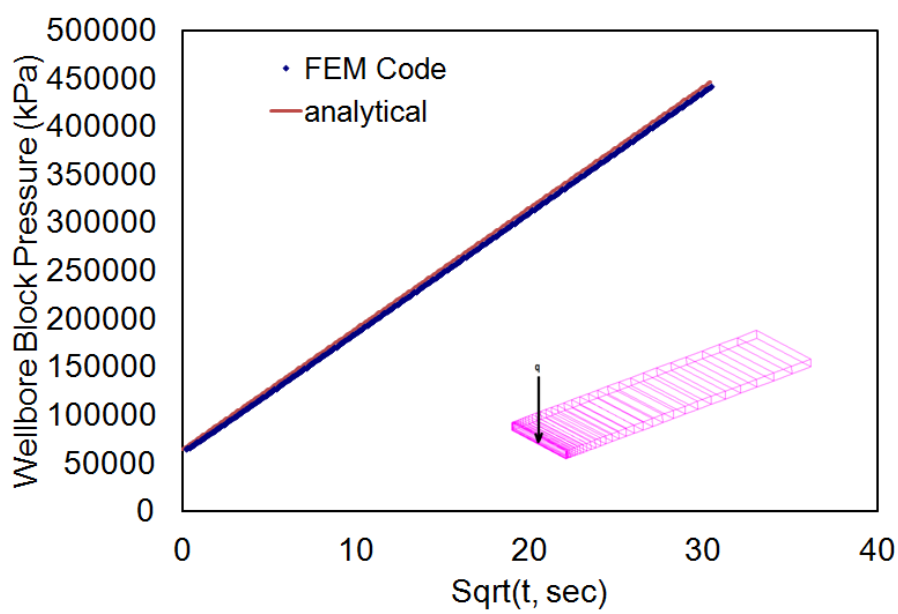

Figure 5.7- Analytical and numerical solution comparison, linear flow

5.2 Mechanical behavior of fractured block

The geomechanical part of the developed FEM code has been first tested for different simple example problems with linear elastic materials. The code has given the

same results as the respective analytical solutions for different tests such as uniaxial and triaxial compression. Here we begin the description of the geomechanical validation part from the testing of the constitutive model of a single fracture and then the equivalent medium representation of fractured blocks, to keep the writing brief (Nassir et. al. 2009).

5.2.1 Single fracture

Single fracture mechanical behavior comprises of two parts depending on the deformation direction; normal and shear. In this section, the validity of the developed finite element code for estimating the mechanical behavior of a single fracture will be shown.

5.2.1.1 Normal deformation

As previously described in the theory chapter, the normal behavior of a single fracture is described by a hyperbolic model proposed by Barton et. al. (1985). Hyperbolic

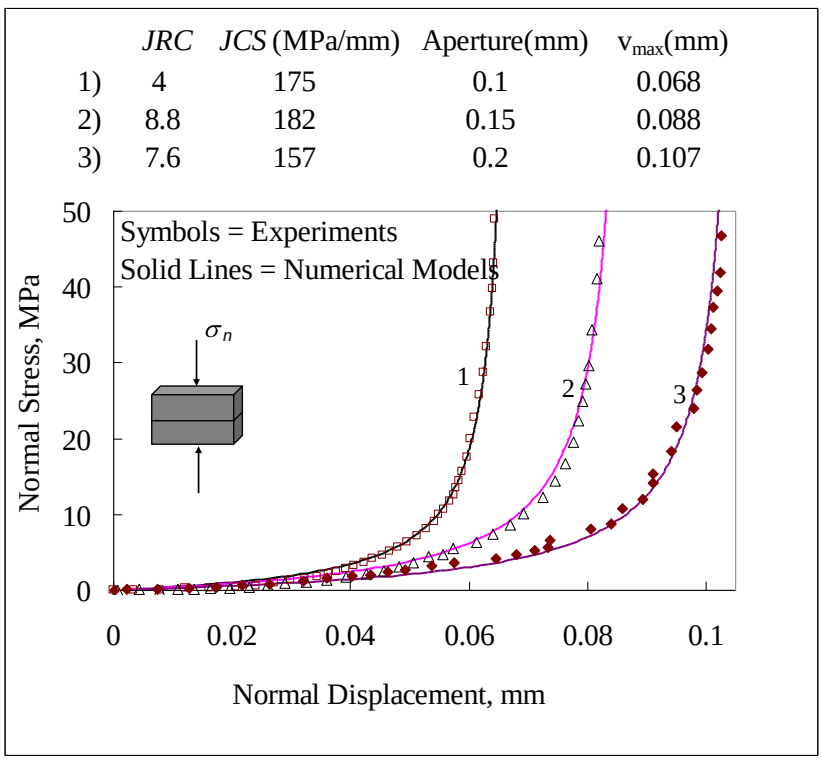

Figure 5.8 - Comparison between the analytical fit of Barton's experimental data and the developed code results for normal deformation of a range of fresh joints

model fitting parameters were obtained from their experimental data. The experimental results (from Barton 1985) are compared with our numerical solution as shown in Figure 5.8. Since the model is non-linear, Newton iteration is used to eliminate out of balance forces when increment of normal stress is applied. Although only two iterations were used in the numerical solution in Figure 5.8, the results agree very well.

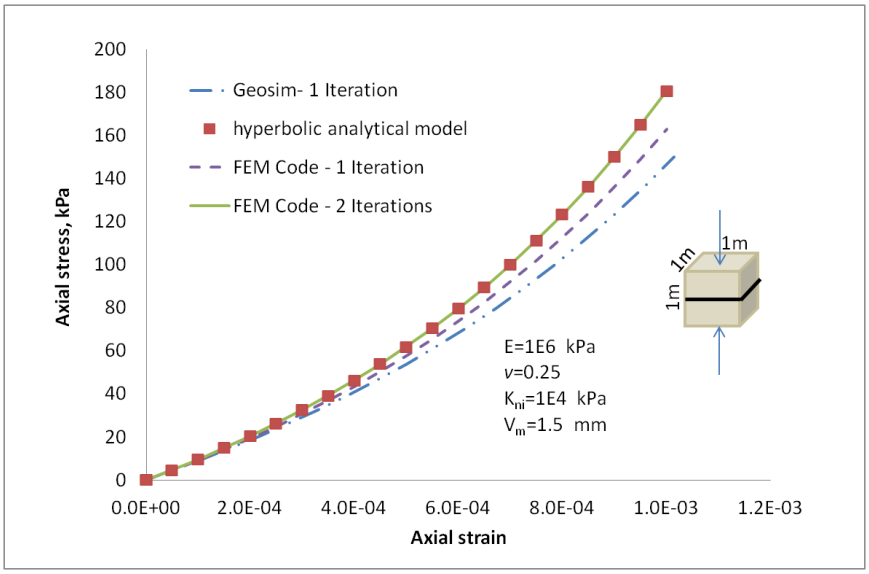

Figure 5.9 - Comparison between the analytical fit of Barton's experimental data and the developed code results for normal deformation of a range of fresh joints

In the next example, normal deformation of a cubical block which contains a single horizontal fracture is compared with the result from the GEOSIM as shown in Figure 5.9. The analytical model is very well approximated by the developed code using 2 iterations. Although the load increments are the same in GEOSIM and in our FEM code, the results for 1 iteration case from GEOSIM and the current code are not the same. This is explained by the fact that in GEOSIM the fracture normal stiffness at the first iteration is estimated at a normal effective stress which is the average of the stress at the current time step and one time step before; whereas in the FEM code it is estimated at the current time step. GEOSIM will also present a good match with the analytical solution if larger number of iterations is used. The above comparison shows that even small details in the iteration strategy can cause significant differences in accuracy.

5.2.1.2 Shear deformation

The new non-linear hyperbolic model for pre-peak shear behavior of a single fracture proposed in this work is evaluated here to see how well it predicts some of the Barton's experimental data (Barton et al., 1985). It should be noted that the model is not elasto-plastic and it is simply a non-linear (pre-peak) model. A schematic of an initially loaded fracture (with 2 MPa of confining normal stress), the way it is sheared and all the fracture properties are shown in Figure 5.10. The tested fracture is horizontally embedded within a very hard rock (high value of Young's modulus, 10^{15} kPa) to eliminate the rock effect on the overall fracture deformation. The bottom of the sample problem is fixed in all three directions. On the top displacement will be applied in one of the shear directions in lieu of shear stress increments.

We can see in Figure 5.10 how closely the proposed model fits the experimental data for pre-peak shear and dilation behavior of different tested fractures. The value of γ_{coef} used in the numerical solution is 0.3 which is what has been observed in majority of the tested joints by Barton et. al. (1985). The new hyperbolic model has also proved to be valid for a wide range of normal effective stresses as shown in Figure 5.11.

Post-peak portion of a fracture shear deformation with shear stress is modeled by elasto-plastic model as developed in previous chapter. The set of example problems selected for the model validation is the same as presented for the pre-peak shear deformation part, with further extension of shear displacement into the post-peak region which activates the elasto-plastic constitutive model.

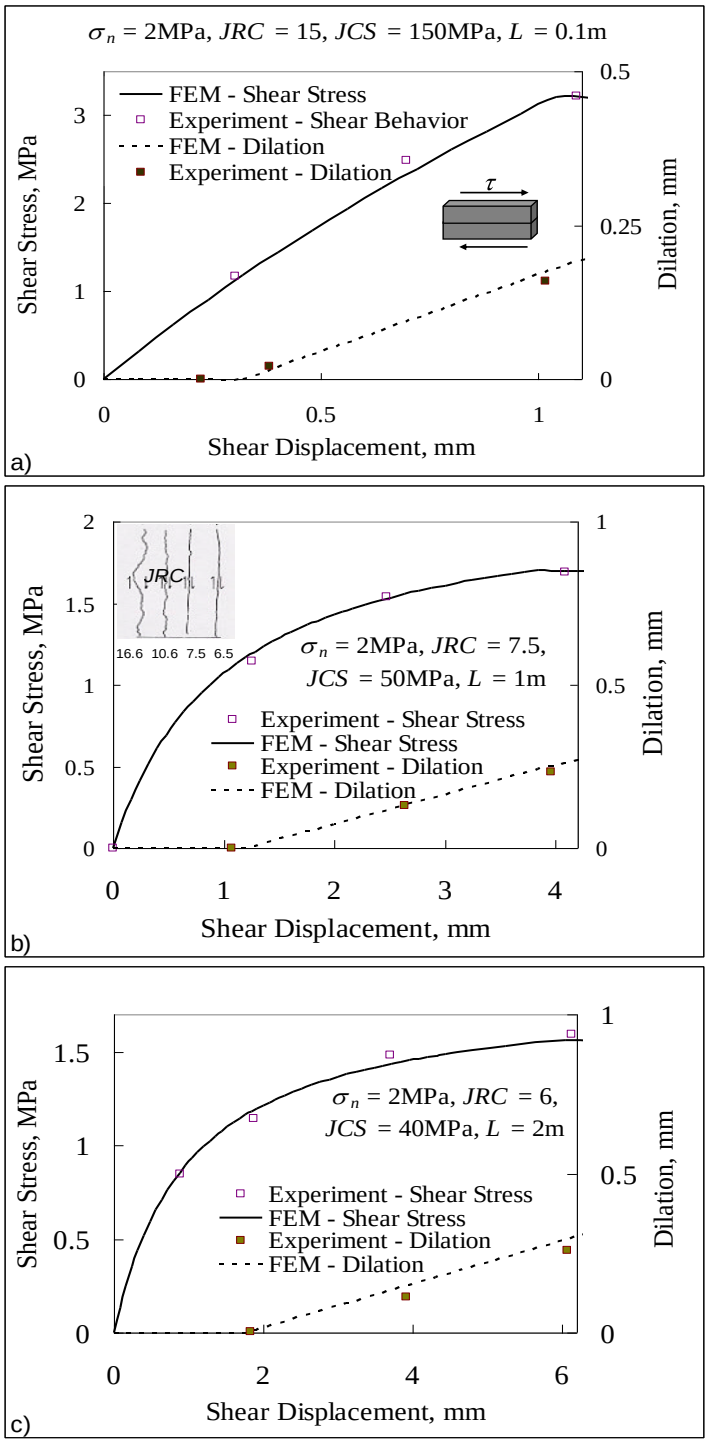

Figure 5.10 - Comparison between the numerical model and Barton experimental data for shear stress and dilation vs. displacement

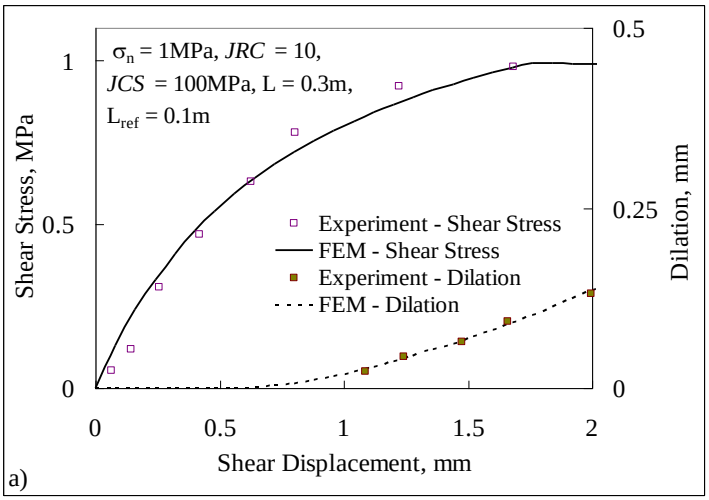
σn = 1MPa, JRC = 10,
JCS = 100MPa, L = 0.3m,
Lref = 0.1m
Experiment - Shear Stress
FEM - Shear Stress
Experiment - Dilation
FEM - Dilation
Shear Stress, MPa
Dilation, mm
Shear Displacement, mm
0
0.5
1
0.25
0.5
1.5
2
a)

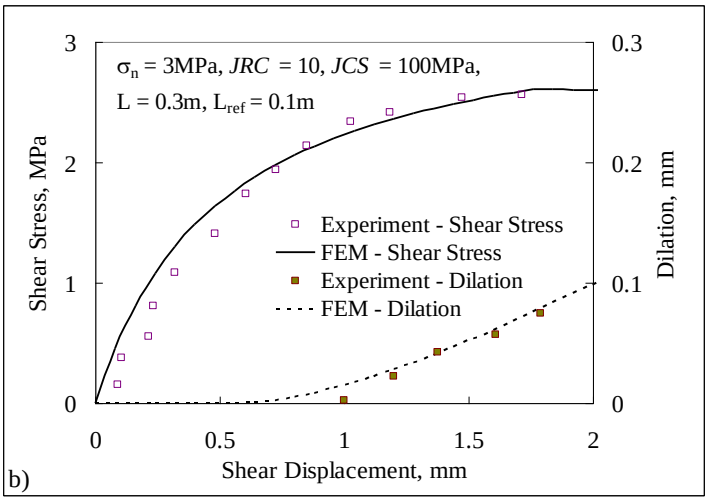
σn = 3MPa, JRC = 10, JCS = 100MPa,
L = 0.3m, Lref = 0.1m
Experiment - Shear Stress
FEM - Shear Stress
Experiment - Dilation
FEM - Dilation
Shear Stress, MPa
Dilation, mm
Shear Displacement, mm
0
1
2
3
0.1
0.2
0.3
0.5
1.5
2
b)

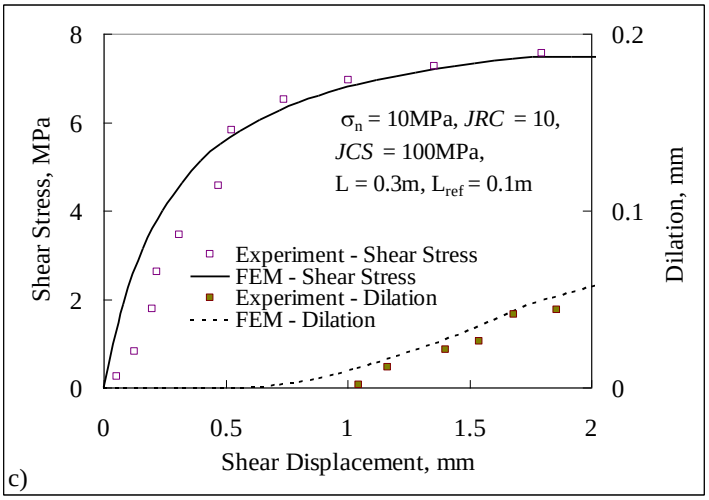
σn = 10MPa, JRC = 10,
JCS = 100MPa,
L = 0.3m, Lref = 0.1m
Experiment - Shear Stress
FEM - Shear Stress
Experiment - Dilation
FEM - Dilation
Shear Stress, MPa
Dilation, mm
Shear Displacement, mm
0
2
4
6
8
0.1
0.2
0.5
1
1.5
2
c)

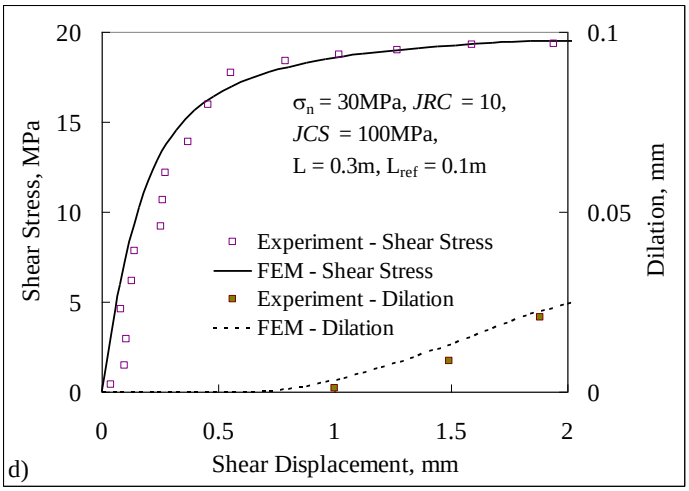

Figure 5.11 - Comparison of shear stress and dilation vs. displacement between the numerical model and Barton experimental data for the effect of normal stress – only pre-peak part

Figure 5.12 indicates the full pre-peak and post-peak shear and dilation comparison between experimental data and numerical results for different fractures. Properties of each fracture are shown in the respective figure. Shear softening in the post-peak portion (which is the same as asperities degradation) is controlled by the exponent parameter *n* relating the mobilized friction angle and the plastic shear strain. The higher the magnitude of *n* and the larger the *JRC*, the higher is the amount of degradation (i.e., as seen for *JRC* =15). The peak shear displacement is increasing with the length of the fractures as shown in the figure. The peak shear stress rises with *JRC* when confining normal stress is kept fixed. Dilation angle is usually a portion of, and not exactly equal to the mean asperity angle since asperities deform elastically when shear deformation occurs. The elastic deformation of the asperities will not affect the peak shear stress calculation, as explain in the literature review chapter (Seidel and Haberfield, 1995).

Number of iterations quoted on the Figures refers to the number of iterations in Newton solution implemented in the code for the non-linear constitutive model. As shown in Figure 5.12, when only one iteration is used, the induced out of balance forces due to the non-linearity of the problem will result in an inaccurate solution (in particular in the top part). Larger number of iterations results in a better solution but involves more running time. However, not a large difference is observed between the cases with 2 and

higher number of iterations. In many real large models where the running time is an important issue, 2 iterations for the Newton solution might be sufficient. The rapid convergence of the technique developed here is an important result.

In the current results it is obviously seen that the stress state is not checked to be either below or at the fracture shear failure surface. The constitutive model for the post-peak is just the elasto-plastic model developed in the previous Chapter. Later on in this chapter (especially for more practical examples) a special method of checking the stress state with respect to shear failure surface, the drifting of the shear failure surface and a technique to control the possible divergence in the Newton loop will be implemented and used in example problems.

The depicted figures are all for 2D models; however, the developed code handles 3D models as well. In the 3D model there are two shear directions in the fracture constitutive model. Two mean asperity angles are defined for the two shear directions which initially are assumed to be the same and the degradation in any shear direction depends on the respective cumulative plastic strain.

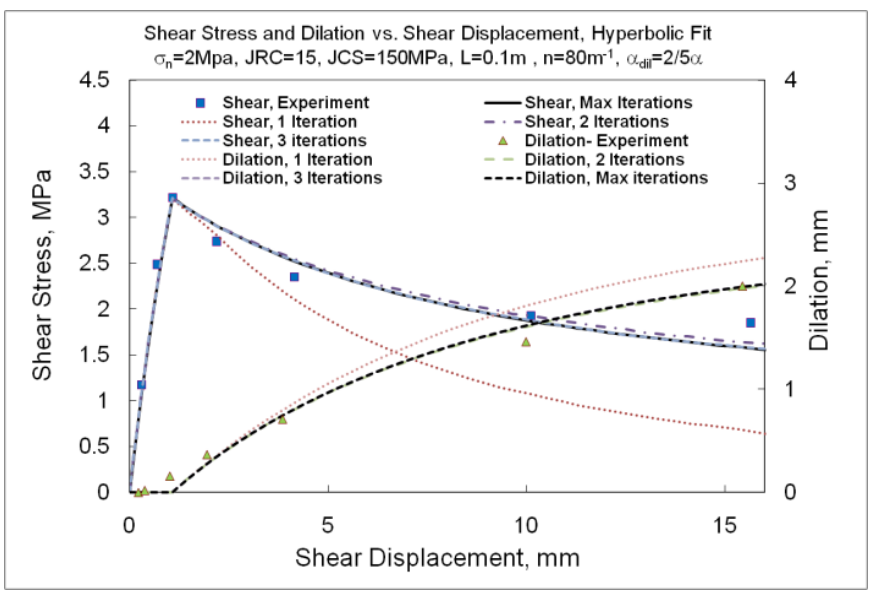

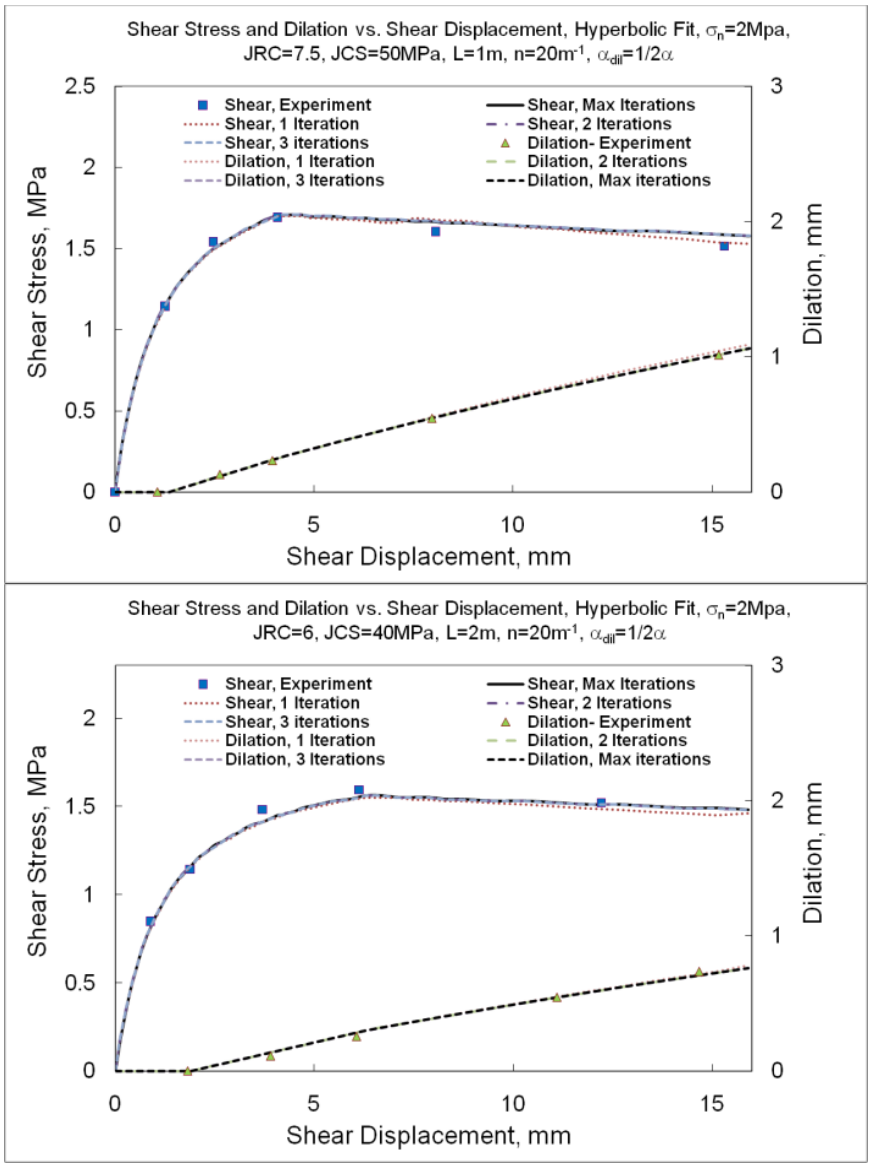

Figure 5.12 – Shear and dilation behavior of single fractures with different properties

The next step in a single fracture constitutive model validation is to subject the code to different confining normal stresses and to check for the applicability of the model. Depending on the depth of the fractured reservoir and the fluid pressure in it, fractures are subjected to a wide range of effective normal stresses. For example in a deep reservoir during fluid production and depletion, the confining stresses on the existing fracture planes are usually high. On the other hand in injection scenarios, high pressure may lead

to very low amount of effective confining stresses. Therefore, it is crucial for a fracture constitutive model to be applicable for a wide range of effective normal stresses.

A relatively good match is observed between the numerical results and the experimental data for a range confining stresses in Figure 5.13. One iteration appears to be insufficient in the Newton solution as shown in the figure. Two iterations usually result in almost the same outcome as the case when the Newton solution fully converges in these studied cases.

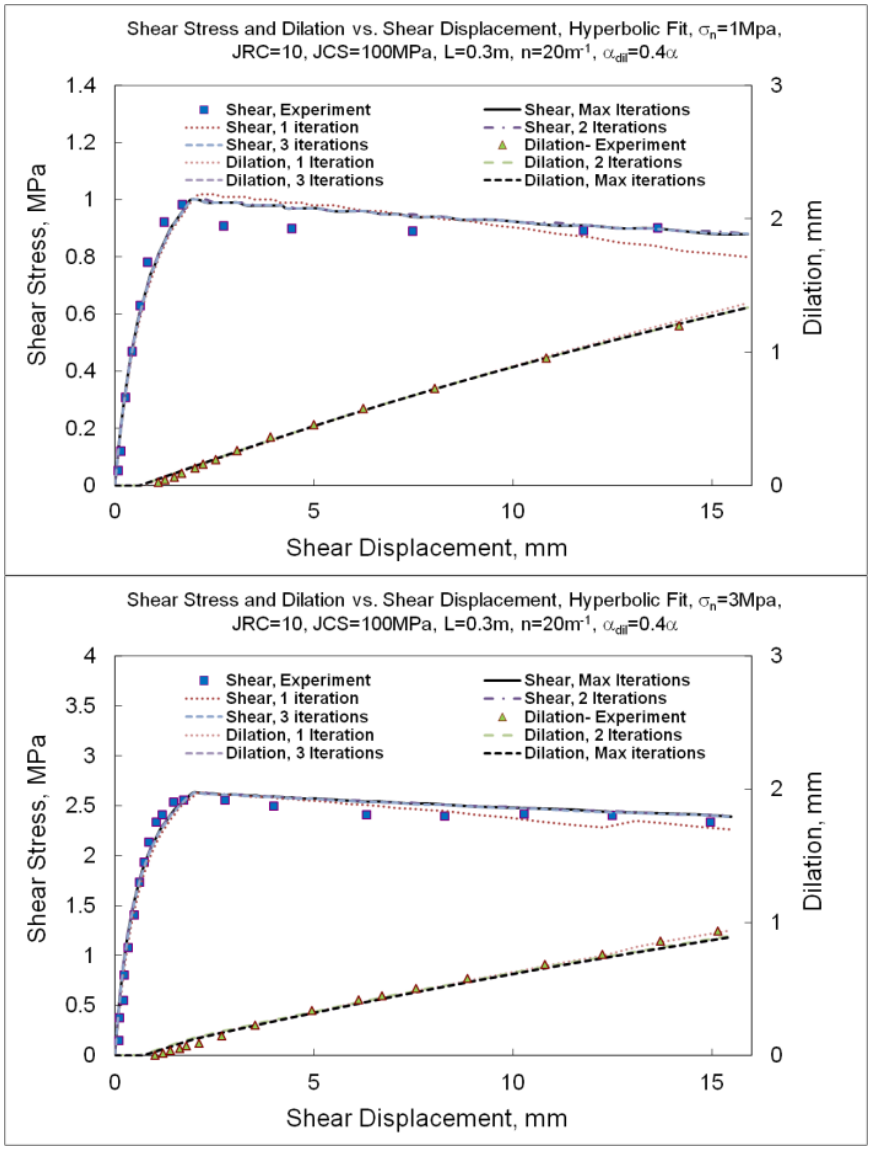

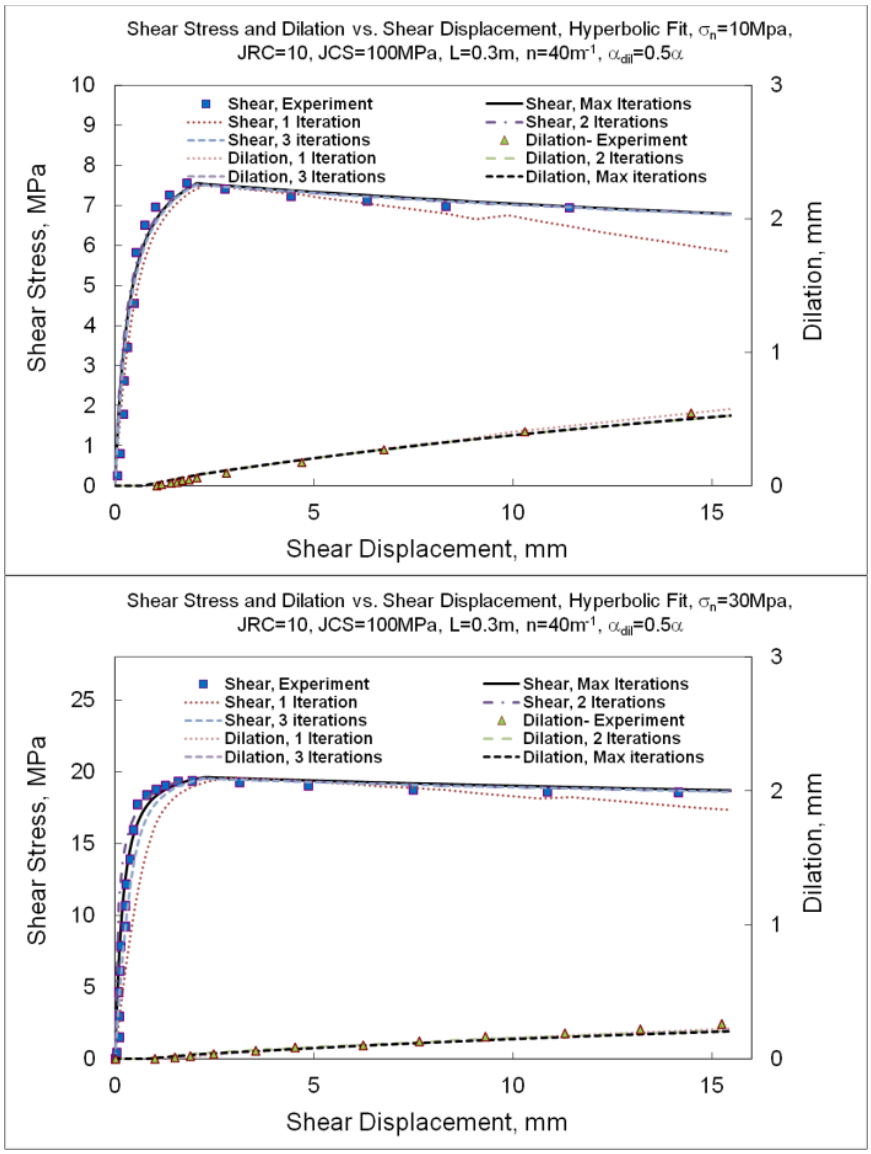

Figure 5.13 – Shear and dilation behavior of a single fracture under different confining stresses

5.2.2 Equivalent fractured block compliance matrix from known fracture sets

The technique implemented to obtain the equivalent modulus of a fractured block has been extensively discussed in the theory chapter. Here the same method is used to obtain the analytical solution for a triaxial test and to validate the accuracy of the numerical solution. A single fracture in 3D space is defined with a set of dip and azimuth angles as follows,

$$\begin{array}{ccc} \underline{normal} & \underline{strike} & \underline{tangential} \\ \end{array}$$
$$\begin{bmatrix} \sin d \cos a & \sin a & -\cos d \cos a \\ -\sin d \sin a & \cos a & \cos d \sin a \\ \cos d & 0 & \sin d \end{bmatrix} \tag{5.5}$$

Local coordinates for a fracture are defined based on the local normal, strike and tangential directions as defined above. If the stress and strain tensors are known for a block that contains a single fracture defined above, the three stress components, one normal and two shear, can be obtained by a transformation matrix as follows (Cook et al., 1989),

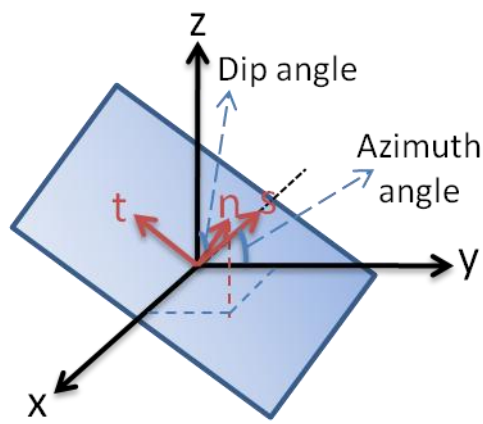

Figure 5.14 – A sketch of a fracture plane specified by a set of dip and azimuth angles

$$T_J = \begin{bmatrix} \sin^2 d \cos^2 a & \sin^2 d \sin^2 a & \cos^2 d & -\sin^2 d \sin 2a & -\sin 2d \sin a & \sin 2d \cos a \\ 1/2 \sin d \sin 2a & -1/2 \sin d \sin 2a & 0 & \sin d \cos 2a & \cos d \cos a & \cos d \sin a \\ -1/2 \sin 2d \cos^2 a & -1/2 \sin 2d \sin^2 a & 1/2 \sin 2d & 1/2 \sin 2d \sin 2a & \cos 2d \sin a & -\cos 2d \cos a \end{bmatrix} \tag{5.6}$$

The above transformation matrix can be used to obtain the compliance matrix of a single fracture in global coordinate system (x, y, z) from the local ones (n, s, t) by the following equation,

$$F_J^G = \frac{1}{S_J} T_J^T F_J^L T_J \tag{5.7}$$

In a triaxial test if we assume that the axial load exclusively leads to increase in the axial stress, only the third column of the total compliance matrix will be needed to calculate the strain components (F_{13}, F_{23}, F_{33}, F_{43}, F_{53}, F_{63}).

$$\begin{bmatrix}\epsilon_{11}\\ \epsilon_{22}\\ \epsilon_{33}\\ \epsilon_{12}\\ \epsilon_{23}\\ \epsilon_{13}\end{bmatrix}=\begin{bmatrix}F_{11} & F_{12} & F_{13} & F_{14} & F_{15} & F_{16}\\ F_{21} & F_{22} & F_{23} & F_{24} & F_{25} & F_{26}\\ F_{31} & F_{32} & F_{33} & F_{34} & F_{35} & F_{36}\\ F_{41} & F_{42} & F_{43} & F_{44} & F_{45} & F_{46}\\ F_{51} & F_{52} & F_{53} & F_{54} & F_{55} & F_{56}\\ F_{61} & F_{62} & F_{63} & F_{64} & F_{65} & F_{66}\end{bmatrix}\begin{bmatrix}0\\ 0\\ \sigma_{33}\\ 0\\ 0\\ 0\end{bmatrix} \tag{5.8}$$

Let's assume the single fracture compliance matrix in the local coordinate system contains two equal shear compliance terms as follows.

$$F_J^L=\begin{bmatrix}1/K_n & 0 & 0\\ 0 & 1/K_s & 0\\ 0 & 0 & 1/K_s\end{bmatrix} \tag{5.9}$$

Now from Eq. (5.6), the third row of the compliance matrix for a single fracture set in the global coordinates can simply be calculated by the following equations.

$$\begin{aligned}
F_{31} &= \frac{1}{4SK_n}\sin^2 2d\cos^2 a-\frac{1}{4SK_s}\sin^2 2d\cos^2 a\\
F_{32} &= \frac{1}{4SK_n}\sin^2 2d\sin^2 a-\frac{1}{4SK_s}\sin^2 2d\sin^2 a\\
F_{33} &= \frac{1}{SK_n}\cos^4 d+\frac{1}{4SK_s}\sin^2 2d\\
F_{34} &= -\frac{1}{4SK_n}\sin^2 2d\sin 2a+\frac{1}{4SK_s}\sin^2 2d\sin 2a\\
F_{35} &= -\frac{1}{SK_n}\cos^2 d\sin 2d\sin a+\frac{1}{4SK_s}\sin 4d\sin a\\
F_{36} &= \frac{1}{SK_n}\cos^2 d\sin 2d\cos a-\frac{1}{4SK_s}\sin 4d\cos a
\end{aligned} \tag{5.10}$$

Compliance matrix for a fractured block containing n fracture sets is then calculated by the following summation.

$$F^G=F_I+\sum_{J=1}^{n}F_J^G \tag{5.11}$$

Table 5.2 gives the properties of three fracture sets in a block of fractured rock (1m x 1m x 1m) for the first case studied here. In the second and third cases, the dip angles of fracture sets 1 and 2 are changed to 30 and 45 respectively.

Table 5.2 – Fracture sets' properties

Case#1	FS#1	FS#2	FS#3
Dip angle	15	15	90
Azimuth angle	0	180	90
Kn(kPa/m)	1.00E+06	1.00E+06	1.50E+06
Ks(kPa/m)	1.00E+05	1.00E+05	1.50E+05
Spacing(m)	0.4	0.4	0.4

Table 5.3 shows the comparison between the analytical and numerical solutions as well as the results from the GEOSIM code when 1 MPa of axial load is applied on the assumed fractured blocks in the triaxial test. In GEOSIM, Chang and Huang (1988) approach is implemented by Bagheri and Settari (2006). A perfect match is seen between all methods which prove the accuracy of the numerical code in calculating the equivalent modulus of the fractured blocks from known sets of fracture moduli.

Table 5.3 – Comparison of strains caused by 1 MPa of axial load between analytical and numerical solutions

		ε_{11}	ε_{22}	ε_{33}	ε_{12}	ε_{23}	ε_{13}
Case 1 # (α = 15°)	Analytical	-0.0281375	-0.0000125	0.0748256	-3.446E-18	-5.01E-18	6.25E-34
	Numerical	-0.0281375	-0.0000125	0.0748256	0	0	0
	Geosim	-0.0281375	-1.252E-05	0.0748256	-5.933E-18	6.939E-18	1.39E-17
Case 2 # (α = 30°)	Analytical	-0.0843875	-0.0000125	0.121925	-1.034E-17	-5.57E-18	6.25E-34
	Numerical	-0.0843875	-0.0000125	0.121925	0	0	0
	Geosim	-0.0843875	-1.252E-05	0.121925	-4.291E-17	4.857E-17	1.73E-17
Case 3 # (α = 45°)	Analytical	-0.1125125	-0.0000125	0.13755	-1.378E-17	-1.17E-17	6.25E-34
	Numerical	-0.1125125	-0.0000125	0.13755	0	0	0
	Geosim	-0.1125125	-1.252E-05	0.13755	7.6734E-17	-7.63E-17	0

In the second example the fracture sets are assumed in a way such that the compliance matrix of the fractured rock becomes non-symmetric. The properties of the fracture sets are shown in Table 5.4.

Table 5.4 – Different fracture sets' properties

Case#1	FS#1	FS#2	FS#3
Dip angle	45	15	90
Azimuth angle	0	180	90
Kn(kPa/m)	1.00E+06	5.00E+06	3.50E+06
Ks(kPa/m)	2.00E+05	4.00E+05	1.50E+05
Spacing(m)	0.6	0.4	0.5

In this example where the compliance matrix of the fractured rock is non-symmetric or anisotropic, the applied normal stress usually induces a certain shear stress which arises from the nature of the anisotropy and the displacement fixity assumptions which have been specified on the back (x direction), left (y direction) and bottom (z direction) faces of the block in the triaxial test. In the current example τ_{13} is induced when axial stress is applied. Since the term τ_{13} is non-zero, according to Eq. (5.8) we will need the last column of the fractured block compliance matrix which can be obtained by the following equations.

$$F_{16} = \frac{1}{SK_n}\sin^2 d \sin 2\mathrm{d} \cos^3 a + \frac{1}{4SK_s}\sin 2\mathrm{d} \sin 2\mathrm{a} \sin \mathrm{a} + \frac{1}{4SK_s}\sin 4d \cos^3 a$$

$$F_{26} = \frac{1}{SK_n}\sin^2 d \sin 2\mathrm{d} \sin^2 a \cos a - \frac{1}{4SK_s}\sin 2d \sin 2a \sin a + \frac{1}{4SK_s}\sin 4\mathrm{d} \sin^2 a \cos a \tag{5.12}$$

$$F_{36} = \frac{1}{SK_n}\cos^2 d \sin 2d \cos a - \frac{1}{4SK_s}\sin 4d \cos a$$

$$F_{46} = -\frac{1}{SK_n}\sin^2 d \sin 2d \sin 2a \cos a + \frac{1}{2SK_s}\sin 2d \cos 2a \sin a - \frac{1}{4SK_s}\sin 4d \sin 2a \cos a$$

$$F_{56} = -\frac{1}{2SK_n}\sin^2 2d \sin 2a + \frac{1}{2SK_s}\cos^2 d \sin 2a - \frac{1}{2SK_s}\cos^2 2d \sin 2a$$

$$F_{66} = \frac{1}{SK_n}\sin^2 2d \cos^2 a + \frac{1}{SK_s}\cos^2 d \sin^2 a + \frac{1}{SK_s}\cos^2 2d \cos^2 a$$

Still to have the problem solved completely, it is required for the shear term, τ_{13}, to be known whereas the only given loading data is the applied axial stress. When the example problem is run by the developed code, the shear term, τ_{13}, will result when the stress is updated from the displacement in the stress update routine. In order to compare the developed code, the shear stress which resulted from the numerical solution is used in the analytical solution to obtain the additional strain components. Table 5.5 shows the comparison between the analytical solution and the numerical solution from the developed code as well as the GEOSIM results. The value of the induced shear stress

Table 5.5 - Comparison between the analytical and numerical methods for the fractured block with non-symmetric compliance matrix

		ε_{11}	ε_{22}	ε_{33}	ε_{12}	ε_{23}	ε_{13}
Case 1	Analytical	-0.0196367	-0.0000125	0.0309929	2.5889E-19	-5.68E-18	0.011835
	Numerical	-0.0196367	-0.0000125	0.0309929	-4.78E-06	-5.26E-06	0.011835
	Geosim	-0.0196367	-0.0000125	0.0309929	-4.779E-06	-5.26E-06	0.011835

from numerical solution for this example is obtained to be -118.57 kPa which is used in analytical solution as discussed above. Like in the previous example, the comparison

results of this example indicate that the developed code is totally correct in terms of calculating the compliance matrix of a fractured block.

5.2.3 Examples on fractured rock mechanical behavior

This section comprises of two parts. In the first part some examples of stress-train behavior of fractured rock subjected to different loading conditions and fracture configurations will be shown and discussed. In the second part, the model is used to match the results from the experiments conducted by Kulatilake et al. (2001) on fractured blocks.

Planes of weakness in a block have a major influence on the deformation behavior of the block compared with the intact one. The deviation is even more pronounced when the weak planes are subjected to high shear loadings and are freed to deform in terms of boundary fixity. The example problem compares axial stress and axial deformation of fractured blocks with different fracture orientations as shown in the schematic sketch of the example setup on Figure 5.15. The block dimensions are 1x1x1 m and the two conjugate fracture sets are spaced equally with 0.4 m of spacing. The initial confining stress is assumed to be 0.25 MPa and the specimen is axially loaded with the means of displacement boundary loading. The intact rock Young's Modulus is 80 GPa and the Poisson's ratio is 0.25.

In the example problem among all the fracture configurations, shear slippage occurred only in the case with 60° of dip angle. As shown in Figure 5.15 the axial stress reaches in this case a plateau in which sliding on the fracture planes occurs. The shear slippage is usually associated with opening of the fracture aperture or dilation as indicated from the solution. Since shear associated dilation is considered to be plastic and permanent (such as in the SRV created by hydraulic fracturing), this phenomenon is quite favorable. In other cases where the dip angles are not large enough for shear slippage, axial loading resulted in increase in axial stress and decrease in fracture aperture as shown in Figure 5.15. The lower the dip angle, the higher the magnitude of the axial stress if someone wants to generate the same axial strain. This is due to the influence of the pre-

peak shear term in total deformation of the fractured block. Only in the last case (dip angle= 60°), the shear stress can reach its peak value and then slippage happens.

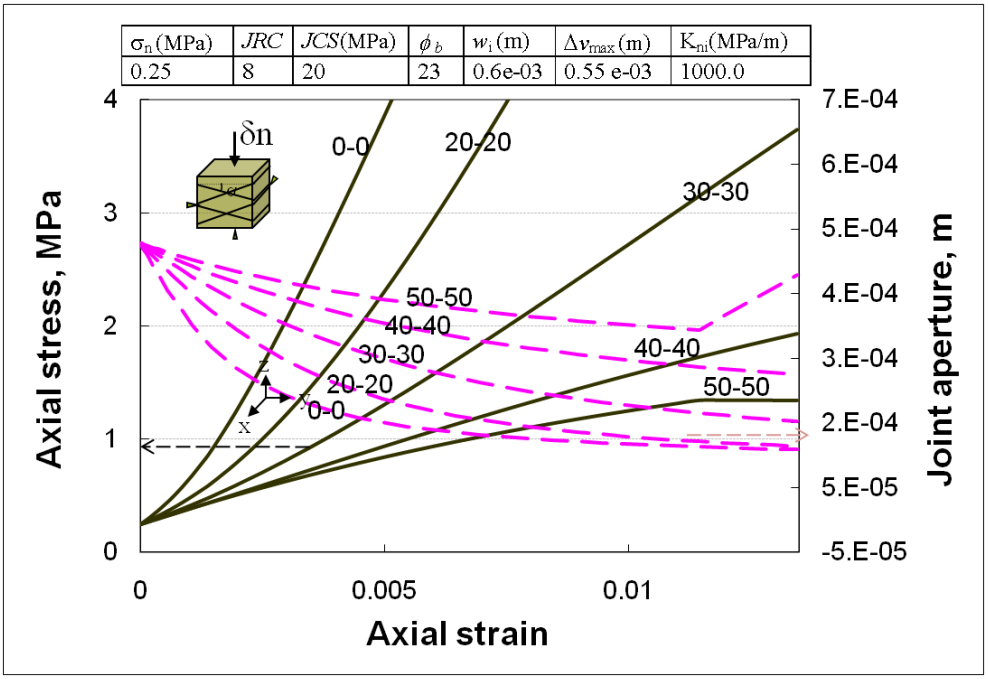

Figure 5.15 – Axial stress vs. axial strain of fractured blocks with different fracture orientations

5.2.4 Matching the experimental data by the use of pre-peak hyperbolic shear model

In this section, we attempt to match a set of experimental data by the aid of fractured block constitutive model in which only pre-peak hyperbolic shear model is used. Despite the large amount of experimental data for shear behavior of a single fracture, not enough experimental work has been carried out to investigate the mechanical deformation of composite fracture/rock or jointed rock system. (Kulatilake et al., 2001) conducted a series of laboratory experiments on jointed material blocks. The constituent prismatic parts of the jointed blocks made of plaster, sand, and water were separately mixed, cast and cured. About 15 wooden frames were constructed to use as molds to prepare prismatic jointed block samples with different joint geometry configurations.

It should be noted that the initial normal stiffness and the maximum fracture closure for the first loading cycle were correlated as functions of *JCS*, *JRC* and initial unstressed joint aperture a_j by Bandis et al. (1983) as follows:

$$K_{ni} = -7.15 + 1.75JRC + 0.02\left(\frac{JCS}{a_j}\right) \tag{5.13}$$

$$v_m = -0.296 - 0.0056JRC + 2.24\left(\frac{JCS}{a_j}\right)^{0.245} \tag{5.14}$$

From Eqs. (5.13), (5.14) and initial aperture size of 1.4 mm, the initial guesses for *JCS* and *JRC* were obtained to be 4 MPa and 4.4 respectively. Since no two real joints are the same in term of their physical properties, the resulting simulation data based on the above joint properties will not necessarily match all experimental data.

To model stress-strain behavior of the jointed rock, one needs to know both the properties of the intact rock as well as the embedded joints. The average intact rock Poisson's ratio, compressive strength and Young's modulus were taken as 0.24, 5.15 MPa and 1.1 GPa respectively.

Unfortunately not enough measurement was performed to obtain physical properties of all the joints. The only available experimental data was the normal stress-normal strain of a jointed rock containing a single horizontal joint, subjected to uniaxial vertical loading as shown in Figure 5.16. Bandis normal deformation model with k_{ni} = 0.55 MPa/mm and v_m = 1.22 mm appeared to be the best fit for this experimental data. *JCS* and *JRC* are usually estimated by Schmidt hammer and tilt tests in the laboratory; however, the experimental data did not include such measurements. *JCS* can take a maximum value of the intact rock compressive strength when the joint faces are completely mated and non-weathered (Barton and Choubey, 1977). However, in this case study the surfaces were not fully matched, since the two slabs of the joints were molded separately.

Figure 5.17 shows a picture of the experimental setup as well as the grid geometry used for modeling the jointed block stress-strain behavior with the finite element code. Conjugate joints with 0.075 m of spacing in a single element construct the numerical

model. The experimental setup in Figure 5.17 indicates the direction along which the jointed block is uniaxially loaded. It is assumed that the bottom face is fixed in z direction and only a quarter of the whole block is modeled to take advantage of no displacement boundaries in the vertical planes of symmetry.

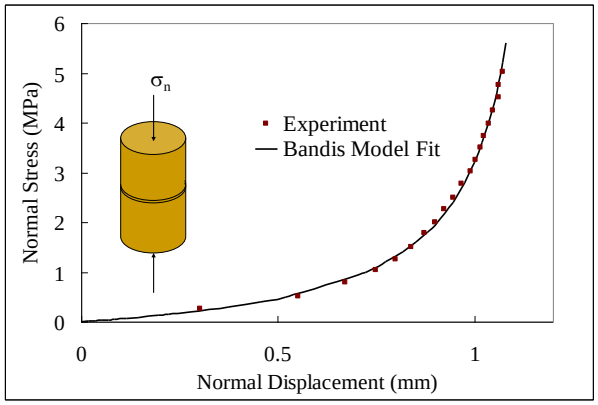

Figure 5.16 - Normal stress-normal displacement behavior of a single horizontal joint under uniaxial vertical loading

Table 5.6 - Joint properties used in numerical modeling of different jointed blocks

Dip Angles	5-5	10-10	15-15	20-20
JRC =	4.4	4.4	4.4	0.6
JCS (Mpa) =	4	4	4	4
L_{ref} (m) =	0.13	0.13	0.13	0.13
Φ_b =	22	22	22	24
a_i (mm) =	0.2	0.4	0.55	0.6
Δv_{max} (mm) =	0.15	0.37	0.49	0.55
K_{ni}	0.7	1.0	0.4	7
Spacing (m) =	0.07	0.075	0.075	0.075

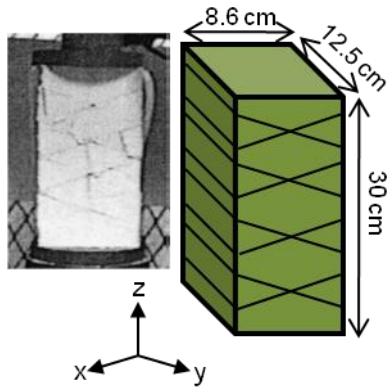

Figure 5.17 - A schematic of the sample jointed block for numerical modeling

Figure 5.18 shows the comparison between the experimental data for jointed blocks with different joint dip angles 5°-5°, 10°-10°, 15°-15° and 20°-20° and the numerical model which did not consider any shear effect of the joints. Figure 5.19 presents the same experimental data in comparison with a model which accounts for the shear effects, using the non-linear hyperbolic modeled method developed in this work. Low dip angles of the embedded fractures have kept the shear constitutive model to move only in the pre-peak non-linear part. Comparison of Figure 5.19 with Figure 5.18 indicates how much the shear deformation can affect the overall deformation of a loaded jointed rock. The deviation in the match caused by neglecting the shear effects is more noticeable for joints with larger dip angle. The joint properties used to obtain the match for each jointed blocks are listed in Table 5.6.

For blocks containing dip angle sets of 5°-5°, 10°-10° and 15°-15° as shown in Table 5.6, the input values for the maximum joint closure are not the same. This indicates how initial assemblage of the jointed block constituents can affect the initial aperture and consequently the maximum deformation of the joints. An abnormal behavior is observed in stress-strain diagram of the sample 20°-20°. The experimental data shows that in this case, both initial normal and shear stiffness of the rock are of large magnitude. Lower *JRC* usually results in lower peak shear displacement which will increase the pre-peak

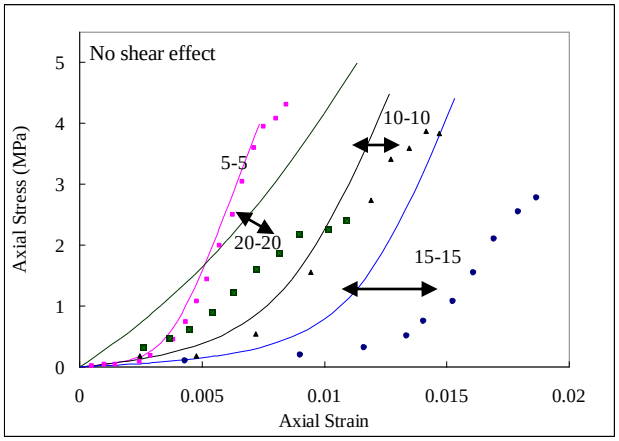

Figure 5.18 - Stress-strain behavior comparison between jointed blocks having symmetric joint configurations without considering the shear effect

shear stiffness at lower stress levels. It seems that in this jointed block sample (20°-20°), the embedded joint physical properties are quite different from the physical properties of the sample tested joint.

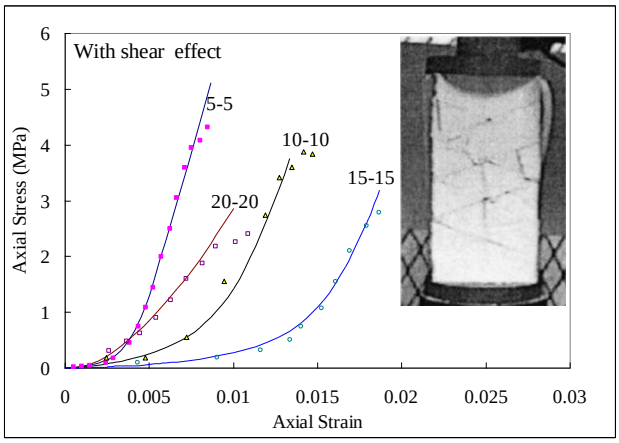

Figure 5.19 - Stress-strain behavior comparison between jointed blocks having symmetric joint configurations with shear effect

5.3 Conventional tensile hydraulic fracturing by Pseudo-continuum element

In conventional hydraulic fracturing, tensile, vertical plane of fracture with two wings growing symmetrically from the well is usually assumed for the fracture geometry. Here we attempted to model the conventional tensile fracturing by iterative coupling of the single phase flow and FEM models. In the FEM the constitutive models of the fracture and the block containing it are averaged. The tensile type fracture is a discontinuity and one may fundamentally question considering the problem as a continuum or pseudo-continuum; however, in the developed numerical model the stiffness of the fractured block perpendicular to the fracture plane is assumed to be extremely low which can be considered as a discontinuity in practice. On the other hand, as long as the discontinuity holds even a small hypothetical amount of stiffness, the pseudoized model reasonably describes a real tensile type fracturing problem, as will be shown below.

The key element is that the Bandis et. al. hyperbolic model for normal deformation already used in this work must be extended into tensile effective stress region to find a hypothetical stiffness for a fracture under tensile condition (see Figure 5.20). Although the assumption made is not based on real physics, the extremely low strength of the hyperbolic model in the tensile region somehow replicates the discontinuity. The highly non-linear nature of the problem demands the use of an efficient Newtonian solution which has been coded and implemented in this work.

A rather straightforward strategy is implemented here to model conventional fracturing, somewhat similar to the technique used by (Ji and Settari, 2008) except that the fracture is treated in pseudoized form. The block at the tip of the fracture is pressurized by fluid injection. When the minimum effective stress in the Gauss point ahead of fracture tip falls below the tensile strength of the rock, a single fracture is then embedded in the failed Gauss point perpendicular to the minimum effective stress. If two or more Gauss points fail at a specific time step, the time increment is cut and the solution is repeated to assure that only one Gauss point fails at a time step. Pseudo-continuum constitutive model will be constructed for the fractured Gauss point. The

above is then repeated for other Gauss points of this or other blocks in a row until a certain length of fracture is attained.

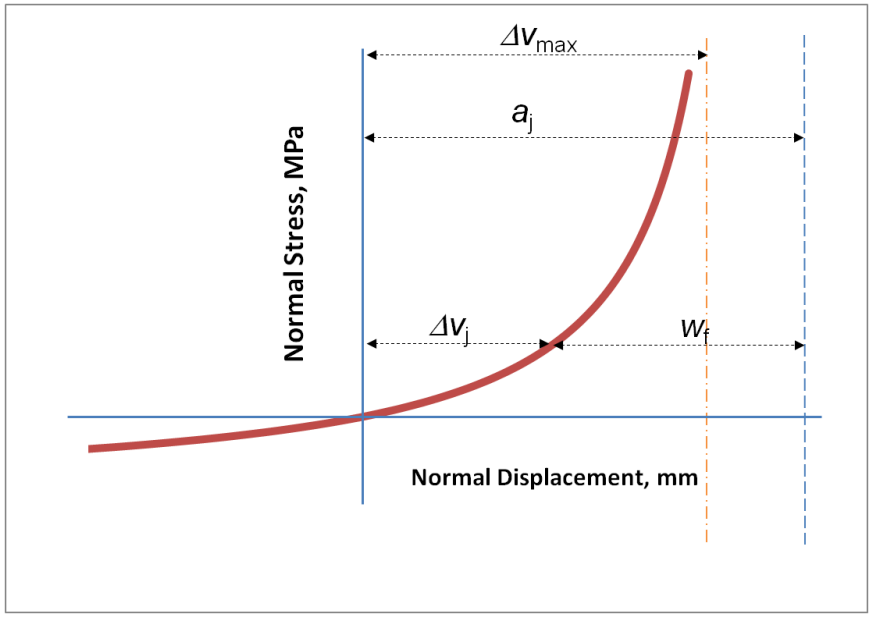

Figure 5.20 – Bandis et. al. fracture normal deformation extended into tensile region

After failure, the forces are rebalanced in the failed Gauss point and the Gauss points around. This is due to the fact that for tensile fracturing, at a certain plus time step when the minimum effective stress of a block falls below the block's tensile strength a fracture is needed to be embedded in the block, time step is repeated plus the effective stress perpendicular to the fracture plane is manually set to zero. Manual modification of any block's stress components requires forces rebalancing. The difference between the internal forces before and after forcing the minimum effective stress to zero will be used to rebalance the stresses in all the Gauss points. Here to obtain a better control a term called "**stress norm**" is introduced, which is the maximum stress change allowed within a time step solution in all the existing Gauss points. The model won't allow the Gauss point stress to change more than a specified *stress norm* within a time step. The norm is further forced to be as low as 200 kPa when the minimum stress approaches the tensile failure. If the norm is violated the time step Δt is cut and the solution is repeated with the cut Δt.

Selecting appropriate physical properties for the induced tensile fracture is also important. The residual fracture width (the difference between the fracture aperture at zero effective stress and the maximum fracture deformation), is assumed to be very low because the fracture is new and it is not of shear type. The product of the maximum fracture deformation and the initial fracture stiffness gives the maximum assumed tensile stress that the fracture can sustain. In order to avoid numerical divergence problems, it is not desirable to select a very small value for; around 100 kPa is chosen in our study.

The fracture length growing under tensile mode is an unknown obtained from geomechanical solution. The fracture width can either be obtained from the hyperbolic constitutive model by knowing the updated effective stress at any time step or from the fractured block strain term perpendicular to the fracture plane. Although tensile fracturing is modeled, spacing is needed to be defined for the single fracture because pseudo-continuum model requires that. If the spacing is defined the same as the width of the block containing the tensile fracture, it means only one single fracture exists in that block which suits our purpose. If the problem is a quarter of symmetry and only half of the fracture exists in the block, then spacing can be defined to be as twice as the block width. The tensile fracture length is the distance from the last Gauss point failed in tensile mode to the well block.

Although fractured rocks can be modeled, for simplicity single porosity and single permeability assumption has been made in the flow solution. The fractured rock permeability term is the coupling between the geomechanical and flow models.

5.3.1 Harmonic treatment of permeabilities

The example problem chosen to validate the developed numerical model is a 2-D *KGD* plane-strain tensile fracture model. The analytical solution is given in the theory chapter. Table 5.7 provides the reservoir, geomechanical and the tensile fracture properties. In this section the permeability between two consecutive blocks is harmonically averaged in the FEM solution. This is what naturally occurs in the FEM solution without any special treatment of coefficients.

Table 5.7 – Reservoir flow, fracture and geomechanical properties

ϕ =	0.09		a_j =	1.001e-2	mm	E =	4.14×10^7	kPa
$k_{xi} = k_{yi} = k_z =$	0.6	md	Δv_{max} =	1.0e-2	mm	v =	0.2	
$k_{xyi} = k_{yzi} = k_{zxi}$ =	0	md	K_{ni} =	10,000	kPa/m	k_{gr} =	2.35×10^7	kPa
ρ =	1,000	Kg/m^3	η =	1.0		T_0=	0	kPa
μ =	0.2	cp	S_f =	fractured block width	m	$S_{h,i}$ =	71,550	kPa
$c_f = c_r =$	0.6×10^{-6}	kPa^{-1}	Pay Thickness =	1	m	$S_{H,i}$ =	72,000	kPa
p_i =	64,000	kPa	Q (full model) =	355.6	M^3/Day	$S_{v,i}$ =	78,450	kPa

The example problem consists of a quarter of symmetry of a full model with the well block located at the left bottom corner. In this example problem and in the rest of the example problems studied in this research, no wellbore model has been taken into consideration. Injection is simply assumed to be a source term in the flow diffusivity equation. Three gridding scenarios are examined. Tensile fracture propagates in x direction through equally gridded blocks with 6 m in length for the first case, 3 m in the second case and 1 m in the last (most refined) case. The width of the first grid size in y direction is 0.05 m and will contain a tensile fracture with 0.1 m of spacing (element of symmetry). To eliminate the poroelasticity effect, Biot's constant is set to be almost zero by equating the bulk modulus and the grain modulus. The comparisons between the analytical and numerical solutions are shown in Figure 5.21, Figure 5.22 and Figure 5.23.

If there is no initial shear stress in the model, at the line of symmetry the shear stress must be zero. Since the fracture grows through the elements which have only one side at the boundary line, some shear stress is also induced which re-orients the principal stress directions. The problem is resolved here by selecting smaller width for the boundary elements and also neglecting the small induced shear stress when the fracture orientation is calculated in the numerical model.

In the fluid flow FEM solution the diffusivity equation coefficients are treated explicitly and there is no upstream treatment of permeability unless the solution is forced to use upstream permeability for each Gauss point. Since tensile fracture also propagates Gauss point by Gauss point, the well block pressure oscillates with time which also causes oscillation in the maximum fracture width with time as opposed to the fracture length which monotonically increases as fracture grows along. Hence expressing the compressibility of the fractured blocks as a function of fracture length (rather than

fracture width) is preferable. Here the tensile fracture contribution to the pore volume of the fractured blocks can be represented by compressibility of the blocks in the fluid flow solution, which is obtained from the following approximation as a function of fracture half length,

$$C_{fr} = \frac{w_f}{w_b}\frac{1}{P_{wf} - \sigma_{\min}} = \frac{w_f}{w_b}\frac{4L_f\left(1-\upsilon^2\right)}{w_f E} = \frac{4L_f\left(1-\upsilon^2\right)}{w_b E} \tag{5.15}$$

where L_f is the fracture half length, E is Young's Modulus and v is the Poisson's ratio and w_b is the width of the block which contain the tensile fracture.

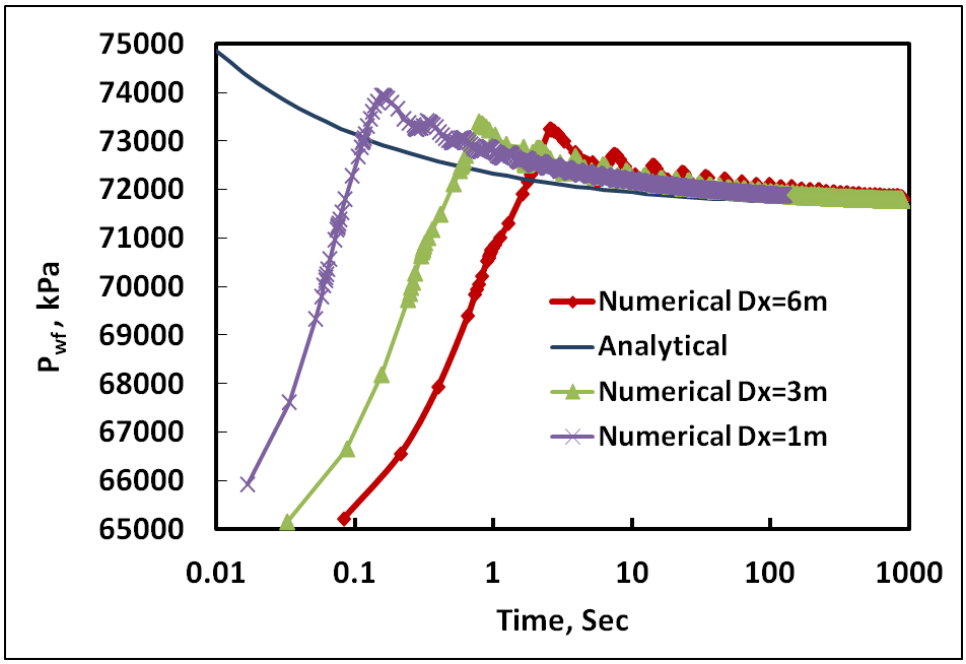

Figure 5.21 – Numerical and analytical fracture well block pressure comparison for different blocks' length

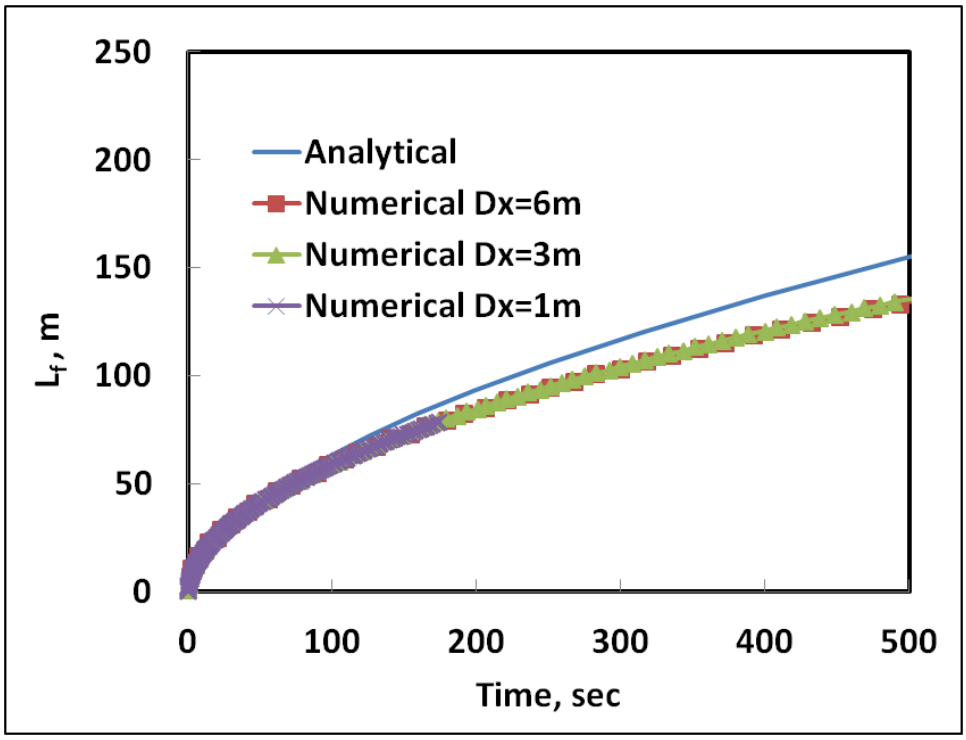

Figure 5.22 – Numerical and analytical fracture half length comparison for different blocks' length

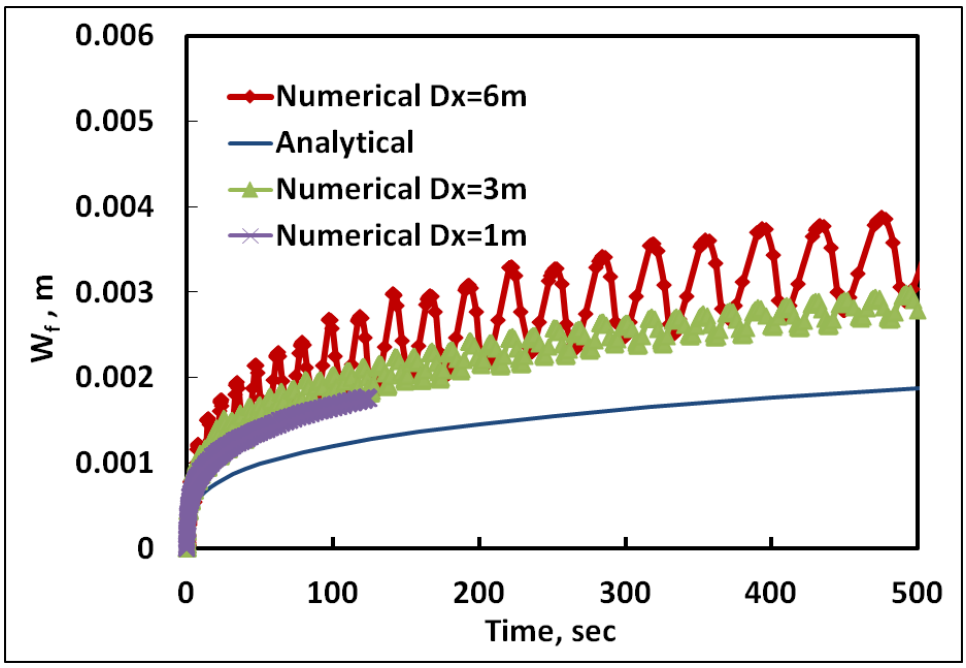

Figure 5.23 – Numerical and analytical fracture width comparison for different blocks' length

The numerical model is quite sensitive to the grid size around the fracture tip as shown in the figures. When the grid size decreases from 6 m to 1 m the well block pressure moves toward the analytical solution and better matches will be obtained for the fracture width. A perfect match between the analytical and numerical solution requires the grid size to be substantially refined. This will eliminate the grid size effect in the numerical model.

A simple test is conducted here to show the net pressure effect on the quality of matches between the numerical and analytical results. To obtain the match for the case with 6 m size of the block length, the net pressure or the net stress ($p_{wf} - \sigma_{min}$) in the *analytical* solution has been multiplied by 2 and the results are shown in Figure 5.24. The similar factor for the 3 m block length case has reduced to 1.6 and for the last case of 1m was found to be 1.37. This can be justified as follows.

The stress profile at the tip of the fracture is extremely non-linear and the linear shape function implemented in the FEM code cannot capture the extreme non-linearity very well. The net pressure is overestimated in the numerical solution when the block length is not well refined. More net pressure results in more fluid loss, which also causes the fracture length to be smaller in numerical solution. In addition, in the numerical solution leak-off is computed to be 2 dimensional whereas in the analytical solution it is based on 1-D leak-off Carter model. That's why if in the analytical solution the well pressure is manually modified to match the well block pressure from the numerical solution, other fracture parameters such as length and width will also match.

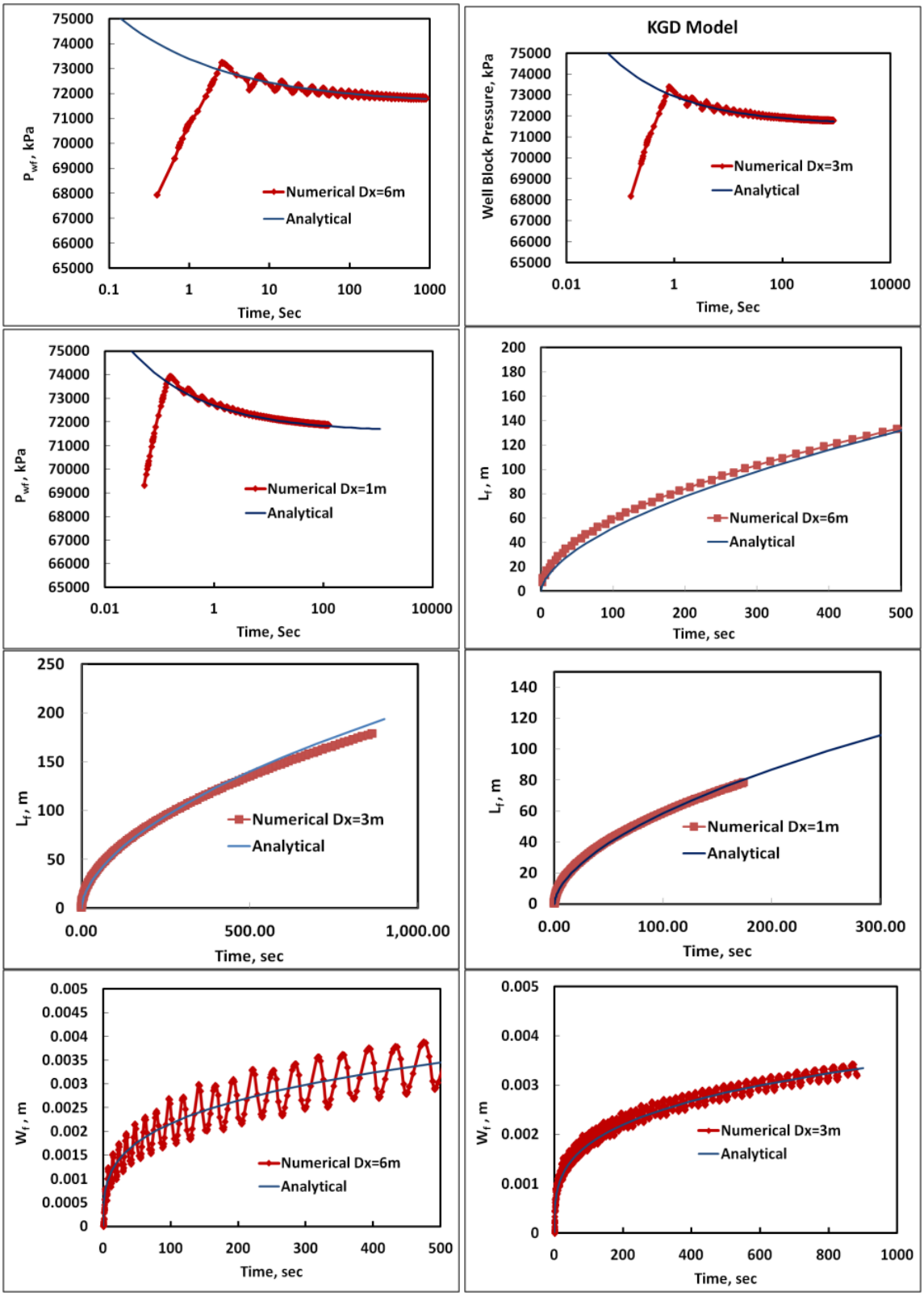
KGD Model
Pwf, kPa
Well Block Pressure, kPa
Lf, m
Wf, m
Time, Sec
Time, sec
Numerical Dx=6m
Numerical Dx=3m
Numerical Dx=1m
Analytical

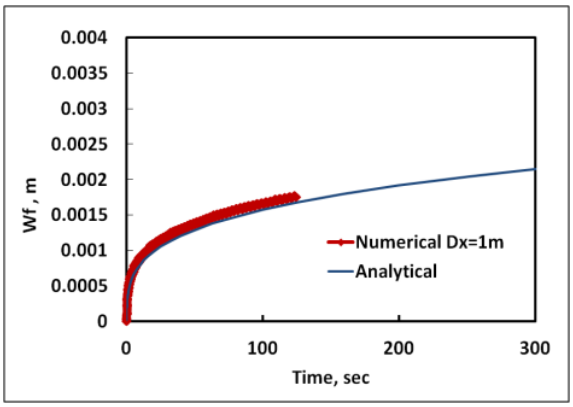

Figure 5.24 – Comparison between numerical and analytical solutions for KGD type fracture, the analytical net pressure is modified

5.3.2 Upstream treatment of permeabilities

In most finite difference numerical solution, transmissibilities or permeabilities along the blocks which are going to be fractured are treated by "upstream" technique. The upstream means using the permeability of the block which has the higher potential when calculating the flow resistance between each two consecutive nodes. At any time step the potential at any Gauss point is compared with the potentials of all the Gauss points around either in the same block or the blocks around and if a certain Gauss point located around has a higher potential, its permeability will be used for the Gauss point being evaluated.

The example problem discussed in the previous sub-section is repeated here with the difference that the permeability of each block is approximated by upstream technique. As indicated in Figure 5.25, less oscillation is observed in the well block pressure compared with the case where permeability between the blocks is harmonically averaged. A better match for fracture width is also observed as the block size is refined from 6 m to 1 m. The fracture length on the other hand is overestimated by the upstream technique as opposed to the harmonic example case in which the fracture length is slightly underestimated (Figure 5.26 compared with Figure 5.22).

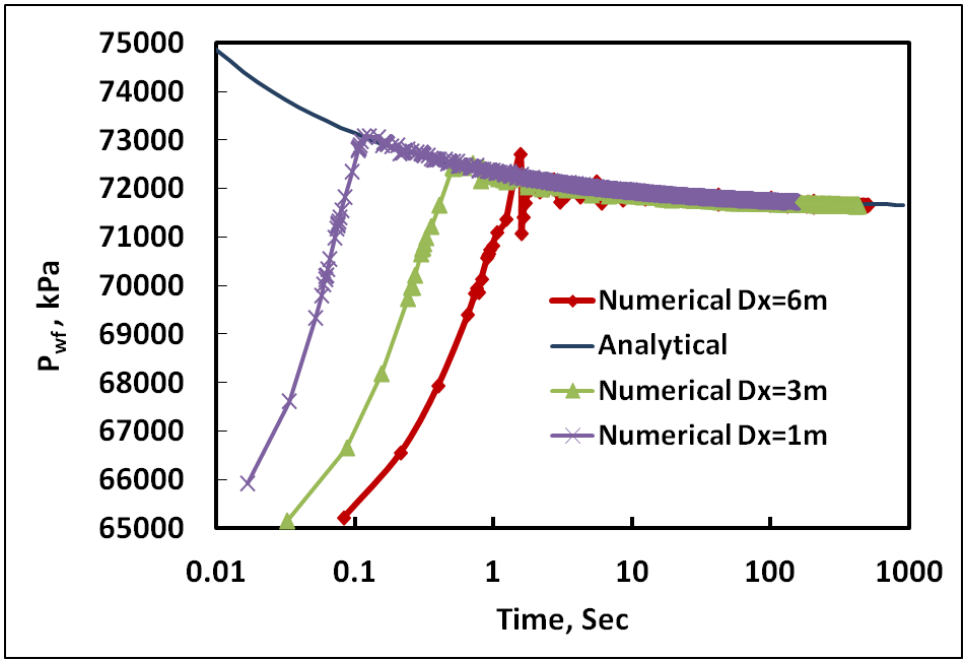

Figure 5.25 – Numerical and analytical fracture well block pressure comparison for different blocks' length, upstream permeability

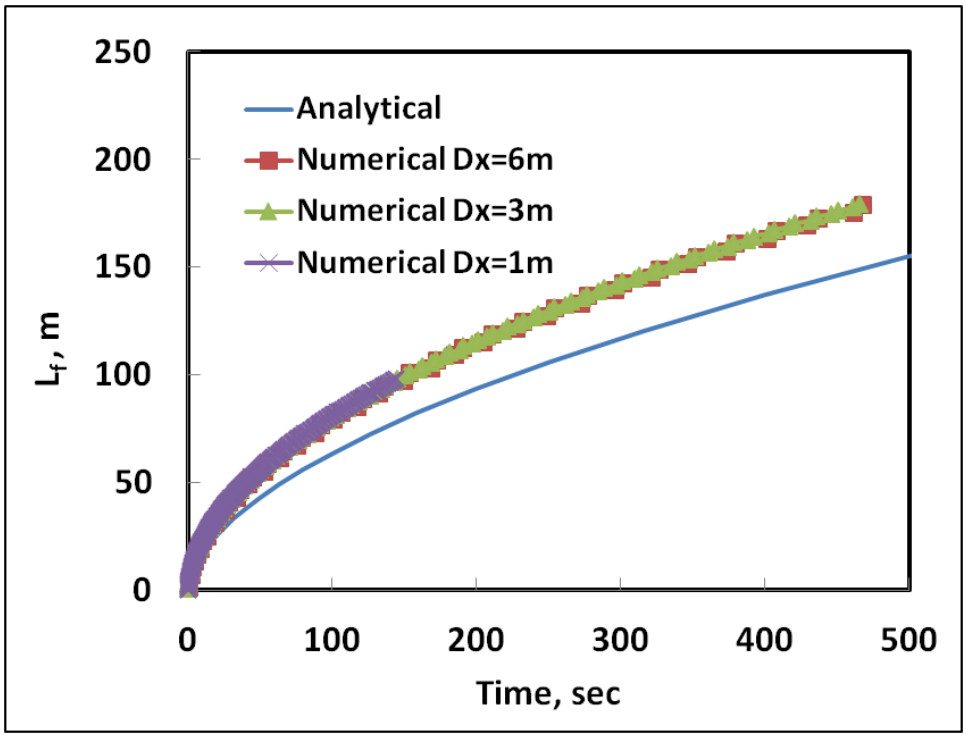

Figure 5.26 – Numerical and analytical fracture half length comparison for different blocks' length, upstream permeability

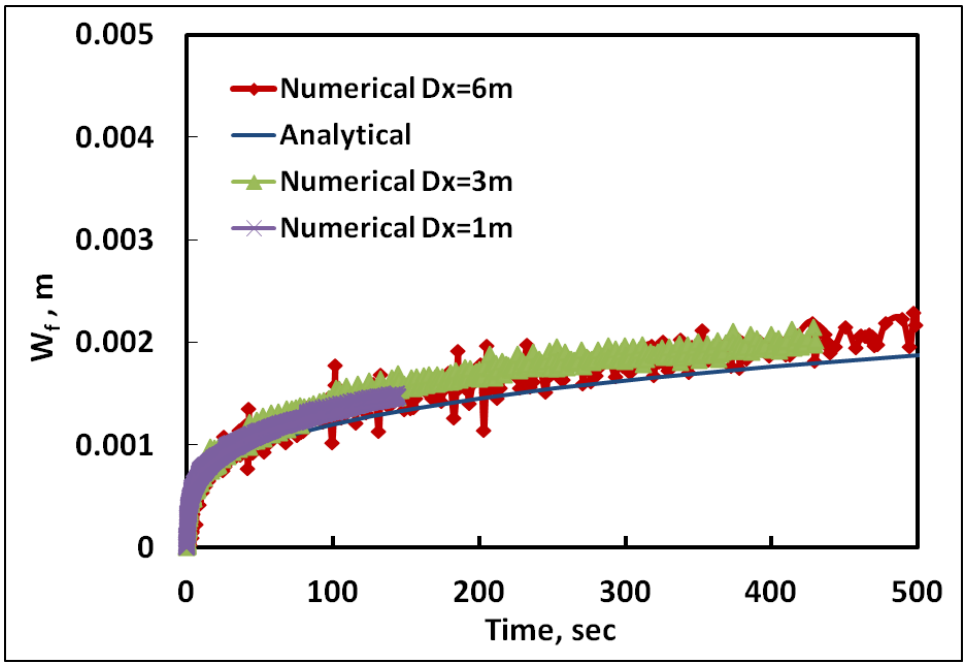

Figure 5.27 – Numerical and analytical fracture width comparison for different blocks' length, upstream permeability

5.3.3 Poroelasticity effect

The poroelasticity effect on the tensile fracture propagation problem has also been investigated here. The example problem is the same as the case with 3 m grid size mentioned in Section 5.3.1 except the grain modulus is selected to be a large number (10^{15} kPa) to make the Biot's constant almost equal to 1.

The comparison with the no-poroelasticity case is shown in Figure 5.28 . In general if pore pressure effect or the back stress is taken into consideration, the well block pressure and the maximum fracture width increase while the fracture length decreases. The effect in this example is small in magnitude.

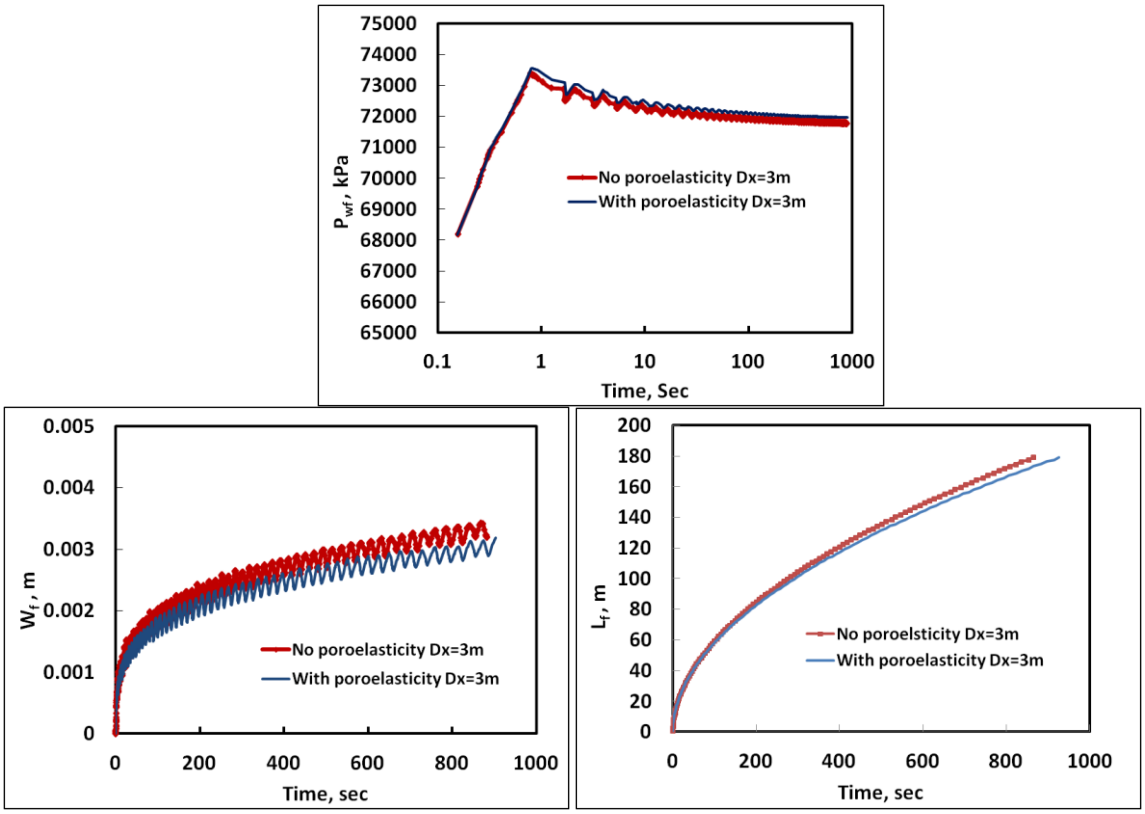

Figure 5.28 – Poroelasticity effect on fracturing pressure and geometry

5.4 Intact rock shear fracture modeling in a single block

Shear fracturing in an intact brittle rock occurs when the stress state of the block reaches the shear failure surface. In the current numerical analysis for shear fracturing, loading is provided by contained fluid pressurization in the problem elements or blocks. Couple of displacement loading examples will be shown to illustrate the technique implemented for shear fracturing.

The types and directions of the induced shear fractures in the current work are obtained by rather simple assumptions. By using Mohr-Coulomb failure criterion and assuming only two conjugate shear fractures are induced in a single numerical element, the induced shear fracture orientations can be calculated. As an example a cubical block (1 m^3) with cohesion of 500 kPa, internal friction angle of 30 deg, initial effective stress vector of [5000 2000 3500 450 450 450] kPa, and initial pore pressure of 1000 kPa is

pressurized up to the failure point. The example is a kind of triaxial test in which the specimen is loaded by increase in the pore pressure. At the failure point the effective stress is obtained to be [3905 905 2405 450 450 450] kPa from the numerical solution. Since the internal friction angle and cohesion of the intact rock are known, the orientation of the created fracture can be easily calculated. At any time steps, if failure occurs at the end of the time step, the shear fractures are embedded in the model and time step is repeated. It should be noted here that the shear fracture orientation calculation is carried out using the stress tensor at the beginning of the time step.

Finding principal stresses of a stress tensor is an Eigenvalue problem which can be calculated from the following equation:

$$(\boldsymbol{\sigma} - S_n \boldsymbol{I}).V = 0, \quad or \quad det \begin{vmatrix} \sigma_{11} - s_n & \sigma_{12} & \sigma_{13} \\ \sigma_{12} & \sigma_{22} - s_n & \sigma_{23} \\ \sigma_{13} & \sigma_{23} & \sigma_{33} - s_n \end{vmatrix} = 0 \tag{5.16}$$

By substituting for $\boldsymbol{\sigma}$, the maximum, intermediate and minimum principal stresses are obtained to be 4126, 2341 and 747 kPa respectively. After substituting the respective values of principal stresses in Eq. (5.16) and solving the system of linear equations, the eigenvector $V = V(v_1,v_2,v_3)$ or the principal directions for each of principal stresses are then calculated (V_1=[0.941 0.172 0.291], V_2=[-0.322 0.190 0.928] and V_3=[0.104 -0.967 0.234]).

Since it is assumed only two conjugate shear fractures are created when shear failure occurs, according to Mohr-Coulomb criterion the normal vectors of the two induced fractures from Eq. (3.68) are calculated to be n_{fp1}=[-0.380 -0.923 0.057] and n_{fp2}=[0.561 -0.751 0.348]. Here the dip angle of a fracture ranges between 0° and 90°, and the azimuth angle varies from 0° to 360°. For the two fracture normal vectors, the fracture dip and azimuth angles are also (86.72^o, 112.38^o) and (69.62^o, 52.24^o) respectively.

The simple technique explained above for determining the shear failure point and orientation of induced fractures has been implemented in all dynamic shear fracturing problems which will be discussed in the following sections.

5.4.1 Intact rock shear fracturing under triaxial displacement loading

In this example problem a homogenous intact rock with linear elastic constitutive model is loaded by controlling the axial displacement under the triaxial test conditions. The purpose of the example is to indicate how the developed numerical model predicts the stress-strain behavior of a non-fractured rock when it fails in shear mode as explained in previous section.

The numerical technique implemented to apply the displacement loading is simple. The stiffness matrix of an element is multiplied by the prescribed element displacement vector and will be integrated over the Gauss points to obtain the change in the force associated with displacement loading. Instead of adding the load to the external load vector, the load will be subtracted from the internal load vector and in the next step, the residual vector (the difference between external and internal forces) is obtained. The prescribed displacements will not be considered in counting of the number of degrees of freedom; therefore, one should manually insert the prescribed displacements of the specified nodes in the local element displacement vector in the stress updating step of the FEM solution.

Under axial displacement loading, the axial stress increases up to a peak point at which the intact rock fails in shear. Two conjugate shear fractures with dip angle of 60 will be induced in all 8 Gauss points due to the fact that stress changes in all Gauss points are the same in triaxial loading. Deviatoric stress softening or loss of cohesion is commonly observed in brittle rock materials after the shear failure. To capture the softening behavior in this work, a hypothetical exponential function with coefficient (exponent) of n is used to represent the declining form of the mobilized friction angle with respect to the plastic shear strain. The initial value of the mobilized friction angle is calculated from the normal and shear stresses at the hypothetical fracture planes on which failure is about to occur ($\phi_{mi} = \arctan(\tau/\sigma_n)$). The elasto-plastic solution derivation has been given in the constitutive models chapter. The intact rock elastic data and the fracture elastic/plastic physical properties are given in Table 5.8.

Table 5.8 – Rock and fracture physical properties

Intact Rock	E	ν	Cohesion	Friction Angle	σ_{xi}, σ_{yi}, σ_{zi}
	10 GPa	0.2	1 MPa	30°	0.9, 1.9, 2.4 MPa
Fracture	K_{ni}	ν_{max}	Spacing	Exponential coefficient, n	Basic Friction Angle
	0.5 GPa/m	6mm	1 m	100 m^{-1}	25°

The exponential coefficient (n) effect on the post-failure deviatoric stress-strain relationship is indicated in Figure 5.29. Higher n corresponds to quicker softening of the fractured rock shear modulus. On the other hand, the solution is relatively insensitive to the value of the shear modulus. Figure 5.30 compares an intact rock post-failure deviatoric stress-strain behavior for different values of fracture elastic shear modulus (K_s) when n=100 m^{-1}. Only a slight change in the results is observed when the fracture elastic shear modulus varies from 0.2 to 0.8 times the intact rock shear modulus divided by the induced fracture spacing.

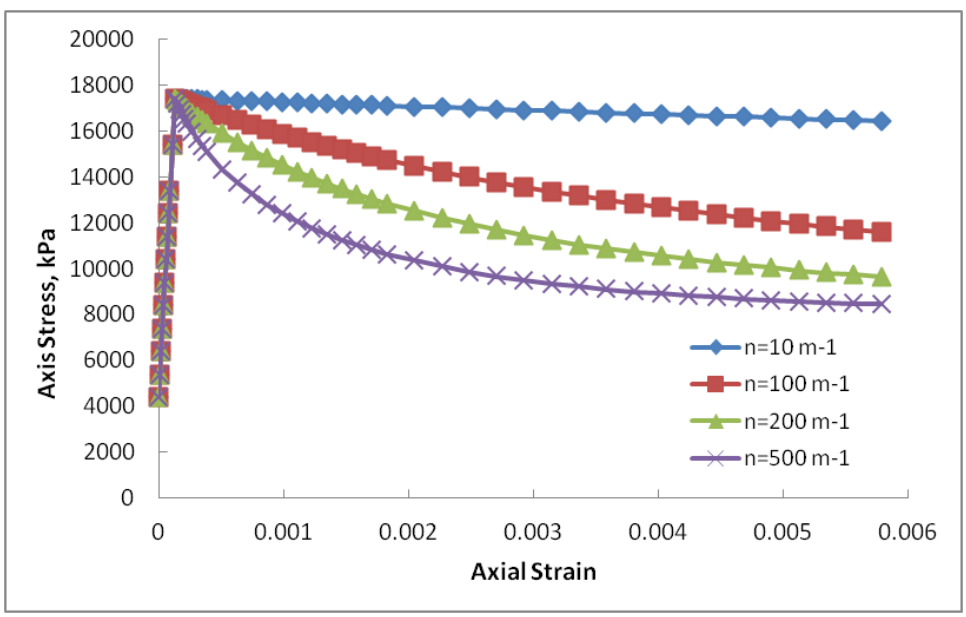

Figure 5.29 – Intact rock post-failure deviatoric stress-strain behavior comparison for the effect of exponential coefficient, n, ($K_s = 0.2\ G\ /\ Spacing$).

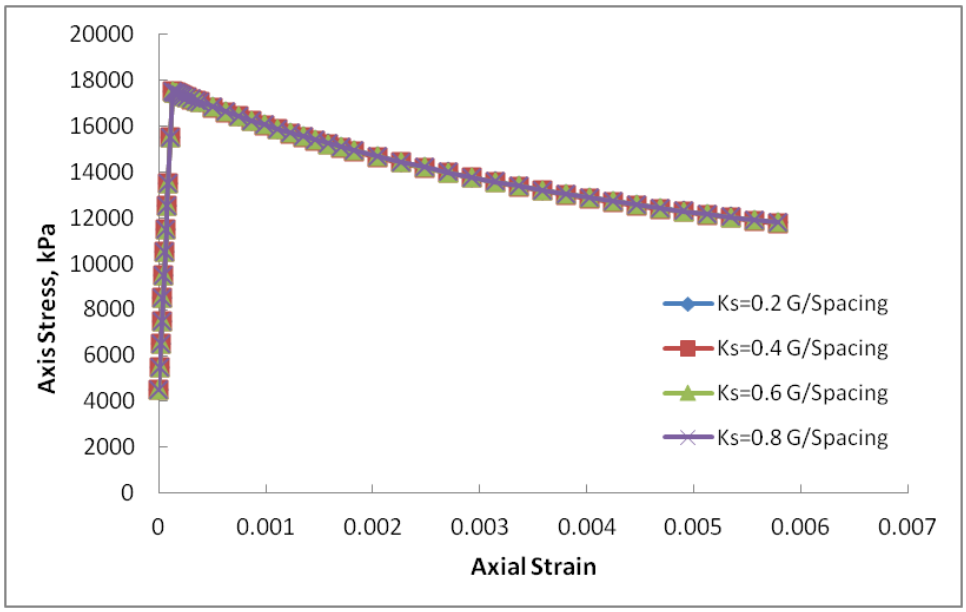

Figure 5.30 – Impact of fracture elastic shear modulus, K_s on the post-peak shear softening, n =100 m^{-1}.

5.4.2 Intact rock shear fracturing by fluid pressurization

In real hydraulic fracturing, injected fluid usually pressurizes the rock to fail mainly in tensile mode. Only under some unusual physical conditions such as high stress contrast and low rock cohesion, shear failure, or combination of both can occur. It is believed that shear fracturing (which triggers the microseismic events) usually occurs in blocks close to the main tensile fracture. We attempted to model a 2-D plane-strain shear type fracture example problem which comprises of 21 by 21 grid blocks with the injection block located at center. There is no real cylindrical wellbore in the injection block, the wellbore is represented by a fluid source or sink in the well block in the numerical analysis. Only the well block is allowed to fail in shear and after failure. It is also important to investigate how the developed constitutive model for the fractured blocks behaves under loading and unloading conditions. In this example problem the injection is manually switched to production and vice versa in cycles to model the loading and unloading effect on the stress path. The reason for cyclic loading assumption in this particular example is explained by the fact that in dynamic fracturing in which fluid is continuously injected; the blocks are fractured one after another. The newly fractured blocks permeability

enhancement and pressure redistribution will create pressure oscillation with time in the previously fractured blocks but that will not reverse the flow. The rock, fracture and fluid physical properties for the example problem are given in Table 5.9.

Table 5.9 – Rock, fracture and fluid physical properties

Intact Rock	E	ν	Cohesion	Friction Angle	σ_{xi}, σ_{yi}, σ_{zi}
	100 GPa	0.2	2 MPa	30°	22, 12, 15 MPa
Fracture	K_{ni}	v_{max}	Spacing	Exponential coefficient, n	Basic Friction Angle
	0.1 GPa/m	6mm	1 m	800 m^{-1}	25°
Fluid	*Permeability*, k_h & k_v	ϕ	c_f & c_r	μ	Injection, production rates
	1 μd	0.2	10^{-6} kPa^{-1}	1 cp	-40, 40 M^3/Day

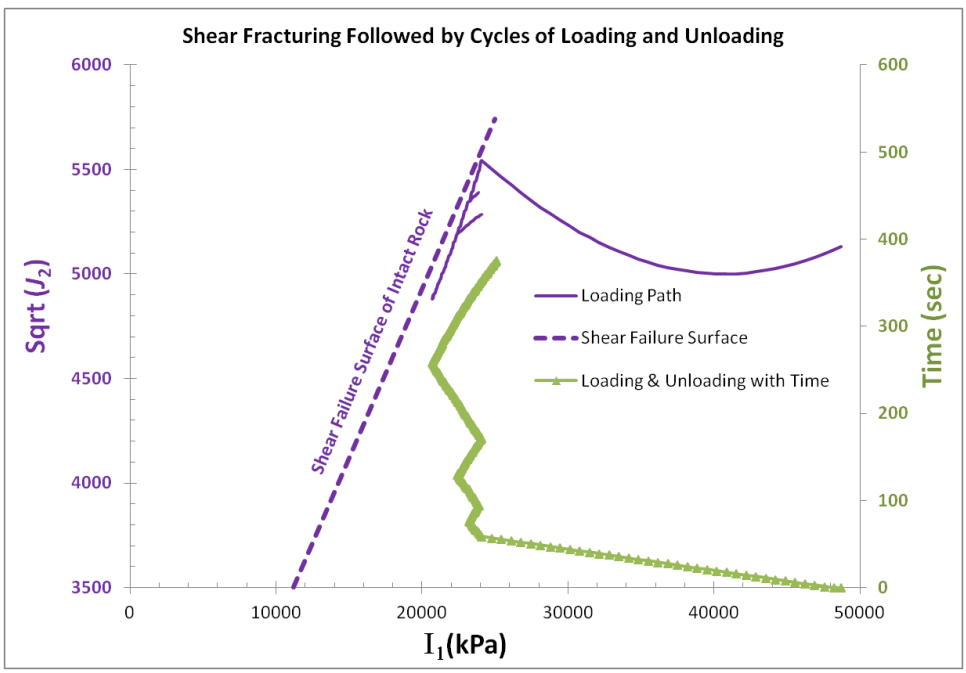

Figure 5.31 – Stress path of intact rock shear fracturing caused by fluid pressurization with post-failure cyclic loading and unloading.

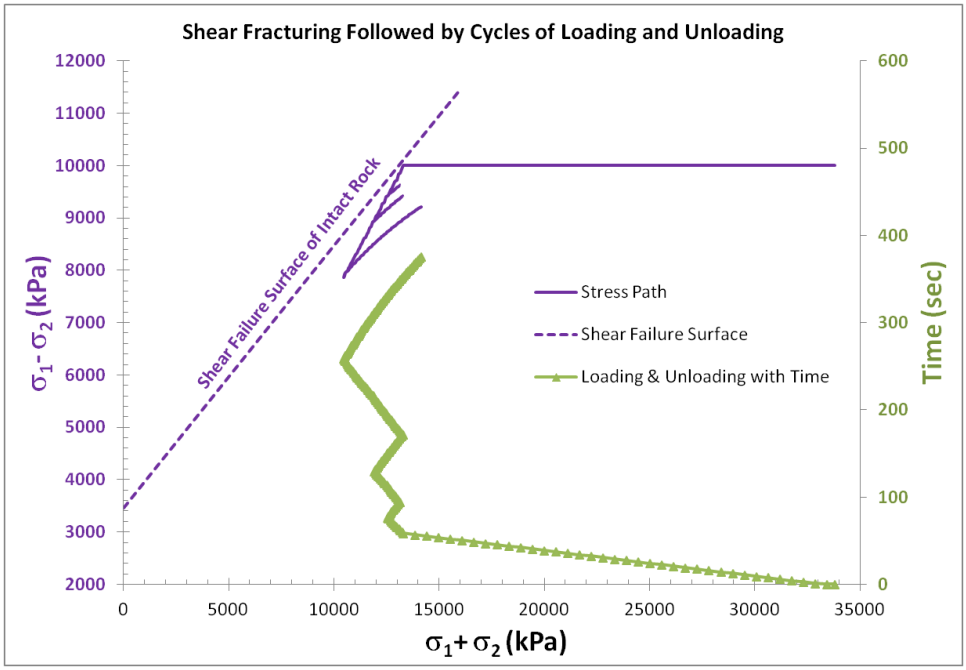

Figure 5.32 – Stress path of intact rock shear fracturing caused by fluid pressurization with post-failure cyclic loading and unloading.

Figure 5.31 pictures the failure of the well block and cycles of loading and unloading after failure. The Mohr-Coulomb shear failure criterion in terms of σ_1 and σ_2 and I_1 and J_2 can respectively be written as follows (Wan, 2010):

$$(\sigma_1 + \sigma_2)\sin\emptyset - (\sigma_1 - \sigma_2) - 2S_0\cos\emptyset = 0 \tag{5.17}$$

$$F = \frac{I_1}{3}\sin\emptyset + \sqrt{J_2}\left(\cos\theta - \frac{1}{\sqrt{3}}\sin\theta\sin\emptyset\right) - S_0\cos\emptyset = 0 \tag{5.18}$$

Here ϕ is the friction angle, S_0 is cohesion and θ is called Lode angle obtained from the following equation,

$$\theta = \frac{1}{3}\sin^{-1}\left(-\frac{3\sqrt{3}}{2}\frac{J_3}{J_2^{3/2}}\right) \tag{5.19}$$

The Lode angle varies between -30 to 30 degrees and in this example problem is obtained to be around -25^0. The loading and unloading is obtained in fact from the internal product of two vectors; one is the gradient of the failure function and the other is the loading vector. Positive product value means loading. Here we assumed that the

fracture elastic modulus remain the same in loading and unloading stages. Accumulation of plastic shear strain will shift the fracture failure surface downward as shown in the figure. The fracture elastic shear modulus in this example is picked to be 0.1×G/Spacing. Higher fracture elastic shear modulus steepens the slope of the loading and unloading curve in Figure 5.31. The same results but plotted in terms of the minimum and maximum effective stresses are shown in Figure 5.32. Fracture failure surface shifting from the initial intact rock failure surface can better be seen when compared to Figure 5.31. In fact expressing the stress path of a block in terms of stress invariants after the block failure is incorrect. The fractured block constitutive model is no longer isotropic and depends on the direction. Figure 5.31 is presented here only for more illustration.

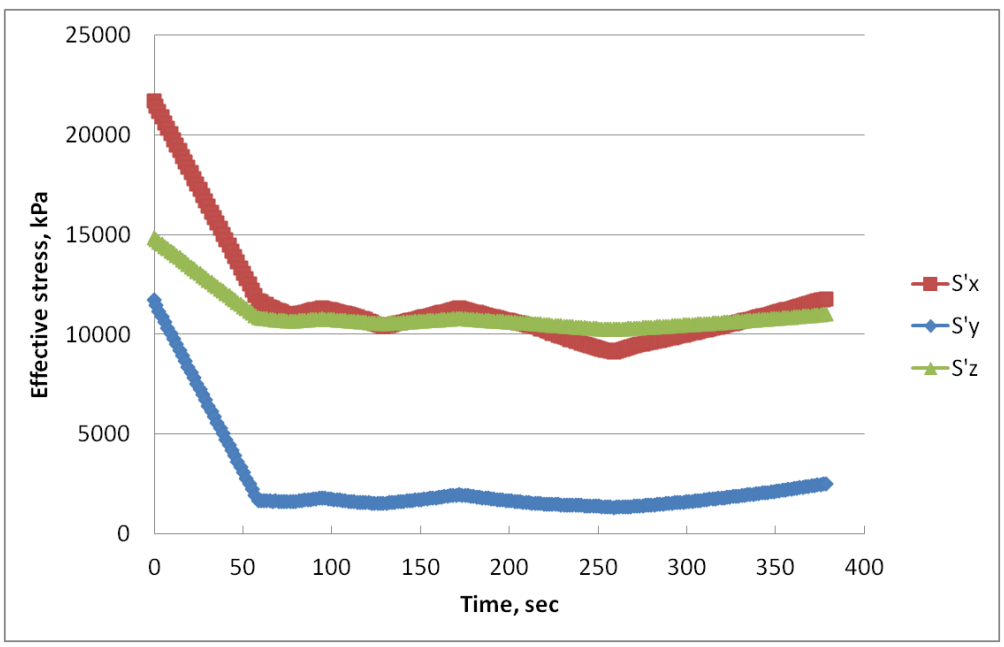

Figure 5.33 – Wellbore block effective stresses in cyclic pressure loading example problem

Figure 5.33 shows the well block effective stresses verses time. After failure, although the block has experienced number of loading and unloading stages, the change in the maximum principal effective stress, σ'_x, was substantially higher than the minimum principal stress, σ'_y. Immediately after failure, it is observed that the minimum principal

stress remains almost constant while the maximum effective stress declines. Reduction in the deviatoric stress can result from both decreasing of the maximum effective stress and/or increasing in the minimum effective stress. It is a *significant result* that the reduction in the deviatoric stress in this type of example problems is mainly caused by the reduction in the maximum effective stress.

In summary, selecting the right input data for the elasto-plastic model is a key issue for the accuracy of the numerical model. The question of how fast the post-failure softening occurs and which value of the exponential coefficient should be selected is difficult to answer.

CHAPTER 6 - MODEL APPLICATION

Sets of 2-D and 3-D example problems will be presented in this section to indicate the application of the developed code in dynamic shear/tensile fracturing. The input data were selected to be representative of actual typical shale gas reservoirs data. In the first section, different possible modes of shear fracturing (including primary shear fracturing, primary shear plus tensile fracturing and secondary fracturing or 'block crushing') are examined by 2-D example problems. In the second section, the effects of reservoir initial conditions on the extent of the SRV will be discussed. This will be followed by some discussion on fracturing issue in the third section. The 2-D example problem will be extended into 3-D in the fourth section. Finally, in the last section an example problem with completely different initial conditions will be shown and discussed both in 2-D and 3-D formats.

6.1 Example problems of fracturing

In this section all examples are again 2-D plane-strain quarter of symmetry problems where water is injected at the left bottom corner. It should be reiterated here that in 2-D plane strain case, the failure is still computed considering all three stresses; furthermore, the fracture aperture changes and the permeability are also calculated 3-dimensionally. Displacements at the boundary nodes are fixed in the directions perpendicular to the six boundary faces (top, bottom, left, right, front and back). Rock, fluid and fracture properties used in the example problems are shown in Table 6.1.

In the applied pseudo-continuum technique which represents the constitutive law for the blocks after fracturing occurred, each fracture sets widths are updated based on the Bandis's hyperbolic equation as shown in the Constitutive equations chapter. The induced dilation term resulting from the plastic shear strain and the dilation angle is also added to the conductive width of each fracture set.

For a single tensile fracture modeling as shown in the previous chapter the compressibility of the blocks containing tensile fracture was modified according to an equation which was an inverse function of the well block pressure. However, in

combined shear and tensile fracture example problems in the following sections, ***no*** block pore volume modification due to fracture creation (either tensile or shear) has been considered in the numerical calculation. In other words, the coupling between the flow and geomechnical modules is merely through the permeability term. The pore volume coupling and the compressibility variation of the respective blocks in naturally fractured reservoirs have been investigated by Bagheri and Settari (2006).

The assumptions made above will be valid for all the following example problems including in those where an additional tensile fracture is added. Example problems are categorized based on different initial reservoir conditions as follows:

1) Only shear fracturing, no tensile plane of fracture is considered. σ'_x is the maximum and σ'_y is the minimum effective stress.
2) A plane of possible tensile failure is added to the first example problem. From here all example problems will contain a tensile plane perpendicular to minimum stress in j=1 row.
3) σ'_z is the maximum and σ'_y is the minimum effective stress; otherwise as Example 2).
4) Example 3 with secondary fracturing (crushing mechanism).
5) Grid refinement and comparison with Example 4
6) Example 3, two close initial horizontal stresses

6.1.1 Only shear fracturing - maximum stress in horizontal direction

In this section the shear fracturing is allowed to propagate in all Gauss points beginning from the well block's when the stress state touches the shear failure surface. It is important to remind the reader that shear fracturing mechanism and the created fracture pattern (especially from microscopical point of view) are much more complex than the physics represented in the model, and assumptions were made here to make the problem easier for the modeling purposes. The high stress intensity and the required grid refinement around the tip of the created fractures are other important factors that may influence the accuracy of the results. However, in this work an overall estimation of the complex phenomena suits the modeling purposes.

Table 6.1 – Rock, fluid and fracture physical properties

ϕ (porosity)=	0.07		a_j, Δv_{max} =	0.13, 0.1	mm	E =	2 x10^7	kPa
$k_{xi} = k_{yi}$ =	7E-5	md	K_{ni} =	1.0E6	kPa/m	v =	0.18	
k_{zi} =	3E-5	md	JRC =	2		k_{gr} =		kPa
ρ =	1000	Kg/m^3	JCS =	30000	kPa	S_0	500	kPa
μ =	0.4	cp	ϕ_{bf} (fracture)=	25°		ϕ (rock)=	30°	
$c_f = c_r$=	0.6x10^{-6}	kPa^{-1}	K_s/ K_n =	0.6		$S_{h,i}$ =	**40,000**	kPa
p_i =	**36000**	kPa	n =	0.5	m^{-1}	$S_{H,i}$ =	47,000	kPa
Q (full model) =	12000	M^3/Day	η =	1.0		$S_{v,i}$ =	42,000	kPa
Pay Thickness =	40	m	S_f =	0.2 (Shear frac)	m			

The simulation results presented in Figure 6.1 indicate how the shear fracture zone propagates in the y and (more preferentially) the x directions. Two sets of conjugate shear fractures are embedded in the failed Gauss points and their orientations are calculated based on the principal stress directions and the intact rock shear failure parameters. In this example problem both induced fracture sets are vertical (we consider the x-y plane to be the horizontal plane) and are propagating preferentially towards x direction. Figure 6.1 shows the permeability enhancement in the stimulated reservoir volume after selected specified injection times of 100, 500 and 1722 seconds. It is clearly shown that the stimulation is not confined solely to a single plane and it forms a much more spread out SRV.

Perpendicular to the minimum stress direction, a plane originating from the well block with relatively large permeability enhancement is also observed. In these blocks the elasto-plastic model has forced the minimum and maximum effective stresses to decline down to zero or even fall into the tensile zone at higher fluid injection rates (see Figure 6.2).

The well block pressure and stress profile versus time are presented in Figure 6.2. In spite of this being a 2-D model, in contrary to KGD tensile fracture the well block pressure gradually increases with time which is a characteristic behavior in a shear dominated fracturing problem.

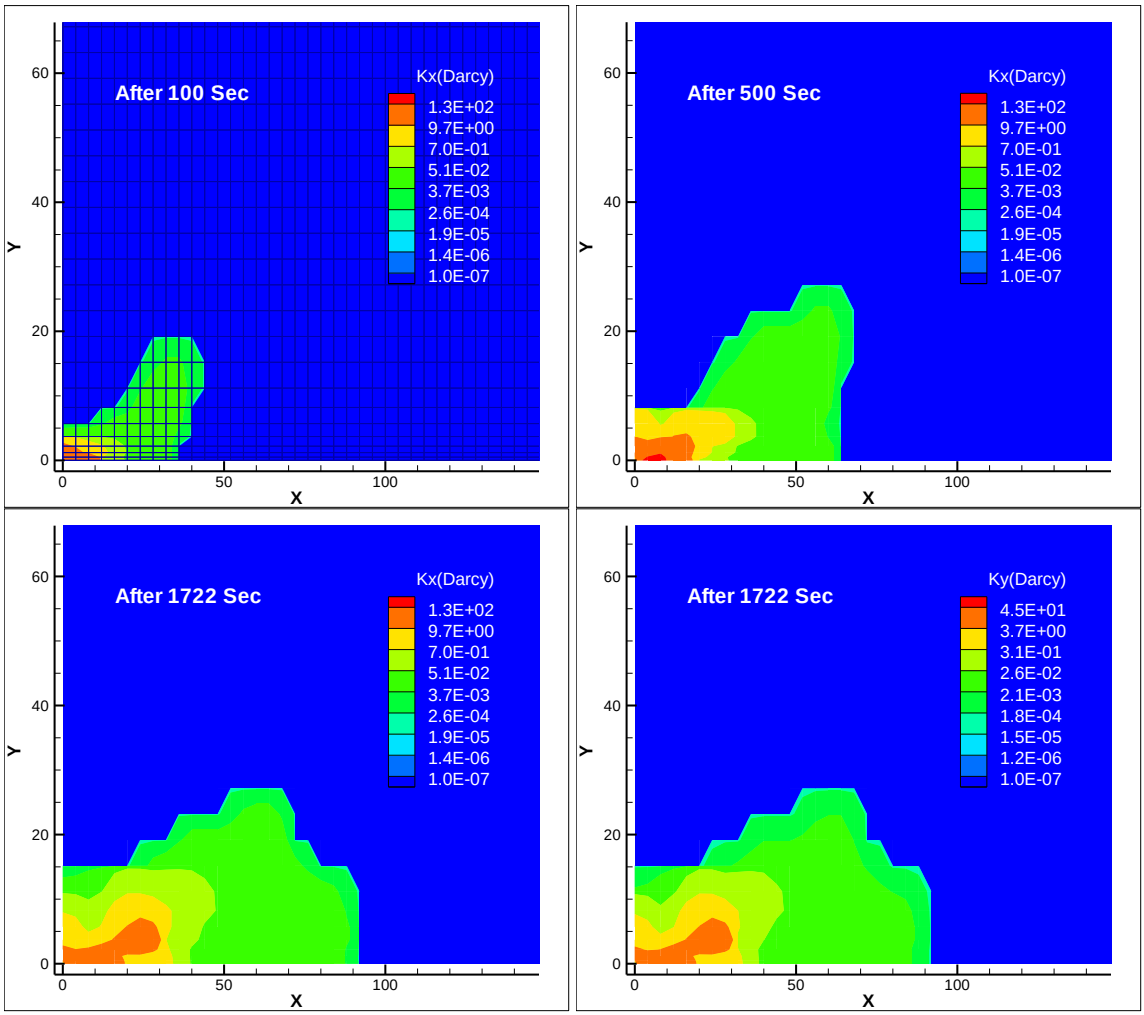

Figure 6.1 – Permeability variation with time in only shear fracturing case

As discussed before, the two main reasons for shear fracturing are low rock cohesion and high contrast between the initial minimum and maximum total stresses. The maximum and minimum effective stresses in the shear fractured block decline to zero or even to tensile in relatively tighter formations as the stimulation proceeds (Figure 6.2). The concept is better explained in the effective stress path plot of the well block's first Gauss point as shown in Figure 6.3. Prior to fracturing, it is clearly seen that the plane, which later becomes the fracture plane and is initially close to the shear failure point is loaded toward the shear failure plane. The sudden drop in the stress path is caused by the post-failure stress correction as explained before. The effective stress path proceeds on the fracture shear surface afterwards until it reaches the tension surface. Below a pre-

determined small effective stress (here it is assumed to be 10 kPa), the fracture constitutive model is switched to only tensile with very low shear resistance (a "tension cut-off" model). In any time step it is assumed that the constitutive model type of any fracture set remains the same during the Newton iteration. For example, if the constitutive model of a specific fracture is elasto-plastic at the beginning of a time step it won't be switched to tension cut-off during the Newton iteration.

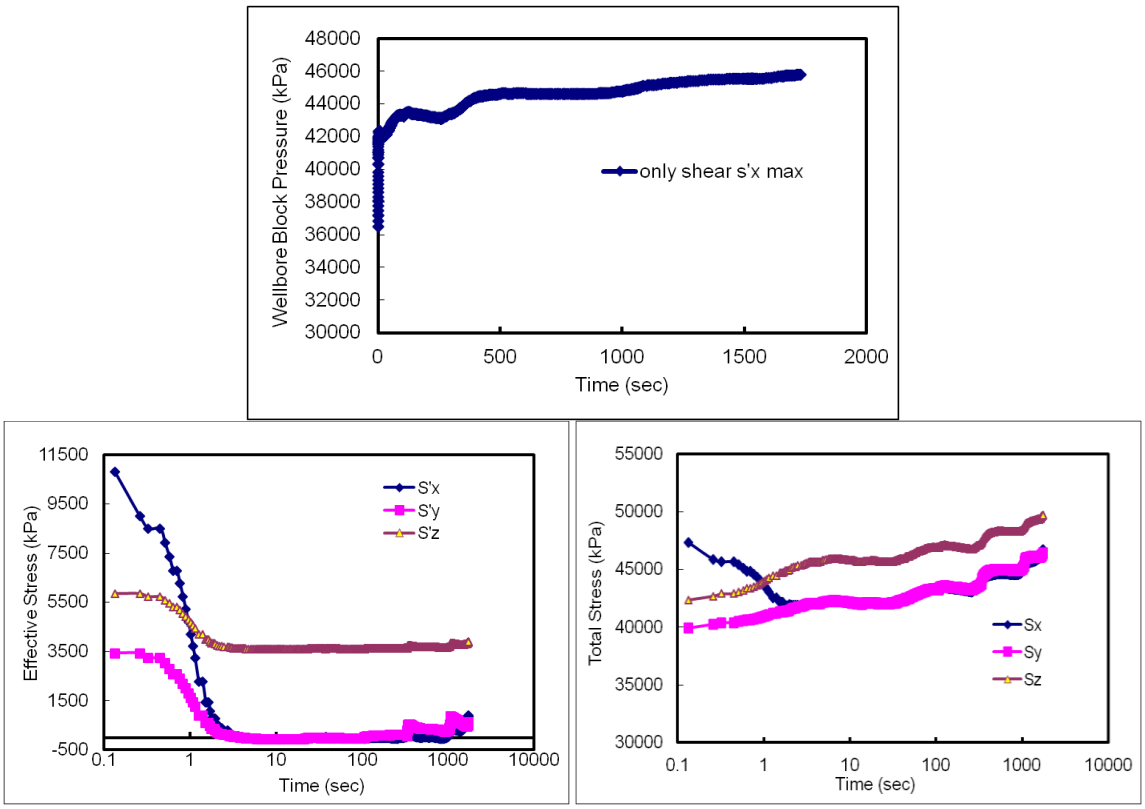

Figure 6.2 – Pressure, total and effective stresses of the well block in only shear fracturing case

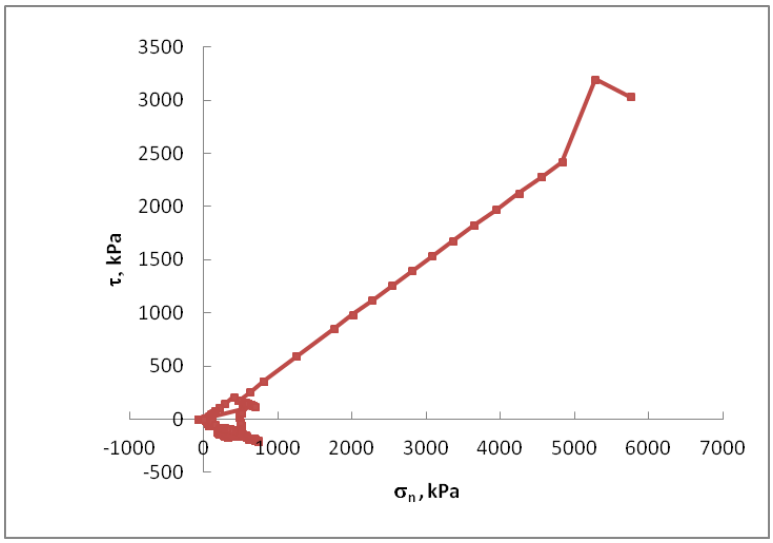

Figure 6.3 – Stress path in one of the well block Gauss points during the stimulation process.

One of the most common problems in the Newtonian loop is the drift from the yield surface in different iterations of a specific time step. If divergence occurs at a certain iteration, the respective displacement vector at that iteration is instead projected by a factor of λ which is calculated by either quadratic or cubic functions of the calculated residual vectors' norms of older iterations (Dennis and Schnabel, 1983; Wawrzynek, 1997). The iteration proceeds until the residual force vector norm is forced below a desired stop norm. For details, see Chapter 3 (Mathematical Models).

6.1.2 Shear & tensile fracturing - maximum stress in horizontal direction

In this example problem in addition to two conjugate shear fractures a tensile fracture perpendicular to the initial minimum stress direction is allowed in the well block and the blocks located at j=1. This example serves to examine how the simulation results may change if a fracture set perpendicular to the initial minimum effective stress (i.e., a planar fracture) is added as another failure mechanism. The tensile fracture parameters a_j, v_m and k_{ni} are assumed to be 1.01×10^{-4}, 1.0×10^{-4} and 1.0×10^{6} respectively. The resulting permeability enhancement as indicated in Figure 6.4 is almost the same as previous example problem, which indicates the fact that under the current initial problem

conditions the back stress on the expected tensile plane constricts its opening as the SRV length and width grow.

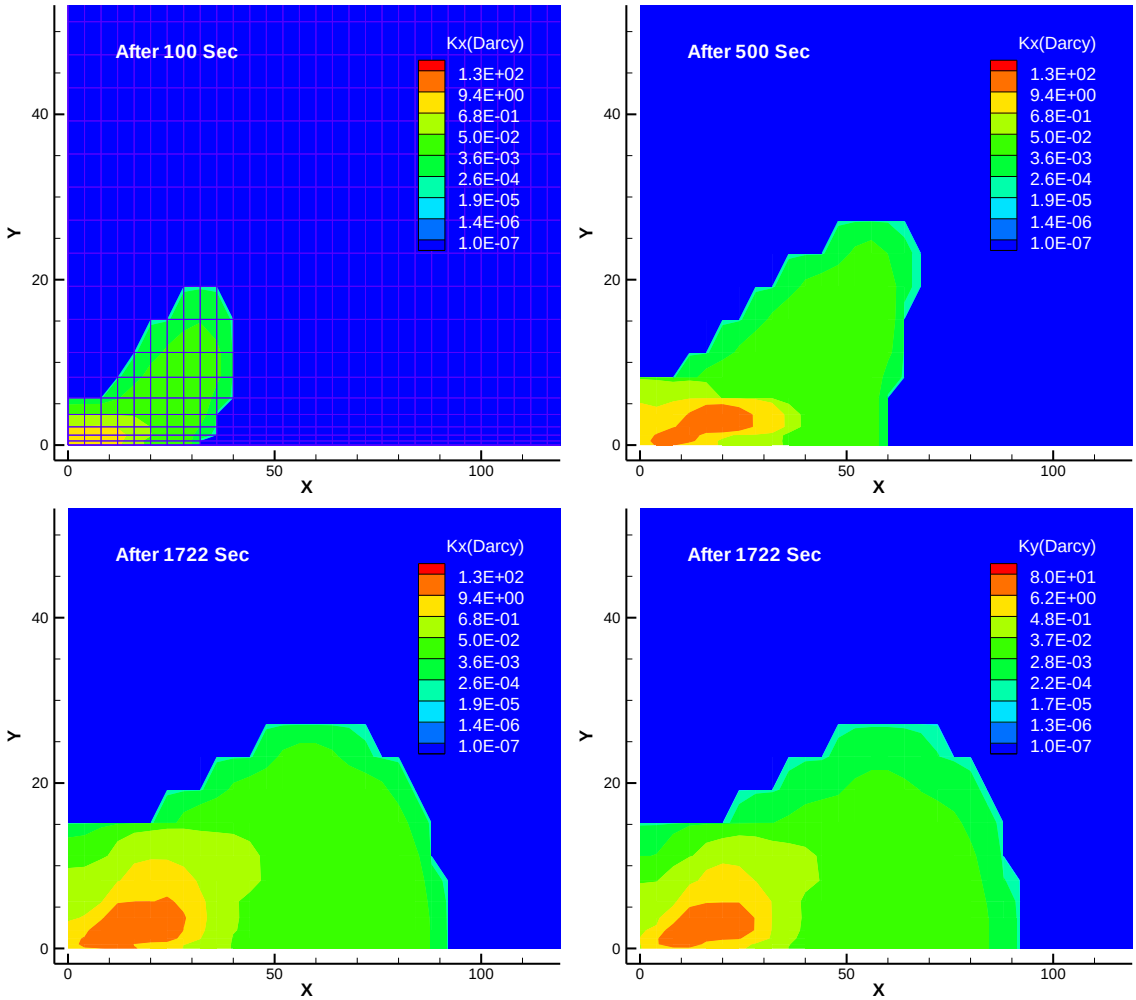

Figure 6.4 – Permeability variation with time in combined shear and tensile fracturing case

Pressure versus time profile is also plotted in Figure 6.5 which is almost the same as the well block pressure behavior in the previous example problem. The raise in the well block pressure verses time is mainly caused by the non-tensile (shear) SRV development.

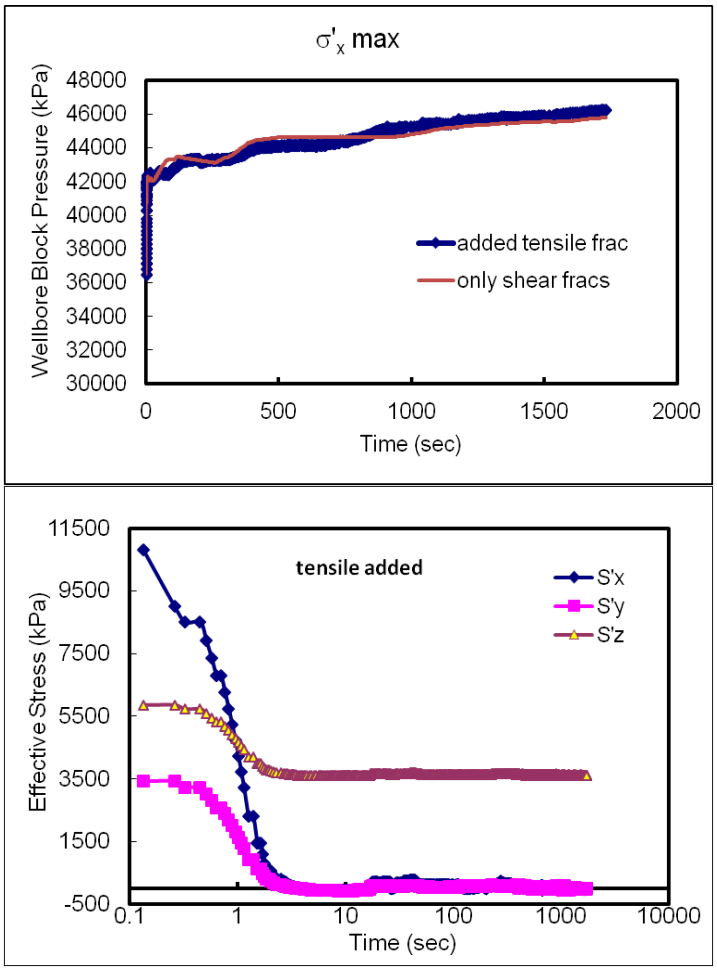

Figure 6.5 – Pressure-time profile comparison between only shear fracturing and the one with added tensile cases and the effective stresses profile

6.1.3 Shear & tensile fracturing – maximum stress in vertical direction

In the previous example problems the maximum stress was in the horizontal y direction. In this and the following sections the maximum stress is assumed to be in the vertical direction to see how the stimulated region evolves with time under this more common stress regime. In majority of underground formations, the maximum stress is in the vertical direction caused by sediments deposition loading.

Figure 6.6-I indicates the orientation of induced shear and tensile fractures along the blocks in which both tensile and shear fracturing occurs (j=1). Figure 6.6-II also shows the conjugate shear fracture orientation in other surrounding blocks. The dip and azimuth

angles of the induced fractures depend on the orientation of principal stresses at the time of fracturing.

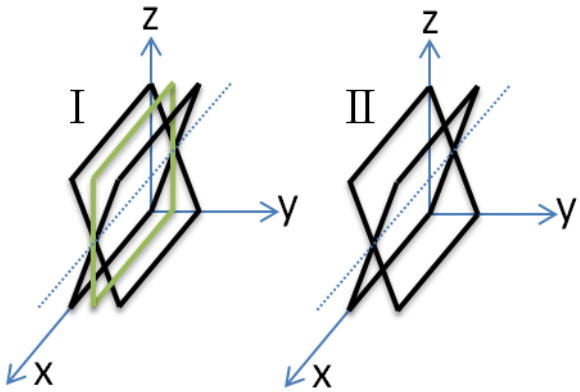

Figure 6.6 – Induced conjugate shear and tensile fractures when z is the maximum stress direction and y is the minimum

Figure 6.6 presents the development of the SRV after 100, 500 and 1700 seconds of fluid injection. The SRV shape is more elongated compared with the previous cases (Figure 1.1 or 1.4 in Section 6.1.2). The so-called pseudo-tensile fracture length is also better visible under the current example problem initial conditions.

After the early stage of the stimulation, the rate of increase in the well block pressure in the current case appears to be less when compared with the previous case (both cases are compared in the top graph of Figure 6.8). The reason is simply due to the shape of SRV which is more elongated; in the current case (similar to tensile fracturing) stress localization also contributes to the SRV propagation. Stress localization is not an effective fracturing mechanism in cases which the SRV is more of a circular shape and more off-planar SRV development is observed.

The effective stress in the x direction increases with time after the early stimulation time. It suggests the possibility of secondary fracturing which can be also called “crushing” in the already stimulated or “primary” fractured blocks (Figure 6.8). It should be noted that no secondary fracturing was permitted in the current case. In the next

example problem the secondary fracturing or crushing of the blocks also will be investigated.

Figure 6.9 indicates the stress path along the created shear fracture for the first Gauss point of the well block. The shear stress declines along with the normal effective stress under pressurization of the well block by the injecting fluid. This demonstrates the efficiency of the elasto-plastic model developed in this work,

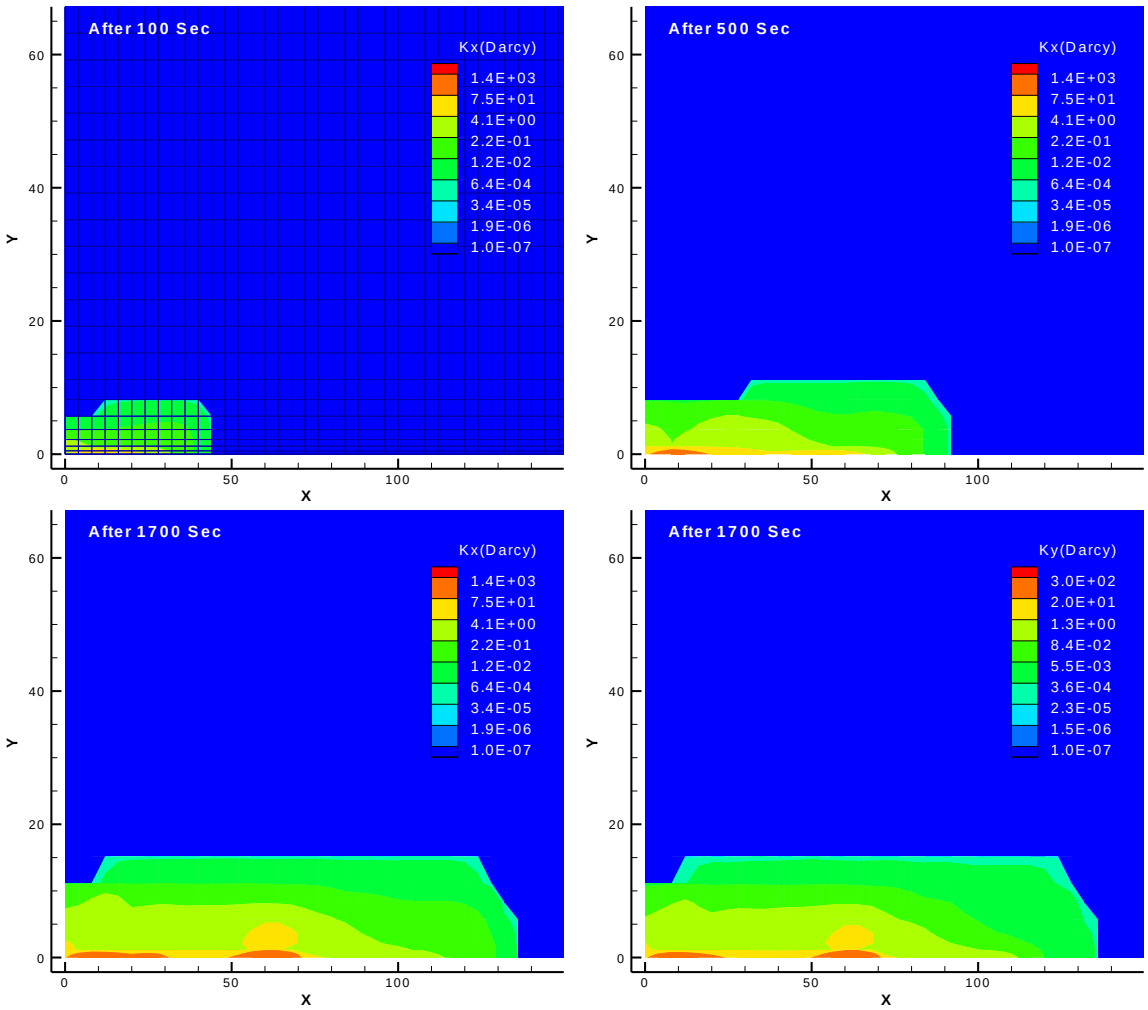

Figure 6.7 – Permeability variation with time in the combined shear and tensile fracturing case, vertical stress is the maximum

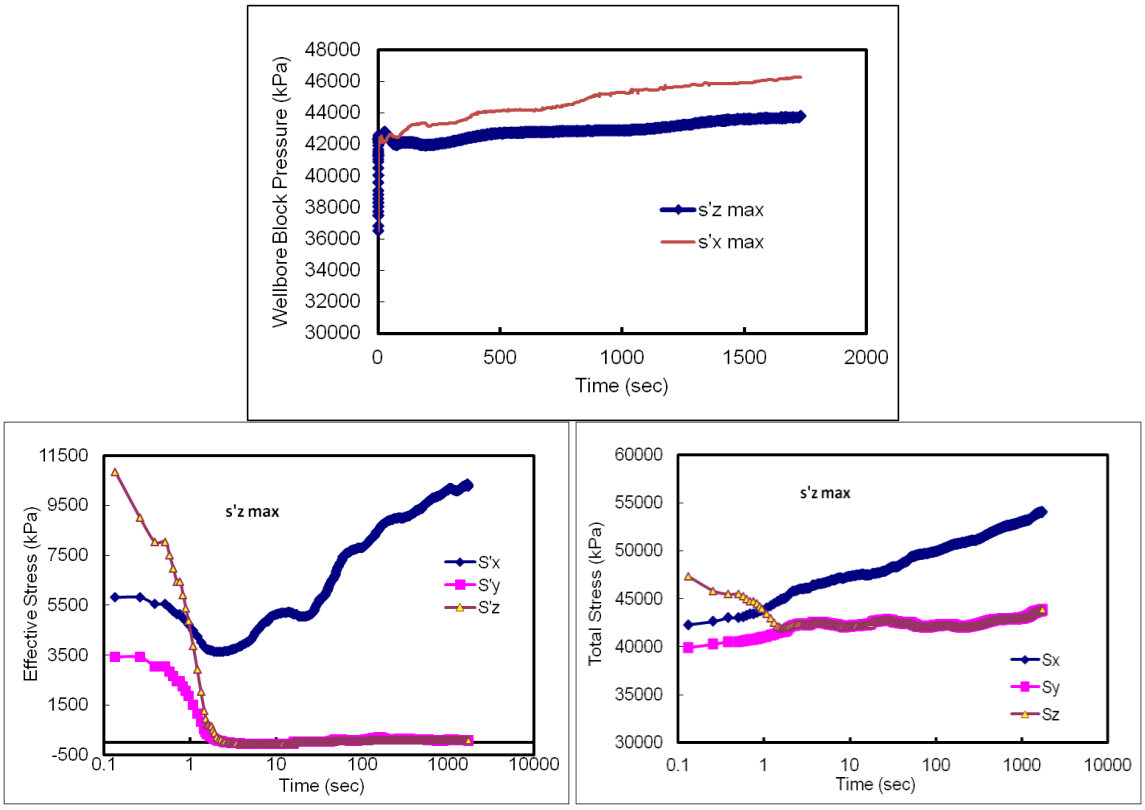

Figure 6.8 – Pressure, effective and total stresses - time profile, vertical stress is the maximum

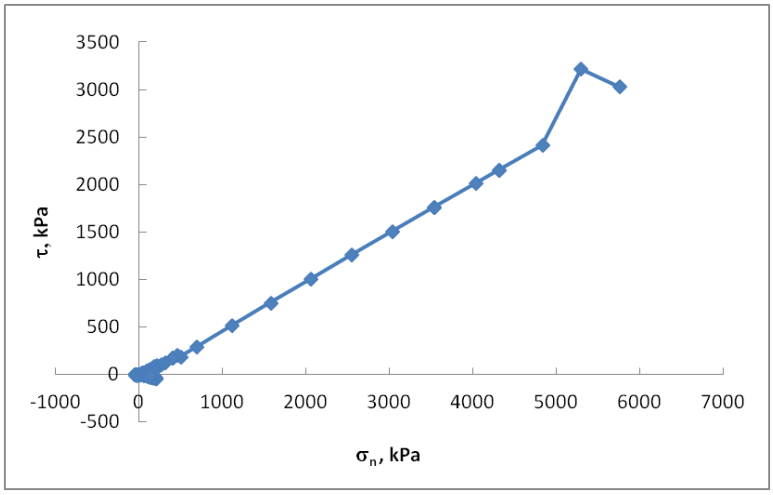

Figure 6.9 – Stress path in one of the well block Gauss points during the stimulation process, vertical stress is the maximum

6.1.4 Shear & tensile fracturing – crushed blocks allowed

In this example, we consider two modes of shear fracturing. In the first, a block which has been already fractured can subsequently fail in the code in shear along a different direction. This phenomenon of multiple fracturing will be referred to as "block crushing". The crushing leads to more complexity (and density) of fracturing and therefore the capability of our code to capture it is important.

In the previous example problems, either the case where the maximum stress was in the horizontal x direction or in the vertical z direction, a high possibility of secondary fracturing is expected as a large deviatoric stress may build up between the two other principal stresses. The minimum effective stress which has declined to zero is also a main contributing factor (Figure 6.2 and Figure 6.8). In the current example problem, the vertical stress is the maximum and secondary fracturing is also allowed in the dynamic fracture modeling as depicted in Figure 6.10.

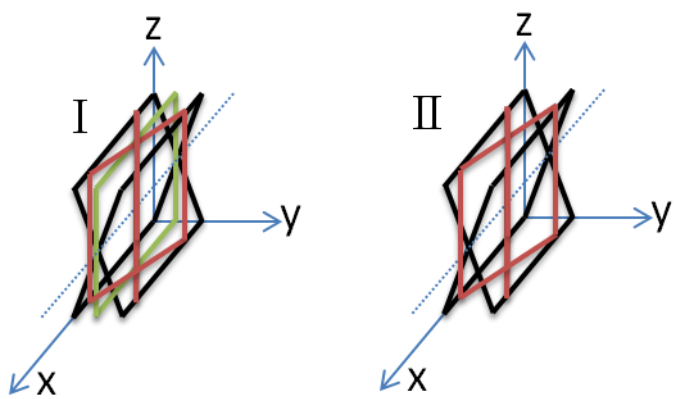

Figure 6.10 – Induced conjugate shear and tensile fractures when z is the max stress direction and y is the minimum

Figure 6.11 presents the permeability in x and y directions along with the development of the SRV after 100, 500 and 1730 seconds of fluid injection. The pseudo-tensile fracture plane is also observed when "block crushing" is the dominant fracturing mechanism.

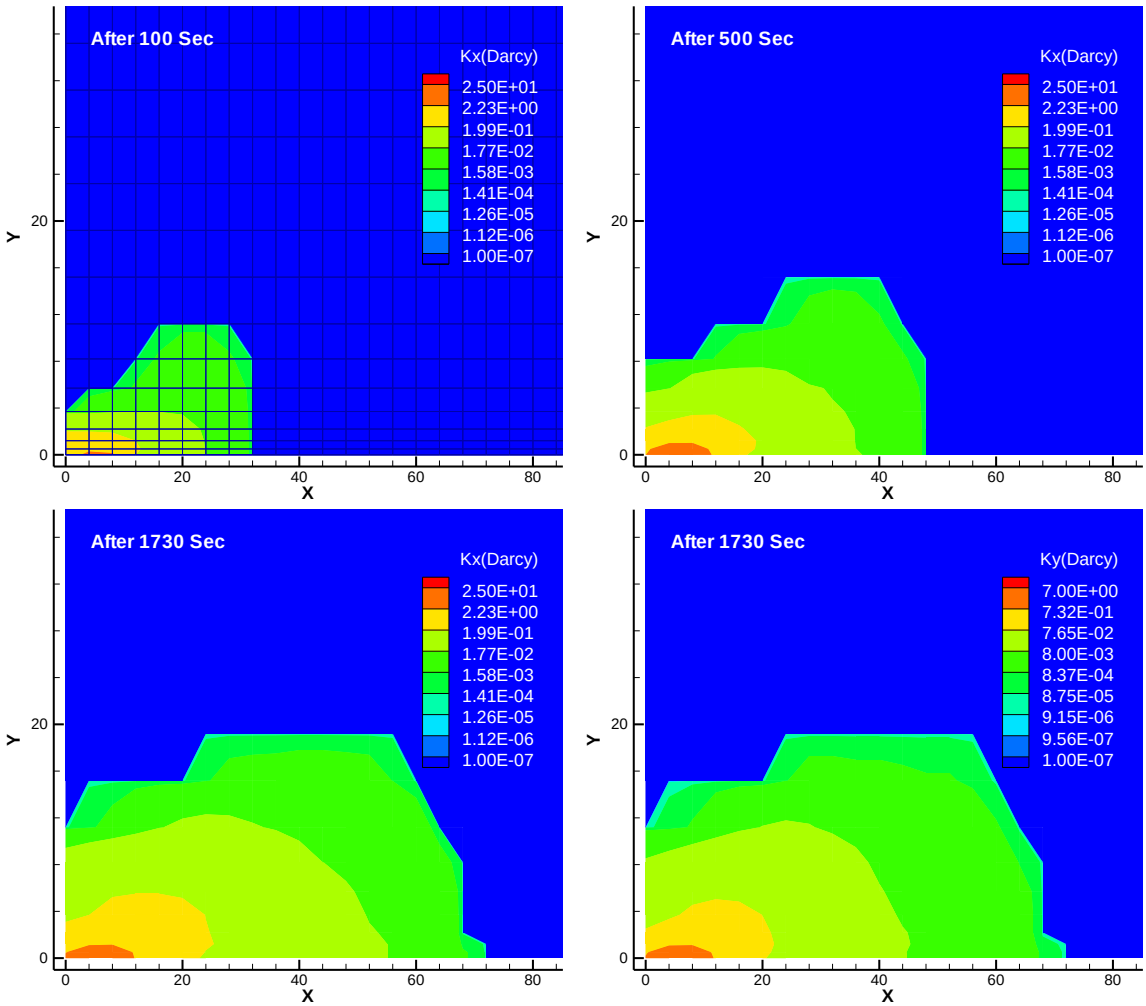

Figure 6.11 – Permeability variation with time in the crushed fracturing case - vertical stress is the maximum

As expected and shown in Figure 6.12, in the block crushing mechanism all stresses become almost the same. A continuous increase in the well block pressure is also observed which presents a gradual off-planar propagation of the SRV after the early stages of the stimulation process. It is worthwhile to recall that the minimum initial total stress is 40 MPa. The rate of off-planar SRV increase at the early stages of the stimulation is observed to be larger when compared with the later time of the stimulation process. The diagnostic is the larger increase in the well block pressure as shown in Figure 6.12.

The secondary fracturing in this example problem is explained by the increase in the intermediate stress caused by the directional SRV growth and force rebalancing. However, after secondary fracturing the mechanical behavior of the crushed blocks under high fluid pressure condition will be of liquefaction type with low shear resistance.

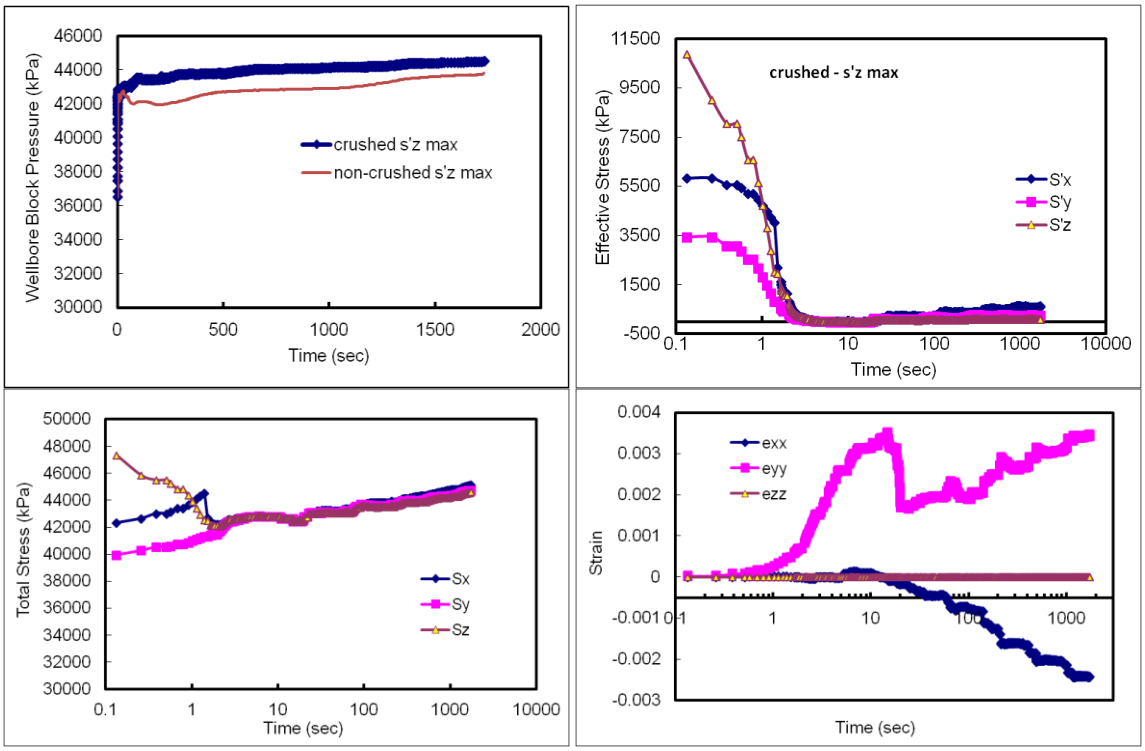

Figure 6.12 – Pressure, effective stresses, total stresses and strains - time profile of the first Gauss point of the well block

Figure 6.13 presents the stress path for the two shear fracture sets induced during the crushing mechanism. One fracture set is between the z and y direction (dip angle of round 60° and azimuth angles of about 90° and -90°), the second fracture set is between the x and y direction (dip angle of around 90° and azimuth angles of about 60° and -60°). It should be noted that the dip angle varies between 0° and 90°; whereas the azimuth angle varies between -180° to 180°.

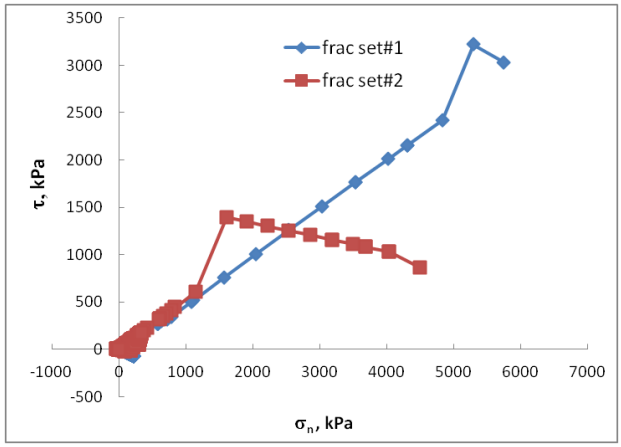

Figure 6.13 – Stress path and y direction displacement in the first Gauss point of the crushed well block during the stimulation process

6.1.5 Crushing mechanism– grid refinement

Sensitivity of the developed fracturing model to grid size is investigated in this section. The grids sizes were reduced to half in both x and y directions while the remaining input data were assumed to be the same as the previous example problem (crushed mechanism). It should be noted here that the fracture spacing is an input data which remain the same regardless of the grid size in the grid refinement analysis.

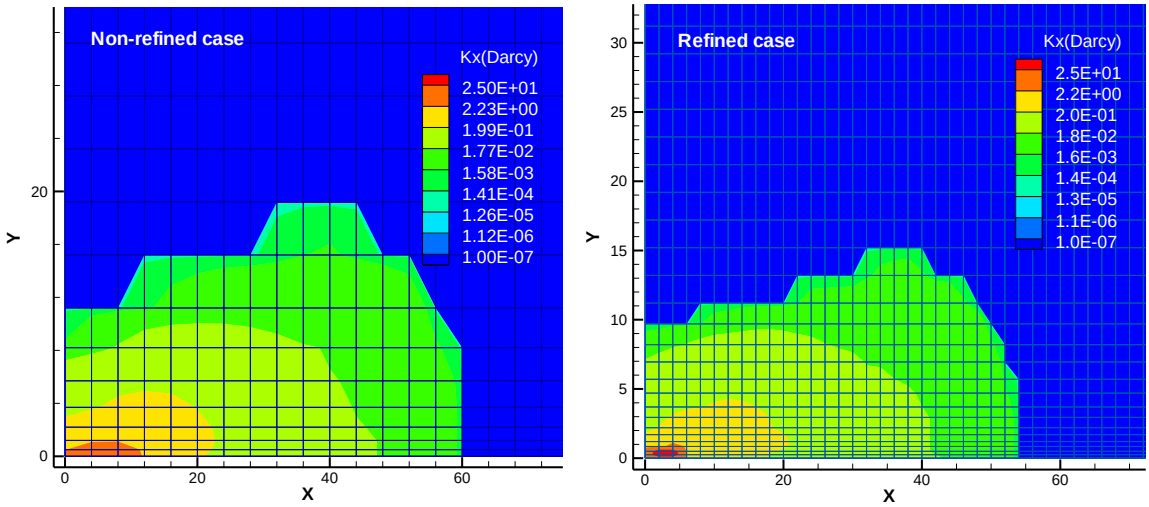

Figure 6.14 – Permeability variation with time in the refined grids case after 1130 seconds of stimulation

In general the stimulated region is slightly smaller in the refined grid case. Coarser block gridding slightly overestimates the SRV size. The overall configuration of the permeability enhancement is shown to be very similar to the non-refined case (Figure 6.14 which compares the two cases).

The well block pressure during the stimulation period is also compared with the base crushing case non-refined model in Figure 6.15. Both pressure profiles follow the same trend; however in the refined case less perturbation is observed at the early time. The well block total and effective stresses were almost the same in both non-refined and refined cases.

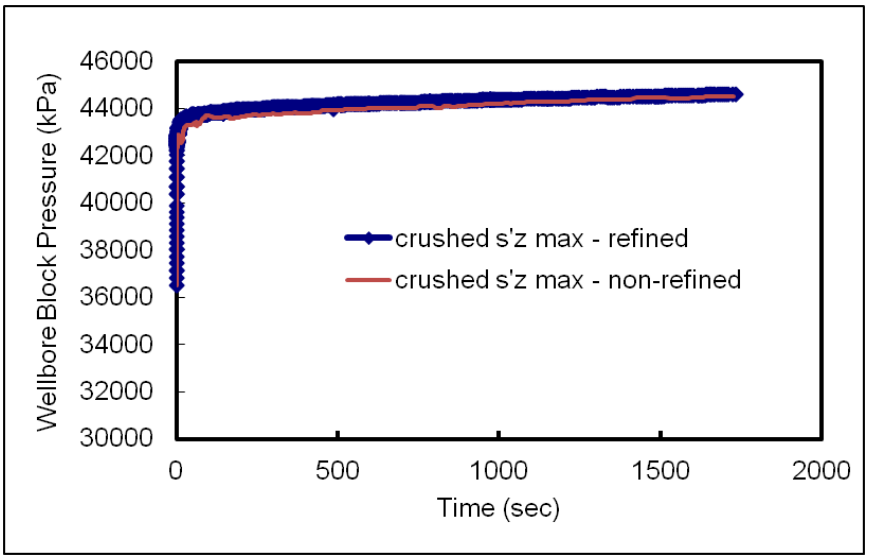

Figure 6.15 – Pressure-time profile comparison between refined and non-refined cases, grid block crushing mechanism in both

6.1.6 Close horizontal stresses – crushing mechanism

Intuitively it is expected that the SRV would grow in a circle if the two horizontal stresses were identical or very close in magnitude. Since the induced fracture directions are obtained from the principal stress directions, if two of the initial stresses are assumed to be identical then no unique principal directions can be obtained as the minimum and the intermediate principal stresses can take any directions in their plane. In this example

problem the two horizontal stresses in the x and y directions are chosen to be 40100 kPa and 40000 kPa respectively; whereas the vertical stress remains the same as previously, 47000 kPa. The maximum deviatoric stress is obviously between the vertical and horizontal directions.

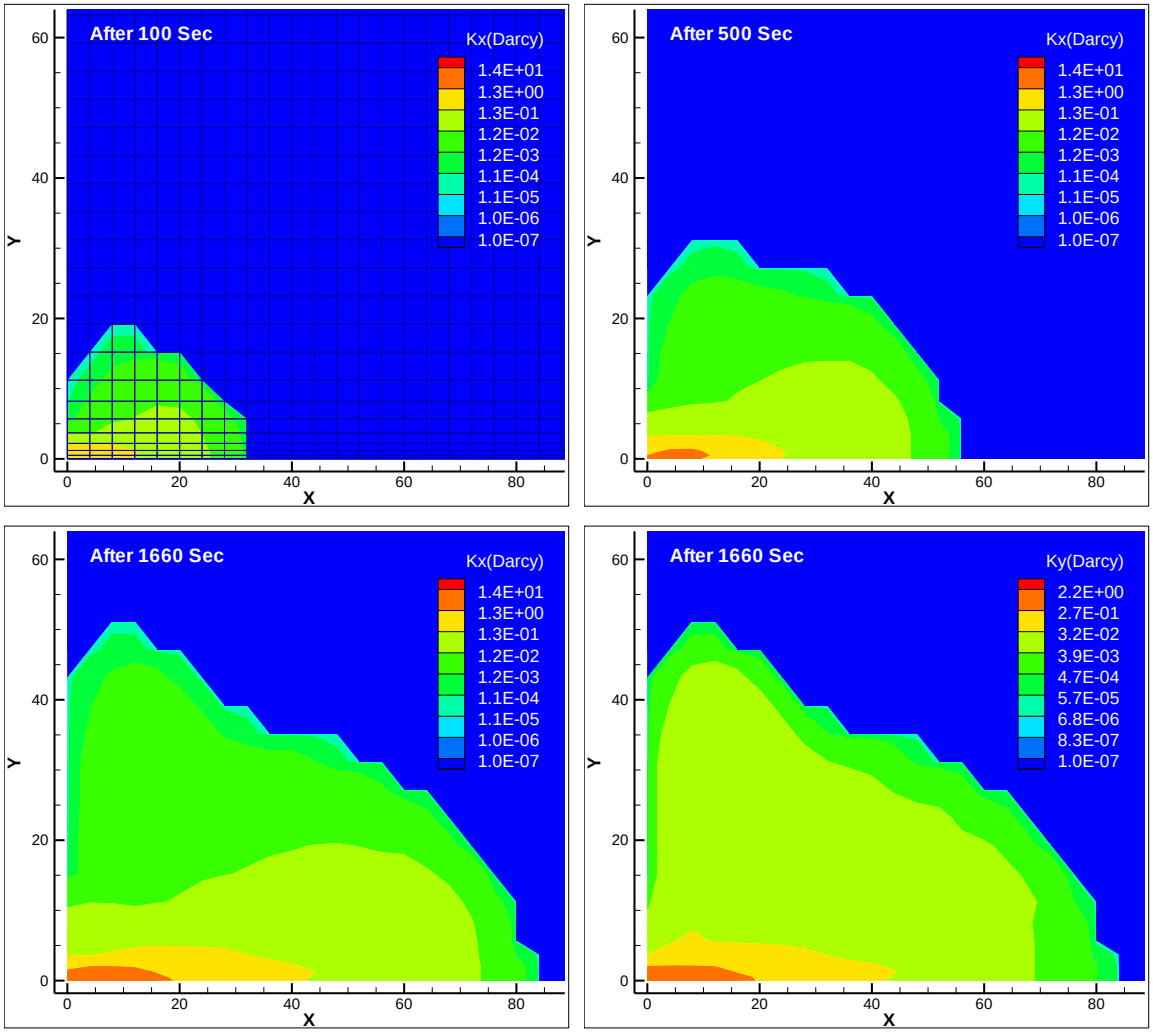

Figure 6.16 – Permeability variation for the case with close horizontal stresses

Permeability enhancement due to shear fracturing (including crushing) and tensile opening is shown in Figure 6.16. As expected the stimulated zone grows more in y direction compared with the previous example problem and a wider, almost symmetric SRV results. At first, because of the small difference between the two horizontal stresses,

the SRV growth is mainly in the x direction; however, after a while due to increase in total stress in y direction and switching of the minimum stress direction from y to x in areas above the initial failed zone, the SRV begins to propagate further in y direction as well, as shown after 1660 seconds in Figure 6.16. The contrast between the x and y permeability is also greatly diminished and the SRV approaches a radial growth. The well block pressure profile versus time in Figure 6.17 indicates a lower slope when compared with the crushed blocks case for the base case (Section 6.1.4).

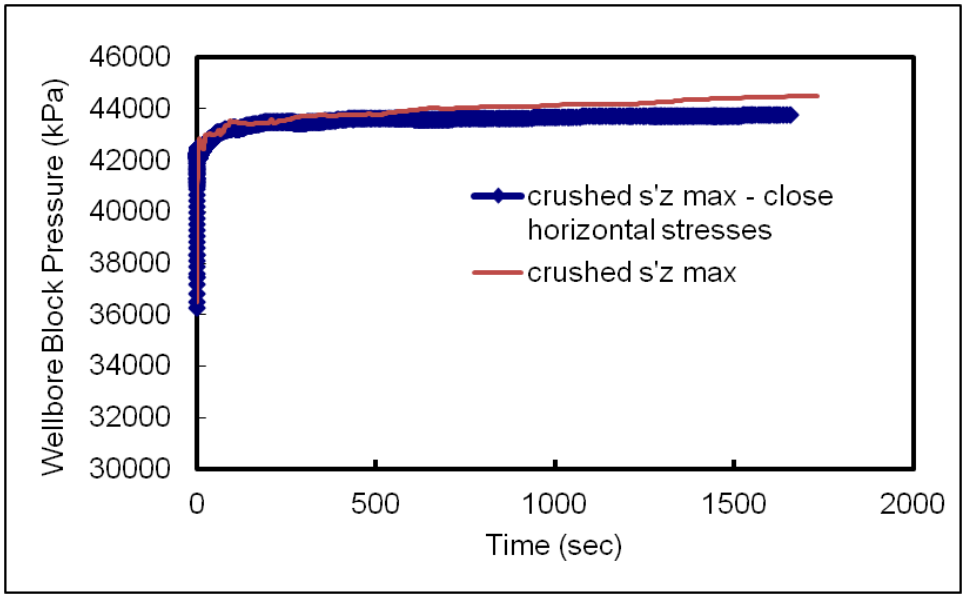

Figure 6.17 – Pressure vs. time for the case with close horizontal stresses

6.2 Significance of the initial conditions for the SRV shape

The SRV shape was found to be dependent substantially on the initial reservoir conditions such as initial stresses, initial reservoir pressure, rock resistance to shear failure, and other parameters which control failure. The closer the initial conditions to the shear fracturing point, the wider the width of the SRV will be in the stimulation of tight formations. If the initial conditions are far from the shear fracturing point, since the fluid diffusivity of a tight formation is low, the blocks around the main plane of tensile fracture cannot be pressurized enough to fail in shear and compete with the stress localization

mechanism which occurs at the tip of the SRV zone. As a result, the width of the SRV zone grows much less than the length, such that the SRV will be elongated. In the following sections the above will be further demonstrated by means of a few example problems.

The shear fracturing mechanism in all the following example problems is set to be of the "crushing" type and the base case is also given from Section 6.1.4.

6.2.1 Lower reservoir initial pressure

For the example problem given in Section 6.1.4 if one decreases the initial reservoir pressure, the reservoir blocks will then require more pressure build up to reach the shear failure surface. The initial reservoir pressure is assumed to be 31000 kPa instead of 36000 kPa of the base case. The dynamic combined shear and tensile fracturing simulation presents much narrower SRV in comparison with the base case as shown in Figure 6.18. The single plane tensile fracture is well developed and provides majority of the injectivity.

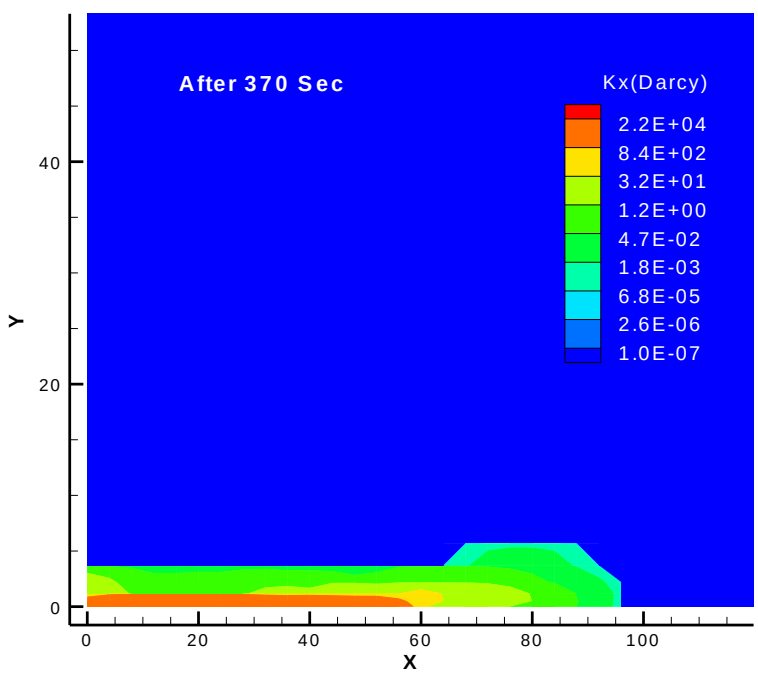

Figure 6.18 – Permeability variation for the case with lower initial reservoir pressure

6.2.2 Effect of reservoir rock cohesion

The reservoir rock cohesion was found to be an extremely important factor controlling the shape of SRV. The higher the rock cohesion, the larger the fluid pressurization in each grid block is required for shear fracturing to occur. In the base example problem the rock cohesion was assumed to be 0.5 MPa whereas in this section magnitudes of 1 MPa and 2 MPa for cohesion are tested. Figure 6.19 maps the permeability distribution for all three rock cohesion values. The simulation results reveal how the SRV shape narrows down to a single line when the rock cohesion increases from 0.5 MPa to 2 MPa. Associated with this is the increase in the propagation of the SRV in the x direction. The well block pressures for the three different cohesion cases are also compared in Figure 6.20. The continuous pressure increase for the rock cohesion of 0.5 MPa indicates an uninterrupted elliptical-like growth of the SRV with time. The decline in the well block pressure after 60 seconds of fluid injection in the case with 1 MPa of rock cohesion indicates narrower form of SRV growth whereas the increase in pressure that follows later is the diagnostic of a wider SRV development at later time. In the last case with 2 MPa of rock cohesion, the SRV has only grown along one row of grid blocks which indicates that only tensile fracturing has occurred in this case. The fracture has propagated very fast - up to 160 m within one minute which may be considered excessive. There may be several reasons for overestimating the growth in the purely tensile case. It should be noted first that the porosity term coupling has not been used in these simulations; therefore the fracture volume is not accounted for and the length growth is therefore exaggerated if there is virtually no leak-off. Secondly, the 52 bbls/min injection rate for 40 m of pay zone is also a high rate if there is no off-planar SRV growth. Finally, there may be also some matrix permeability enhancement with fluid pressurization which is not accounted for.

The above proves the fact that a large SRV is imminent when the reservoir initial conditions are relatively close to the shear failure surface of the formation rock or the pre-existing planes of weakness. One obvious example would be stimulation in a naturally fractured reservoir in which the fractures are poorly cemented and by a slight increase in the pore pressure, the rock shear failure is triggered. Another example could

be tight or shale gas reservoirs in which the existing micro- or meso-scale fractures have weakened the shear strength of the formation rock.

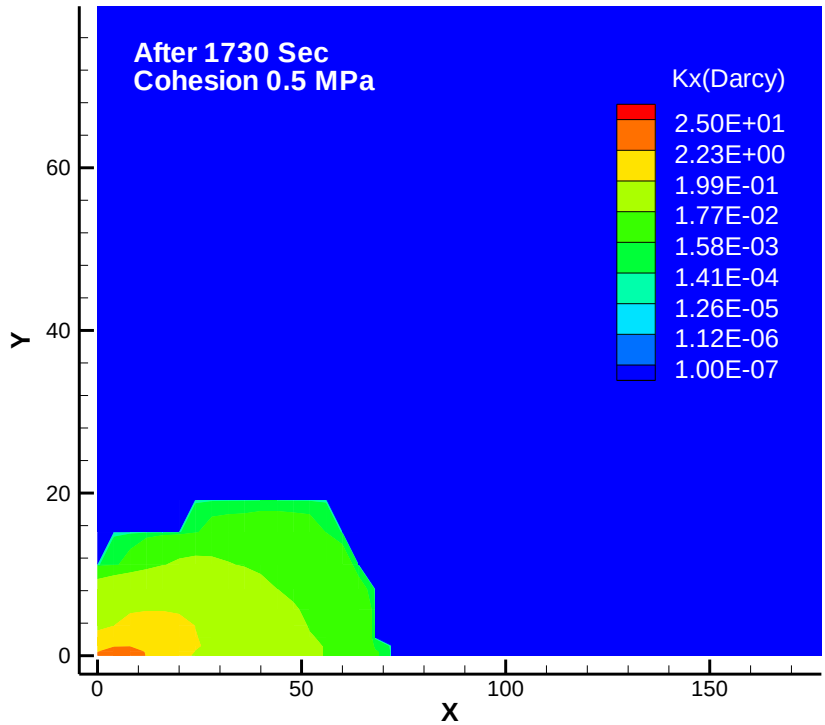

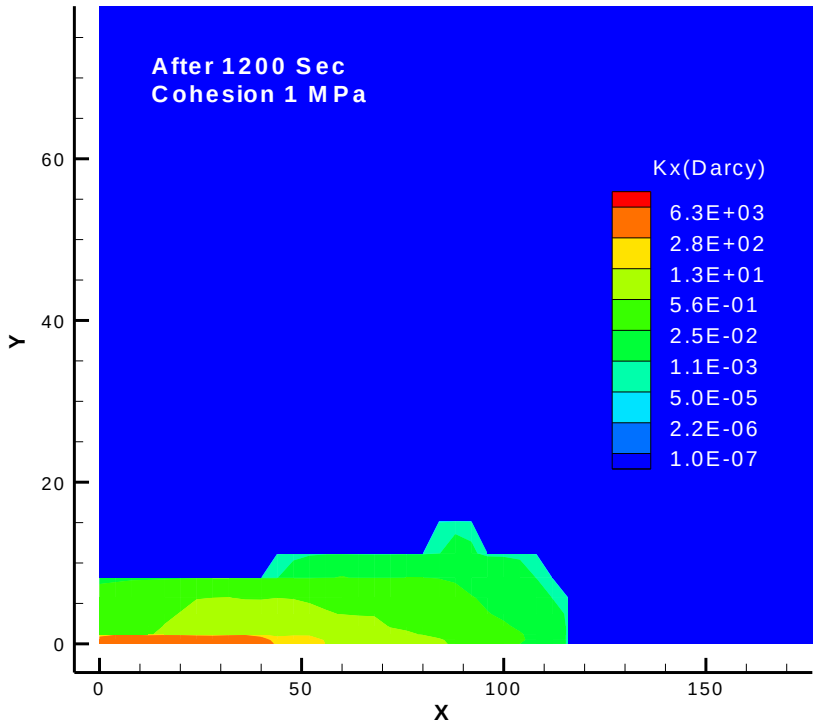

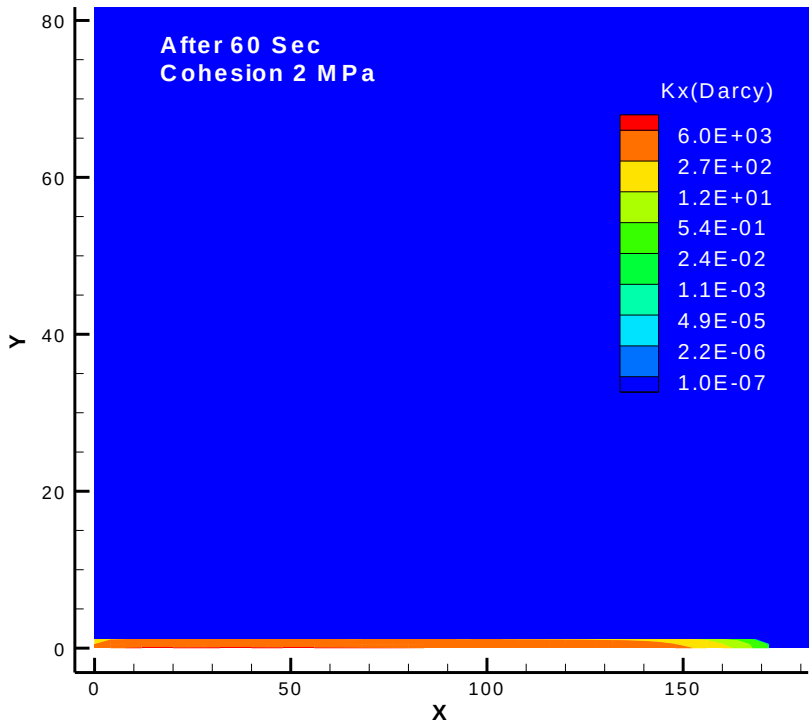

Figure 6.19 – Permeability variation for three different cohesion values

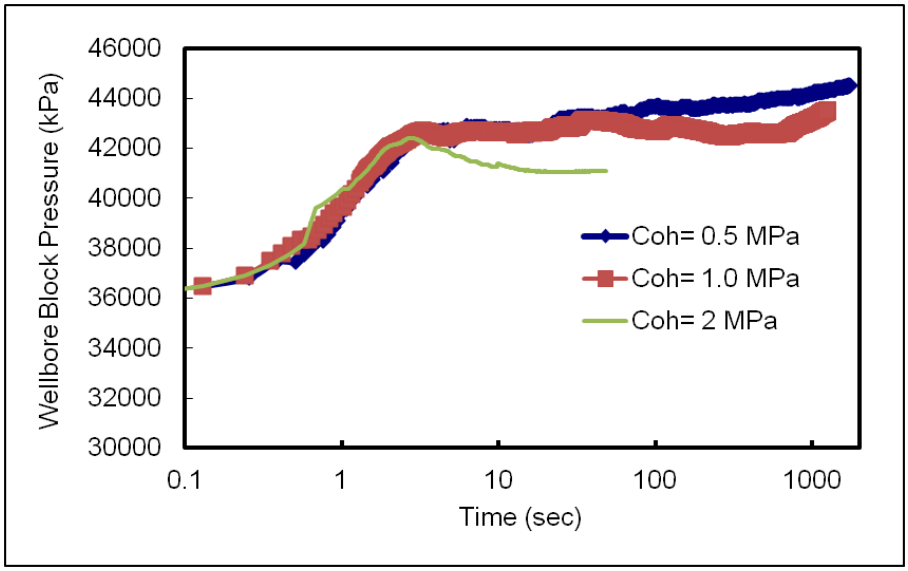

Figure 6.20 – Rock cohesion effect on the pressure vs. time profile

6.3 Discussion of some aspects of fracturing

6.3.1 Important discussion on the tensile fracture width calculation

In all the examples above the fracture width at any time step is updated by the Bandis et. al. normal effective stress/displacement hyperbolic equation plus the dilation term obtained from the plastic shear displacement. For tensile fractures the hyperbolic relationship is extended into the pseudo tensile region as explained before.

In the shear/tensile fracturing modeling, along with shear fracture sets (which can occur everywhere), a tensile fracture perpendicular to the minimum effective stress is embedded in the blocks along the designated fracture plane (at j=1). In this situation, the opening of the tensile fractures calculated by the pseudo-continuum technique may not correspond to what is seen in reality. The above does not question the validity of the pseudo-continuum method; but since other shear fracture sets are also embedded in the crushed block, the crushed block overall deformation has to be distributed among all the fracture sets. However, if one assumes that the single tensile fracture width is the same as the overall deformation of the block containing the tensile fracture (neglecting the intact rock deformation), permeability enhancement of the block calculated from such “modified” tensile fracture width in the tensile fracture plane direction would certainly be much greater in comparison with the non-modified case. Figure 6.21 depicts a schematic of the crushed blocks containing tensile fracture and the blocks around them. Only one shear fracture set is shown in the figure, although usually a minimum of two fracture sets are induced in our simulation cases with the crushing mechanism. Now if one assumes the overall displacement of the crushed block in direction perpendicular to minimum stress to calculate the change in the tensile fracture width, then a more dominant tensile fracture will result from the numerical model.

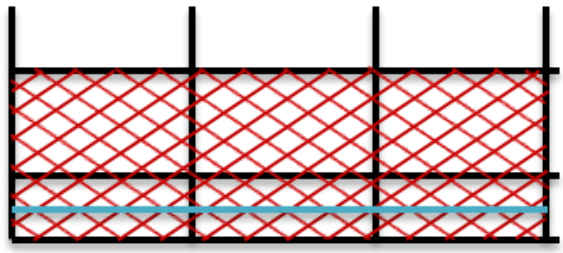

Figure 6.21 – Shear and tensile fracture sets in a stimulated region

The example problem modeled in Section 6.1.4 (crushing mechanism) is repeated here with the difference described above. In other words, the tensile fracture width is obtained from the total block deformation of the block in y direction (perpendicular to the initial minimum stress). The resultant permeability distribution map is shown in Figure 6.22. The single tensile fracture is relatively better developed in this example when the tensile fracture width is calculated from the total block displacements. The SRV dimensions are substantially more elongated for this case when compared with the base case. The lower well block pressure shown in Figure 6.23 indicates a longer SRV development for the modified case and also the development of a more conductive path for flow in the middle of the SRV region when compared with the non-modified case.

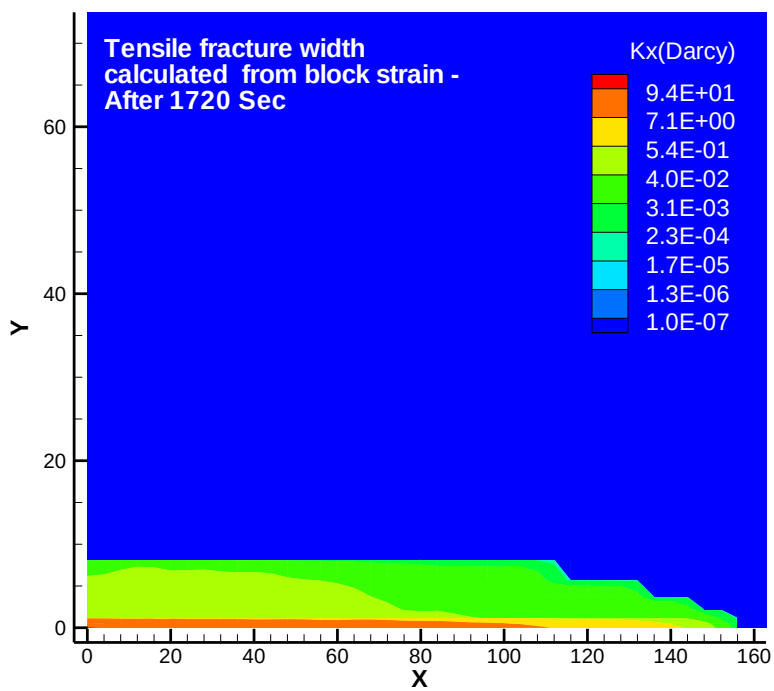

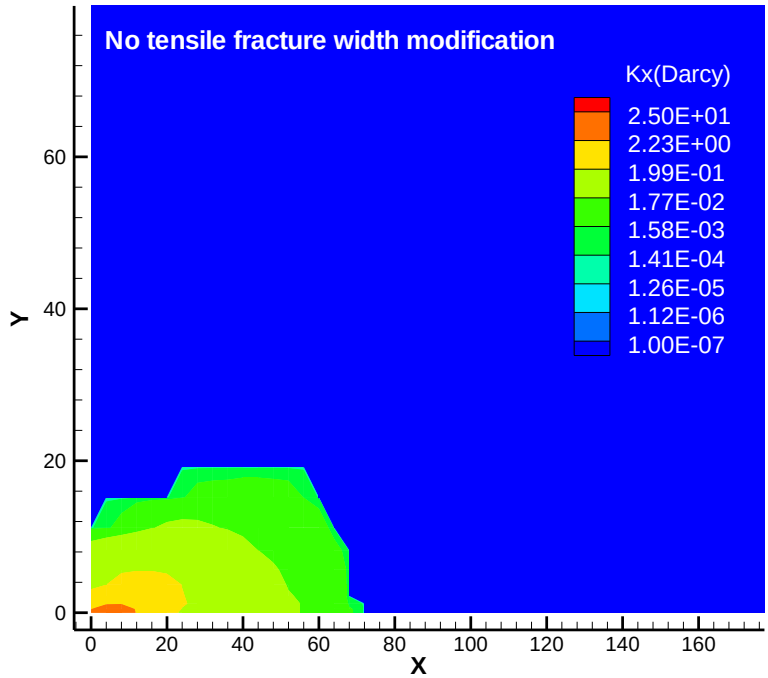

Figure 6.22 – Permeability variation for the case with modified tensile fracture width and non-modified case after 1720 seconds of injection

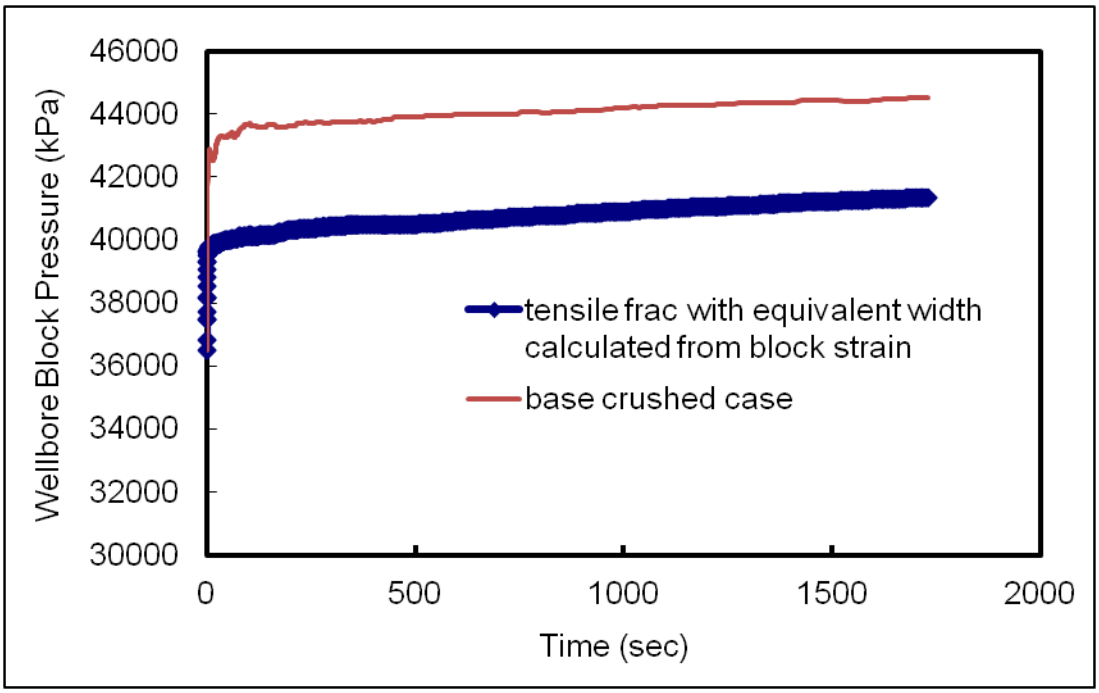

Figure 6.23 – Pressure vs. time for the case with tensile fracture width correction compared with the base non-corrected case

6.3.2 Significance of stress rebalancing

Shear softening after shear fracturing as discussed in the previous section and in the theory chapter is modeled by two techniques; first, the deviatoric stress is forced to decline by means of mobilized friction angle, and second, through immediate correction of the fracture Gauss point effective stresses by decreasing the maximum principal effective stress and rebalancing the forces afterward. Drifting of the shear failure surface in the former technique sometimes causes uncontrollable divergence problem in the Newton loop especially when the stress path approaches the tension cut-off surface. Choosing an appropriate value of the exponent for the softening function, n, is also a problem that needs further study.

The technique implemented in all the example problems to treat the post-shear failure deviatoric stress drop is to modify (re-set) the effective stress of the failed Gauss point to a residual. Forces acting on different nodes are then required to be rebalanced when the magnitude of stress at some Gauss points has been manually altered. In this section the significance of the force rebalancing after failure is shown by comparing the base case from Section 6.1.4 with a problem which is the same except that no force rebalancing after shear failure is carried out. The effective stress at the failed Gauss point is just modified to the residual amount by reducing the maximum principal effective stress. The comparison is presented in Figure 6.24. A major difference is observed between the two SRV sizes, and we believed that the solution with force rebalancing resembles more the real phenomenon happening in most non-conventional reservoirs fracturing in which micro-seismic events are also observed. When a block fails in shear, the non-fractured blocks around are loaded by force rebalancing mainly in the maximum effective stress direction. Since the geomaterial is bounded, the blocks minimum stress increases as well and the stress state of the non-fractured blocks is drifted away from the shear failure surface. This is explained the smaller SRV when force re-balancing technique is implemented in the numerical solution.

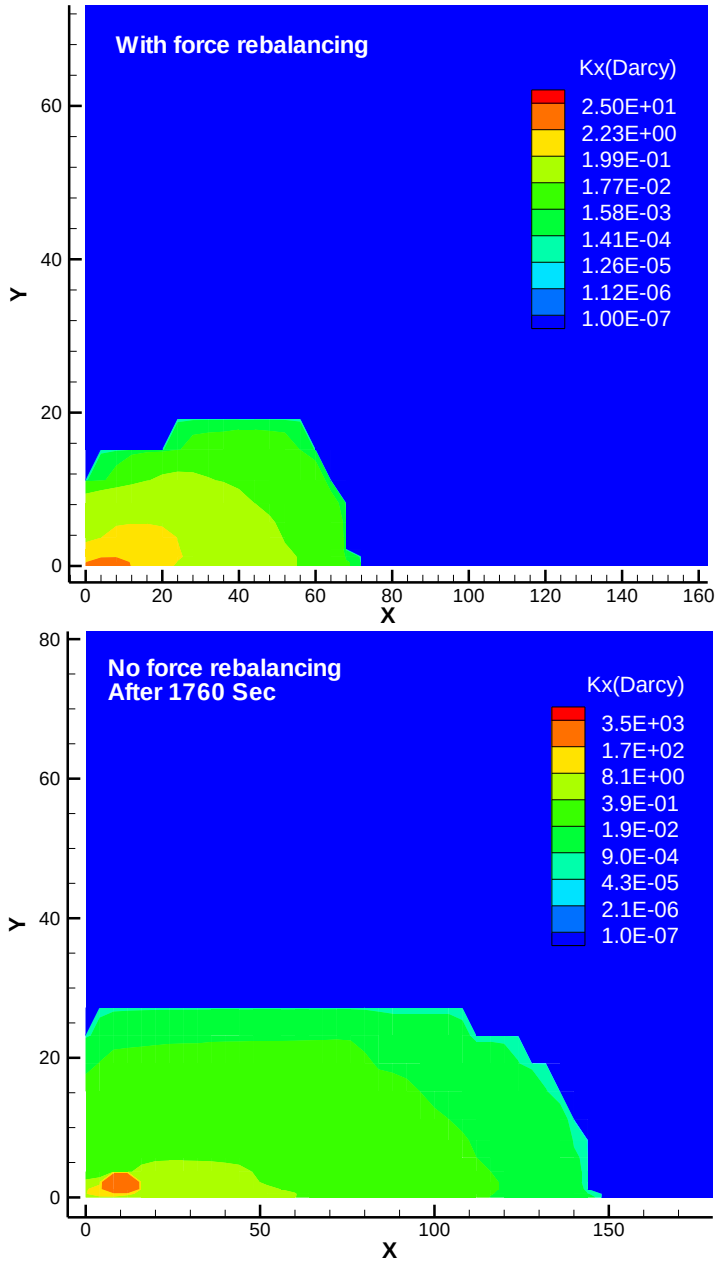

Figure 6.24 – Effect of post-failure forces rebalancing on the SRV distributions

Figure 6.25 compares the well block pressure profile for the two cases. The larger SRV size in the non-rebalanced case is associated with a greater pressure drop within the SRV zone from the well block to the boundary of the larger SRV within the same stimulation time.

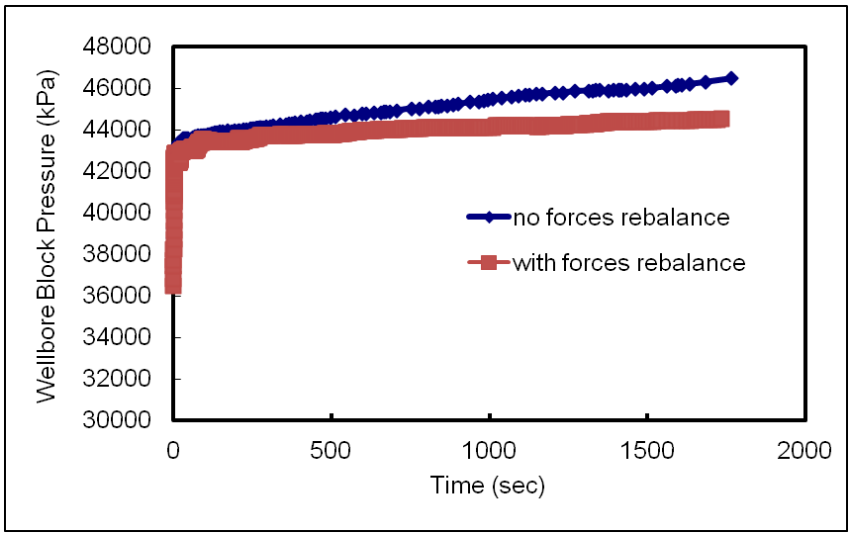

Figure 6.25 – Pressure vs. time profiles, effect of forces rebalancing

6.3.3 Alternate method for stress rebalancing

The other approach for post-shear failure treatment, defining a mobilized friction angle and reducing it from a maximum value calculated at the failure point to a predetermined residual level, is also investigated here. The example shown is for exponent coefficient *n* of 1000 m^{-1} in the equation of friction angle reduction as a function of plastic shear strain. The effective stresses, strain and the stress paths of the fracture sets for the first Gauss point of the well block are shown in Figure 6.26. It is apparent that after shear fracturing occurs, the maximum effective stress smoothly declines as a function of cumulative plastic shear strain. Likewise, after secondary shear fracturing σ'_z, σ'_x also decreases to zero as expected. Strain component in y direction increases, whereas the component in the x direction decreases after shear failure.

The most difficult challenge in this technique is the uncontrollable divergence which may occur after fracture propagation within some blocks around the well block. It might be explained mainly by the large drift in the shear failure surface, or by frequent switching of the constitutive model from elasto-plastic to tensile at the tensile cut-off surface. As indicated in Figure 6.26, after the model has been run only for 34 seconds divergence caused so many time step cuts in the solution that the simulation could not continue. The other post-shear failure treatment technique, in which the failed Gauss

point effective stress tensor is modified followed by forces rebalancing, has been found to be more stable in terms of solution convergence.

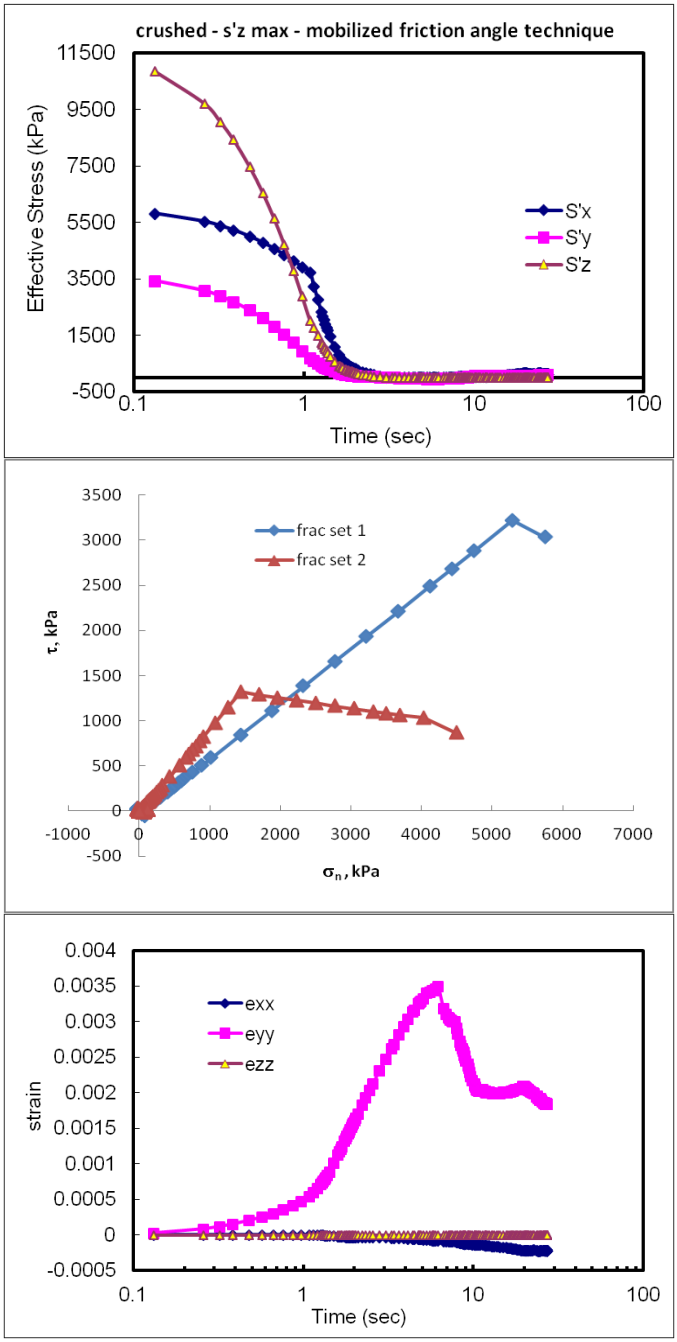

Figure 6.26 – Effective stresses, strains and the fracture sets stress paths for the first Gauss point of the well block

6.4 3D fracture modeling of the base case

The 2-D example problem solved in Section 6.1.4 is extended here to 3-D to investigate the permeability distribution, the well block pressure and other fracturing properties in realistic 3-D settings. The gridding in the x and y directions is retained the same as in the 2-D case but the number of grids in the z direction has increased to 8 (300, 15, 15, ***14, 12, 14***, 15, 200 m from top to bottom, reservoir thickness of 40 m consisting of layers 4-6). In the vertical direction the SRV is assumed to be confined between strong cap and base rocks. The elastic properties of the cap and base rocks are the same as for the reservoir rock; however, the cohesion and tensile strength are much higher (18 MPa and 8 MPa respectively) such that failure will not occur. Obviously, the failure of the cap rock is also of interest and the model is capable of investigating it, but this topic is beyond the scope of this thesis.

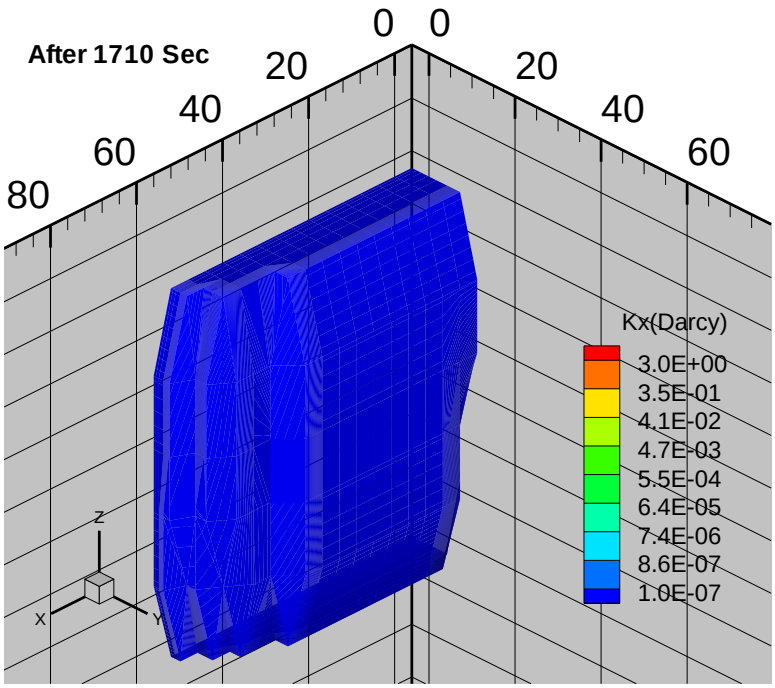

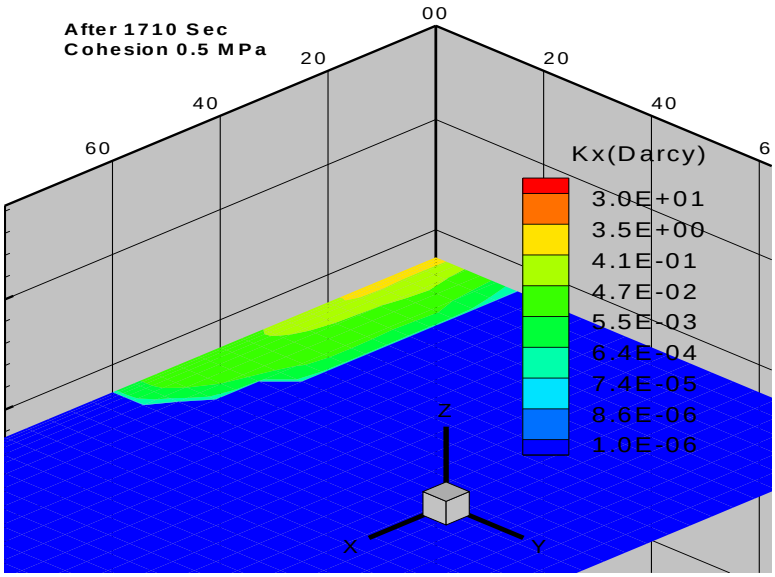

Figure 6.27 – Induced SRV after 1710 seconds of stimulation in the crushed fracturing case – 3-D model

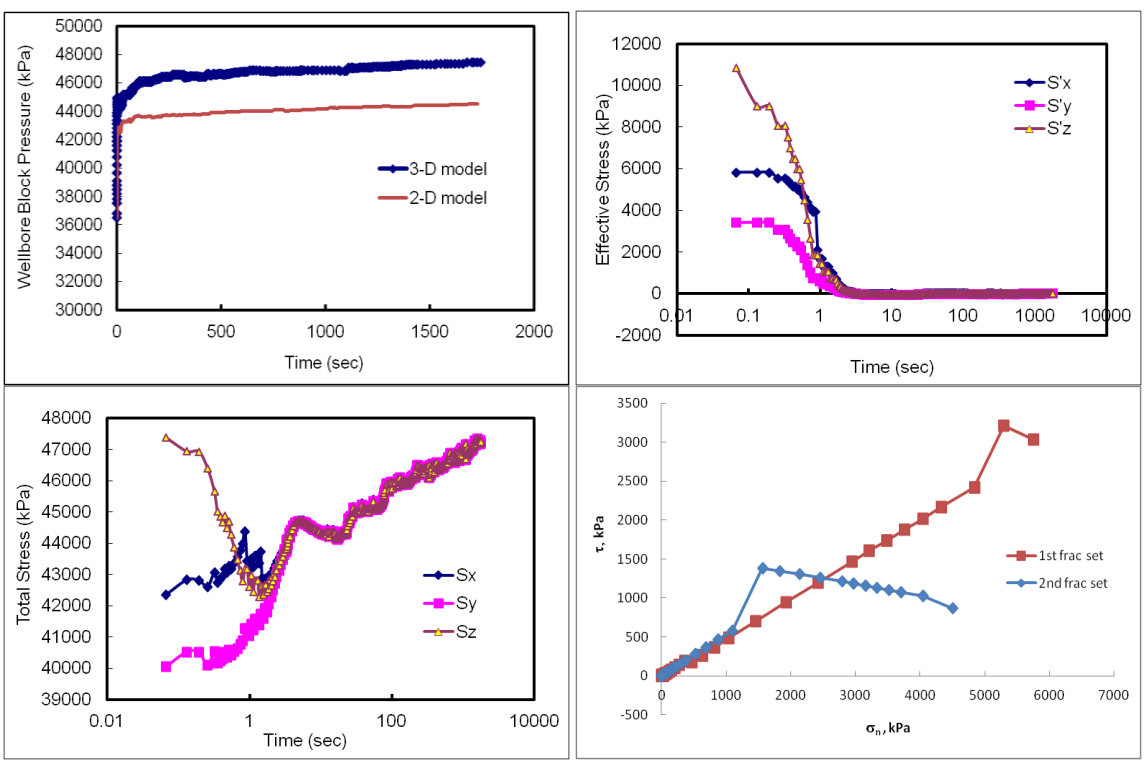

Figure 6.28 – Well block pressure, effective stresses, total stresses and stress path in the first Gauss point of the well block in the 3-D model

Figure 6.27 indicates the SRV growth after 1710 seconds of reservoir stimulation which is around 60 m in half length, 12 m in half width and of course is confined vertically to 40 m pay zone. In comparison with the 2-D model the SRV areal extent is less in the 3-D case. However, as shown in Figure 6.28 the overall injection pressure is higher. Similar to the 2-D case after crushing, all the effective stresses at the first Gauss point of the well block decline to around zero. The stress path at the respective Gauss point also moves along the shear surface all the way to around zero coordinates.

To provide an estimate of the computational time, it took about 9 seconds for one geomechanical Newton iteration and about 8 hours for the entire 3-D model run to be completed. The run consisted of 612 time steps and each time step required between 3 to 5 iterations in the geomechanical Newton loop to converge. Furthermore as explained before when a Gauss point fails, the model is first run through the Newton loop to rebalance the forces and next the whole time step is repeated. There is also a maximum stress variation controlling parameter (***SNORM***) which causes time cut and repeat whenever it is exceeded. The time repeats could be as many as the number of time steps.

In the second 3-D example problem, the cohesion has been increased to 2 MPa. As expected (and observed also in the 2-D analysis), the fracture plane was much narrower and more tensile-like in comparison as shown in Figure 6.29. Each oscillation in the well block pressure profile represents one step of lateral growth in the SRV width as presented in Figure 6.29 and Figure 6.30.

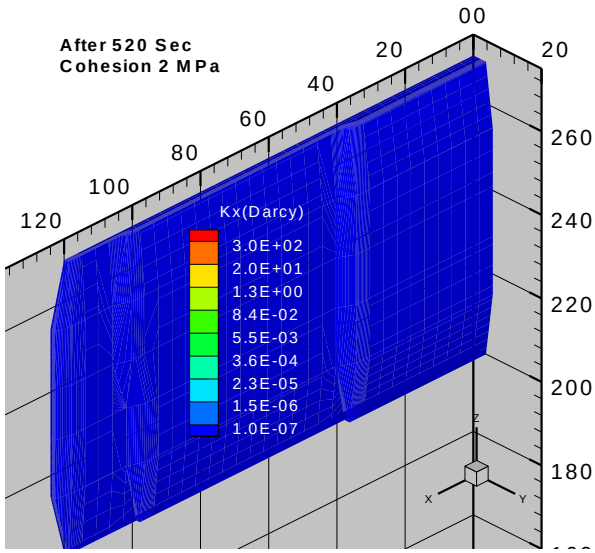

Figure 6.29 – Induced SRV after 520 seconds of stimulation in the crushed fracturing case – 3-D model, cohesion 2 MPa

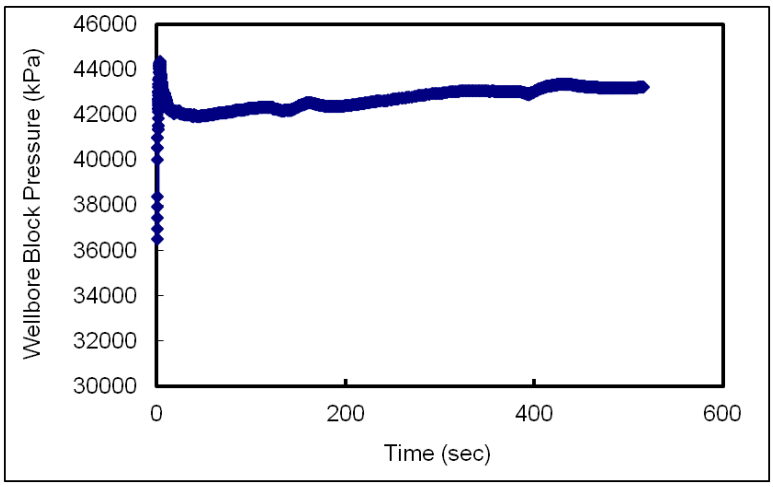

Figure 6.30 – Well block pressure in the first Gauss point of the well block in the 3-D model – cohesion 2 MPa

6.5 Example problems for deeper reservoir

The example problems in the previous section were all various forms of a base case fracture problem. In this section another example problem with different initial reservoir conditions are chosen to further evaluate the applicability of the developed work project. The formation of interest is assumed to be deeper and the initial pressure and all stresses

are higher. The water is injected at various rates from low to high in magnitudes. The fluid, reservoir, rock and fracture properties are given in Table 6.2.

6.5.1 2-D model

The gridding procedure for this example is the same as the previous problem (50 x 25 x 1). The blocks are equally spaced in x direction (4 m each) and in y direction are selected to be in increasing sequence of 0.5, 0.7, 1, 1.5, 2, 2.5, 4, 4,… in meters. The model has been run for three different full field injection rates of 5200, 10400 and 20800 M^3/Day (~ 23, 45, 90 bbls/min). Other required data to set up the model are given in Table 6.2.

As mentioned before, a tensile fracture set is allowed in the row of blocks in which tensile fracturing is assumed to propagate (j=1). The embedded tensile fracture has a spacing defined as twice as the grid block width size due to the quarter of symmetry assumption (grid width =0.5m and tensile fracture spacing =1m for all blocks at j=1). This ensures that only half of tensile fracture will exist in the boundary blocks to meet the quarter of symmetry requirement. The residual tensile fracture width is assumed to be 0.01 mm (a_j, Δv_{max} = 0.11 mm, 0.1 mm as assumed for all induced tensile fracture in previous sections). Other tensile fracture properties are the same as the shear fracture sets given in the second column in Table 6.2.

Table 6.2 – Rock, fluid and fracture physical properties for the 2nd example problem

ϕ (porosity)=	0.07		a_j, Δv_{max} =	0.13, 0.1	mm	E =	3×10^7	kPa
$k_{xi} = k_{yi}$ =	1E-5	md	K_{ni} =	1.0E6	kPa/m	v =	0.3	
k_{zi} =	1E-5	md	JRC =	2		k_{gr} =	15.0×10^{15}	kPa
ρ =	1000	Kg/m^3	JCS =	30000	kPa	S_0	500	kPa
μ =	0.3	cp	ϕ_{bf} (fracture)=	25°		ϕ (rock)=	30°	
$c_f = c_r$=	0.6×10^{-6}	kPa^{-1}	K_s / K_n =	0.6		$S_{h,i}$ =	63000	kPa
p_i =	60000	kPa	n =	0.5	m^{-1}	$S_{H,i}$ =	64000	kPa
Pay Thickness =	66	m	η =	0.6		$S_{v,i}$ =	70000	kPa
			S_f =	0.2 (Shear frac)	m			

The simulation results of the SRV distribution after 1700 seconds of stimulation job are presented in Figure 6.31 for the three different injection rates. The main difference

between the three cases is the maximum amount of permeability enhancement which is the highest for the case with the maximum injection rate.

The well block pressure is also compared in Figure 6.32. It is worth to recall that the minimum total stress is 63000 kPa and therefore in all the three cases a substantial increase in the well block pressure is observed at the early stage of fracturing. For the low injection rate the profile is then almost flat whereas for the other higher injection rates there is some degree of raise in the well block pressure afterward. The higher the rate of the fluid injection, the higher the slope of the well block pressure versus time.

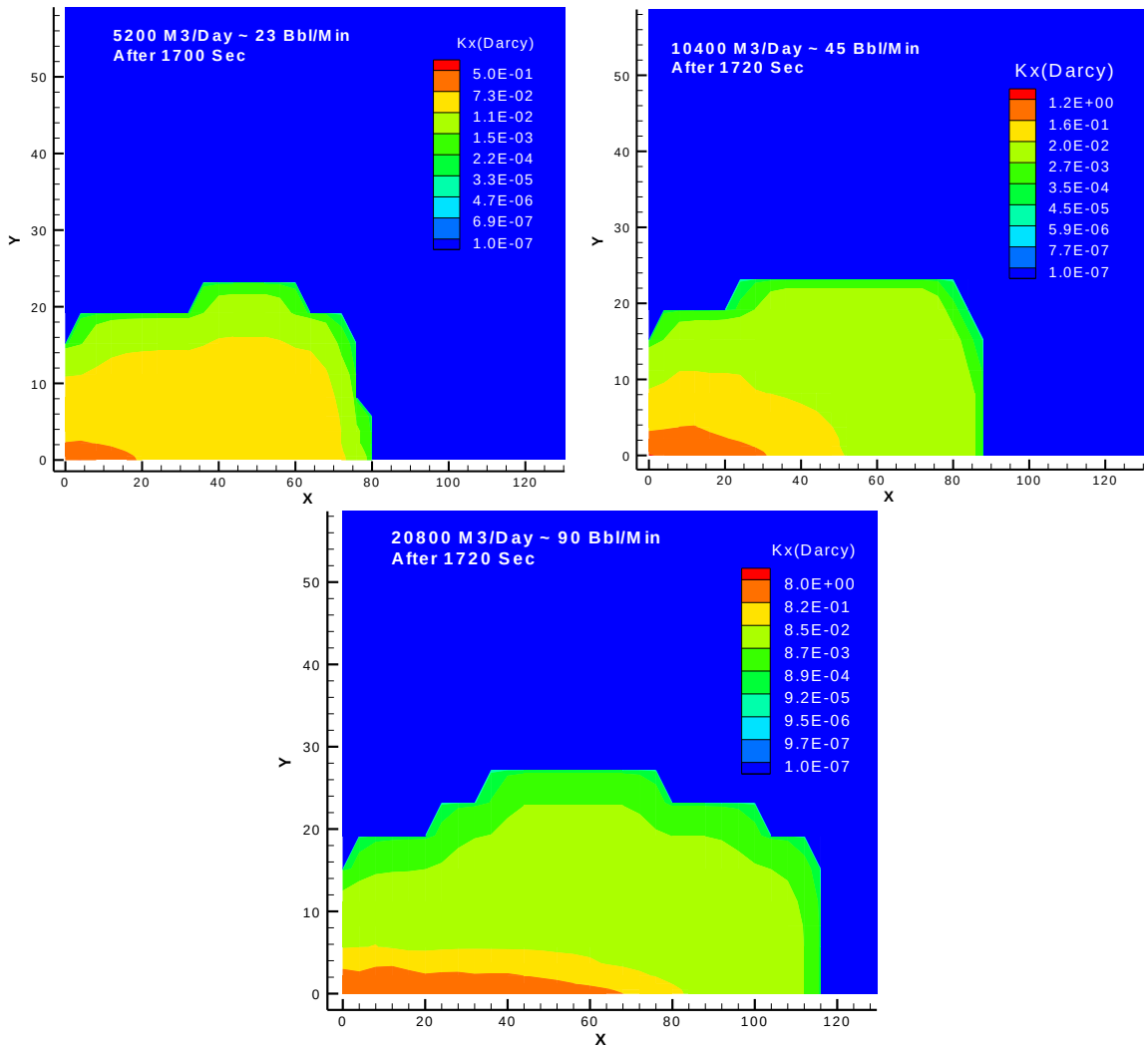

Figure 6.31 – Induced 2-D SRV development for three different injection rates

The effective stress profiles for the first Gauss point of the well block as shown in Figure 6.32 reveal the fact that for the low injection flow rate, no secondary fracturing has occurred; whereas in the mid and high injection rates both primary and secondary fracturing (i.e., block crushing) were the dominant mechanism. The Gauss point strain profiles indicate higher contrast between normal strain in y and x directions as the injection flow rate is ramped up. It is worthwhile to mention that the well block strain in the main SRV propagation direction is compressive as opposed to the strain in the perpendicular direction.

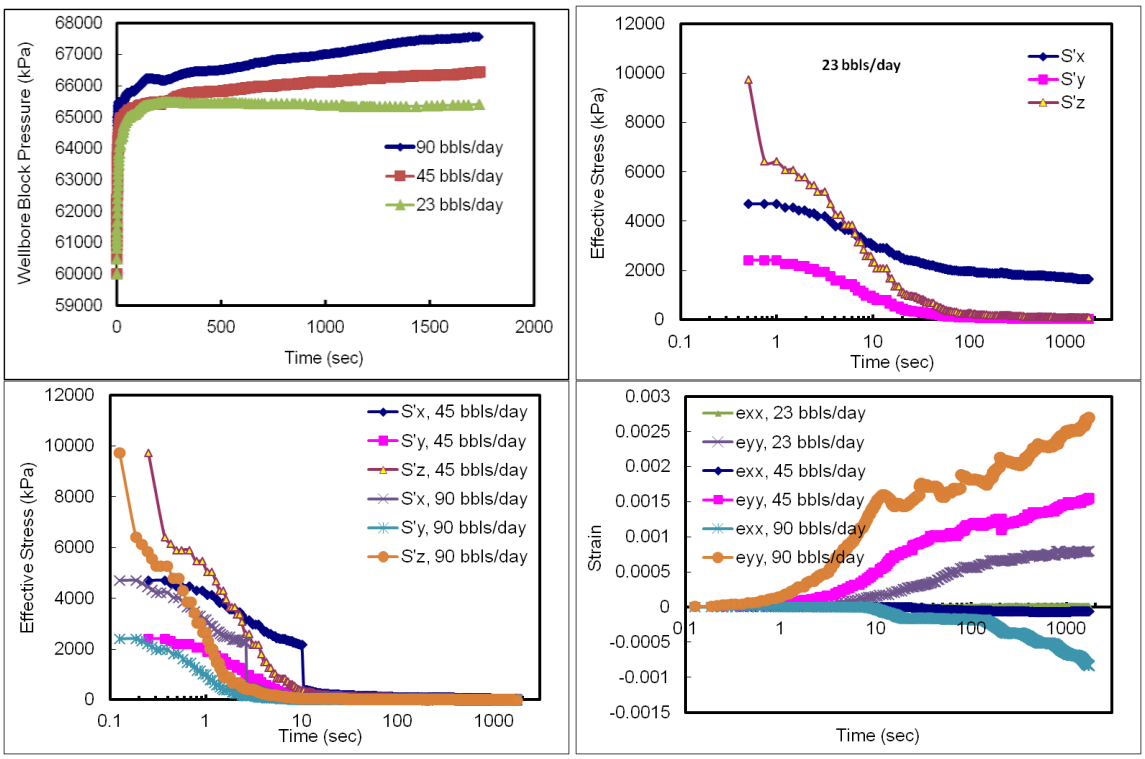

Figure 6.32 – Well block pressure, effective stresses and x, y strain components in the first Gauss point of the well block (4m x 0.5m x 66m) for the 2nd example, 2-D plane-strain model

6.5.2 3-D model

The 2-D example problem in the previous section is extended here to 3-D by retaining the gridding in the x and y directions and increasing the number of grids in the z

direction to 8 (300, 24, 24, ***22***, ***22***, ***22***, 24, 200 m from top to bottom, 66 m of reservoir thickness consisting of layers 4-6). The initial stresses for the reservoir layers are kept the same as in the 2-D case. The cap and base rocks have been again assumed to be strong enough against shear or tensile fracturing such that the SRV only grows within the 66m pay zone.

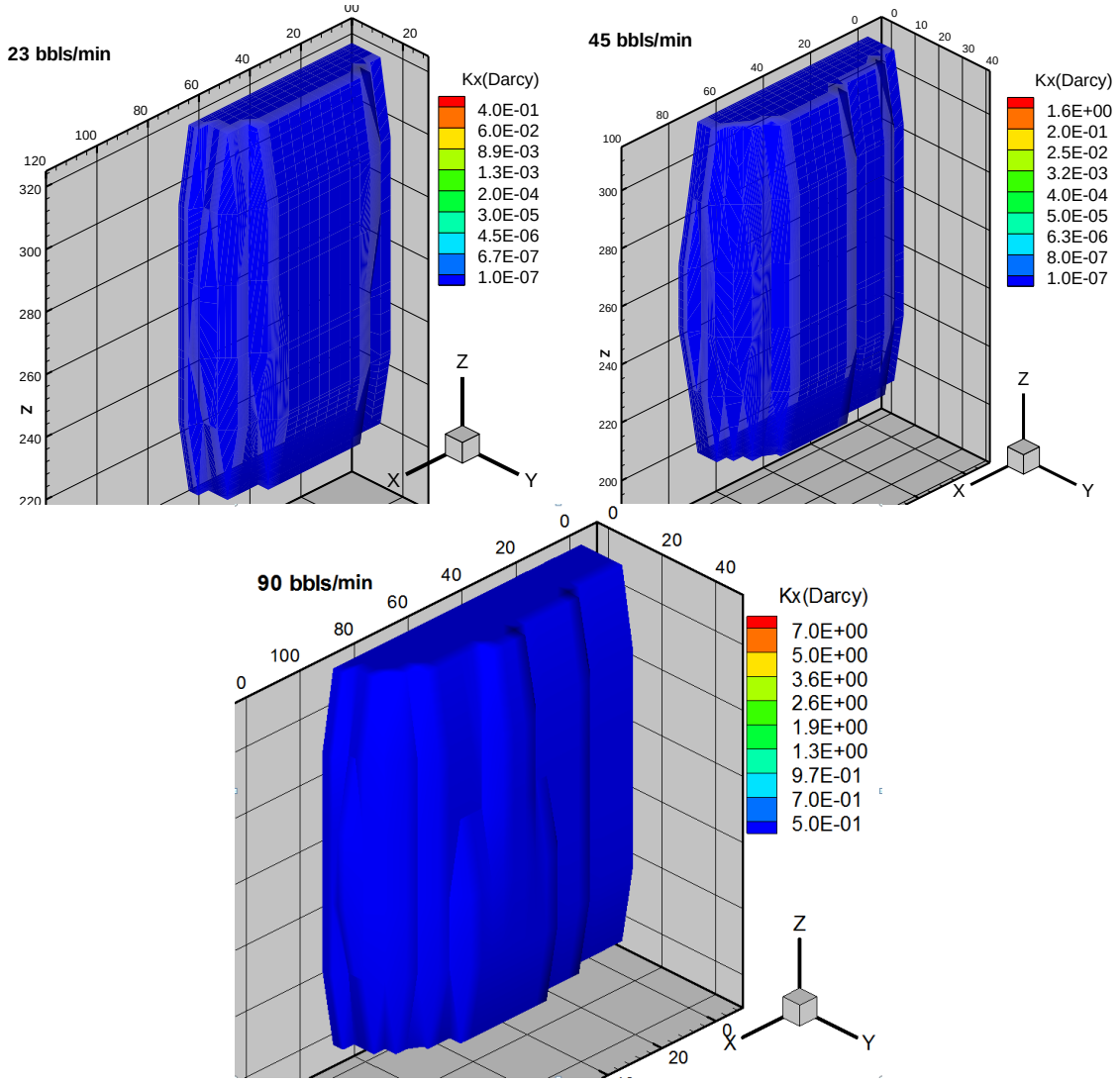

Figure 6.33 – Induced 2-D SRV development for three different injection rates

The SRV propagations for the three low, mid and high injection rates are presented in Figure 6.33. Since we compare results for the same stimulation period, increasing the

rate also means increasing the treatment volume. As one expects, the SRV size increases with the injection rate (or volume); likewise the maximum permeability enhancement also rises with the treatment volume. In the case of the injection rate of 23 bbls/min, the running time was about 4 hours, for 45 bbls/min the running time was around 8 hours and for the maximum injection rate of 90 bbls/min the respective value reached about 9 hours.

Similar to what resulted in the 2-D example analysis, higher injection rate steepens the well block pressure versus time curve as shown in Figure 6.34. In all three tested injection rates the main rise in the pressure profile occurred at the early time and pressure exceeded significantly the minimum total stress of 63000 kPa. In the case of 23 bbls/min injection rate only primary shear fracturing occurred, but secondary fracturing was observed in the mid and high injection rates. The well block strain in the y direction reaches values as high as 0.0025. This gives the equivalent displacement in the full field model of 5 mm. It should be noted that the well block (which was crushed) contains two shear fracture sets with 0.2 m of fracture spacing in addition to the tensile fracture; the block in total undergoes 5 mm of deformation in the y direction.

In Section 6.2.2 the significance of the rock cohesion on the overall shape of SRV has been discussed. The sensitivity of the above results to this parameter is presented next. Figure 6.35 presents the shape of SRV for the case of 23 bbls/min injection rate when the rock cohesion is chosen to be 2 MPa instead of 0.5 MPa. The induced SRV almost resembles a single tensile plane of fracture with only minor shear fracture development at the sides.

The well block pressure as indicated in Figure 6.36 remains almost constant after an early drop which is the typical for the low viscous fluid injection in the field. The effective stress in the x direction increases with time; however secondary shear fracturing will not occur due to the relatively higher rock cohesion. Strain component in y direction increases with time (0.005 x 0.5m = 2.5 mm, 5mm in the full field model), the respective value in z direction however declines after a slight increase in the early time. This is explained by the creation of conjugate shear fracture planes between the maximum direction of z and the minimum direction of y in the well block first and the blocks around it afterward.

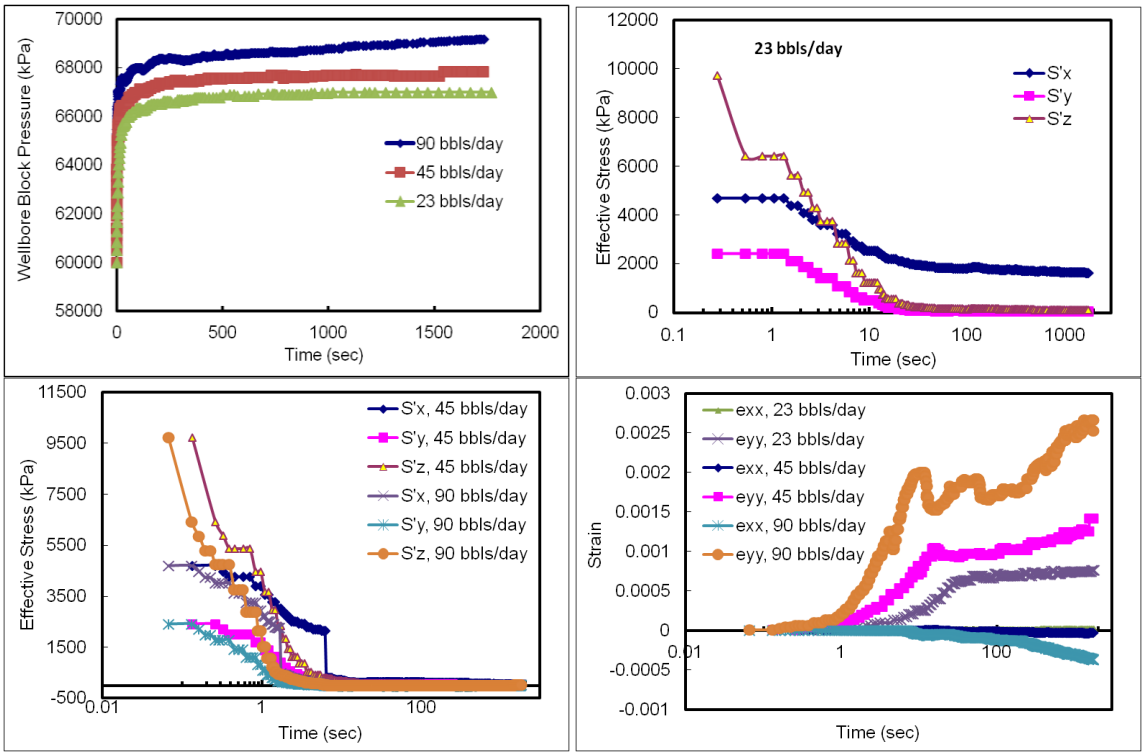

Figure 6.34 – Well block pressure, effective stresses and x, y strain components in the first Gauss point of the well block (4m x 0.5m x 22m) for the 2nd example, 3-D model

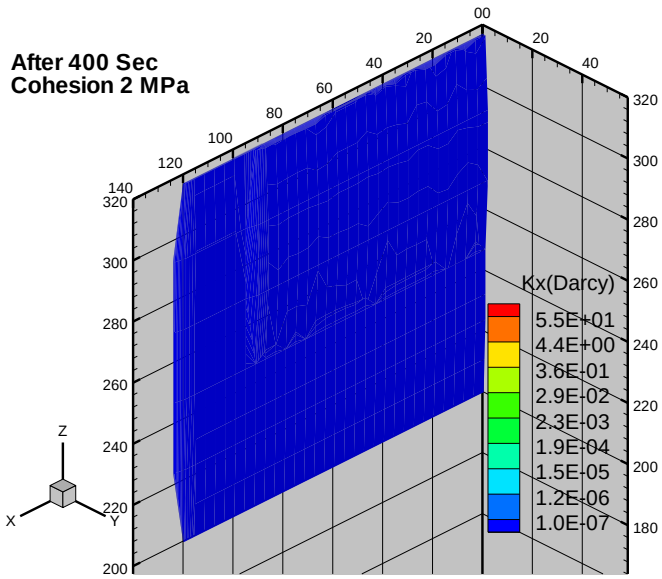

Figure 6.35 – Induced SRV after 400 seconds of stimulation in the crushed fracturing case – cohesion 2 MPa

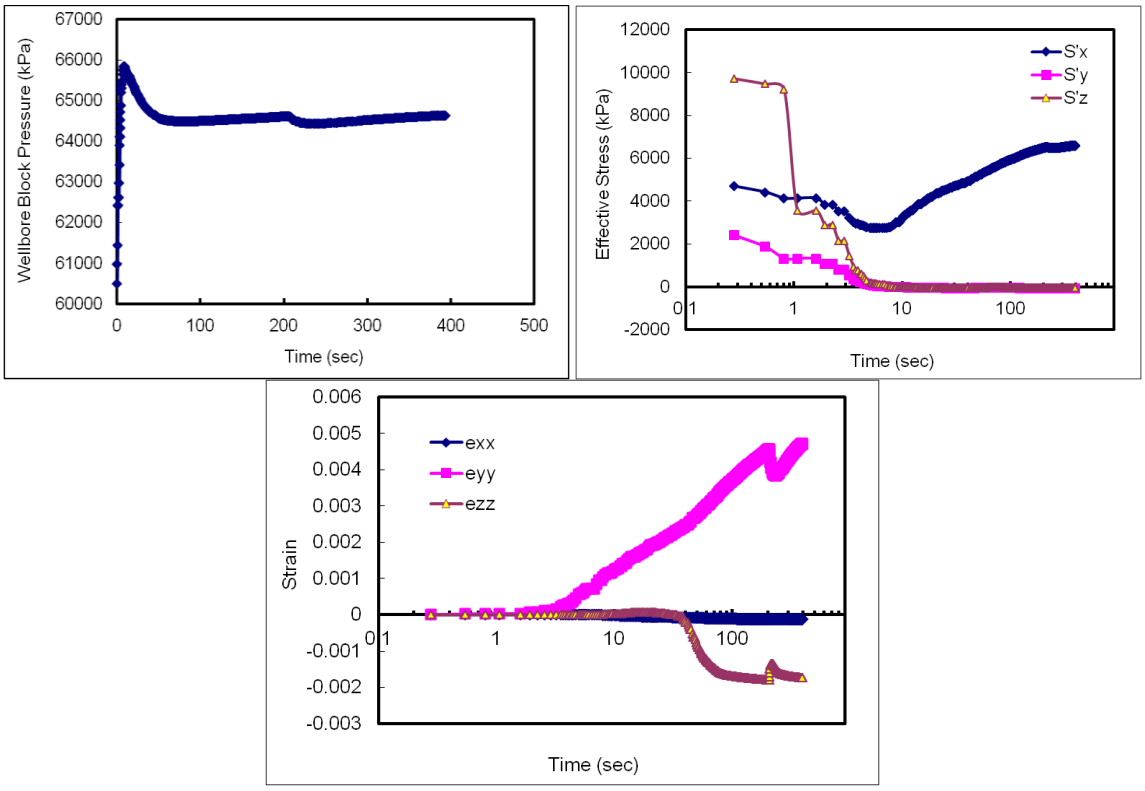

Figure 6.36 – Pressure, effective stresses and strain in the first Gauss point of the well block in the 3-D model – cohesion 2 MPa

CHAPTER 7 - CONCLUSIONS & RECOMMENDATIONS

During the course of this research project, dynamic tensile/shear fracturing which occurs in stimulation of unconventional reservoirs was studied and modeled by the use of an iteratively coupled single phase flow/geomechanical code. Permeability was the main coupling term between the flow and geomechanical modules.

The developed code captured successfully the main aspects of the dynamic fracturing problem including:

1) fluid flow injection and the respective pore pressure variation in the porous media,
2) variation in the stress/strain tensors for each reservoir block prior fracturing,
3) dynamic creation of tensile and shear fractures in the model elements when their respective failure (fracturing) criteria are met,
4) shear softening behavior after fracture creation due to sudden release of the stored elastic energy, and its modeling by force-rebalancing technique
5) estimating the mechanical behavior of the fractured blocks both in normal and shear directions by pseudo-continuum approach,
6) Changing the permeability tensor in failed blocks as a function of creation and further deformation of the fractures, and its link to flow modeling,
7) predicting the extent of the stimulated reservoir volume (SRV) and the permeability distribution within the SRV during the formation stimulation.

The above were the main elements of the developed code; however integration of all the parts required implementation or development of other techniques as well. Some examples are: the use of an efficient non-symmetric solver (bi-conjugate gradient solver), special techniques in managing the allocated memory for all required arrays including the global stiffness matrix, solver, all Gauss points' state variables, special techniques for time step control, and so on.

7.1 Conclusions

We have succeeded to model simultaneous development of tensile and shear fracturing, as well as the phenomena of secondary shear fracturing (leading to "block crushing"), it occurs in well stimulation.

The numerical techniques developed can accurately represent elasto-plastic shear behavior of created (or existing) fractures including shear softening and dilation. Extensive validation of the code on examples contributed significant insight into the combined normal and shear behavior of the fractures induced in well stimulation.

It is believed that the model is sufficiently realistic to be used in predictive mode for estimating the size and permeability of the SRV. Therefore the methodology developed in this work can be now applied to optimization of the multi-stage stimulation treatments with respect to fracturing job parameters, which is a significant advance compared to existing tools.

Simulation results of field applications indicate a substantial difference between the cases where tensile fracturing is the dominant mechanism and the cases where the initial reservoir conditions are such that the shear fracturing is the dominant fracturing mechanism. Some of the major differences between the two cases when water is the stimulation fluid are listed below in a table:

Table 7.1 – Tensile and shear dominated fracturing comparison

Tensile dominated fracturing	**Shear dominated fracturing**
A large SRV with considerable width is generated, an opening path for proppant injection sometime is created in the middle	A single tensile fracture is created, the length of the created fracture is substantially longer in comparison
A continuous raise in the well block pressure for 2-D and 3-d cases	An almost constant well block pressure for 3-D and declining for 2-D cases
Well block pressure is substantially higher than the minimum total stress	Well block pressure is slightly higher than the minimum total stress

Permanent permeability enhancement due to dilation	Considerable permeability enhancement if proppant is injected

Fracturing analysis revealed that the closeness of the initial reservoir conditions to the shear failure surface is the main cause for the shear failure to be the dominant fracturing mechanism. Low formation rock cohesion, high contrast between the initial total stresses and abnormally high reservoir initial pore pressure are some factors increasing tendency for shear failure. The levels of rock cohesion below which relatively wide SRV's were observed in the simulations were of low magnitude (less than 1 MPa). Therefore, only in formations where the rock is weakened by pre-existing fractures or micro fractures, a large and wide SRV is probable; otherwise conventional tensile fracturing mechanism will prevail.

The main problem with stimulation of tight formations (such as shale gas reservoirs) is the very low matrix permeability which substantially impedes the injected fluid from diffusing and pressurizing the blocks that are about to join the body of the SRV. The pre-existing opened micro-fractures might expedite this process and the subsequent shear fracturing. This phenomenon can be modeled by stress-dependent matrix permeability and has been used successfully in several detailed studies in tight gas (Settari et al., 2002; Settari et al., 2009; Islam et al., 2012) Although it was not captured in this research work, it is thought to play a significant additional role in the SRV modeling. Thermal effect has also not been investigated in this study. Cooling the formation creates tensile stresses which may lead to secondary tensile fracturing (Tran et al., 2012). Created permeability might have a significant influence on the SRV growth. These aspects will be investigated in future studies.

In general the pseudoization or averaging technique appears to be an efficient tool in the SRV modeling in terms of capturing the main physical aspects of fracturing, while being time-efficient. Numerically discrete consideration of fracture networks in a big model, although having the potential to be more accurate in cases with large dominant fractures, require a large number of elements both for the intact rock and the fracture sets

which heavily increases the running time and requires detailed data on the fracture network. It should be emphasized that a modeling problem involving dynamic fractures is highly non-linear and requires iterations to eliminate out of balance forces. Furthermore, whenever some fracture sets are added to a certain block either in the primary or secondary fracturing phase, a repeat in the time step is required. The time repeat was found to be a significant factor in escalating the running time.

7.2 Recommendations

There are still several details which require further study and development both in the flow and geomechanical parts of the code resulting from the current work. Most of these are concerned with extending the physics or further integration of the system components. Some of the recommended studies on the fluid flow part might be:

1) Extension of the 3-D flow model to multi-phase flow
2) Inclusion of the thermal effect which requires further development in the flow model. The fracturing fluid in the hydraulic fracturing operation is usually colder than the formation fluid and there will be a considerable thermal effect on the stresses and therefore final fracturing results
3) In the current developed code at any time step in the flow module, the permeability term is assumed to be constant. A non-linear pressure dependent permeability function for the fractured rock in the flow module can be defined to better estimate the elements pressures changes. The permeability function can then be corrected by the stress-strain results of the geomechanical solution following the flow solution
4) Determining the fractured block compressibility from the stress-strain data and implementing it in the flow solution
5) In real shale gas reservoirs, the reservoir rock is macroscopically and microscopically fractured, heterogeneous such that the linear elastic and simple Mohr-Coulomb failure criterion for the non-stimulated rock may not be a valid assumption. A recommended and better approach is to assume that pre-existing

natural fractures exist in the reservoir rock such that pseudo-continuum constitutive model accounts for the jointed reservoir rock prior to being stimulated. The challenge is to specify an appropriate mean friction angle and specially an average cohesion for the naturally fractured rock. It should be recalled that in the presented example problems in the Model Application Chapter, the upper limit of rock cohesion below which a wide SRV has been generated was as low as 1 MPa. Since intact non-fractured shale cohesion is typically at least an order of magnitude higher than 1 MPa, unless the reservoir rock is weakened by some natural failure planes, there would be no justification for such low rock cohesion. Therefore the small-scale heterogeneity characterization is important for future applications.

The geomechanical part and the coupled software would also benefit from further work. Some of the issues suggested are:

1) Further work on the post-failure shear softening part which implements the mobilized friction angle and large exponent coefficient value to soften the material. We have encountered some divergence problems in the Newton solution due to presence of strong shear softening while the stress path is moving toward tensile failure surface.
2) Optimization of the numerical solution such as adding pre-conditioners to the non-symmetric bi-conjugate solver, minimizing the required memory storage for the existing arrays, etc.
3) Running more example problems with different input data to further sensitize the problem with respect to various input variables. The goal would be to provide practicing engineers with some guidelines about expected behavior of the SRV as a function of operating conditions and geomechanical parameters.

It would be also desirable to apply the developed code for the analysis of field hydraulic fracturing data with sufficient data to perform detailed history match and field calibration. This exercise would also provide real bounds on some of the geomechanical data, especially for the created shear fractures. Unfortunately, such study was beyond the scope

of this thesis, but it is hoped that the code developed here will be used in the future in this mode.

References

Amadei, B. and S. Saeb (1990), "Constitutive Models of Rock Joint", Rock Joints (Barton & Stephansson, eds.) Conference, Balkemma, Rotterdam.

Archambault, G., M. Fortin, D. E. Gill, M. Aubertin and B. Ladanyi (1990), "Experimental Investigation for an Algorithm Simulating the Effect of Varaible Normal Stiffness on Discontinuities Shear Strength", Proc. Int. Symp. on Rock Joints, Loen, Norway, Balema.

Bagheri, M. and A. Settari (2006), "Modeling Geomechanical Effects on the Flow Properties of Fractured Reservoirs", Dept. of Chemical & Petroleum Eng., University of Calgary.

Bandis, S. C., A. C. Lumsden and N. R. Barton (1983), "Fundamental of Rock Joint Deformation", Int. J. Rock Mech. and Min. Sci. & Gemech. Abstr., Vol. 20 (6), pp. 249-268.

Barree, R. D. and P. H. Winterfeld (1988), "Effect of Shear and Interfacial Slippage on Fracture Growth and Treating Pressure", SPE 48926.

Barton, N. (1973), "Review of a New Shear-Strength Criterion for Rock Joints", Eng. Geo., Vol. 7 (4), pp. 287-332.

Barton, N. and S. Bandis (1982), "Effects of Block Size on the Shear Behavior Jointed Rock", 23rd U.S. Symp. on Rock Mechanics. Berkeley, California.

Barton, N., S. Bandis and B. K. (1985), "Strength, Deformation and Conductivity Coupling of Rock Joints", int. J. Rock Mech. Min. Sci. & Gemech. Abstr., Vol. 22 (3), pp. 121-140.

Barton, N. and V. Choubey (1977), "The Shear Strength of Rock Joint in Theory and Practice", Rock Mechanics, Vol. 10 pp. 1-54.

Barton, N. R. (1986), "Deformation Phenomena in Jointed Rock", Geotechnique, Vol. 36 (2), pp. 147-167.

Barton, N. R. and V. Choubey (1977), "The shear strength of rock joints in theory and practice", Rock Mechanics, 10 pp. 1-54.

Beer, A. J., D. Stead and J. Coggan (2002), "A Critical Assessment of Discontinuity Roughness Characterization", J. Rock Mech. Rock Eng., Vol. 35 pp. 65-74.

Belytschko, T. and R. Gracie (2007), "On XFEM Applications to Dislocations and Interfaces", Int. J. Plasticity, Vol. 23 (10), pp. 1721-1738.

Boulon, M. and R. Nova (1990), "Modeling of Soil-Structure Interface Behavior- A Comparison Between Elastoplastic and Rate Type Laws", Computers and Geomechanics, Vol. 9 pp. 21-46.

Brady, B. H. G. and E. T. Brown (2004), "Rock Mechanics of Underground Mining", Page: 588.

Cai, M. and H. Horii (1992), "A Constitutive Model of Highly Jointed Rock Masses", Mechanics of Materials, Vol. 13 pp. 217-246.

Carter, R. D. (1957), "Derivation of the General Equation for Estimating the Extent of the Fractured Area", Appendix I of 'Optimum Fluid Characteristics for Fracture Extension', Drilling and Production Practice, G.C. Howard and C.R. Fast, New York, New York, American Petroleum Institute pp. 261-269.

Chen, Z. (2008), "Reservoir Simulation: Mathematical Techniques in Oil Recovery", Cambridge University Press.

Chin, L., R. R. Boade, J. H. Prevost and G. H. Landa (1993), "Compaction in the Ekofisk Reservoir", Int. J. Rock Mech. Min. Sci. @ Geomech, Vol. 30 (7), pp. 1193-1200.

Cho, N., C. D. Martin and D. C. Sego (2007), "A Clumped Particle Model for Rock", Int. J. Rock Mech. Min. Sci., 44 (7), pp. 997-1010.

Chuprakov, D. A., A. V. Akulich and E. Siebrits (2010), "Hydraulic Fracture Propagation in a Natuarally Fractured Reservoir", SPE Oil and Gas India Conference, Mumbai, India.

Cipolla, C. L., N. R. Warpinski and M. J. Mayerhofer (2008), "Hydraulic Fracture Complexity: Diagnosis, Remediation, and Exploitation", SPE (115771).

Cleary, M. P., R. G. Keck and M. E. Mear (1983), "Microcomputer Models for the Design of Hydraulic Fractures", SPE/DOE Symposium on Low Permeability, Denver, Colorado, USA. SPE 11628.

Cleary, M. P. and K. Y. Lam (1983), "Development of a Fully Three-Dimensional Simulator for Analysis and Design of Hydraulic Fracturing", SPE/DOE Symposium on Low Permeability, Denver, Colorado, USA. SPE 11631.

Clifton, R. J. and A. S. Abou-Sayed (1981), "A Variational Approach to the Prediction of the Three-Dimensional Geometry of Hydraulic Fractures", SPE/DOE Symposium on Low Permeability, Denver, Colorado, USA., SPE 9879.

Clough, G. W. and J. M. Duncan (1971), "Finite Element Analysis of Retaining Wall Behavior", J. Soil Mech. Found. Div., Vol. 97 (12), pp. 1657-1673.

Cook, R. D., D. S. Malkus and M. E. Plesha (1989), "Concepts and Applications of Finite Element Analysis", New York, Wiley.

Cundall, P. and J. V. Lemos (1988), "Numerical Simulation of Fault Instabilities with a Continuously Yeilding Joint Model", Proc. of the 2nd Int. Symp. on Rockbursts and Seismicity in Mines, Minneapolis. pp. 147-152.

Cundall, P. A. and R. D. Hart (1992), "Numerical Modeling of Discontinua", J. Eng. Comput., Vol. 9 pp. 101-114.

Dahi-Taleghani, A. and J. E. Olson (2009), "Numerical Modeling of Multi-stranded Hydraulic Fracture Propagation: Accounting for The Interaction Between Induced and Natural Fractures", SPE 124884, SPE Annual Conference and Exhibition, New Orleans, Louisiana, USA.

Dennis, J. E. and R. B. Schnabel (1983), "Numerical Methods for Unconstrained Optimization and Nonlinear Equations", Prentice-Hall.

Desai, C. S. and K. L. Fishman (1987), "Constitutive Models for Rocks and Discontinuities", Proc. 28th US Symp. on Rock Mechanics, Tucson, Arizona. pp. 609-619.

Economides, M. J. and K. G. Nolte (2000), "Reservoir Stimulation ", Third Edition, Wiley.

England, A. H. and A. E. Green (1963), "Some Two-Dimensional Punch and Crack Problems in Classical Elasticity", Proceedings Cambridge Phil. Soc., Vol. 59 pp. 489-500.

Fossum, A. F. (1985), "Effective Elastic Properties for a Randomly Jointed Rock Masses", Int. J. Rock Mech. Min. Sci. & Gemech. Abstr., Vol. 22 (6), pp. 467-470.

Gale, J. F. W., R. M. Reed and J. Holder (2007), "Natural Fractures in the Barnett Shale and Their Importance for Hydraulic Fracture Treatment", AAPG Bulletin, Vol. 91 (4), pp. 603-622.

Geertsma, J. and F. d. Klerk (1969), "A Rapid Method of Predicting Width and Extent of Hydraulically Induced Fractures.", J. Pet. Tech., Vol. 21 pp. 1571–1581.

Gerasseli, G. and P. Egger (2003), "Constitutive Law for Shear Strength of Rock Joints Based on Quantitative 3-Dimensional Surface Parameters", Int. J. Rock Mech. Min. Sci., Vol. 40 (1), pp. 25-40.

Gerrard, C. M. (1982), "Elastic Models of Rock Masses Having One, Two and Three Sets of Joints", Int. J. Rock Mech. Min. Sci. & Gemech. Abstr., Vol. 19 pp. 15-23.

Gerrard, C. M. and G. N. Pande (1985), "Numerical Modeling of Reinforced Jointed Rock Masses. I. Theory", Comput. Geotech., Vol. 1 pp. 293-318.

Ghaboussi, J., E. L. Wilson and J. Isenberg (1973), "Finite Element for Rock Joints and Interfaces", J. Soil Mech. Found. Div. Proc. ASCE, Vol. 99 pp. 833-848.

Gidley, J. L., S. A. Holditch, D. E. Nierode and J. R. W. Veach (1989), "Recent Advances in Hydraulic Fracturing", Soc. of Pet. Eng. , Richardson, TX. pp. 243-267.

Goodman, R. E. (1976), "Methods of Geological Engineering in Discontinuous Rocks". San Francisco, West Publishing Company.

Hill, R. (1963), "Elastic Properties of Reinforced Solids: Some Theoretical Principles", J. Mech. Phys. Solids, Vol. 11 pp. 357-372.

Hoek, E. (1983), "Strength of Jointed Rock Masses", Geotechnique, Vol. 33 (3), pp. 187-223.

Hossain, M. M., M. K. Rahman and S. S. Rahman (2002), "A Shear Dilation Stimulation Models for Production Enhancement from Naturally Fractured Reservoirs", SPE 78355.

Howard, G. C. and C. R. Fast (1970), "Hydraulic Fracturing", Dallas TX, Millent the Printer.

Islam, A., A. Settari and V. sen (2012), "Productivity Modeling of Multifractured Horizontal Wells Coupled with Geomechanics - Comparison of Various Methods", SPE 162793, Canadian Unconventional Resources Conference. Calgary, Alberta.

Jaeger, J. C. (1971), "Friction of Rock and Stability of Rock Slopes", Geotechnique, Vol. 21 (2), pp. 97-134.

Jeffrey, R. G., X. Zhang and A. P. Bunger (2010), "Hydraulic Fracturing of Naturally Fractured Reservoirs", Thirty-Fifth Workshop on Geothermal Reservoir Engineering, Stanford University, Stanford, California.

Ji, L. and A. Settari (2008), "Modeling Hydraulic Fracturing Fully Coupled with Reservoir and Geomechanical Simulation", Dept. Chemical & Petroleum Eng., University of Calgary.

Jing, L. (1990), "Numerical Modeling of Jointed Rock Masses by Distinct Element Method for Two and Three Dimensional Problems", Lulea University of Technology.

Jing, L., E. Nordlund and O. Stephansson (1994), "A 3-D Constitutive Model for Rock Joints With Anisotropic Friction and Stress Dependency in Shear Stiffness", Int. J. Rock Mech. Min. Sci. & Geomech. Abstr., Vol. 31 (2), pp. 173-178.

Kaliakin, V. N. (2001), "Introduction to Approximate Solution Techniques, Numerical Modeling, and Finite Element ethods", Taylor & Francis.

Karami, A. and D. Stread (2007), "Asperity Degradation and Damage in the Direct Shear Test: A Hybrid FEM/DEM Approach", Rock Mech. Rock Engng. - Springer DOI 10.1007/s00603-007-0139-6.

Keck, R. G., M. P. Cleary and A. Crockett (1984), " A Lumped Numerical Model for the Design of Hydraulic Fractures", SPE/DOE/GRI Unconventional Gas Recovery Symposium, Pittsburgh, PA, USA. SPE/DOE/GRI 12884.

Keshavarzi, R. and S. Mohammadi (2012), "A New Approach for Numerical Modeling of Hydraulic Fracture Propagation in Naturally Fractured Reservoirs", SPE/EAGE European Unconventional Resources Conference and Exhibition, Vienna, Austria.

Kulatilake, P. H. S. W., A. Fellow, J. Liang and H. Gao (2001), "Experimental and Numerical Simulation of Jointed Rock Block Strength Under Uniaxial Loading", Journal of Engineering Mechanics, Vol. 127 (12).

Kulatilake, P. H. S. W. and B. Maama (2004), "A new model for normal deformation of single fractures under compressive loading", ARMA/NARMS, Vol. 4 (511).

Kulatilake, P. H. S. W., G. Shou, T. H. Huang and R. M. Morgan (1995), "New Peak Shear Strength Criteria for Anisotropic Rock Joints", Int. J. Rock Mech. Min. Sci. Gemech. Abstr., Vol. 32 (7), pp. 673-697.

Kulatilake, P. H. S. W., J. Um, B. B. Panda and N. Nghiem (1998), "Development of a New Shear Strength Criterion for Anisotropic Rock Joints", Int. J. Rock Mech. Min. Sci., Vol. 35 pp. 4-5.

Ladanyi, B. and G. Archambault (1969), "Simulation of Shear Behavior of a Jointed Rock Mass", Proc. of the Symposium on Rock Mechanics, "Rock Mechanic - Theory and Practice", Berkeley, CA. Chapter 7. pp. 105 -125.

Laubach, S. E. (2003), "Practical Approaches to Identifying Sealed and Opened Fractures", AAPG Bulletin, Vol. 7 (4), pp. 561-579.

Lewis, R. W. and B. A. Schrefler (1998), "The Finite Element Method in the Static and Dynamic Deformation and Consolidation of Porous Media", Chichester, Wiley.

Lin, J. S. and K. Cheng-Yu (2006), "Two-Scale Modeling of Jointed Rock Masses", Int. J. Rock Mech. and Min. Sci., Vol. 43 pp. 426-436.

Mahin Roosta, R., M. H. Sadaghiani, A. Pak and Y. Saleh (2006), "Rock Joint Modeling Using a Visco-Plastic Multilaminate Model at Constant Normal Load Condition", Geotechnical and Geological Engineering, Vol. 24 pp. 1449-1468.

McLennan, J., D. Tran, N. Zhao, S. Thakur, M. Deo, I. Gil and B. Damjanac (2010), "Modeling Fluid Invasion and Hydraulic Fracture Propagation in Naturally Fractured Rock: A Three-Dimensional Approach", International Symposium and Exhibition on Formation Damage Control, Lafayette, Louisiana, USA.

Morris, J. P., M. B. Rubin, S. C. Blair, L. A. Glenn and F. F. Heuze (2004), "Simulation of Underground Structures Subject to Dynamic Loading Using Distinct Element Method", Eng. Comp., Vol. 21 pp. 384-408.

Nassir, M., A. Settari and R. Wan (2009), "Joint Stiffness and Deformation Behavior of Discontinuous Rock", J. Canadian Petroleum Tech., Vol. 49 (9), pp. 78-86.

Nassir, M., A. Settari and R. Wan (2012), "Prediction and Optimization of Fracturing in Tight Gas and Shale using a Coupled Geomechanical Model of Combined Tensile and Shear Fracturing", SPE 152200. The Woodlands, Texas.

Nassir, N., A. Settari and R. Wan (2010), "Modeling Shear Dominated Hydraulic Fracturing As a Coupled Fluid-Solid Interaction", SPE 131736, SPE International Oil & Gas Conference and Exhibition, Beijing, China.

Nguyen, T. S. and A. P. S. Selvadurai (1998), "A Model for Coupled Mechanic and Hydraulic Behavior of Rock Joints", Int. J. Numer. Anal. Meth. Geomech., Vol. 22 pp. 29-48.

Nicot, F., F. Darve and H. D. V. Khoa (2007), "Bifurcation and Second-Order Work in Geomaterials", Int. J. Num. Anal. Methods in Geomechanics.

Nordgern, R. P. (1972), "Propagation of Vertical Fracture", SPEJ pp. 306-314.

Palmer, I., Z. Moschovidis and J. Cameron (2007), "Modeling Shear Failure and Stimulation of the Barnett Shale After Hydraulic Fracturing", SPE 106113.

Patton, F. D. (1966), "Multiple Modes of Shear Failure in Rock", Proc. First congress of Int. Soc. Rock Mech., Lisbon. Vol. 1. pp. 509-513.

Plesha, M. E. (1987), "Contitutive Model for Rock Discontinuities with Dilatancy and Surface Degradation", Int. J. Num. Analy. Methods in Geomech., Vol. 11 pp. 345-362.

Plesha, M. E. (1997), "Constitutive Models and Numerical Methods for Discontinuities in Rock", Computer Methods and Advances in Geomechanics, Balkema, Rotterdam. pp. 217-224.

Rahman, M. M. and S. S. Rahman (2009), "A Fully Coupled Numerical Poroelastic Model to Investigate Interaction Between Induced Hydraulic Fracture and Pre-existing Natural Fracture in a Naturally Fractured Reservoir: Potential Application in Tight Gas and Geothermal Reservoirs", SPE124269, SPE Annual Technical Conference and Exhibition, New Orleans, Louisiana, USA.

Roberts, W. J. and H. H. Einstein (1978), "Comprehensive Model Rock Discontinuities", J. Geotech. Engng., Proc. ASCE, Vol. 104 pp. 553-569.

Saada, A. and G. Bianchini (1987), "Constitutive Equations for Granular Non-cohesive Soils", Proc. of the Int. Workshop on Constitutive Equations, Clevend, Balkema.

Seidel, J. P. and C. M. Haberfield (1995), "The Application of Energy Principles to the Determination of Sliding Resistance of Rock Joints", Rock Mech. Rock Eng., Vol. 28 (4), pp. 211-226.

Selvadurai, A. P. S. and M. Boulon (1995), "Mechanics of Geomaterials Interfaces", Vol. 42, Elsevier, Amesterdam.

Settari, A. (2007), "Reservoir Geomechanics", Dept. of Chem. & Pet. Eng., University of Calgary.

Settari, A. and M. P. Cleary (1984), "Three-Dimensional Simulation of Hydraulic Fracturing", JPT, Vol. 36 (7), pp. 1177-1190.

Settari, A. and A. Mourits (1998), "Coupled Reservoir and Geomechanical Simulation System", SPEJ pp. 219-226.

Settari, A., R. B. Sullivan and R. C. Bachman (2002), "The Modeling of the Effect of Water Blockage and Geomechanics in Waterfracs", SPE 77600, Annual Techn. Conf. of SPE. SPE, San Antonio, TX.

Settari, A., R. B. Sullivan, G. Turk, J. Rueda, R. Rother and T. Skinner (2009), "Comprehensive coupled modeling analysis of stimulations and post-frac productivity – case study of the Wyoming field", Paper SPE 119394, presented at the 2009 SPE Hydraulic Fracturing Technology Conference. The Woodlands, Texas, USA.

Singh, B. (1973), "Continuum Characterization of Jointed Rock Masses. Part I - The Constitutive Equations", Int. J. Rock Mech. Min. Sci. Geomech., Vol. 10 pp. 311-335.

Sneddon, I. N. and M. Lowengrub (1969), "Crack Problems in the Classical Theory of Elasticity", New York, John Wiley & Sons Inc.

Son, B. K., Y. K. Lee and C. I. Lee (2004), "Elasto-Plastic Simulation of Direct Shear Test on Rough Rock Joints", Int. J. Rock Mech. and Min. Sci., Vol. 41 (3),

Swan, G. (1980), "Stiffness and Associated Joint Properties of Rock", Proc. Conf. on Applications of Rock Mechanics to Cut-and-Fill Mining, University of Lulea, Sweden.

Tao, Q., C. A. Ehlig-Economides and A. Ghassemi (2009), "Investigation of Stress-Dependent Fracture Permeability in Naturally Fractured Reservoir Using a Fully Coupled Poroelastic Displacement Discontinuity Model", SPE, 124745, SPE Annual Technical Conference and Exhibition, New Orleans, Louisiana, USA.

Teufel, L. W. and D. W. Rhett (1991), "Geomechanical Evidence for Shear Failure of Chalk During Production of the Ekofisk Field", SPE 22755.

Tran, D., A. Settari and L. Nghiem (2012), "Initiation and Propagation of Secondary Cracks in Thermo-Poroelastic Media", ARMA 12-252, 46th US Rock Mechanics / Geomechanics Symposium. Chicago, IL, USA.

Wan, R. (2010), "Continuum Mechanics & Constitutive Laws Notes". Calgary, University of Calgary.

Wan, R., M. Alsaleh and J. Labuz (2011), "Bifurications, Instabilities and Degradations in Geomaterials", Springer - Verlag Berlin Heidelberg.

Wang, J. G., Y. Ichikawa and C. F. Leung (2003), "A Constitutive Model for Rock Interfaces and Joints", Int. J. Rock Mech. and Min. Sci., 40 pp. 41-53.

Warpinski, N. R. and L. w. Teufel (1987), "Influence of Geologic Discontinuities on Hydraulic Fracture Propagation", J. Pet. Tech., Vol. 209

Wawrzynek, P. (1997), "GEOSIM-TRS manual - Elato-Plastic Material Capabilities in FEM3D".

Weijers, L., C. Wright, M. Mayerhofer and C. Cipolla (2005), "Developing Calibrated Fracture Growth Models for Various Formations and Regions Across the United States", SPE 96080 presented at SPE Annual Technical Conference and Exhibition, Dallas, Texas. 96080.

Yang, Z. Y. and D. Y. Chiang (2000), "An Experimental Study on the Progressive Shear Behavior of Rock Joints with Tooth-shaped Asperities", Int. J. Rock Mech. Min. Sci., Vol. 35 (8), pp. 1051-1070.